

F-191-83
P. 11

MICROSTRUCTURE AND MECHANICAL PROPERTIES OF RHEOCAST ALUMINIUM-COPPER ALLOYS

A THESIS

submitted in fulfilment of the
requirements for the award of the degree

of

~~University of Roorkee, Roorkee~~

DOCTOR OF PHILOSOPHY

Certified that the attached Thesis/
Dissertation has been accepted for the
award of Degree of ~~Doctor~~
Philosophy / ~~Master of Engineering~~

in

METALLURGICAL ENGINEERING

Met. Engg. vide notification
No. Ex. 12/P-65 (Degree) dated 10.4.1984



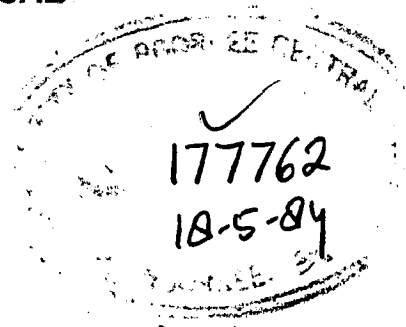
By

Signature

PRIYA RANJAN PRASAD

Asstt. Registrar (Exam)

Signature



12/5/84
20.7.84

DEPARTMENT OF METALLURGICAL ENGINEERING
UNIVERSITY OF ROORKEE
ROORKEE-247667 (INDIA)

August 1983

Gratis

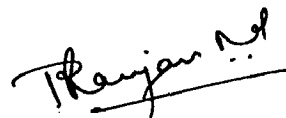


CANDIDATE'S DECLARATION

I hereby certify that the work which is being presented in the thesis entitled 'MICROSTRUCTURE AND MECHANICAL PROPERTIES OF RHEOCAST ALUMINIUM-COPPER ALLOYS' in fulfilment of the requirement for the award of the Degree of Doctor of Philosophy, submitted in the Department of METALLURGICAL ENGINEERING of the University is an authentic record of my own work carried out during a period from July 1980 to June 1983 under the supervision of Dr.S.Ray, Dr.J.L.Gaindhar and Dr.M.L. Kapoor.

The matter embodied in this thesis has not been submitted by me for the award of any other degree.

August 1, 1983



(PRIYA RANJAN PRASAD)

This is to certify that the above statement made by the candidate is correct to the best of my knowledge.



(J.L. GAINDHAR)

Reader

Department of Mech. and Ind.Engg
University of Roorkee, Roorkee.



(S. RAY)

Reader

Department of Met. Engineering
University of Roorkee, Roorkee



(M.L. Kapoor)

Prof. and Head

Department of Met. Engineering
University of Roorkee, Roorkee.

ABSTRACT

Rheocasting is an emerging casting technique in which a liquid alloy is vigorously agitated during its partial solidification to yield a slurry comprising of non-dendritic solid particles uniformly suspended in the remaining liquid. Such a slurry is subsequently cast into desired shapes by conventional methods. Most of the investigations relating to this process deal with the structure and rheological behaviour of alloy slurries and are primarily aimed at process development rather than product characterisation. A critical survey of the published literature reveals that the interrelationship of processing, microstructure and mechanical properties of rheocast products has not yet been clearly understood and therefore, the need for a detailed study of the microstructural features of rheocast products and their role in modifying the mechanical properties cannot be overemphasized.

In view of the above, the present investigation has been undertaken to study the microstructure and mechanical properties of rheocast Al-Cu alloys in the composition range of 4.5 to 10 Wt. % copper. The Al-Cu system has been chosen for the study because of large amount of available information regarding its solidification characteristics and also because this system forms base for a large number of industrially important alloys in this composition range.

Three alloys of nominal composition Al-4.5 Wt.% Cu, Al-6 Wt.% Cu and Al-10 Wt.% Cu have been used for making rheocastings. The microstructural features of rheocastings such as, morphology, size and distribution of proeutectic α -phase have been studied by optical microscopy and the effects of rheocasting parameters, pouring temperature and stirring speed, have been examined. Tensile tests have been performed to evaluate the strength of castings and tensile fractured surfaces have been examined under Scanning Electron Microscope (SEM) to study the fracture behaviour. For a better understanding of the physical metallurgy of the mechanical properties, the rheocastings have been modeled as particulate composites containing ductile α -particles and brittle α +CuAl₂ eutectic. Two theoretical models for the strength of rheocast alloys- one for the case when eutectic is continuous and the other, for the case when α -particles join to form a continuous phase- have been proposed. The experimental data have been compared with theoretical predictions. The entire work reported in this thesis has been spread over six chapters.

In Chapter I, a critical review of the published literature has been presented. Various hypotheses concerning morphology, size and distribution of primary particles have been critically examined in the light of classical theories of nucleation and growth. Theories relating to the mechanical properties of composite materials have been presented. Lastly,

in the perspective of present understanding, the problem under investigation has been posed.

Chapter II deals with the theoretical analysis of the mechanical properties of model rheocast alloys as conceived in the present investigation. After defining the physical state of constituent phases, two theoretical models on the basis of the concept of particulate composites have been developed - one, for the case when eutectic is continuous and the other, when α -phase is continuous. A parametric model has been developed to examine the effect of porosity on the strength of real life castings.

In Chapter III, the details of experimental set-up, alloy selection, choice of process parameters and experimental procedure have been presented.

The results pertaining to microstructural features of the rheocast alloys have been presented and discussed in Chapter IV. The effects of process parameters on morphology, size and distribution of proeutectic α -phase have been examined on the basis of prevailing solidification condition.

In Chapter V, mechanical properties of rheocastings have been presented and analysed on the basis of theoretical models developed in Chapter II. From the least square fit of experimental data, the effects of average size of α -particles and porosity on the tensile strength have been evaluated. Strength values of rheocastings have been compared with those of conventional casting at equivalent

porosity level. In the end of the chapter, results of SEM fractographic observations have been presented to throw light on the mechanism by which strengths of rheocast Al-Cu alloys is governed.

Lastly, conclusions based on the present investigation have been presented in Chapter VI.

ACKNOWLEDGEMENTS

The author wishes to record his deep sense of gratitude and indebtedness to Dr.S.Ray, Reader, Dr.M.L. Kapoor, Professor and Head, Department of Metallurgical Engineering, and Dr. J.L. Gaindhar, Reader, Department of Mechanical and Industrial Engineering, University of Roorkee, Roorkee, for their guidance, constructive criticism, thought-provoking discussions and suggestions that they have very kindly made available to him during all phases of the investigation and preparation of this thesis. Without their timely and untiring help, it could not have been possible to present the work contained in this thesis in its present form.

The author is highly obliged and wishes to express his sincere thanks to the staff of various laboratories of Metallurgical Engineering Department, especially to Mr. M.Pandey, Mr. Ajmer Singh and Mr. Dharam Pal Singh who have helped him in all possible ways during the experimental work. The assistance rendered by the staff of University Service and Instrumentation Centre, University of Roorkee, Roorkee, during fractographic studies by Scanning Electron Microscopy is also gratefully acknowledged. Thanks are also due to M/S Indian Aluminium Company, Calcutta for carrying out chemical analysis.

The author is indebted to Govt. of Bihar for deputing him in the Department of Metallurgical Engineering, University of Roorkee, for higher studies and to Govt. of India for granting a QIP Fellowship.

Special thanks are due to Sri S.K. Seth, for preparing high quality micrographs, to Sri M.C.Vaish for neat tracing and drawing work, and to Sri R.C. Sharma for flawless typing of the thesis.

Finally, the author expresses his gratitude to all his friends and relations who have shown keen interest in his work and contributed directly or indirectly towards his achievements.

August 1, 1983


(PRIYA RANJAN PRASAD)

C O N T E N T S

Chapter	Page
CERTIFICATE	... i
ABSTRACT	... ii
ACKNOWLEDGEMENTS	... vi
CONTENTS	... viii
LIST OF FIGURES	... x
LIST OF TABLES	... xxi
NOMENCLATURE	... xxii
1- INTRODUCTION	... 1-57
1.1 General	... 1
1.2 Rheocasting Practice	... 7
1.3 Structure of Rheocast Slurries	... 10
1.3.1 Nucleation	... 12
1.3.2 Growth	... 15
1.3.3 Interface Stability	... 16
1.3.4 Solidification in Rheocasting	... 20
1.4 Size Distribution of Primary Particles	... 27
1.5 Mechanical Properties of Rheocast Products	... 37
1.5.1 Mechanical Properties of Composite Materials: General Concept	... 38
1.5.2 Fracture Modes in Composites	... 44
1.5.3 Application to Rheocast Products	... 54
1.6 Formulation of Problem	... 54
2- MECHANICAL PROPERTIES: THEORETICAL ANALYSIS	... 58-76
2.1 Introduction	... 58
2.2 Model for Composite Strength when eutectic is continuous	... 60
2.3 Model for Composite Strength when α -phase is continuous	... 67
2.4 Effect of Porosity on Tensile Strength	... 69

Chapter	Page
3- EXPERIMENTAL WORK	... 77-95
3.1 Alloy selection	... 77
3.2 Alloy preparation	... 79
3.3 Rheocasting set-up	... 79
3.4 Selection of process variables	... 83
3.5 Casting procedure	... 84
3.6 Metallography	... 87
3.7 Porosity and shrinkage-pipe measurements...	89
3.8 Mechanical properties measurements	... 92
3.9 SEM fractographic studies	... 95
4- RESULTS AND DISCUSSION: MICROSTRUCTURE	... 96-167
4.1 Introduction	... 96
4.2 Results: Microstructure of Al-10% Cu Alloy	... 97
4.3 Results: Microstructure of Al-6% Cu Alloy	... 114
4.4 Results: Microstructure of Al-4.5% Cu Alloy	... 130
4.5 Discussion: Microstructure of Rheocast Al-Cu Alloys	... 154
5- RESULTS AND DISCUSSION: MECHANICAL PROPERTIES...	168-214
5.1 Introduction	... 168
5.2 Mechanical Properties of Rheocast Al-10% Cu Alloy	... 168
5.3 Mechanical Properties of Rheocast Al-6% Cu and Al-4.5% Cu Alloys	... 181
5.4 Fracture Behaviour	... 196
6- CONCLUSIONS	... 215-217
REFERENCES	... 218
APPENDIX	... 225

LIST OF FIGURES

<u>Sl.No.</u>	<u>Fig. No.</u>	<u>Title</u>	<u>Page</u>
1.	1.1	Rheocasting of an alloy solidifying over a wide temperature range ...	2
2.	1.2	Rheocasting of a metal or an alloy solidifying at a constant temperature ...	4
3.	1.3	Some examples of batch type rheocasting units (a) paddle type stirrer, top pouring (b) angled blade impeller, in situ casting by inserting suitable chills into the melt (c) concentric cylinder design, bottom pouring ...	8
4.	1.4	Schematic diagram of a typical continuous rheocasting unit ...	9
5.	1.5	Representative microstructure of Sn-15% Pb alloy obtained by (a) rheocasting, showing non-dendritic morphology, (b) conventional casting showing dendritic morphology ...	11
6.	1.6	Schematic variation of nucleation rate with undercooling in heterogeneous nucleation ...	14
7.	1.7	Schematic variation of growth rate with undercooling (a) liquid diffusivity independent of undercooling (b) liquid diffusivity decreases with undercooling ...	17
8.	1.8	Constitutional supercooling (a) variation of liquid composition and corresponding liquidus temperature at the interface (b) condition for planar interface stability (c) condition for planar interface instability ...	18
9.	1.9	Solidification of a pure metal with planar interface under zero temperature gradient inside liquid ...	21

<u>Sl.No.</u>	<u>Fig.No.</u>	<u>Title</u>	<u>Page</u>
10.	1.10	Temperature profile near the crucible wall under vigorous agitation of the melt (a) slow cooling (b) fast cooling ...	22
11.	1.11	Schematic variation of primary particle size with rheocasting temperature ...	31
12.	1.12	Effect of cooling rate on nucleation events (a) ideal cooling curve during rheocasting, (b) dN vs n at different cooling rates C_1 , C_2 and C_3 . $C_1 > C_2 > C_3$	35
13.	1.13	Discontinuous fibre composite (a) single fibre model (b) distribution of stress in a discontinuous fibre (c) elemental force balance. ...	41
14.	1.14	Pull-out and debonding processes close to the crack due to crack-fibre interaction ...	47
15.	1.15	Schematic variation of work of fracture due to pull-out with fibre length ...	49
16.	1.16	Linkage of cavities formed at second phase particles. ...	53
17.	2.1	(a) Schematic representation of a single particle composite model (b) elemental force balance at a section of the particle. ...	62
18.	2.2	Variation of load carrying capacity of material near a pore on a planar section perpendicular to the direction of applied force. ...	72
19.	2.3	Isoweakening diagram ...	75
20.	3.1	Equilibrium phase diagram of Al-Cu alloy system ...	78
21.	3.2	Schematic diagram of experimental set-up ...	81

<u>Sl.No.</u>	<u>Fig.No.</u>	<u>Title</u>	<u>Page</u>
22.	3.3	Location of various specimens machined out from the cast ingot. ...	86
23.	3.4	Dimensions of the specimen used for tensile test. ...	94
24.	4.1	Microstructure of conventionally cast Al-10% Cu alloy poured from 950 K. ...	98
25.	4.2	Microstructure of rheocast Al-10% Cu alloy stirred at 700 r.p.m. and poured from (a) 900 K, (b) 896 K. ...	99
26.	4.3	Microstructure of rheocast Al-10% Cu alloy stirred at 700 r.p.m. and poured from (a) 894 K (b) 892K ...	100
27.	4.4	Microstructure of rheocast Al-10% Cu alloy stirred at 700 r.p.m. and poured from (a) 886K (b) 880K. ...	101
28.	4.5	Microstructure of rheocast Al-10% Cu alloy stirred at 1000 r.p.m. and poured from (a) 900 K, (b) 898K. ...	102
29.	4.6	Microstructure of rheocast Al-10% Cu alloy stirred at 1000 r.p.m. and poured from (a) 894K, (b) 892K. ...	103
30.	4.7	Microstructure of rheocast Al-10% Cu alloy stirred at 1000 r.p.m. and water-quenched from 898K. ...	104
31.	4.8	Effect of pouring temperature on α -particle size in rheocast Al-10% Cu alloy stirred at 700 r.p.m. ...	106
32.	4.9	Effect of pouring temperature on α -particle size in rheocast Al-10% Cu alloy stirred at 1000 r.p.m. ...	107
33.	4.10	Frequency distribution curves of α -particle size in rheocast Al-10% Cu alloy stirred at 700 r.p.m. and poured from 900 K. ...	108

<u>Sl.No.</u>	<u>Fig.No.</u>	<u>Title</u>	<u>Page</u>
34.	4.11	Frequency distribution curves of α -particle size in rheocast Al-10% Cu alloy stirred at 700 r.p.m. and poured from 886K.	... 109
35.	4.12	Frequency distribution curves of α -particle size in rheocast Al-10% Cu alloy stirred at 1000 r.p.m. and poured from 900K.	... 110
36.	4.13	Frequency distribution curves of α -particle size in rheocast Al-10% Cu alloy stirred at 1000 r.p.m. and poured from 886K.	... 111
37.	4.14	Effect of pouring temperature on standard deviation and coefficient of variation of α -particle size in rheocast Al-10% Cu alloy stirred at 700 r.p.m.	... 112
38.	4.15	Effect of pouring temperature on standard deviation and coefficient of variation of α -particle size in rheocast Al-10% Cu alloy stirred at 1000 r.p.m.	... 113
39.	4.16	Microstructure of conventionally cast Al-6% Cu alloy poured from 950K.	... 115
40.	4.17	Microstructure of rheocast Al-6% Cu alloy stirred at 1000 r.p.m. and poured from (a) 903K, (b) 898K	... 116
41.	4.18	Microstructure of rheocast Al-6% Cu alloy stirred at 1000 r.p.m. and poured from (a) 895K, (b) 886K	... 117
42.	4.19	Microstructure of rheocast Al-6% Cu alloy stirred at 700 r.p.m. and poured from (a) 905K, (b) 898K.	... 118
43.	4.20	Microstructure of rheocast Al-6% Cu alloy stirred at 700 r.p.m. and poured from 890K.	... 119

<u>Sl.No.</u>	<u>Fig.No.</u>	<u>Title</u>	<u>page</u>
44.	4.21	Microstructure of rheocast Al-6% Cu alloy stirred at 700 r.p.m. and poured from 886K (a) Structure of cast ingot (b) structure of water-quenched slurry.	...120
45.	4.22	Effect of pouring temperature on α -particle size in rheocast Al-6% Cu alloy stirred at 700 r.p.m.	...122
46.	4.23	Effect of pouring temperature on α -particle size in rheocast Al-6% Cu alloy stirred at 1000 r.p.m.	...123
47.	4.24	Frequency distribution curves of α -particle size in rheocast Al-6% Cu alloy stirred at 1000 r.p.m. and poured from 903 K	...124
48.	4.25	Frequency distribution curves of α -particle size in rheocast Al-6% Cu alloy stirred at 1000 r.p.m. and poured from 890K	...125
49	4.26	Frequency distribution curves of α -particle size in rheocast Al-6% Cu alloy stirred at 700 r.p.m. and poured from 905K	...126
50	4.27	Frequency distribution curves of α -particle size in rheocast Al-6% Cu alloy stirred at 700 r.p.m. and poured from 890 K	...127
51.	4.28	Effect of pouring temperature on standard deviation and coefficient of variation of α -particle size in rheocast Al-6% Cu alloy stirred at 700 r.p.m	...128
52.	4.29	Effect of pouring temperature on standard deviation and coefficient of variation of α -particle size in rheocast Al-6% Cu alloy stirred at 1000 r.p.m.	...129
53	4.30	Microstructure of conventionally cast Al-4.5% Cu alloy poured from 960K	...131
54	4.31	Microstructure of rheocast Al-4.5% Cu alloy stirred at 1000 r.p.m. and poured from 919K	...132
55	4.32	Microstructure of rheocast Al-4.5% Cu alloy stirred at 1000 r.p.m. and poured from 916K	...133

Sl.No.	Fig.No.	Title	Page
56.	4.33	Microstructure of rheocast Al-4.5%.Cu alloy stirred at 1000 r.p.m. and poured from (a) 914K (b) 911K ...	134
57.	4.34	Microstructure of rheocast Al-4.5%.Cu alloy stirred at 1000 r.p.m. and poured from (a) 908K (b) 905K ...	135
58.	4.35	Microstructure showing the evidence of boundaries (shown by arrow) within large primary particles (P) shown in Fig.4.34(b). ...	136
59.	4.36	Microstructure of rheocast Al-4.5%.Cu alloy stirred at 700 r.p.m. and poured from (a) 922K (b) 919K ...	137
60.	4.37	Microstructure of rheocast Al-4.5%.Cu alloy stirred at 700 r.p.m. and poured from (a) 914K (b) 911K. ...	138
61.	4.38	Effect of pouring temperature on α -particle size in rheocast Al-4.5%.Cu alloy stirred at 500 r.p.m. ...	140
62.	4.39	Effect of pouring temperature on α -particle size in rheocast Al-4.5% Cu alloy stirred at 700 r.p.m. ...	141
63.	4.40	Effect of pouring temperature on α -particle size in rheocast Al-4.5%.Cu alloy stirred at 1000 r.p.m. ...	142
64.	4.41	Effect of pouring temperature on α -particle size in rheocast Al-4.5%.Cu alloy stirred at 1200 r.p.m. ...	143
65.	4.42	Effect of stirring rate on α -particle size in rheocast Al-4.5%. Cu alloy poured from 922K and 911K ...	145
66.	4.43	Frequency distribution curves of α -particle size in rheocast Al-4.5%.Cu alloy stirred at 700 r.p.m. and poured from 922 K ...	146
67.	4.44	Frequency distribution curves of α -particle size in rheocast Al-4.5%.Cu alloy stirred at 700 r.p.m. and poured from 911K ...	147

<u>Sl.No.</u>	<u>Fig.No.</u>	<u>Title</u>	<u>Page</u>
68.	4.45	Frequency distribution curves of α -particle size in rheocast Al-4.5% Cu alloy stirred at 1000 r.p.m. and poured from 922K.	... 148
69.	4.46	Frequency distribution curves of α -particle size in rheocast Al-4.5% Cu alloy stirred at 1000 r.p.m. and poured from 911K.	... 149
70.	4.47	Effect of pouring temperature on standard deviation and coefficient of variation of α -particle size in rheocast Al-4.5% Cu alloy stirred at 500 r.p.m.	... 150
71.	4.48	Effect of pouring temperature on standard deviation and coefficient of variation of α -particle size in rheocast Al-4.5% Cu alloy stirred at 700 r.p.m.	... 151
72.	4.49	Effect of pouring temperature on standard deviation and coefficient of variation of α -particle size in rheocast Al-4.5% Cu alloy stirred at 1000 r.p.m.	... 152
73.	4.50	Effect of pouring temperature on standard deviation and coefficient of variation of α -particle size in rheocast Al-4.5% Cu alloy stirred at 1200 r.p.m.	... 153
74.	4.51	Effect of stirring rate on standard deviation of α -particle size in rheocast Al-4.5% Cu alloy poured from 922K and 911K.	... 155
75.	4.52	Effect of stirring rate on coefficient of variation of α -particle size in rheocast Al-4.5% Cu alloy poured from 922K and 911K.	... 156
76.	5.1	Schematic representation of tensile load-extension curve for Al-10% Cu alloy	... 171
77.	5.2	Comparison between experimental and calculated (according to equation 5.2) tensile strength values of rheocast Al-10% Cu alloy	... 173

Sl.No.	Fig.No.	Title	Page
78.	5.3	Comparison between experimental and calculated (according to equation 5.6) tensile strength values of rheocast Al-10% Cu alloy	... 176
79.	5.4	Variation of tensile strength with $(\bar{D}_i \bar{Z})^2$ in rheocast Al-10% Cu alloy at 6.3% porosity level	... 177
80.	5.5	Dependence of $\bar{D}_i \bar{Z}$ on coefficient of Variation of α -particle size $(\bar{\sigma} / \bar{D})$... 179
81.	5.6	Schematic representation of tensile load-extension curve for Al-6% Cu alloy.	... 184
82.	5.7	Schematic representation of tensile load-extension curve for Al-4.5% Cu alloy.	... 185
83.	5.8	Relationship between $\sigma_c(\epsilon_f) / \sigma_c(\epsilon_s)$ and $(\epsilon_f / \epsilon_s)^{1/2}$ according to equation 5.10 for rheocast Al-6% Cu alloy	... 188
84.	5.9	Relationship between $\sigma_c(\epsilon_f) / \sigma_c(\epsilon_s)$ and $(\epsilon_f / \epsilon_s)^{1/2}$ according to equation 5.10 for rheocast Al-4.5% Cu alloy	... 189
85.	5.10	Comparison between experimental and calculated (according to equation 5.12) tensile strength values of rheocast Al-6% Cu alloy.	... 191
86.	5.11	Comparison between experimental and calculated (according to equation 5.13) tensile strength values of rheocast Al-4.5% Cu alloy	... 192
87.	5.12	Variation of tensile strength with α -particle size in rheocast Al-6% Cu alloy at 3.5% porosity level.	... 194
88.	5.13	Variation of tensile strength with α -particle size in rheocast Al-4.5% Cu alloy at 1.5% porosity level.	... 195

<u>Sl.No.</u>	<u>Fig. No.</u>	<u>Title</u>	<u>Page</u>
89.	5.14	SEM fractograph of rheocast Al-10% Cu alloy showing discontinuous α -phase.	... 197
90.	5.15	SEM fractograph of rheocast Al-6% Cu alloy showing joined and continuous α -phase particles	... 198
91.	5.16	SEM fractograph of rheocast Al-4.5% Cu alloy showing joined and continuous α -phase particles.	... 199
92.	5.17	SEM fractograph of conventionally cast Al-4.5% Cu alloy showing dendritic morphology of α -phase	... 200
93.	5.18	SEM fractograph of rheocast Al-10% Cu alloy showing cleavage of eutectic and rupture of α -phase	... 202
94.	5.19	SEM fractograph of rheocast Al-10% Cu alloy showing secondary cracking in eutectic along α -CuAl ₂ interface.	... 204
95.	5.20	SEM fractograph of rheocast Al-10% Cu alloy showing dimples formed by pull-out of α -particles	... 205
96.	5.21	SEM fractograph of rheocast Al-10% Cu alloy showing cracks in CuAl ₂ due to pull-out of α -phase ² of eutectic.	... 206
97.	5.22	SEM fractograph of rheocast Al-6% Cu alloy showing cleavage of eutectic and rupture of α -phase	... 208
98.	5.23	SEM fractograph of rheocast Al-4.5% Cu alloy showing cleavage of eutectic and rupture of α -phase. Some ledge like cleavage facets are also present.	209

<u>Sl.No.</u>	<u>Fig.No.</u>	<u>Title</u>	<u>Page</u>
99.	5.24	SEM fractograph of rheocast Al-6% Cu alloy showing no preferential secondary cracking of eutectic along α -CuAl ₂ interface	... 211
100	5.25	SEM fractograph of rheocast Al-4.5% Cu alloy showing no preferential secondary cracking of eutectic along α -CuAl ₂ interface	... 212
101.	5.26	SEM fractograph of rheocast Al-4.5% Cu alloy showing fracture of α -particles at the neck formed by joining of particles.	... 213

LIST OF TABLES

<u>Sl.No.</u>	<u>Table No.</u>	<u>Title</u>	<u>Page No.</u>
1.	3.1	Chemical analyses of alloys in weight percent	... 80
2.	3.2	Effect of processing condition on casting yield of Al-4.5% Cu alloy.	... 91
3.	3.3	Effect of processing condition on hardness and impact strength of Al-10% Cu alloy.	... 93
4.	5.1	Effect of processing condition on mechanical properties of Al-10% Cu alloy.	... 169
5.	5.2	Effect of processing condition on mechanical properties of Al-6% Cu alloy	... 182
6.	5.3	Effect of processing condition on mechanical properties of Al-4.5% Cu alloy.	... 183

NOMENCLATURE

A_o	cross sectional area
b	Burger's vector
B_o	a universal constant in equation 2.30
C_o	initial composition of alloy
C_L	bulk liquid composition
$(C_L)_{LS}$	bulk liquid composition at low stirring speed
$(C_L)_{HS}$	bulk liquid composition at high stirring speed
d	diameter
\bar{D}	average size of α -particles
D_i	diameter of particle on a planar section
\bar{D}_i	average diameter of particles on a planar section
D_L	liquid diffusion coefficient
D_{LM}	liquid diffusion coefficient at melting temperature
D_p	interparticle spacing
D_v	true diameter of particle
E	elastic modulus
E_f	elastic modulus of fibre
f	force
f_s	fraction of solid particles
$f(r)$	variation of force per unit area with radius r
$f(\theta)$	a function of contact angle
F	total force
G_L	temperature gradient in liquid
G_m	shear modulus of matrix
G_p	shear modulus of particle

$P_2(\cos\theta)$	Legendre polynomial
r	radius
r_p	radius of pore on a planar section
\bar{r}	average radius of primary particles
\dot{r}	deformation mode integer
r^*	critical size of nucleus
R	cell radius
R_p	radius defining weakened zone
R_v	true radius of pore
\dot{R}	growth rate
S	a determinant given by equation 2.8
S_1	a determinant given by equation 2.9
t	time
t_L	time at which solidification begins
t_S	time at which solidification ends
t_R	time after which slurry is cast
T	temperature
T_L	liquidus temperature
T_M	melting temperature
T_P	pouring temperature for fully liquid metal
T_S	solidus temperature
T_R	rheocasting (pouring) temperature
ΔT	undercooling
ΔT_k	kinetic undercooling
ΔT_L	difference between liquidus temperature of alloy (T_L) and melting temperature of pure component (T_M)

v_s	molar volume
V_e	volume fraction of eutectic
V_f	volume fraction of fibres
V_m	volume fraction of matrix
V_p	volume fraction of particle or pore
V_α	volume fraction of α -phase
W	work of pull-out
W_d	work of debonding per unit area
W_D	work of debonding
x	distance
γ	surface energy
Z	parameter equal to $1/D_i$
\bar{Z}	average of $1/D_i$ values
$\dot{\alpha}$	magnitude of weakening
γ	total strain away from particle
γ_y	yield strain away from particle
$\mu(o)$	shear modulus term in equation 2.30
η	strain hardening exponent
λ	Lame's constant
λ_p	Lame's constant for particle
λ_m	Lame's constant for matrix
ν	Poisson's ratio
τ	shear stress
τ_y	yield stress in shear

τ_e	shear stress around a particle
ρ_o	observed density
ρ_{th}	theoretical density
ϵ	strain
ϵ_b	strain at which parabolic deformation begins
ϵ_f	fracture strain
ϵ_s	strain at which serrated flow begins
σ	stress
$\sigma_c(\epsilon)$	composite stress as a function of strain
$\sigma_c(\epsilon_f)$	composite stress at fracture
$\sigma_c(\epsilon_s)$	composite stress at which serrated flow begins
σ_e	stress in eutectic
σ_f	stress in fibre
$\bar{\sigma}_f$	average stress in fibre
σ'_f	stress in fibre at fracture strain of matrix
σ_m	stress in matrix
σ_p	stress in particle
$\bar{\sigma}_{D_i}$	average stress in particles of D_i section size on a planar section
σ_o	strength of pore free material
σ_p^*	strength of material containing P% porosity
σ_{uc}	tensile strength of composite
σ_{uf}	tensile strength of fibre
σ_{um}	tensile strength of matrix
σ'_m	stress in matrix at fracture strain of fibre
σ_{yc}	yield strength of composite

σ_{α} stress in α -phase
 $\sigma_{u\alpha}$ tensile strength of α -phase
 σ standard deviation of α -particle size measurements.

CHAPTER I

INTRODUCTION

1.1 GENERAL

Rheological studies of partially solid alloys have revealed(1,2) that vigorous agitation of an alloy through its solidification range yields a slurry which may be exploited to develop new metal forming processes or modify the existing processes. One possible application of such a slurry is in the production of castings. The process of slurry production and its subsequent casting into desired shapes by conventional methods has been termed as Rheocasting or Stir-casting.

Let us consider a hypothetical binary alloy system as shown in Fig.1.1. In the conventional casting of an alloy of composition C_0 , the alloy is heated above its liquidus temperature T_L and then poured into the mould from the temperature T_p . The solidification in the mould begins at T_L and ends at the solidus temperature T_S . The solid forming during the solidification has normally a dendritic morphology, and a network of dendritic solid is formed a few degrees below T_L . In the rheocasting process, the melt is vigorously agitated with a mechanical stirrer as the temperature is lowered below T_L . Under this condition of solidification, the solid formed is

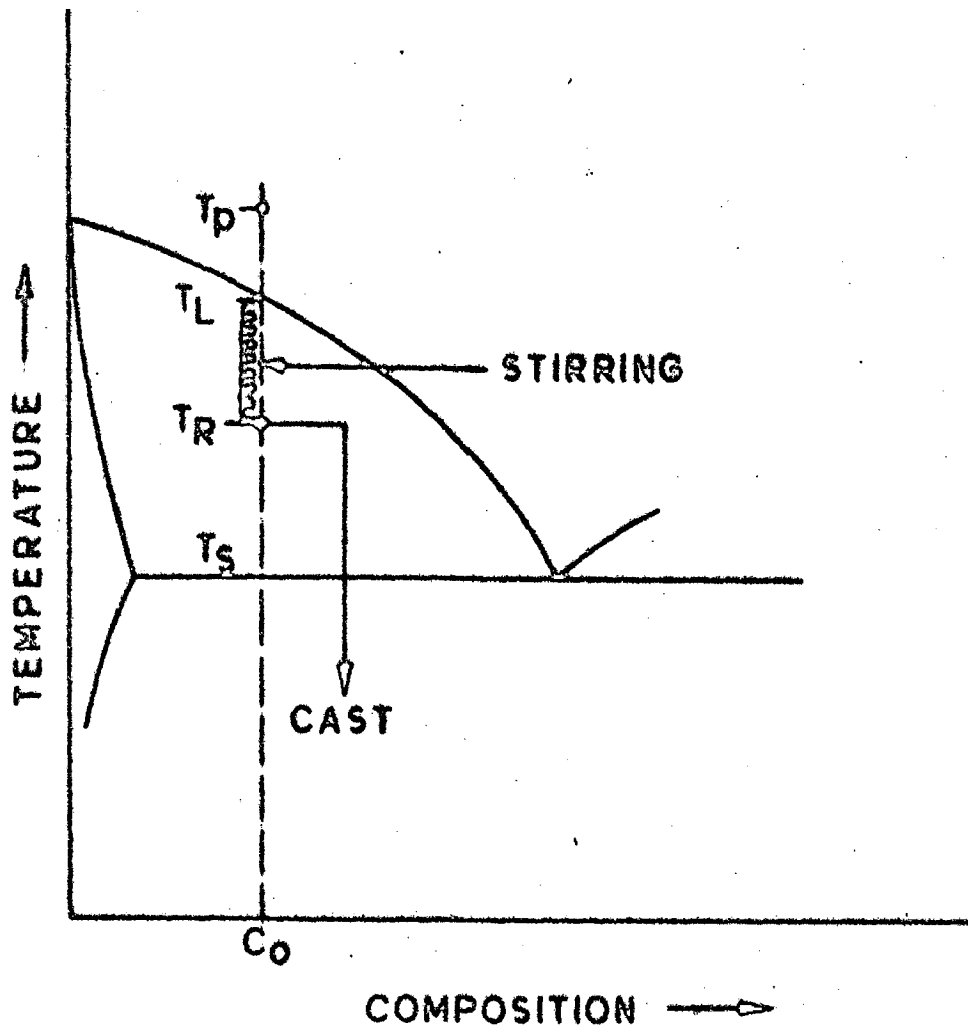


FIG.1.1 RHEOCASTING OF AN ALLOY SOLIDIFYING OVER A WIDE TEMPERATURE RANGE.

non-dendritic and spheroidal, and the formation of the continuous network of solid can be postponed. The mixture of these solids and the remaining liquid behaves as a slurry of low viscosity suitable for making casting. At an appropriate temperature T_R , between the liquidus and the solidus temperatures, the stirring may be stopped and the slurry poured into the mould and cast. T_R is called the rheocasting temperature. The viscosity of the rheocast slurry is manipulated by the process variables namely, cooling rate, stirring rate and rheocasting temperature (alternatively, the volume fraction of solid in the slurry).

The above procedure of rheocasting is generally adopted for alloys which solidify over a wide temperature range. For metals and alloys which solidify at a constant temperature, the stirring may be carried out between t_L and t_S , the time interval between the beginning and the end of solidification as illustrated in Fig. 1.2. In this case, after stirring for an appropriate period of time, say t_R , the stirring is stopped and the resulting slurry is poured into the mould and cast. Alternatively, it has been suggested (3) that the metal or the alloy may be held at its freezing temperature and during stirring, the viscosity of the slurry may be continuously measured and at the desired viscosity, the slurry may be cast.

The principle of rheocasting has aroused considerable interest in recent years since it permits casting in the

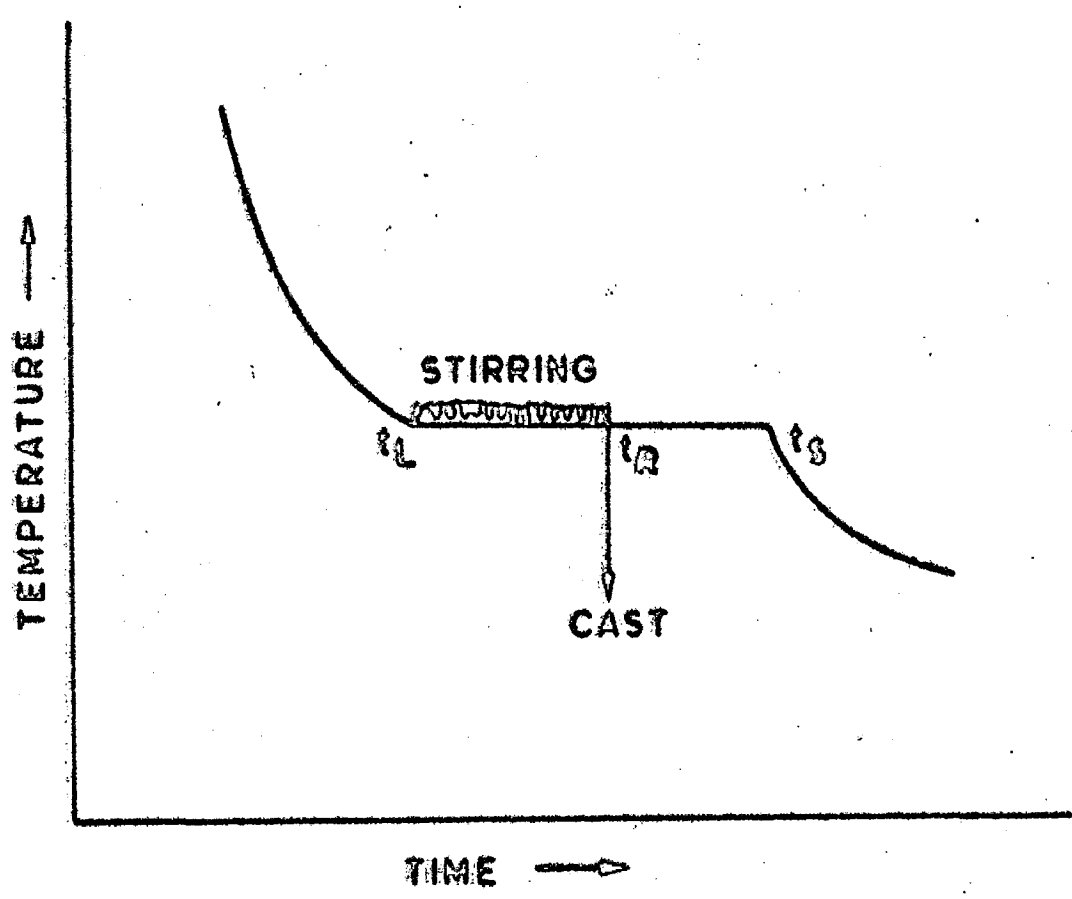


FIG.1.2 RHEOCASTING OF A METAL OR AN ALLOY SOLIDIFYING AT A CONSTANT TEMPERATURE.

semi-solid state. Such a method of casting is believed to offer following technological advantages over the conventional methods:

- (a) In die-casting of high melting point alloys using rheocast slurry, the life of machine components, such as the die and the shot chamber, is enhanced due to reduced thermal shock and erosion. This arises from the fact that the rheocast slurry has a lower temperature and over 50% of the heat of fusion is removed in the crucible itself before pouring. In addition, due to higher viscosity of the slurry as compared to that of fully liquid metal, the convective heat-transfer during mould filling is reduced. Theoretical predictions of heat-flow studies confirm that the die-surface temperature and the surface temperature gradient are lower than those in conventional process (3,4).
- (b) Since slurry is already partially solid before entering into the mould, the resulting shrinkage porosity in casting is less and whatever porosity is present is uniformly distributed. High speed motion picture photography has revealed (3) that, fully liquid metal splashes and sprays more than the partially solid slurries in the die cavity. Slurries fill the mould with a smooth fluid-front resulting in lower trapped porosity. The break-down of dendritic network improves 'mass-feeding' and flow of liquid through inter-dendritic channels. This reduces the tendency of 'hot-tearing' (5,6). The casting quality is thus improved by the rheocasting process (7,8)

- (c) Rheocast ingots cut into pre-weighed slugs and reheated in the liquid-solid temperature range behave as soft solids and can be conveniently transferred to a die-casting machine. The shearing of the metal at the die-gate reduces the viscosity to a reasonably low value so that the die is filled completely by the semi-solid alloy. This is achieved due to thixotropic character of the metal alloy slurries and therefore, this modified process is called 'Thixocasting'. The advantage of thixocasting over and above those of rheocasting is that the slurry producer and the die-casting system need not form the part of the same industrial unit. Rheocast slugs may be produced and stored at one place and then supplied to the die-caster at convenience(3).
- (d) Rheocasting process may be employed to bring about grain-refinement in castings without any grain-refining agent (6,9,10). This is achieved because rheocast slurries contain large number of uniformly distributed solid particles which may act as nuclei during subsequent solidification in the mould. The exploitation of rheocasting process for grain-refinement may be particularly advantageous in the production of ingots required for further deformation-processing operations where the presence of nucleants might cause difficulties in fabrication.
- (e) Mixing in the semi-solid state by mechanical stirring yields flat solute concentration profile and the scale of segregation is also refined(6,11,12, 34). Consequently, the homogenisation heat-treatment time for rheocastings is considerably reduced.

1.2 RHEOCASTING PRACTICE

Rheocasting is carried out either in batch type rheocasting units (2,8,13,14) or continuous rheocasting units(3,5). In the batch type rheocasting, each time the solid metal is **charged** into a crucible placed inside a furnace and then melted or the molten metal is directly poured into a preheated crucible. The stirring is carried out by rotating a suitable impeller in the melt. After stirring, the slurry is either poured into the mould and cast or it is cast in situ by spraying water over the walls of the crucible or by inserting suitable chills within the slurry. In some of the designs a vertical hollow cylinder forms the crucible and a concentric cylinder inside the crucible forms the rotor. The annular gap between the crucible and the rotor carries the liquid metal. Some typical examples of batch type rheocasting units are shown in Fig.1.3.

A typical continuous rheocasting unit has been shown in Fig.14. It consists of two chambers - the upper chamber which acts as a reservoir of molten metal and the lower chamber where the stirring is carried out and is called the mixing chamber. The mixing chamber is similar in design as the concentric cylindrical arrangement of crucible and rotor described above. The metal continuously flows from the reservoir to the mixing chamber and the slurry is discharged from the bottom of the mixing chamber. The rotor functions as a valve on an exit port at the bottom of the mixing chamber. Both batch type and continuous type rheocasting units are considered equivalent but for the high

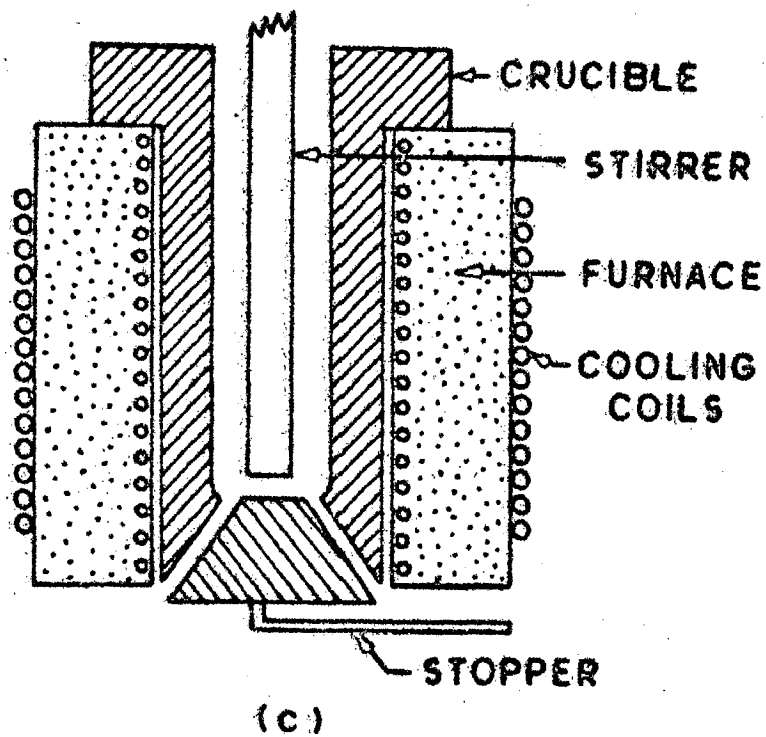
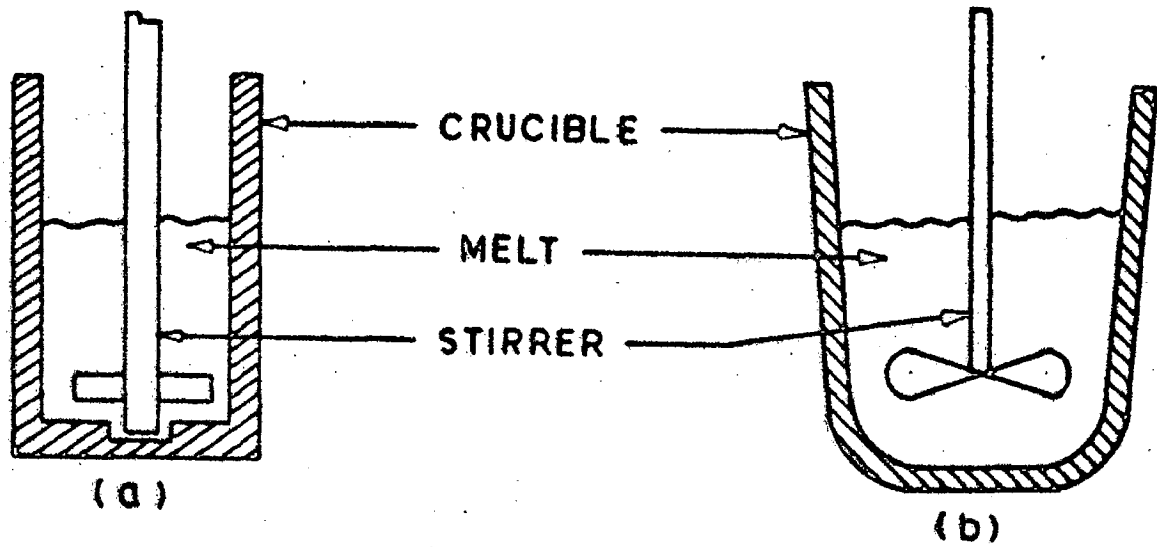


FIG.1.3 SOME EXAMPLES OF BATCH TYPE RHEOCASTING UNITS (a) PADDLE TYPE STIRRER, TOP POURING (Ref.10) (b) ANGLED BLADE IMPELLER, IN-SITU CASTING BY INSERTING SUITABLE CHILLS INTO THE MELT (Ref.13) (c) CONCENTRIC CYLINDER DESIGN, BOTTOM POURING. (Ref.14)

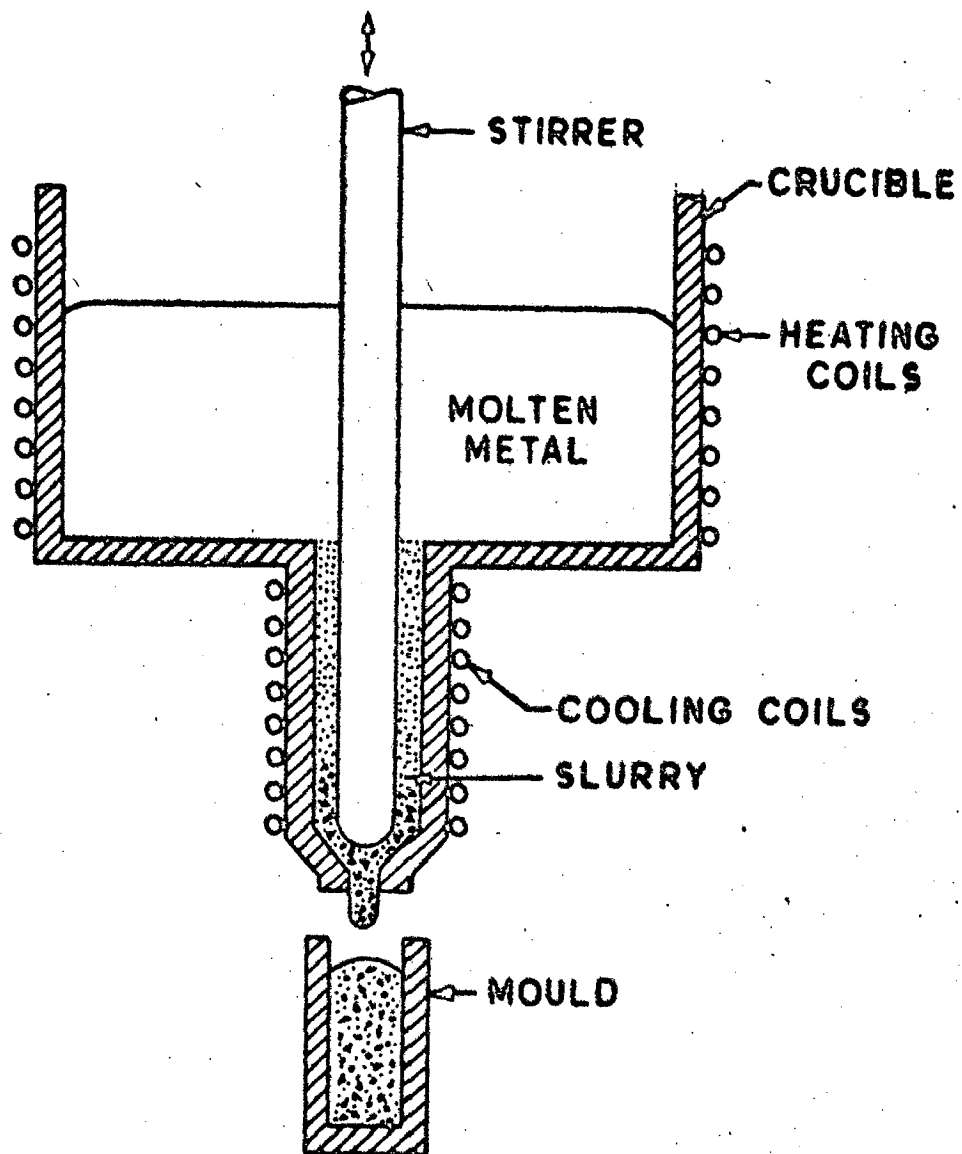


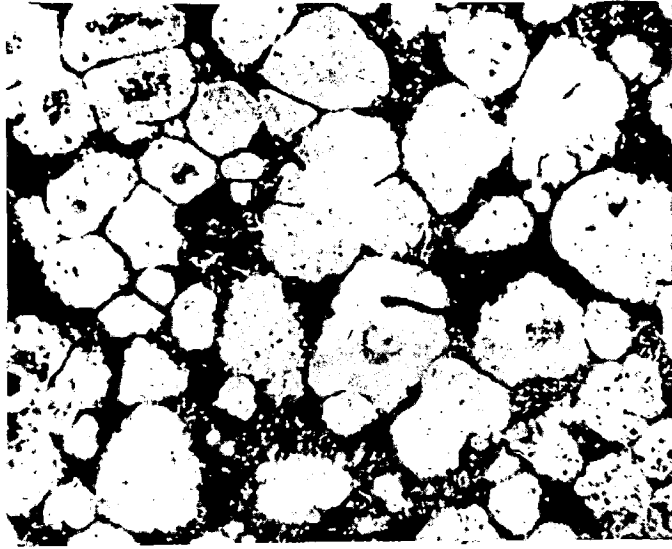
FIG.1.4 SCHEMATIC DIAGRAM OF A TYPICAL CONTINUOUS RHEOCASTING UNIT (Ref.59)

rate of slurry production in the continuous rheocaster.

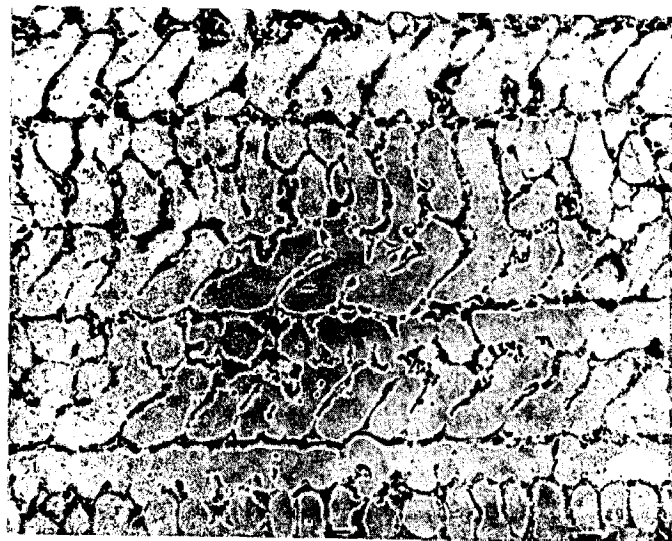
The feasibility studies concerning the application of the rheocasting process in the production of castings of commercial importance were probably initiated in 1971. Many investigators have evinced interest in this process and a variety of metals and alloys have since then been rheocast. The most important alloy systems investigated are aluminium alloys (5,6,9,10,13-27), ferrous alloys(3,11, 12,23,28-38), copper alloys(7, 8,23, 32, 33, 35, 36, 39, 40, 41,42), and nickel and cobalt base superalloys (23,28,32, 33,35,43).

1.3 STRUCTURE OF RHEOCAST SLURRIES

A representative structure of the rheocast slurry obtained by quenching the slurry directly from a temperature within the liquidus and the solidus temperature is shown in Fig.1.5a. The microstructure consists essentially of non-dendritic spheroidal particles, normally referred to as primary particles, uniformly distributed in a matrix of fine dendritic structure. The fine dendritic matrix results from the rapid solidification of the liquid present at the rheocasting temperature and the primary particles are the solid particles which are formed during the stirring of the melt. In a normal solidification process, the solids formed are dendritic, Fig.1.5b. The transformation of the dendritic to the non-dendritic morphology by mechanical stirring has aroused considerable interest



(a)



(b)

FIG.1.5 REPRESENTATIVE MICROSTRUCTURE OF Sn-15% Pb ALLOY OBTAINED BY (a) RHEOCASTING SHOWING NON-DENDRITIC MORPHOLOGY (b) CONVENTIONAL CASTING SHOWING DENDRITIC MORPHOLOGY. (Ref.59)

in the recent years and many attempts have been made to understand the underlying mechanism (5,14,16,44). Since solidification is basically a nucleation and growth process, it will be appropriate to examine the morphology of primary particles on the basis of classical theories of nucleation and growth.

1.3.1 Nucleation

The classical theory of nucleation defines the conditions under which a stable nucleus is formed during liquid to solid transformation either by homogeneous or by heterogeneous nucleation process. In almost all the practical solidification processes, the nucleation is heterogeneous because of the presence of some preferential sites such as suspended impurities, mould-wall etc. which activate the nucleation process. From the energetics of the transformation it has been shown(45) that both the critical size of the stable nucleus, r^* , and the work of nucleation, ΔG^* , decrease with the increase in the supercooling of the melt, ΔT , below its equilibrium freezing temperature. In the presence of potent nucleation sites, ΔG^* is small and the stable nuclei begin to form at very small undercoolings.

The rate of heterogeneous nucleation, I , is given by the expression (45),

$$I = B_1 \frac{D_L}{D_{LM}} \exp \left[- \frac{16\pi Y^3 T_m^2 V_S^2}{3\Delta H^2 \Delta T^2 K T} f(\theta) \right] \dots (1.1)$$

where the parameter B_1 depends upon critical nucleus size,

surface energy, and the number of surface atoms of the nucleating substrate per unit volume of liquid. D_L is the liquid diffusion coefficient, D_{LM} is the liquid diffusion coefficient at equilibrium melting point T_M , γ is the surface energy, V_s is the molar volume, ΔH is the enthalpy change, ΔT is the undercooling, K is Boltzman constant and T is absolute temperature. $f(\theta)$ is the function of contact angle determining the wetting between the crystal and the substrate and is given by $f(\theta) = \frac{1}{4}(2+\cos\theta)(1-\cos\theta)^2$.

From equation 1.1, it is apparent that the rate of heterogeneous nucleation, I , is very sensitive to the undercooling ΔT of the melt. The variation of I with ΔT has been shown in Fig.1.6. It is observed that the nucleation rate passes through a maxima and then drops off at higher undercoolings. This happens when the formation of large number of nuclei eventually reduces the available potent nucleation sites for the formation of new nuclei(46).

The application of dynamic stimulants, such as stirring, may enhance the nucleation activity by dynamic nucleation process. The dynamic nucleation is induced in two ways. Firstly, the solids already formed during the solidification may be fragmented and the smaller fragments of solid so formed may increase the effective nucleation sites. This mechanism has been widely used to explain the grain-multiplication under the influence of dynamic stimulants (49-52). Such a nucleation process does not require undercooling and

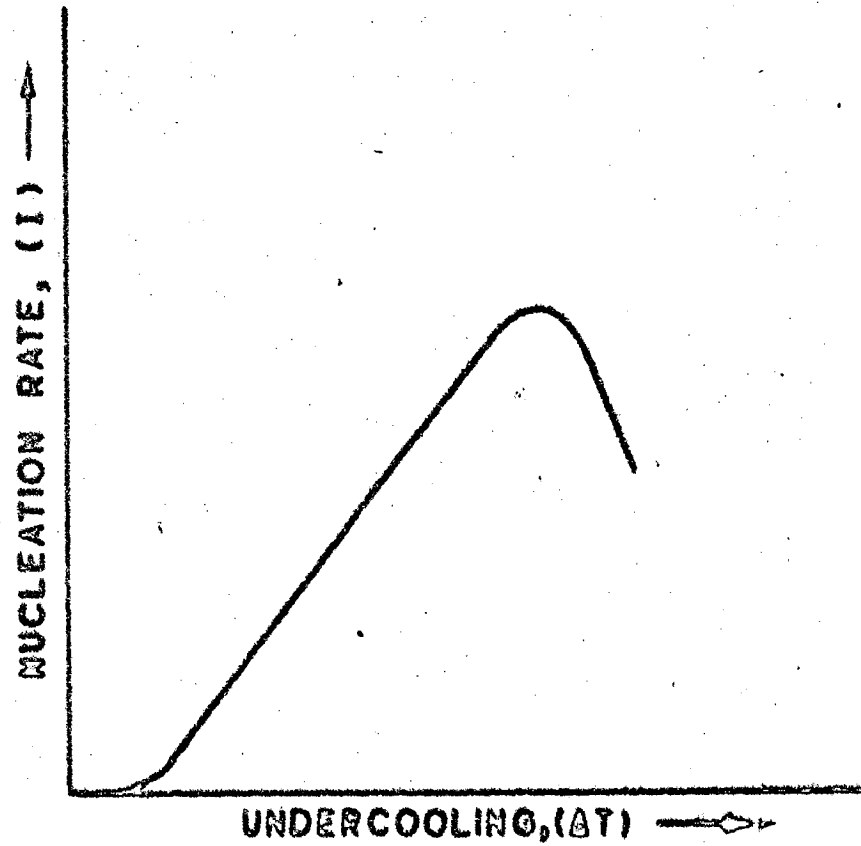


FIG.1.6 SCHEMATIC VARIATION OF NUCLEATION RATE WITH UNDERCOOLING IN HETEROGENEOUS NUCLEATION (Ref. 46)

therefore, it is probably not a true nucleation event. The second way in which the dynamic nucleation may be induced is by causing changes in the conditions determining the true nucleation events. Some hypotheses, such as a cavitation followed by internal evaporation (47) and generation of pressure waves by the collapse of cavities (48) have been invoked to explain the enhanced nucleation activity by dynamic stimulations. However, in absence of sufficient reliable data, the theories concerning true dynamic nucleation events remain uncertain.

1.3.2 Growth

Once a stable nucleus has formed, it grows by addition of atoms, one by one, on its surface. The kinetics of advancement of the solid-liquid interface is generally described by the growth rate, \dot{R} , and all the theories (46) of crystal growth predict increase in \dot{R} with the increase in ΔT . The classical kinetic law for continuous growth is given by (45):

$$\dot{R} = B_2 \frac{D_L}{D_{LM}} \cdot \Delta T_K \quad \dots (1.2)$$

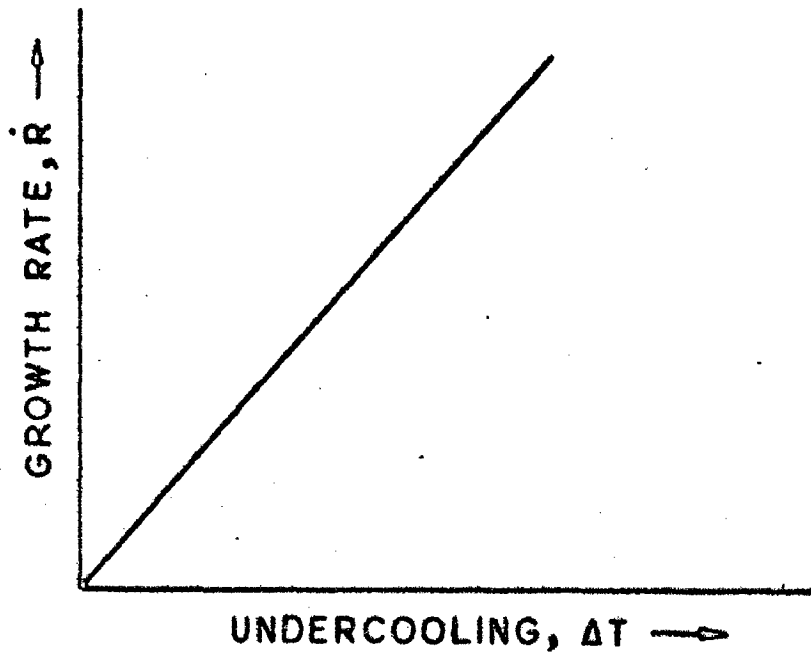
where B_2 is a constant and ΔT_K represents kinetic undercooling required to drive the interface. The validity of equation 1.2 especially at large undercooling is based on the assumption that D_L does not vary appreciably from D_{LM} with temperature. If D_L is strongly influenced by the temperature, \dot{R} will pass through a maxima and then decrease with ΔT_K ,

as shown in Fig.1.7. Another important consideration in the growth process is the removal of latent heat. If the latent heat is not removed to a cooler region, the interface temperature is raised and ΔT_k is diminished.

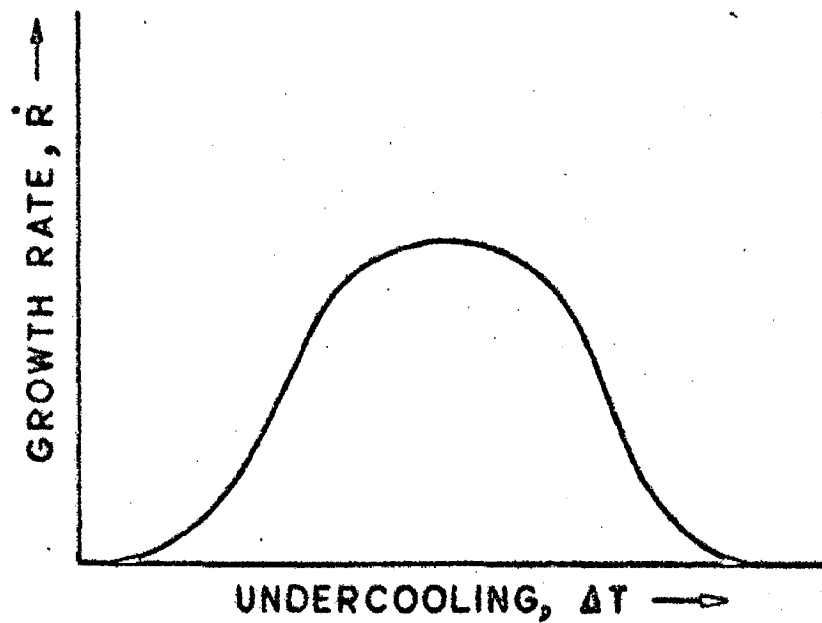
1.3.3 Interface Stability

The morphology of solids which form during solidification depends upon the prevailing growth conditions. Two approaches- the morphological stability approach due to Mullins and Sekerka (53) and the constitutional supercooling approach due to Chalmers(54)- are generally used to determine the conditions as to whether a crystal will grow with a planar interface or the interface will break down. The morphological stability approach considers the time dependence of a general sinusoidal perturbations of the interface with respect to solute and heat-diffusion fields and the surface tension. The constitutional supercooling approach does not consider the kinetic factor, and for most of the solidification processes, both the approaches lead to similar results. Because of its simplicity, the latter approach is therefore extensively used to determine the interface stability conditions.

Fig.1.8 shows qualitatively the condition for instability of a planar front according to constitutional supercooling theory. It is assumed that a solute rich layer is present in front of the growing interface in which the liquid composition is maximum at the interface and decreases with increasing distance from the interface into the liquid (Fig.1.8a). As a



(a)



(b)

FIG.1.7 SCHEMATIC VARIATION OF GROWTH RATE WITH UNDERCOOLING (a) LIQUID DIFFUSIVITY INDEPENDENT OF UNDERCOOLING (b) LIQUID DIFFUSIVITY DECREASES WITH UNDERCOOLING. (Ref. 45)

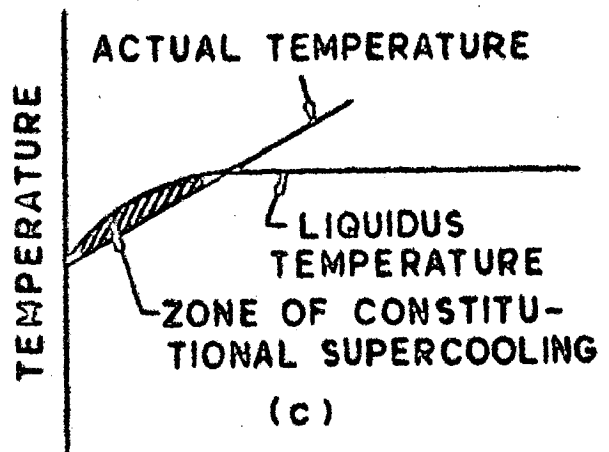
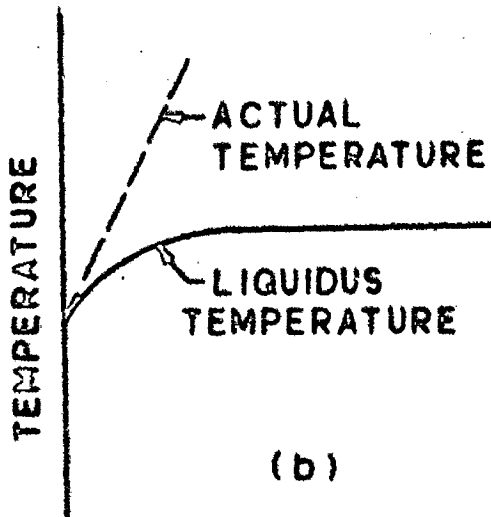
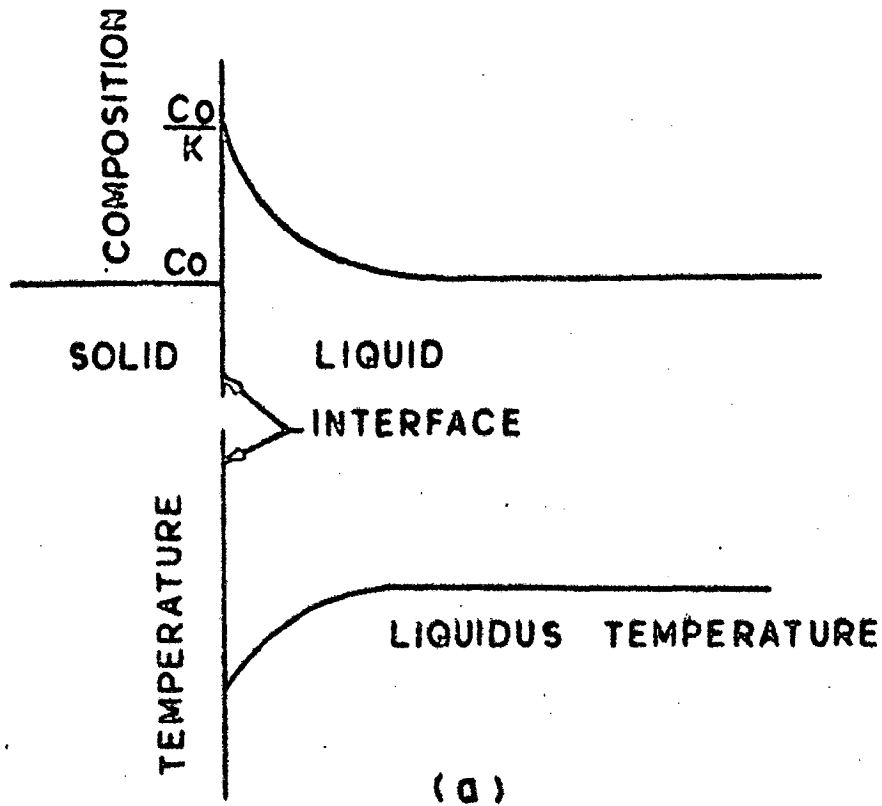


FIG. 1.0 CONSTITUTIONAL SUPERCOOLING (a) VARIATION OF LIQUID COMPOSITION AND CORRESPONDING LIQUIDUS TEMPERATURE AT THE INTERFACE (b) CONDITION FOR PLANAR INTERFACE STABILITY (c) CONDITION FOR PLANAR INTERFACE INSTABILITY. (Ref. 54)

result, the equilibrium liquidus temperature increases with this distance because the lower the solute content the higher is the liquidus temperature. Fig. 1.8b shows a condition where the interface is exactly at the equilibrium liquidus temperature and every point in front of the interface is at a temperature above the liquidus. This represents the condition necessary for stable plane front solidification. If an instability causes a protuberance to form on the interface, it will find itself in a superheated environment and will melt back. Fig. 1.8c on the other hand shows that the liquid immediately in contact with and ahead of the interface is below its equilibrium liquidus temperature and is therefore supercooled even when the temperature gradient in the liquid is positive. Such a supercooling arises from change in composition and not in temperature, and the liquid is said to be constitutionally supercooled. Any protuberance on the interface will find itself in a supercooled environment and will not disappear. Thus, the planar interface will be unstable if a zone of constitutional supercooling exists near the interface. From these theoretical considerations, the interface stability parameter which emerges from the constitutional supercooling approach is the ratio of the temperature gradient in the liquid, G_L , to the rate of interface growth, \dot{R} . The critical G_L/\dot{R} ratio is given by (54),

$$\frac{G_L}{\dot{R}} = \frac{mC_o(1-k)}{D_L k} \quad \dots (1.3)$$

where m is the slope of liquidus line, C_0 is the initial liquid composition and k is the partition coefficient. A higher G_L/R ratio imparts greater interface stability.

It has been shown by Chalmers(55) that when the melt is vigorously stirred, the diffusion boundary layer is eliminated and the solute concentration and temperature in the liquid become uniform as under the ideal conditions of mixing. Such a situation is analogous to the solidification of a pure metal under zero temperature gradient in the liquid, Fig.1.9. This condition has been considered to be conducive to the growth of solids with stable interface.

1.3.4 Solidification in Rheocasting

Due to stirring, both the composition and the temperature of the liquid become uniform in the ideal mixing condition as discussed in the preceding section. However, in practice even with vigorous agitation a boundary layer close to the wall of the crucible will exist. As shown in Fig.1.10, the temperature at the crucible wall from where the heat is extracted is lower and rises steeply through the boundary layer reaching the uniform temperature in the bulk liquid. It is, thus, obvious that the solidification during rheocasting will begin heterogeneously first at the crucible wall and later on in the bulk of the liquid when the temperature of the liquid comes below the liquidus

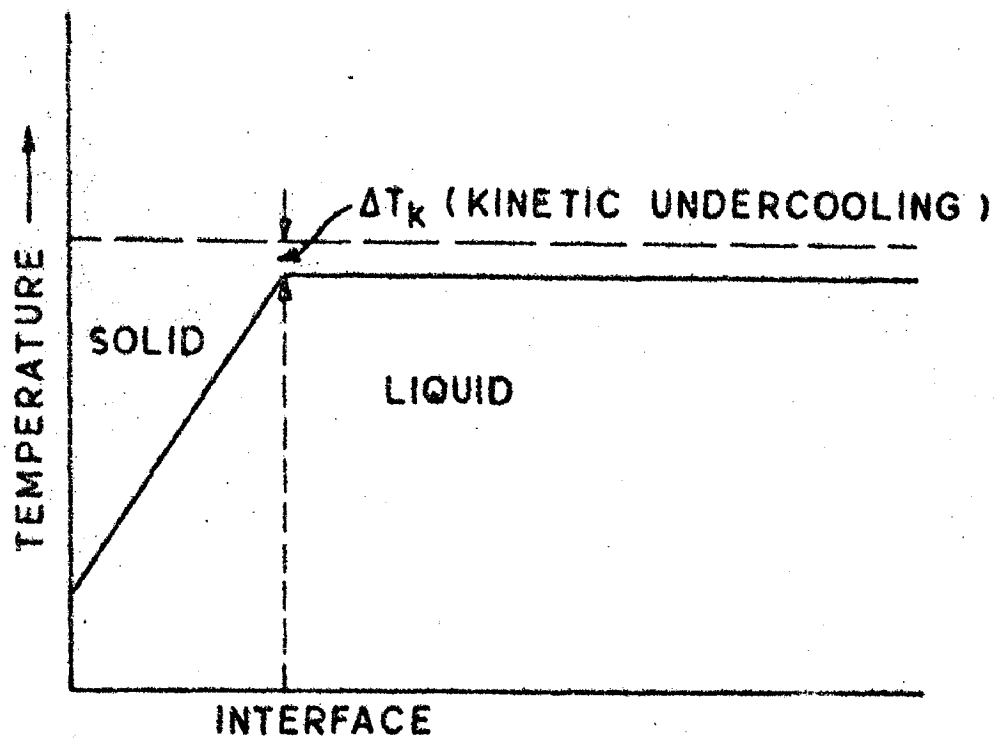


FIG.1.9 SOLIDIFICATION OF A PURE METAL WITH PLANAR INTERFACE UNDER ZERO TEMPERATURE GRADIENT INSIDE LIQUID. (Ref. 55)

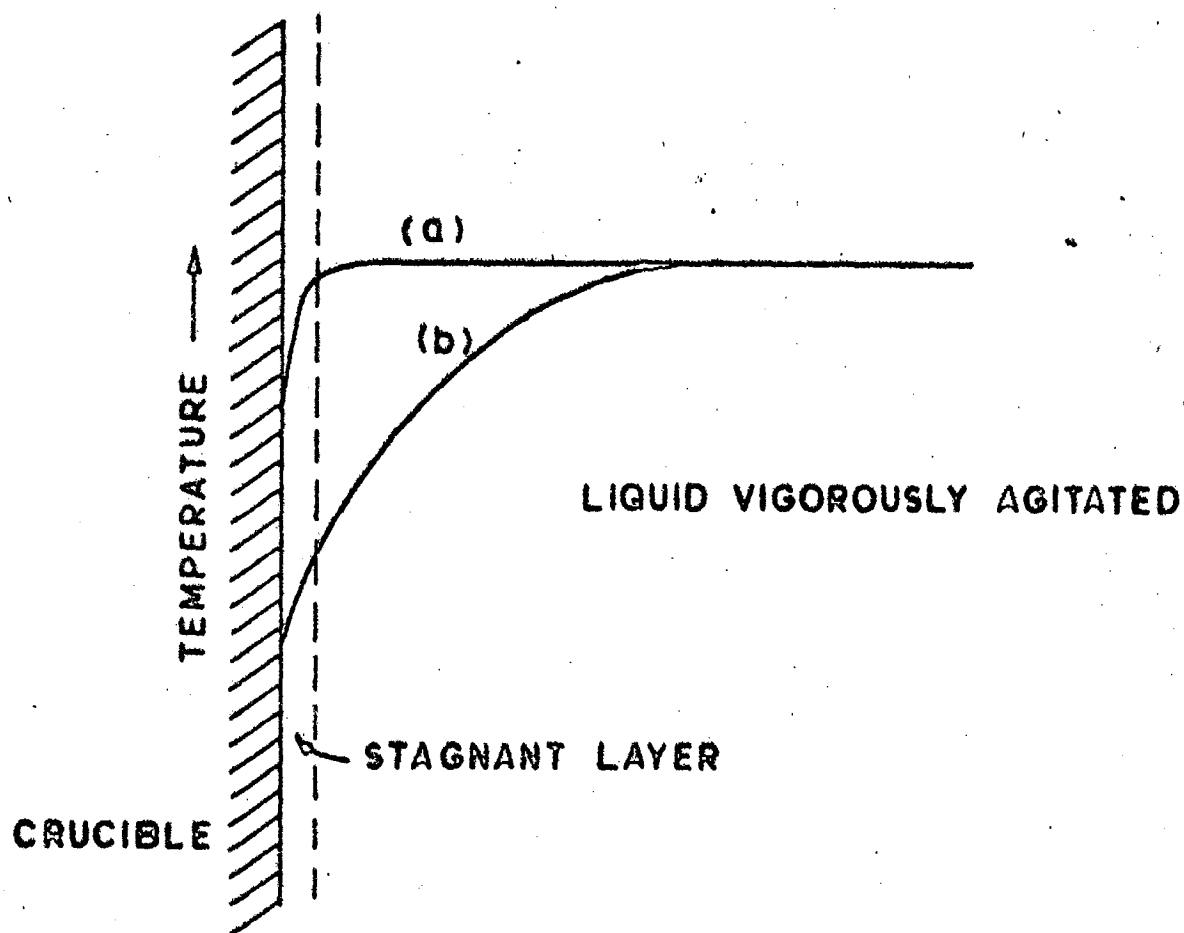


FIG.1.10 TEMPERATURE PROFILE NEAR THE CRUCIBLE WALL UNDER VIGOROUS AGITATION OF THE MELT (a) SLOW COOLING (b) FAST COOLING.

temperature. Any solid forming at the crucible wall is expected to be carried away to the bulk of the liquid by fluid dynamic forces where it will find itself in an environment of relatively higher temperature. The solid particles greater than the critical size r^* at the prevailing temperature will survive while the others will melt. This process will continue as the melt is continuously cooled and stirred.

So long as the solid particles are small, they maintain their spherical shape due to surface energy requirements. The morphology of the larger solids will depend upon the growth conditions prevailing in the bulk of the liquid as well as at the crucible wall. In the bulk of the liquid, a particle will find similar environment around itself since the temperature and composition profiles are flat. The spherical particles will therefore grow isotropically with a stable interface as envisaged in Section 1.3.3. The condition of interface stability at the crucible wall will be governed by the extent to which the constitutional supercooling occurs. The zone of constitutional supercooling will be limited by the thermal and diffusion boundary layers which decrease with increasing stirring rate. It follows then that the constitutionally supercooled zone under the influence of stirring will be small and therefore, the conditions for free dendritic growth are unlikely to exist. Another important factor to be considered is that the build-up of the solute rich layer ahead

of the solid-liquid interface is gradual and therefore, the solid grows to a finite size before the interface instability due to constitutional supercooling sets in. In unidirectional growth of solidifying bar, this critical size may be defined as 'incubation distance' required for interface instability. It is quite probable that solid particles forming at the crucible wall are washed away by the fluid motion before they acquire this incubation size and later on grow isotropically in the bulk of the liquid. It follows therefore that during rheocasting, the primary particles will be non-dendritic and spheroidal. However, this is only possible when the cooling rate is slow and the stirring rate is high. At very high cooling rates, the temperature profile within the bulk of the liquid will no longer remain flat and may change to one represented by curve b in Fig. 1.10. This is more likely to happen in rheocasting set-ups where the thickness of the metal is small, such as in the annular space of the concentric cylinder design mentioned in Section 1.2. Such a situation will lead to enhanced supercooling, both thermal and constitutional, resulting in interface instability in the bulk of the liquid as well as at the crucible wall. This also explains the observations of Flemings (56) that at high cooling rates, at least above a critical value, primary particles formed are dendritic instead of characteristic non-dendritic spheroidal morphology.

In case of turbulent mixing, existence of neutral zones cannot be ruled out. Solid particles in such zones will not find the environment conducive to isotropic growth due to the presence of temperature and concentration gradients. This will lead to the formation of solids of non-spheroidal morphology. In such situations however, when the volume fraction of solid in the slurry increases, the collision of solid particles may randomize the turbulent mixing field. This will eventually provide isotropic growth environment for the formation of spheroidal particles.

In general, Spencer et al.(1) believe that the primary particles formed during rheocasting are dendrite fragments. However, their experimental observations reveal that the non-dendritic spheroidal primary particles are formed only when the melt is stirred right from the liquidus temperature. If the dendrites are allowed to form first and then the melt is stirred, the characteristic non-dendritic spheroidal particles are not formed, instead deformed, bent and fractured dendrites result(1,2). Under these circumstances it is difficult to imagine as to why the formation of non-dendritic spheroidal particles by mechanical fragmentation of dendrites is eliminated when the melt is stirred. Obviously, the dendrite fragmentation mechanism is contradictory to the observed experimental results. Such a mechanism is neither capable of justifying the necessity of stirring right from the liquidus temperature to obtain spheroidal particles. Clearly

therefore, the tenet that the primary spheroidal particles form by dendrite fragmentation is not tenable.

The model of Vogel et al. (16,44,57) predicts theoretically that the dendritic morphology will be favoured in rheocasting, but their experimental observations reveal non-dendritic morphology. In order to resolve this anomaly, they have proposed a dendrite fragmentation mechanism. They consider that the dendrite arms first bend under the action of fluid forces resulting in the formation of high-angle grain-boundaries. These boundaries are completely wetted by the liquid metal eventually releasing a dendrite fragment by high angle grain-boundary remelting. Such a mechanism has, however, been questioned (5).

In many of the recent investigations (5,14,16,22,58) it has been shown that the primary solid particles are 'rosette-shaped' in the beginning and later on transform into spheroidal shape either by fragmentation or by coalescence. Some investigators (14) have identified these 'rosette-shaped' particles as dendrites due to highly branched morphology. If the solid particles start their life as 'rosette-shaped' particles it is wondered as to why the particles nucleated at later stages of solidification do not have similar morphology. This can happen only when the solidification proceeds only by the growth of the solids initially formed and no nuclei are formed later. Obviously, such a situation is difficult to conceive. It appears that precise nature and

origin of such particles are uncertain at present. Moreover, none of these investigations provide adequate experimental evidence that a particular mechanism is operative.

Kievits and Prabhakar(5) hypothesize that a dendrite has two growth fronts- the tip front and the root front. The tip front is assumed to be the most affected by the convection because of difficulty of the flowing fluid to penetrate to the root front. Thus, under the influence of vigorous agitation, growth of the tip front will be decelerated by the heat pulses in comparison with the growth rate of the root front and therefore, the interface protuberances will be smoothed out. Such a mechanism appears feasible and is capable of explaining the non-dendritic morphology, but it does not account for the spherical shape. Moreover, it predicts the formation of large dendrites if the temperature profile in the liquid is evened out due to stirring. This model is therefore, not in tune with the classical concept of the influence of stirring on the growth morphology as a consequence of the elimination of the temperature and composition profiles of the liquid which is realized in practice.

1.4 SIZE DISTRIBUTION OF PRIMARY PARTICLES

Besides morphology, the size and distribution of primary solid particles in the rheocast slurry also depend upon the process variables employed. The effect of rheocasting temperature on the size of primary particles may be visualised

in terms of its effect on the undercooling. Decrease of the rheocasting temperature implies increase of maximum undercooling ΔT , during rheocasting. In order to evaluate the effect of ΔT qualitatively, equation 1.1 and 1.2 may be rewritten as,

$$I = A_1 \exp(-B/\Delta T^2) \quad \dots (1.4)$$

$$\dot{R} = A_2 \Delta T \quad \dots (1.5)$$

where A_1 , A_2 and B are assumed to be constants. Combining equations 1.4 and 1.5,

$$\frac{\dot{R}}{I} = A \Delta T \exp(B/\Delta T^2) \quad \dots (1.6)$$

where A is A_1/A_2 . If the average size of solid particles formed be represented by the radius \bar{r} , and if N number of particles have formed in a unit volume of liquid in a given time, the volume of solid V_p per unit volume of the liquid metal is given by,

$$V_p = N \frac{4}{3}\pi \bar{r}^3 \quad \dots (1.7)$$

and therefore,

$$\bar{r} = \left(\frac{3}{4\pi}\right)^{1/3} \left(\frac{V_p}{N}\right)^{1/3} \quad \dots (1.8)$$

The average size of particles may also be given by,

$$\bar{r} = a t^{1/2} \quad \dots (1.9)$$

where a is a constant and t is the time of solidification which depends upon cooling rate. Differentiation of equation 1.9

yields,

$$\frac{d\bar{r}}{dt} = \frac{a}{2} t^{-1/2} \quad \dots (1.10)$$

Putting $\frac{d\bar{r}}{dt} = R$, equation 1.10 may be rewritten as,

$$t = \frac{a^2}{4R^2} \quad \dots (1.11)$$

It follows therefore that,

$$N = I \times t = \frac{I a^2}{4R^2} \quad \dots (1.12)$$

Substituting equation 1.12 in equation 1.8 and rearranging,

$$\bar{r} = \left(\frac{3}{\pi a^2}\right)^{1/3} (V_p R \times \frac{\dot{R}}{I})^{1/3} \quad \dots (1.13)$$

The variation of V_p with ΔT may be given by the well known Scheil equation (59) for a binary alloy as,

$$V_p = 1 - \left(\frac{\Delta T_L}{\Delta T_L + \Delta T}\right)^{\frac{1}{1-k}} \quad \dots (1.14)$$

where ΔT_L is the difference in the melting temperature of the pure metal and the liquidus temperature of the alloy, and k is the solute partition coefficient. Combining equations 1.5 and 1.14,

$$V_p R = A_2 \left[1 - \left(\frac{\Delta T_L}{\Delta T_L + \Delta T}\right)^{\frac{1}{1-k}} \right] \Delta T \quad \dots (1.15)$$

Since \bar{r} is dependent upon two parameters $V_p R$ and $\frac{\dot{R}}{I}$ (equation 1.13), the variation of \bar{r} with ΔT may be understood in the light of equations 1.15 and 1.6. It is apparent

from equation 1.15 that the parameter $V_p \dot{R}$ will increase with increase in ΔT . A close examination of equation 1.6 reveals that the variation of $\frac{\dot{R}}{I}$ with ΔT is such that at small values of ΔT , $\frac{\dot{R}}{I}$ decreases and at large ΔT values, it increases with increasing ΔT . Thus, on the basis of equations 1.6, 1.13 and 1.15, it can be hypothesized that at higher rheocasting temperatures, i.e. when ΔT is small, increase in ΔT will result in increase in $V_p \dot{R}$ and decrease in $\frac{\dot{R}}{I}$, signifying that \bar{r} may increase, decrease or remain unaltered with decrease in rheocasting temperature depending upon whether the rate of change of $V_p \dot{R}$ with ΔT is respectively higher, lower or equal to that of $\frac{\dot{R}}{I}$. At lower rheocasting temperatures, i.e. when ΔT is high, increase in ΔT will increase $V_p \dot{R}$ as well as $\frac{\dot{R}}{I}$, resulting in the increase of \bar{r} with decrease in the rheocasting temperature. On the basis of above arguments, the possible trends of variation of primary particle size with rheocasting temperature have been depicted schematically in Fig.1.II. Furthermore, at low rheocasting temperatures, collision of particles followed by coalescence may also occur. When this phenomenon occurs, the increase in \bar{r} will be at a significantly greater rate than that accountable by the diffusion controlled growth alone.

In order to assess the influence of other process variables such as cooling rate and stirring speed on the particle size, equations 1.8 and 1.9 are re-examined. It can be shown that,

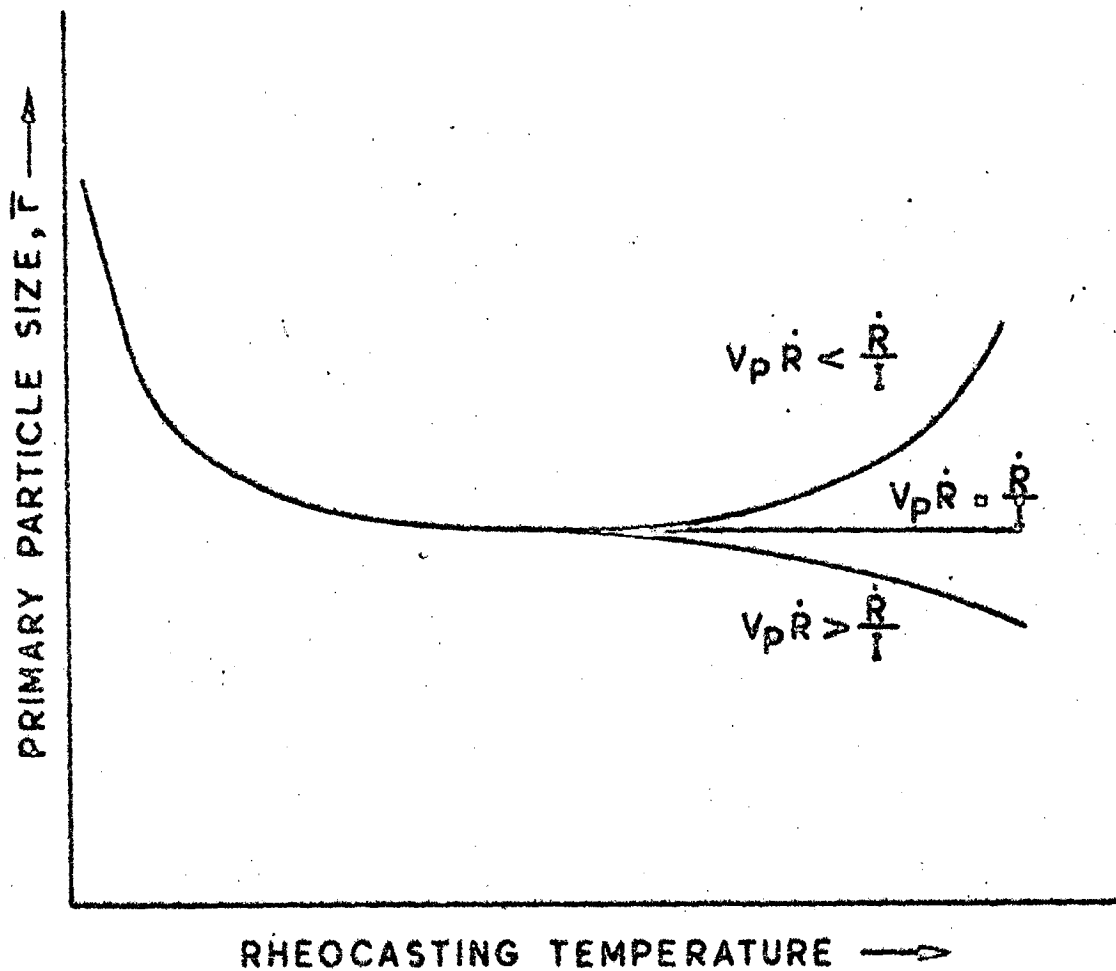


FIG.1.11 SCHEMATIC VARIATION OF PRIMARY PARTICLE SIZE WITH RHEOCASTING TEMPERATURE.

$$\bar{r} = \left(\frac{3V_p}{4\pi}\right)^{1/3} \left(\frac{1}{N}\right)^{1/3} = a t^{1/2} = a\Delta T^{1/2} \left(\frac{1}{C}\right)^{1/2} \dots (1.16)$$

where C is the cooling rate. It is apparent from equation 1.16 that for a constant rheocasting temperature (i.e. constant ΔT and V_p), \bar{r} is dependent only on N which in turn depends on C. Thus, increasing the cooling rate will increase the value of N and therefore, \bar{r} will decrease.

The above observations are primarily based on the assumption that sufficient active sites are available for heterogeneous nucleation. In practical situations, it is likely that the number of active nucleation sites are limited and therefore, N_{\max} , the maximum value of N, will be dictated by the number of nucleation sites available. In the event of nucleation sites getting saturated, N will become constant, i.e. N_{\max} . In such situations when N_{\max} has reached, \bar{r} will increase with decrease in rheocasting temperature as a result of increase in V_p (equation 1.8). However, the cooling rate is unlikely to have any effect on \bar{r} .

In the rheocasting process, N_{\max} may increase due to stirring. The proposal of some investigators (13,16) that dendrite fragmentation is responsible for the enhanced nucleation activity is not tenable since the conditions conducive to the formation of dendrites are unlikely to prevail during rheocasting (Section 1.3.4) and therefore the question of their subsequent fragmentation does not arise. However, fragmentation of non-dendritic particles may not be ruled out.

Another possible mechanism by which N_{\max} may be increased due to stirring may be related to the removal of solid particles forming at the crucible wall or the stirrer. If the solid particles are transported from the crucible wall or the stirrer into the bulk of the melt under fluid motion, fresh surfaces should be continuously exposed to subsequent nucleation. Under such a situation N_{\max} is expected to increase. The rate of removal of solid will be higher at higher stirring rate and consequently N_{\max} should increase with stirring rate. It follows therefore that increase in stirring rate should decrease the size of the particles. In some cases the enhanced nucleation activity due to stirring may be completely masked by enhanced nucleation due to increase in cooling rate. Under such circumstances, when the cooling rate is high, the stirring rate should not have an influence on particle size.

The distribution of particle size is likely to be affected in a similar manner by the process variables as the average particle size. For a given cooling rate, increase in ΔT implies longer solidification time (equation 1.6). It is, therefore, apparent that particles nucleated earlier will avail longer time for growth than those nucleated later. Consequently, the particle size will vary from very large to very small signifying that the size distribution of particles will become broad as the rheocasting temperature is lowered. This will happen when \bar{r} increases with decrease

in rheocasting temperature and for the case when \bar{r} decreases with decrease in rheocasting temperature, the reverse will be true because in this case the transformation is primarily nucleation dominant.

The effect of cooling rate on the size distribution may be understood on the basis of its effect on the nucleation activity. Fig.1.12a shows an idealized cooling curve during rheocasting. The time required to bring down the temperature from T_L to T_R , is the characteristic time which is determined by the cooling rate according to the relation,

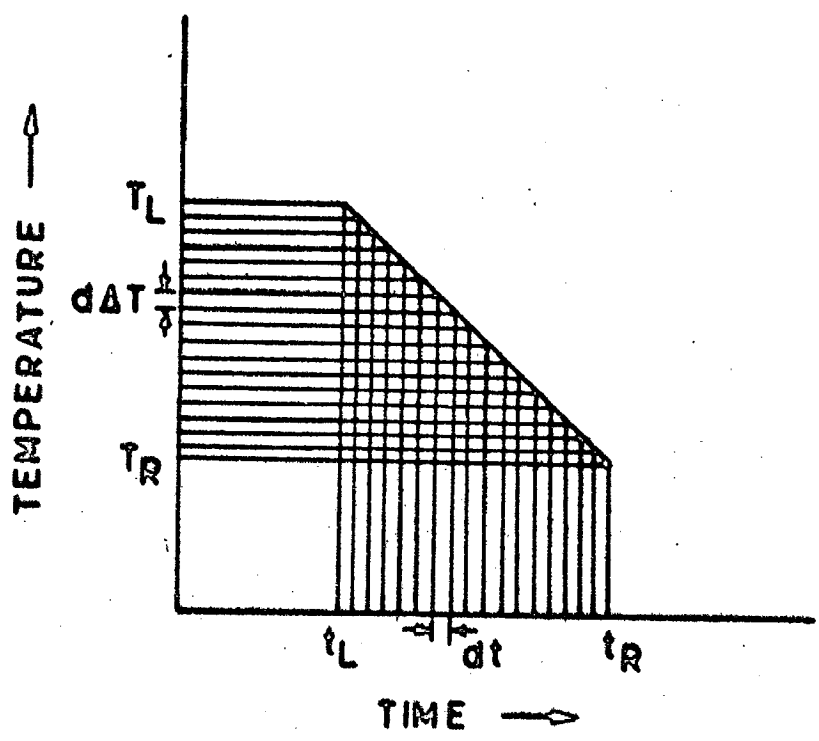
$$t = \frac{T_L - T_R}{C} = \frac{\Delta T}{C} \quad \dots (1.17)$$

If the time t is divided in n number of small time intervals dt , so that $t = ndt$, the number of nuclei dN formed in any given time interval dt will be,

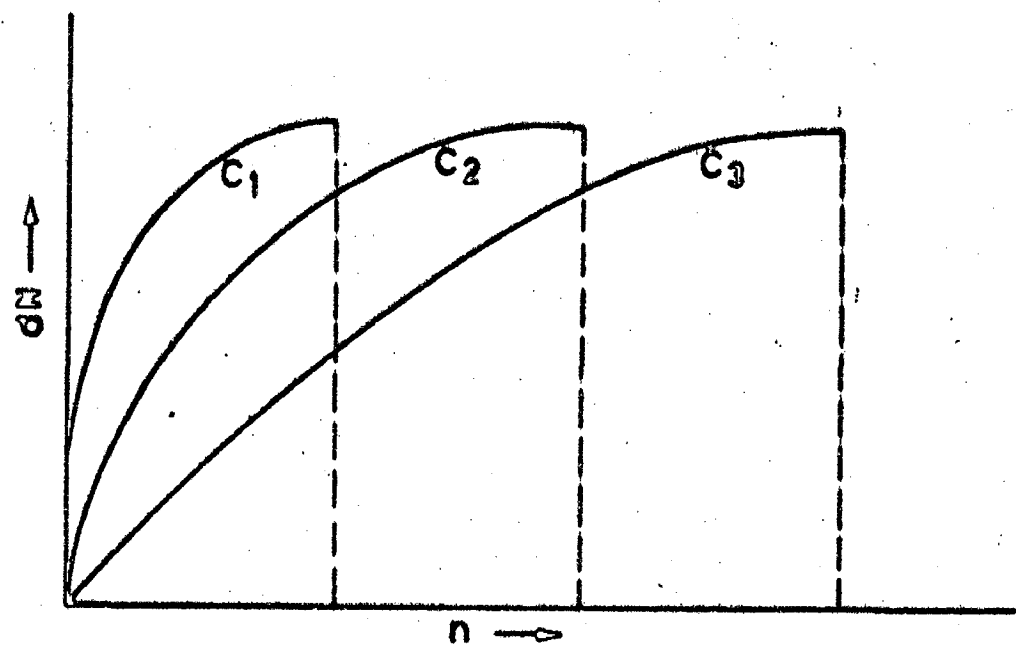
$$dN = A_1 \exp[-B/(nd\Delta T)^2] \cdot dt \quad \dots (1.18)$$

where $d\Delta T$ is given by, $\Delta T = nd\Delta T$.

It is apparent from equation 1.17 that increasing the cooling rate will result in shorter characteristic time and therefore smaller value of n , and also, the decrease in the value of n will cause corresponding increase in the value of $d\Delta T$. On the basis of equation 1.18 the variation of dN with n may be then represented schematically for different cooling rates as shown in Fig.1.12b. The curves reveal that increasing the cooling rate has two distinct consequences-



(a)



(b)

FIG.1.12 EFFECT OF COOLING RATE ON NUCLEATION EVENTS (a) IDEAL COOLING CURVE DURING RHEOCASTING (b) dN vs. n AT DIFFERENT COOLING RATES C_1, C_2 AND C_3 . $C_1 > C_2 > C_3$

(a) The number of nuclei formed during the early stages of solidification are increased and (b) the difference between the times available for growth of particles nucleated earlier and those nucleated later is narrowed down. It follows therefore, that at higher cooling rates both the number and the size of the particles formed at different stages of solidification will not be widely different. Increasing the cooling rate will therefore make the particle size more uniform.

Stirring rate may affect the size distribution in two ways. One effect of stirring is to enhance the cooling rate. If it so happens, the stirring rate will influence the size distribution similarly as the cooling rate, that is increase in stirring rate will result in more uniform sized particles. However, in experiments where the cooling rate is precisely controlled, the stirring rate does not have any effect on the cooling rate. The shear fields produced by stirring may fragment the larger particles to smaller ones. In this event also the particles will become more uniform in size. If the nucleation sites saturate, dN versus n curve is arbitrarily cut off and therefore the cooling rate has no effect on the size distribution. However, if the detachment of the particles occur at the crucible wall and at the stirrer, the effect of the site saturation will be eliminated. This may be another possible mechanism by which the stirring rate will influence the size distribution.

The above mentioned possible trends of variation of

primary particle size and its distribution with the process parameters provide basis for the explanation of most of the published results (2,27,59). However, a comparison of the results of Ramati et al.(59) and of Joly and Mehrabian(2) on Sn-15% Pb alloy shows that the results of these two investigations are not consistent. In the former investigation carried out in a range of high cooling rates, as expected, it has been observed that increasing the cooling rate makes the particle size more uniform while in the latter investigation, carried out in a range of slow cooling rates results to the contrary have been observed. This discrepancy has also been pointed out by Ramati et al., but no satisfactory explanation has been offered. It appears that the apparent anomaly in the results of Joly and Mehrabian is due to some spurious effects.

1.5 MECHANICAL PROPERTIES OF RHEOCAST PRODUCTS

The microstructure depicted in Fig.1.5a represents the general nature of the microstructure normally obtainable in rheocast products. Such a microstructure in which spheroidal particles are uniformly distributed in a given matrix, suggests that the rheocast products may be identified as particulate composites. It is therefore, imperative that the mechanical properties of rheocast products are examined on the basis of theories of composites.

1.5.1 Mechanical Properties of Composite Materials: General Concept

Composite materials are broadly classified as fibre composites or particulate composites. The most widely studied composites are aligned fibre composites in which the fibres are arranged unidirectionally. Such composites are further classified as being continuous if the fibres span the entire length of the material, or discontinuous if shorter fibres are used. When a continuous fibre composite is stressed in tension, the force is directly applied both to the matrix and to the fibre. The composite stress, σ_c , in terms of the stresses partitioned between the matrix and the fibre is then simply given by the rule of mixtures. If the applied stress is parallel to the direction of fibre alignment, under the assumption that the axial strains of fibre and matrix are equal, the tensile strength of the composite, σ_{uc} , is given by the rule of mixtures as,

$$\sigma_{uc} = \sigma_{uf} V_f + \sigma_{um} (1 - V_f) \quad \dots (1.19)$$

when the failure strains of both the components are equal. In equation 1.19, σ_{uf} and σ_{um} are the tensile strengths of fibre and matrix respectively and V_f is the volume fraction of fibres. Usually the failure strains of the individual components of composites are not equal. It has been shown by Kelly and Davies(60) that the largest strain tolerated by the composite when the fracture is incipient is the smallest fracture strain of any individual component. If the

fracture is governed by the smallest fracture strain (say, the fracture strain of fibres), then the largest stress experienced by the matrix would be σ_m' , which is the stress in the matrix corresponding to the fracture strain of the fibre. The composite strength is then given by,

$$\sigma_{uc} = \sigma_{uf} V_f + \sigma_m' (1 - V_f) \quad \dots (1.20)$$

Equation 1.20 suggests that the full stress capacity of the matrix is never utilized and the composite strength is basically fibre controlled. If the volume fraction of the fibres is low so that $\sigma_{uf} V_f < (\sigma_{um} - \sigma_m') (1 - V_f)$, failure of fibres will not lead to the failure of the composite. The stress carried by the fibres will be transferred to the matrix and the composite will fail when the matrix fails. In such a case the fibres do not impart any strengthening effect and the composite strength is primarily matrix controlled. The composite strength is then given by,

$$\sigma_{uc} = \sigma_{um} (1 - V_f) \quad \dots (1.21)$$

It follows therefore that any fibre strengthening effect can be realized only when the fibres exceed a critical volume fraction.

In discontinuous fibre composites the force is not applied directly to the fibres, but it is transferred through the matrix. For a quantitative estimate of the load transfer, consider a single fibre of length l and diameter d .

embedded in a matrix as shown in Figure 1.13a. The stress in the fibre builds up from the ends and reaches a maximum in the central region of the fibre (Figure 1.3b.). The transfer of stress to the fibre may be evaluated by force balance on an element dx of the fibre at a distance x from the fibre end. On the basis of Figure 1.3c; the equation for the elemental force balance may be written as,

$$\sigma \cdot \frac{\pi}{4} d^2 + \pi d \cdot dx \cdot \tau = (\sigma + d\sigma) \frac{\pi}{4} d^2 \quad \dots (1.22)$$

$$\text{or, } d\sigma = \frac{4\tau}{d} dx \quad \dots (1.23)$$

where τ is the fibre matrix interfacial shear stress.

Integration of equation 1.23 from $\sigma = \sigma_0$ at $x = 0$ to $\sigma = \sigma_f$ at $x = x$, yields,

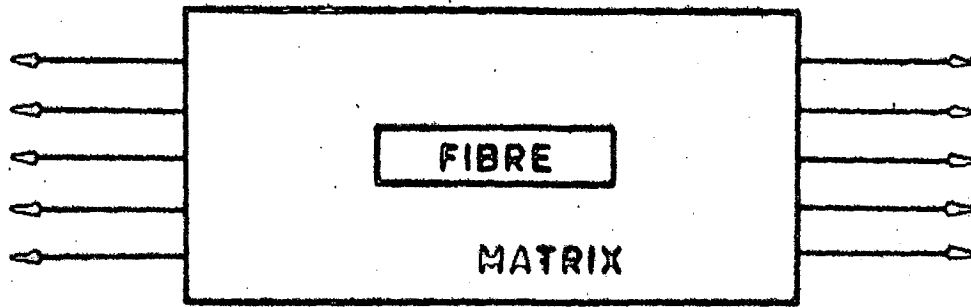
$$\sigma_f = \frac{4\tau x}{d} \quad \dots (1.24)$$

Thus, as x increases, the fibre experiences a larger stress with the limit being $\sigma_f = \sigma_{uf}$. The critical value of x at which such a condition is satisfied is equal to $\ell_c/2$

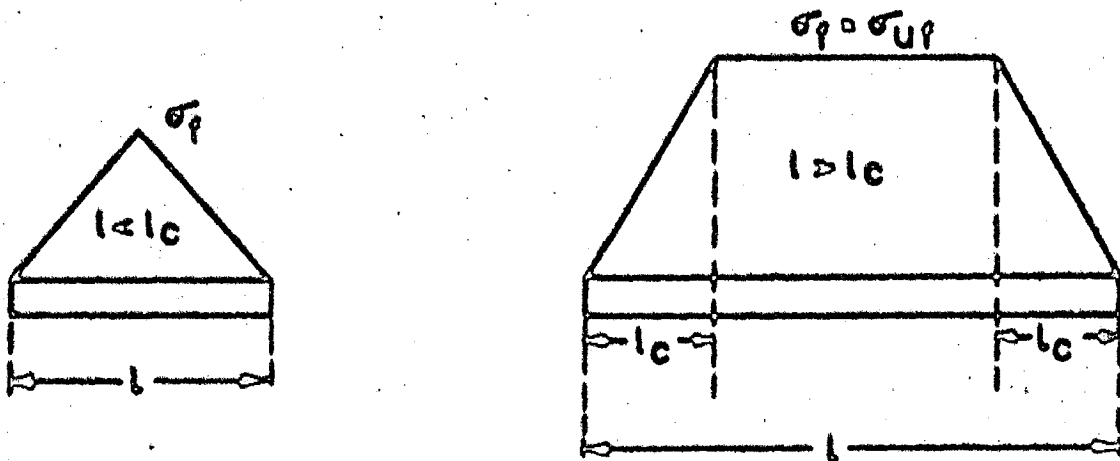
where ℓ_c is the critical fibre length below which the fibres cannot be fractured. Under this limiting condition,

$$\sigma_{uf} = \frac{2\tau \ell_c}{d} \quad \dots (1.25)$$

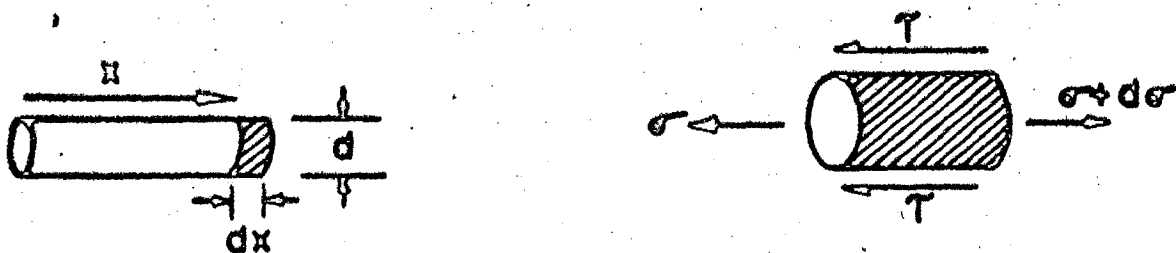
the parameter ℓ_c/d in equation 1.25 is termed as critical aspect ratio. Depending upon the fibre length ℓ , the average stress in the fibre, $\bar{\sigma}_f$, is then given by,



(a)



(b)



(c)

FIG.1.13 DISCONTINUOUS FIBRE COMPOSITE (a) SINGLE FIBRE MODEL (b) DISTRIBUTION OF STRESS IN A DISCONTINUOUS FIBRE (c) ELEMENTAL FORCE BALANCE.

$$\bar{\sigma}_f = \frac{\tau l}{d} \quad \text{when } l < l_c \quad \dots (1.26)$$

$$\bar{\sigma}_f = \frac{\tau l_c}{d} = \frac{1}{2} \sigma_{uf} \quad \text{when } l = l_c \quad \dots (1.27)$$

$$\bar{\sigma}_f = \sigma_{uf} \left(1 - \frac{l_c}{2l}\right) \quad \text{when } l > l_c \quad \dots (1.28)$$

From equations 1.26, 1.27 and 1.28, the tensile strength of discontinuous fibre composites may be written from the rule of mixtures as,

$$\sigma_{uc} = \frac{\tau l}{d} V_f + \sigma_{um} (1 - V_f) \quad \text{when } l < l_c \quad \dots (1.29)$$

$$\sigma_{uc} = \frac{1}{2} \sigma_{uf} V_f + \sigma_{um} (1 - V_f) \quad \text{when } l = l_c \quad \dots (1.30)$$

$$\sigma_{uc} = \sigma_{uf} \left(1 - \frac{l_c}{2l}\right) V_f + \sigma_{um} (1 - V_f) \quad \text{when } l > l_c \quad \dots (1.31)$$

It follows from the above equations that the strength of discontinuous fibre composites will approach to that of continuous fibre composites only when the fibre length is significantly larger than l_c . For fibres shorter than l_c , full fibre reinforcement cannot be achieved.

The transition from fibrous reinforcement to particulate reinforcement occurs gradually as the length to diameter ratio (l/d) of fibres is diminished. In particulate type of reinforcement, the particles are considered to block, restrain or in some way control the phenomena responsible for either extensive plastic deformation or fracture. The models for particulate composites are based on the nature of constraints the particles offer. If the particle constraint

is on dislocation motion, it has been shown (61) that for the non-deformable particles, the yield strength of the composite, σ_{yc} , is given by,

$$\sigma_{yc} = \left[\frac{G_m G_p b}{C' D_p} \right]^{1/2} \dots (1.32)$$

where G_m and G_p are shear moduli of matrix and particle respectively, b is the Burger's vector of the piled up dislocations against the particle, C' is a constant and D_p is the interparticle spacing. Since D_p is decreased by decreasing the particle size and increasing the volume fraction of particles, it follows that σ_{yc} may be increased by decreasing the particle size and increasing the volume fraction. However, when D_p is below a certain minimum (e.g. $\sim 0.5 \mu\text{m}$ in case of WC-Co cermets) the strength drops off because of crack nucleation at weak particle-particle boundaries (61).

In those cases where the constrained matrix can develop stresses sufficient to deform the particles, σ_{yc} is given by (61),

$$\sigma_{yc} = \left[\frac{G_m G_p b}{C''} \right]^{1/2} \dots (1.33)$$

where C'' is a constant. Equation 1.33 suggests that in case of deformable particles, composite yield strength is independent of the physical parameters of the particle such as volume fraction, size, interparticle spacing etc.

It has been shown by Drucker(61,62) that if Griffith type fracture criterion is assumed and if the fracture of particles leads to the fracture of the composite, the composite fracture stress, σ_{uc} , is given by,

$$\sigma_{uc} = \frac{C'''}{d^{1/2}} \quad \dots (1.34)$$

where C''' is a constant and d is the particle diameter.

In brittle matrix composites containing ductile particles, such as glass containing metallic particles, the primary function of the particles is to limit the size of most severe flaws or cracks in the brittle matrix (61). As the volume fraction of a particular size of the particles is increased or at a given volume fraction, the particle size is decreased, the mean free path between the particles is reduced limiting the maximum size of the flaw. Quantitatively, the composite strength is given by,

$$\sigma_{uc} = \frac{C'''}{\left[\left(\frac{1}{V_p} - 1 \right) d \right]^{1/2}} \quad \dots (1.35)$$

where C''' is a constant and V_p is the volume fraction of particles of size d . Both equations 1.34 and 1.35 are based on Griffith type of fracture criteria and show similar functional relationship of σ_{uc} with d .

1.5.2 Fracture Modes in Composites

The fracture mode in composites is determined by the amount of work required to produce unit area of crack surface. This

work is called the work of fracture and is a measure of the resistance to crack propagation. The work of fracture in composite materials is extremely high, much higher than that accountable by adding the contributions of the matrix and the fibre. It is obvious that the enhanced work of fracture in composite materials is due to some interactions of the fibre and the matrix. Based on these interactions, the major factors which have been identified to contribute to the work of fracture are: (a) plastic deformation of matrix or fibre as the crack is opened up, (b) pull-out of broken fibres from their sockets in the matrix on either side of the crack and (c) debonding of the fibre from the matrix.

Plastic Deformation of Fibre/Matrix

The work done in breaking a brittle fibre or matrix is negligibly small and is usually ignored in computing the work of fracture. If the matrix is brittle and fibres are ductile, the total work, W , done in deforming the fibre to failure is given by (63),

$$W = \sigma_{uf} \cdot V_f \cdot d \quad \dots (1.36)$$

If the interface fails in shear at a stress τ , much less than the failure stress of the fibre, σ_{uf} , it has been shown (63) that,

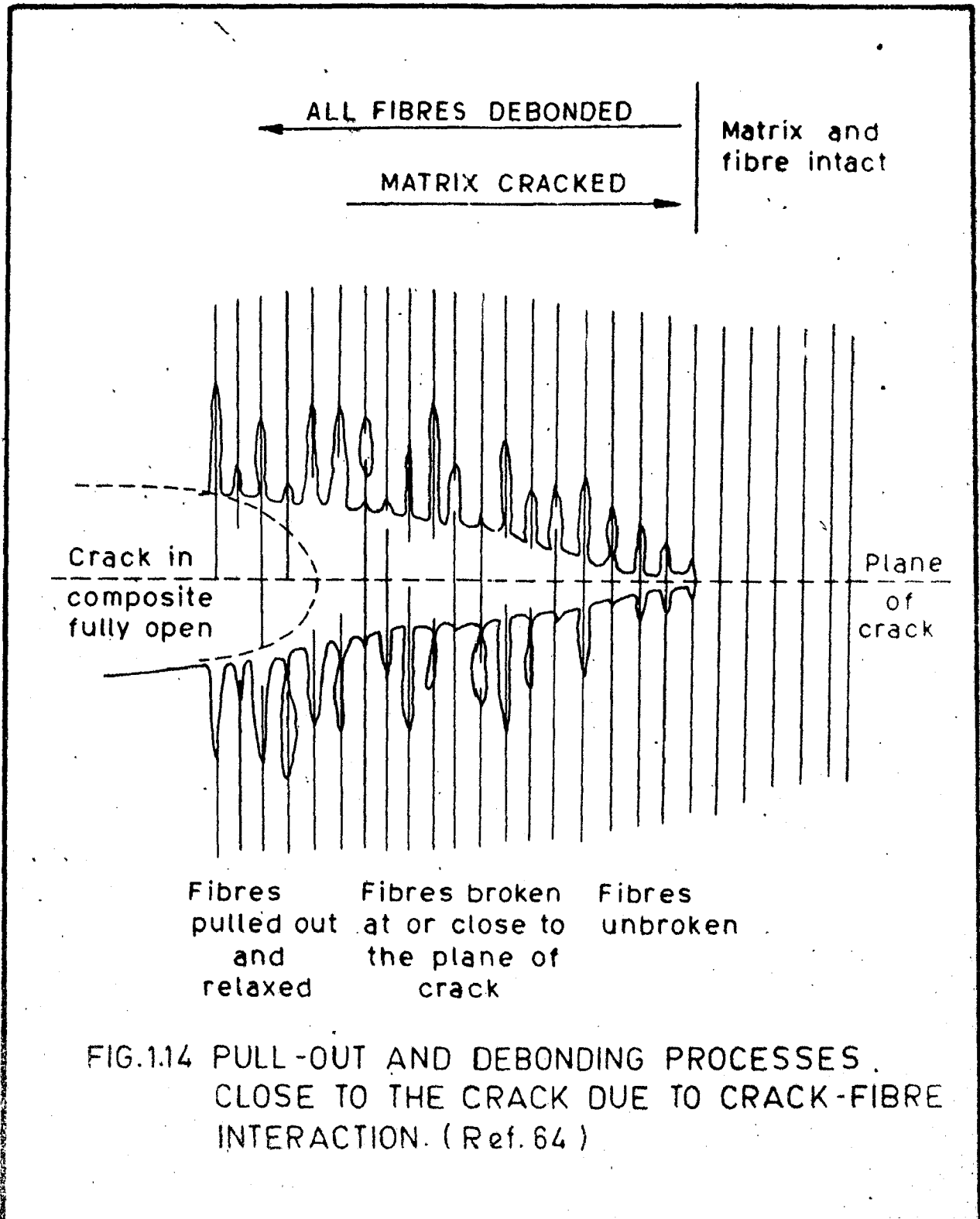
$$W = \frac{d}{4\tau} V_f (\sigma_{uf} - \sigma_f') \int_{\sigma_f'}^{\sigma_{\infty}} \sigma_f d\epsilon \quad \dots (1.37)$$

where the integral is evaluated over the true stress-strain curve of the fibre from σ_f' , stress in the fibre at the failure strain of the matrix, to σ_∞ for complete rupture. ϵ signifies strain. It has been shown (63) that the work of fracture is always higher if the interface fails in shear. In either cases, it is apparent that the work of fracture will increase if the fibre diameter is increased.

If the composite is ductile matrix-brittle fibre type, then also the situation is similar to the one described above, but the roles of the fibre and the matrix are reversed and the work of fracture is controlled by the ductile matrix. Equations similar to 1.36 and 1.37 will describe the net contribution to the work of fracture if subscript 'f' for fibre is replaced by 'm' for matrix and instead of fibre diameter the width of the matrix, between adjacent fibres, is taken into account. In this case also, the work of fracture will increase when the fibre diameter is increased because for a given volume fraction, increase in fibre diameter produces a corresponding increase in the width of the matrix between the adjacent fibres which must be worked to failure.

Fibre Pull-Out

The pull-out and debonding modes of fracture, when a crack proceeding normal to a set of fibres interacts with fibres, are schematically illustrated in Fig. 1.14. If the fracture of a composite occurs by breaking of the fibres, it is



found that all fibres with ends within a distance of $l_c/2$ on either side of the break, pull-out of the matrix instead of fracturing leaving behind a socket in the matrix. Considerable amount of work is done by the applied stress during the fibre pull-out provided that the shear forces between the fibre and the matrix are maintained during the extraction. It has been shown (64) that the work done per unit area of cross-section in withdrawing all those fibres which pull out is given by,

$$W = \frac{V_f}{12} \left(\frac{l_c}{l} \right) \sigma_{uf} \cdot l_c \quad \dots (1.38)$$

Equation 1.38 applies when $l > l_c$. For the case when $l < l_c$,

$$W = \frac{V_f}{24} \pi \tau d l^2 \quad \dots (1.39)$$

On the basis of equations 1.38 and 1.39, the work of fracture in pull-out mode is plotted schematically in Fig. 1.15 against the fibre length. It is seen that the work of fracture increases with l as l^2 when $l < l_c$ and then decreases as $1/l$ when $l > l_c$. In order to maximise the work of fracture the length of the fibre should be kept close to l_c , and l_c should be made large. Increasing l_c implies increasing the fibre diameter (equation 1.25). Thus, the work of fracture will increase with increase in fibre diameter.

Debonding

Theoretical estimate of the work of debonding has been made by Outwater and Murphy (64,65) by equating the energy

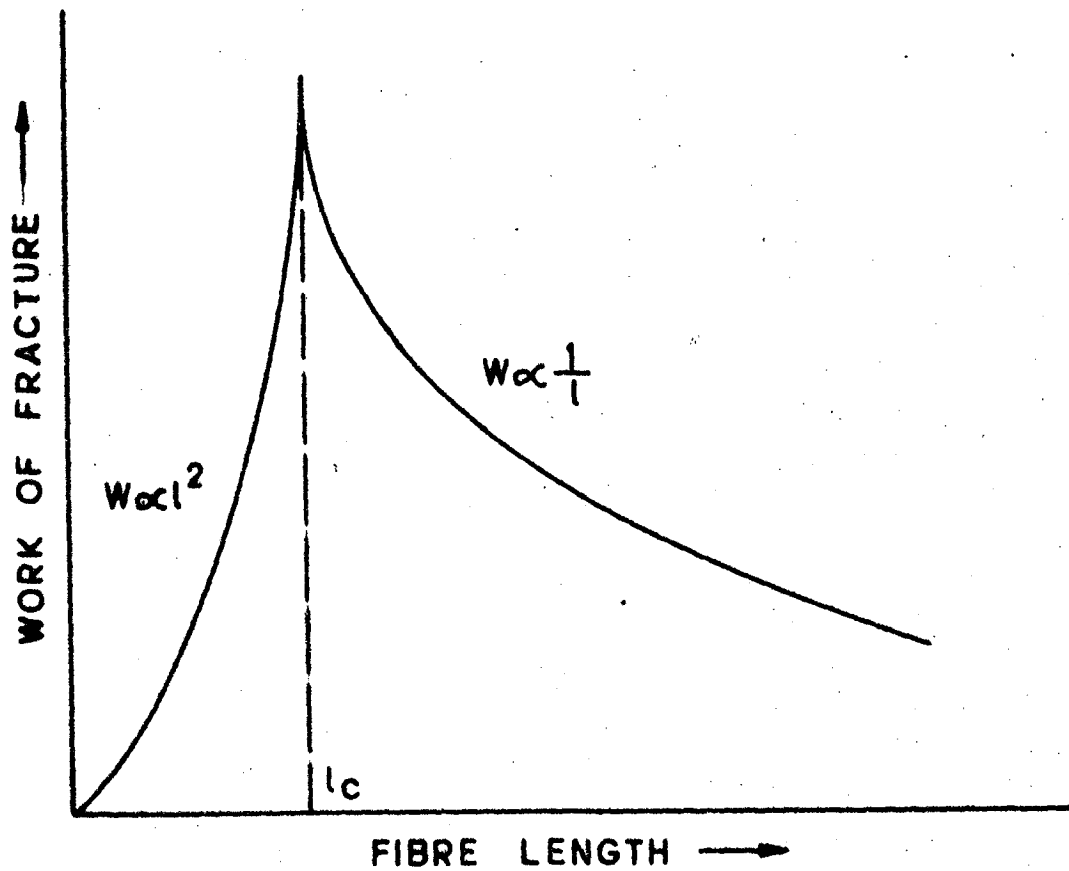


FIG.1.15 SCHEMATIC VARIATION OF WORK OF FRACTURE DUE TO PULL-OUT WITH FIBRE LENGTH. (Ref. 64)

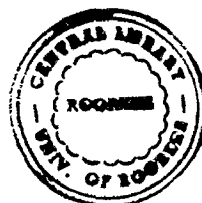
of debonding with the elastic energy stored in the fibre after debonding. The total work of debonding, W_D , has been given by,

$$W_D = \frac{\pi d^2}{24} \left(\frac{\sigma_{uf}}{E_f} \right) \sigma_{uf} \cdot x \quad \dots (1.40)$$

where E_f is the fibre elastic constant and x is the length over which the fibre is debonded. Equation 1.40 also suggests that the work of fracture is increased if fibre diameter is increased. It has been shown (64) that the work of pull-out is usually greater than the work of debonding. However, if W_d , the work of debonding per unit area, satisfies the condition,

$$W_d \geq \frac{\sigma_{uf} d}{8 E_f} \quad \dots (1.41)$$

the fibres break instead of debonding.



177762

Cavitation

Cavitation is an important mechanism by which particulate composites are known to fracture. In cavitation mechanism, cracks or holes are nucleated by particle fragmentation or particle decohesion from the matrix which grow with plastic deformation and ultimately the fracture of the composite results when these growing holes link together by local necking of the intervening material. It has been generally observed that particles of large aspect ratio nucleate holes by multiple internal fragmentation while the equiaxed or

spherical particles almost always nucleate holes by interfacial separation. The models concerning the interfacial separation are based on either energy criteria, local stress criteria or local strain criteria. A model due to Argon et al (66) based on local stress criteria has been found to agree well with the experimental observation. It has been shown that for rigid non-deformable particle, the interfacial tensile stress (σ) may be given by,

$$\sigma = \tau_y \left[\left(\frac{\gamma}{\gamma_y} \right)^{1/\eta} + \sqrt{3} \left(\frac{\sqrt{6}(\eta+1)}{m_1} \frac{\gamma}{\gamma_y} \right)^{\frac{1}{\eta+1}} \right] \dots (1.42)$$

where τ_y is the yield stress in shear, $\frac{\gamma}{\gamma_y}$ is the strain ratio (total strain/yield strain) away from the particle, m_1 is called Taylor factor generally equal to 3.1 and η is the strain hardening exponent of the matrix. The cavity is formed at a critical strain ratio when the interfacial stress equals the interfacial strength. In this model, isolated particles have been assumed so that the interfacial stress is independent of the volume fraction of the particles. This can happen only when the volume fraction is low. At higher fractions the particles will interact when the secondary plastic zones around the particles begin to touch each other. In such a situation, the interfacial stress is greater than that predicted by equation 1.42. Taking into account the particle interaction, the modified equation for interfacial stress has been proposed as,

$$\sigma = \tau_y \left[\sqrt{3} \left[\frac{\sqrt{3}(\gamma/\gamma_y)}{\sqrt{\frac{2\pi}{3V_p} - \sqrt{\frac{8}{3}}}} \right]^{1/\eta} + \frac{\sqrt{6}}{m_1} \left[\frac{2\pi}{3V_p} - \sqrt{\frac{8}{3}} \right] + (\frac{\gamma}{\gamma_y})^{1/\eta} \right] \dots (1.43)$$

where V_p is related to the interparticle spacing (D_p) and particle radius r , by the relation,

$$\frac{D_p}{r} = \sqrt{\frac{2\pi}{3V_p} - \sqrt{\frac{8}{3}}} \dots (1.44)$$

Since the size of the secondary zone increases with increasing plastic strain (i.e. strain-ratio $\frac{\gamma}{\gamma_y}$), for a given volume fraction of particles the critical strain ratio, $(\frac{\gamma}{\gamma_y})_{crit}$, at which the secondary zones touch, may be obtained by considering that the secondary zone size is equal to $D_p/2$, where D_p is given by equation 1.44. Thus, the critical strain ratio above which the particles interact is given by,

$$\left(\frac{\gamma}{\gamma_y}\right)_{crit} = \frac{m_1}{\sqrt{6}(\eta+1)} \left[\frac{\sqrt{2}}{m_1} \left(\frac{2\pi}{3V_p} - \sqrt{\frac{8}{3}} \right) \right]^{\eta+1} \dots (1.45)$$

Once the cavities are formed, they grow with plastic deformation and ultimately link together to cause fracture. Fig. 1.16 represents a typical example of linkage of cavities formed at second phase particles.

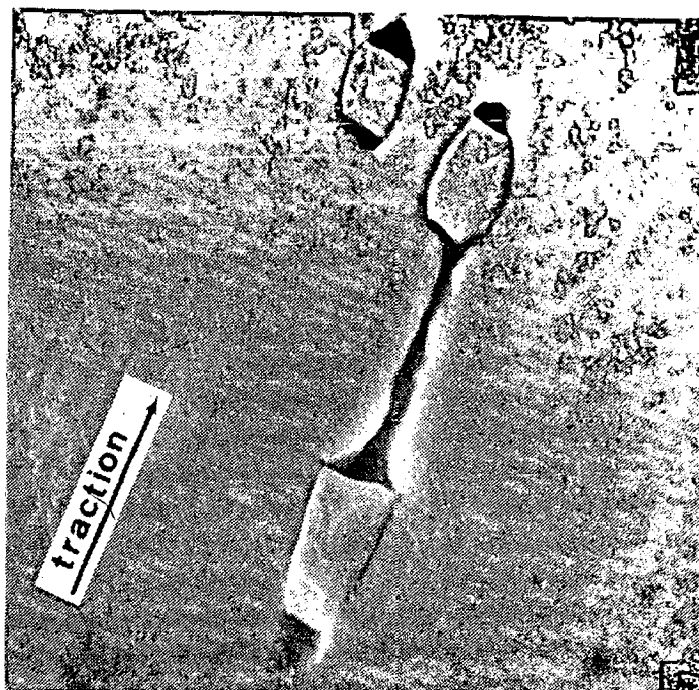


FIG.1.16 LINKAGE OF CAVITIES FORMED AT SECOND PHASE PARTICLES.(Ref.67)

1.5.3 Application to Rheocast Products

In a large number of publications (6, 12, 19, 20, 21, 25, 34, 35, 36, 37, 43), the mechanical properties of rheocast and thixocast products have been reported. Most of the results are preliminary in that they are intended primarily to compare the mechanical properties of these products with those of conventional products. It appears that no detailed study has been undertaken to quantify the mechanical properties in terms of microstructural parameters.

Though in a limited way, Vogel et al. (16) have applied the concept of particulate composites in the evaluation of mechanical properties of rheocast Al-Cu alloys containing 0 to 40% proeutectic α -phase. It has been shown that the fracture toughness is lowered by the presence of small amounts of ductile proeutectic α -phase in brittle α +Cu Al_2 eutectic matrix. Increasing amount of α -phase increases the fracture toughness, but even with 40% of α -phase the fracture toughness is about the same as that of the eutectic. In the absence of theoretical analysis or experimental data for more than 40% of α -phase, the role of the microstructure in modifying the mechanical properties remains uncertain.

1.6 FORMULATION OF PROBLEM

Critical review of the published literature reveals that in spite of the generation of a large volume of data on rheocasting, the fundamental aspects relating to the mechanism of

formation of rheocast microstructure and its role in influencing the mechanical properties have not been clearly understood. Though it is possible to produce quality castings with rheocast slurries, none of the investigations have been able to establish any clear advantage of the rheocasting process over the conventional processes especially in terms of the mechanical properties of castings. Nevertheless, the process is of considerable academic interest from physical metallurgy point of view for a number of reasons. The one which has attracted our attention most is the unconventional microstructure of rheocast products. The role of such a microstructure in modifying the mechanical properties has neither been clearly understood nor it has been investigated systematically. This aspect of study is of cardinal importance for low melting point alloys where the major consideration in the application of the rheocasting process lies in its ability to produce castings of improved mechanical properties. The present research has therefore been planned to enhance our understanding of the inter-relationship of processing, microstructure and mechanical properties of rheocast products.

In order to achieve the above objective, Al-Cu alloys containing 4.5 to 10 Wt% copper have been selected for the present investigation. The choice of Al-Cu alloy system has been prompted by the fact that a large amount of information regarding its solidification characteristics is available and also, this system forms a base for a large number of

industrially important alloys in this composition range. Three major factors have been considered in the design of the detailed plan of the present work:

- (a) Rheocasting of Al-Cu alloys permits dispersion of proeutectic ductile α -phase in a matrix of $\alpha + \text{Cu Al}_2$ brittle eutectic. The particulate nature of the microstructure offers an opportunity to model the rheocast products as particulate composites.
- (b) Stereological studies of rheocast microstructures have so far been carried out mostly on rapidly cooled slurry samples to characterise the primary solid particles. However, the mechanical properties of castings are governed by the overall cast microstructure rather than primary particles only and therefore overall microstructure should be characterised for correlating the mechanical properties with the microstructure.
- (c) Mechanical properties of cast metals are generally strong functions of casting quality and therefore the effect of casting quality must be quantified and its contribution eliminated to understand the role of microstructure in modifying the mechanical properties.

On the basis of the above mentioned considerations, the basic elements of the investigational plan have been formulated as follows:

- (i) To develop a theoretical model for a brittle matrix ductile dispersoid particulate composite to understand the effect of particle parameters on the

mechanical properties for the case when the particles do not interact.

- (ii) To develop a theoretical model as above but for the case when the particles interact.
- (iii) To develop a theoretical model for determining the quantitative effect of casting quality on the mechanical properties in terms of total porosity.
- (iv) To make castings with rheocast slurries and carry out stereological studies of the cast microstructure to understand the effect of the process variables on the microstructure of rheocastings.
- (v) To measure the mechanical properties of the castings, examine the effects of microstructure and porosity, and compare the theoretical predictions with the experimentally observed values.
- (vi) To study the fracture behaviour by SEM fractography to gain further insight into the inter-relationship of microstructure and mechanical properties.

CHAPTER - II

MECHANICAL PROPERTIES: THEORETICAL ANALYSIS

2.1 INTRODUCTION

The major constituent phases present in hypoeutectic aluminium-copper alloys are the Al-rich α -solid solution and $\alpha + \text{CuAl}_2$ eutectic. (Though the eutectic is not a phase in the strict sense, for the purpose of present analysis it will be referred to as a phase). Even in the single phase region, i.e. copper less than 5.7%, some eutectic is almost always present in the cast alloys because of the non-equilibrium nature of the solidification process. Rheocasting of these alloys permits dispersion of non-dendritic spheroidal particles of α -phase in a matrix of eutectic. The α -phase is normally ductile and the eutectic is brittle at room temperature. Such a constitution of the rheocastings allows us to model them as brittle matrix-ductile dispersoid particulate composites. In the present analysis therefore, the concept of particulate composites has been adapted to develop an understanding as to how the strength of apparently sound castings is governed by the microstructural modifications brought about by rheocasting process.

In the development of a theoretical analysis for the type of composite mentioned above, it is pertinent to consider two situations. One, when α -phase is dispersed as discrete particles. This occurs when the volume fraction of α -particles is low. The second situation corresponds to the case when the volume fraction of α -particles is high and the particles join each other. In the former case the eutectic remains continuous and the composite strength is governed largely by eutectic, and in the latter case α -phase becomes continuous and governs the composite strength. It is therefore imperative that the critical volume fraction of the α -phase at which discontinuous α -phase becomes continuous is determined so that it becomes known as to whether for a particular rheocast alloy, the strength is eutectic-controlled or α -phase controlled. In order to determine this critical volume fraction of the α -phase, equation 1.44 may be used which relates the particle size and the interparticle spacing between two neighbouring particles with volume fraction of dispersed particles. By imposing the condition that the interparticle spacing is zero, the critical volume fraction when the particles touch each other may be obtained.

Equation 1.44 shows that the α -phase will be continuous if it is in excess of 78.5%. For the three alloys Al-10% Cu, Al-6% Cu and Al-4.5% Cu used in the present investigation, the average measured volume fractions of α -particles are 70%, 82% and 86% respectively. It follows therefore that

in the Al-10% Cu alloy, the eutectic is continuous and, in Al-6% Cu and Al-4.5% Cu alloys the α -phase is continuous.

In view of the above, two theoretical models for the composite strength have been proposed in the following sections depending upon the physical state of constituent phases. One, for the case when α -particles are discontinuous and the eutectic is continuous and the other, for the case when α -particles are continuous and the eutectic is discontinuous. Besides microstructural parameters, the strength of the cast alloys is also dependent strongly on porosity in castings. In the last section of this chapter therefore, a theoretical analysis for the strength of castings vis-a-vis porosity has also been presented.

2.2 MODEL FOR COMPOSITE STRENGTH WHEN EUTECTIC IS CONTINUOUS

A particulate composite is a special case of discontinuous fibre composite when the length to diameter ratio of the fibre approaches unity. Thus the approach used in the development of theory of discontinuous fibre composites may be adapted to develop theoretical models for particulate composites. From the published literature it appears that no such model exists till todate. In this analysis it is assumed that the matrix is the brittle eutectic and is continuous in which ductile spherical α -particles are embedded. When such a composite is deformed, as with discontinuous fibre composites, the force is not directly

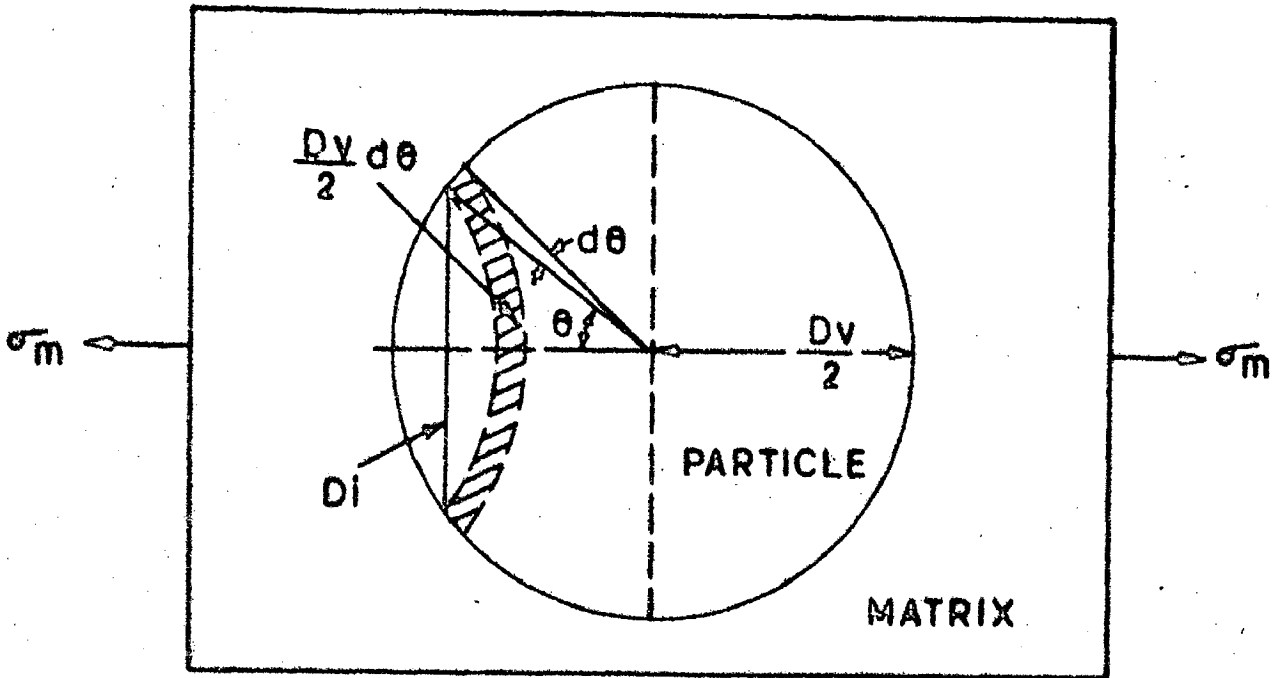
applied to the particles but is transferred through the matrix. In the present work, first the case of load transfer in a single particle model is considered and then the strength of the composite is predicted from the rule of mixtures. In order to simplify the mathematical treatment following assumptions are made:

- i) The matrix is continuous and contains randomly distributed discrete particles.
- ii) Both the matrix and the particles are only elastically deformed.
- iii) Particle-matrix interface is strong enough to affect load transfer.
- iv) Poisson's effect is negligible.
- v) Both the matrix and the particles have equal shear moduli.

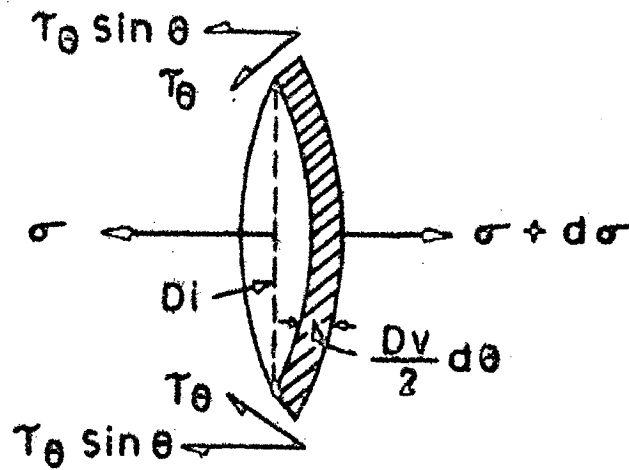
Fig. 2.1(a) shows a single spherical particle of diameter D_v embedded in the elastic matrix subjected to a tensile stress σ_m . If a random plane intersects the particle perpendicular to the direction of the applied stress, the sectional diameter of particle on the plane is denoted by D_i such that,

$$D_i = D_v \sin\theta \quad \dots (2.1)$$

The forces acting on an element of the particle have been shown in Fig. 2.1(b). If τ_0 is shear stress at the particle-matrix interface, the elemental force balance in the direction of the applied stress yields,



(a)



(b)

FIG.2.1 (a) SCHEMATIC REPRESENTATION OF A SINGLE PARTICLE COMPOSITE MODEL (b) ELEMENTAL FORCE BALANCE AT A SECTION OF THE PARTICLE.

$$\tau_{\theta} = \frac{D_v}{2} \frac{d\sigma}{d\theta} \sin\theta = d\sigma \cdot \frac{\pi}{4} D_i^2 \quad \dots (2.2)$$

Simplifying equation 2.2,

$$\frac{d\sigma}{d\theta} = 2\tau_{\theta} \quad \dots (2.3)$$

From equation 2.1, it can be written that,

$$\frac{dD_i}{d\theta} = D_v \cos\theta = [D_v^2 - D_i^2]^{1/2} \quad \dots (2.4)$$

As,

$$\frac{d\sigma}{dD_i} = \frac{d\sigma}{d\theta} \cdot \frac{d\theta}{dD_i} \quad \dots (2.5)$$

Combining equations 2.3, 2.4 and 2.5,

$$d\sigma = 2\tau_{\theta} [D_v^2 - D_i^2]^{-1/2} dD_i \quad \dots (2.6)$$

The case of stress distribution around a spherical elastic particle embedded in an elastic matrix has been treated by Theocaris and Paipetis (68). Following the work of Sezawa and Miyazaki(69), they have shown that if the applied stress be σ , the shear stress distribution τ_{θ} in the particle at the particle-matrix interface is given by,

$$\tau_{\theta} = \sigma \left[2G_p \frac{S_1}{S} \frac{dP_2(\cos\theta)}{d\theta} \right] \quad \dots (2.7)$$

where G_p is the particle shear modulus, $P_2(\cos\theta)$ is a Legendre polynomial and, S and S_1 are determinants given by,

$$S = \begin{array}{cccc} \frac{\lambda_P}{7} & 4G_P & -\frac{9\lambda_m + 10G_m}{3} & -24G_m \\ -\frac{8\lambda_P + 7G_P}{21} & 2G_P & \frac{3\lambda_m + 2G_m}{6} & 8G_m \\ -\frac{\lambda_P}{7} & 2 & \frac{3\lambda_m + 5G_m}{6G_m} & 3 \\ -\frac{5\lambda_P + 7G_P}{42G_P} & 1 & \frac{1}{6} & -1 \end{array} \dots (2.8)$$

$$S_1 = \begin{array}{cccc} \frac{\lambda_P}{7} & \frac{2}{3} & -\frac{9\lambda_m + 10G_m}{3} & -24G_m \\ -\frac{8\lambda_P + 7G_P}{21} & \frac{1}{3} & \frac{3\lambda_m + 2G_m}{6} & 8G_m \\ -\frac{\lambda_P}{7} & \frac{1}{3G_m} & \frac{3\lambda_m + 5G_m}{6G_m} & 3 \\ -\frac{5\lambda_P + 7G_P}{42G_P} & \frac{1}{6G_m} & \frac{1}{6} & -1 \end{array} \dots (2.9)$$

G has been used to denote shear modulus, subscript m and P apply to matrix and particle respectively. λ is Lamé's constant and is a material property given by,

$$\lambda = \frac{\nu E}{(1+\nu)(1-2\nu)} \dots (2.10)$$

where ν is Poisson's ratio and E is elastic modulus.

For the case when the matrix and the particle shear moduli are equal, i.e. $G_m = G_P$, it has been shown (68) that

$$S = 6G_P S_1 \dots (2.11)$$

Substituting the value of S from equation 2.11 in equation 2.7,

$$\tau_{\theta} = \frac{\sigma}{3} \cdot \frac{dP_2(\cos\theta)}{d\theta} \quad \dots (2.12)$$

The Legendre polynomial $P_2(\cos\theta)$ is given by,

$$P_2(\cos\theta) = \frac{1}{2} [3 \cos^2\theta - 1] \quad \dots (2.13)$$

Differentiating equation 2.13, we get,

$$\frac{dP_2(\cos\theta)}{d\theta} = -3 \sin\theta \cos\theta \quad \dots (2.14)$$

From equation 2.1 and 2.14, it may be written that,

$$\frac{dP_2(\cos\theta)}{d\theta} = - \frac{3D_i}{D_v^2} [D_v^2 - D_i^2]^{1/2} \quad \dots (2.15)$$

Substituting equation 2.15 in equation 2.12,

$$\tau_{\theta} = -\sigma \cdot \frac{D_i}{D_v^2} [D_v^2 - D_i^2]^{1/2} \quad \dots (2.16)$$

Taking $\sigma = \sigma_m$ from figure 2.1 and substituting magnitude of τ_{θ} from equation 2.16 in equation 2.6, and rearranging, we get,

$$d\sigma = 2\sigma_m \frac{D_i}{D_v^2} dD_i \quad \dots (2.17)$$

Integrating equation 2.17 within the limits $\sigma = 0$ at $D_i = 0$

and $\sigma = \sigma_{D_i}$ at $D_i = D_i$,

$$\sigma_{D_i} = \sigma_m \left(\frac{D_i}{D_v}\right)^2 \quad \dots (2.18)$$

Equation 2.18 gives the stress in the particle on a planar section D_i as a function of the matrix stress and the ratio of section size to true size of the particle. If the composite contains randomly distributed particles and if on the planar section the average size of particles be \bar{D}_i , the average stress carried by the particles may be written from equation 2.18 as,

$$\bar{\sigma}_{D_i} = \sigma_m \left(\frac{\bar{D}_i}{D_v} \right)^2 \quad \dots (2.19)$$

The true size of particles, D_v , may be determined from the measurements made on the planar section. It has been shown (70) that

$$D_v = \frac{\pi}{2\bar{z}} \quad \dots (2.20)$$

where the parameter z is the reciprocal of the planar section size D_i . Therefore,

$$\bar{z} = \frac{1}{N_0} \sum_{i=1}^{N_0} \frac{1}{D_i} \quad \dots (2.21)$$

where N_0 is the number of section sizes measured.

Now, combining equation 2.19 and 2.20,

$$\bar{\sigma}_{D_i} = \sigma_m \frac{4}{\pi^2} (\bar{D}_i \bar{z})^2 \quad \dots (2.22)$$

Equation 2.22 gives the average stress carried by the particles of average size \bar{D}_i on a planar section. Writing stress in the particle as σ_p for $\bar{\sigma}_{D_i}$,

$$\sigma_p = \sigma_m \frac{4}{\pi^2} (\bar{D}_i \bar{z})^2 \quad \dots (2.23)$$

Now, from the rule of mixtures, the composite stress σ_c may be written as,

$$\sigma_c = \sigma_m V_m + \sigma_p V_p \quad \dots (2.24)$$

where V_m and V_p are the volume fractions of matrix and particle respectively. Substituting equation 2.23 in equation 2.24,

$$\sigma_c = \sigma_m \left[V_m + \frac{4V_p}{\pi^2} (\bar{D}_1 \bar{z})^2 \right] \quad \dots (2.25)$$

Equation 2.25 gives the stress in the composite in terms of matrix stress and particle parameters. If σ_m reaches the fracture stress of the eutectic matrix, σ_{um} , and this condition leads to the fracture of the composite, the tensile strength σ_{uc} may be written from equation 2.25 as,

$$\sigma_{uc} = \sigma_{um} \left[V_m + \frac{4V_p}{\pi^2} (\bar{D}_1 \bar{z})^2 \right] \quad \dots (2.26)$$

In equation 2.26 all the parameters are experimentally determinable and therefore, the estimate of the composite strength can be readily made. The application of this model to the rheocast Al-Cu alloys has been discussed in Chapter 5.

2.3 MODEL FOR COMPOSITE STRENGTH WHEN α -PHASE IS CONTINUOUS

For the case when α -phase is continuous, the eutectic becomes discontinuous and therefore during the deformation of the composite, the force is not applied directly to the

eutectic but it is transferred through the α -phase. Thus, the roles of α -phase and eutectic in the composite are reversed. The composite stress σ_C may be then written from equation 2.24 by replacing subscripts α for m (matrix) and e for P (particle). Subscripts α and e denote α -phase and eutectic respectively. Thus,

$$\sigma_C = \sigma_\alpha v_\alpha + \sigma_e v_e \quad \dots (2.27)$$

Since the geometrical features and the distribution of eutectic are not precisely defined, a unique estimate of σ_e is not possible. However, because the stress in eutectic is transferred through the α -phase, it may be assumed that,

$$\sigma_e = K' \sigma_\alpha \quad \dots (2.28)$$

where K' is a factor which determines the extent to which the stress is transferred to the eutectic. Combining equation 2.27 and 2.28,

$$\sigma_C = \sigma_\alpha [v_\alpha + K' v_e] \quad \dots (2.29)$$

It is apparent from equation 2.29 that the composite stress is governed by the stress in the α -phase.

In the tensile deformation of a strain-hardening material, the flow curve is generally parabolic in the plastic deformation range, and the stress-strain relationship may be represented by a generalized equation (71),

$$\sigma = \left(\frac{2}{3}\right)^{1/2} \mu(0) B_0 \left(1 - \frac{T}{T_M}\right) (\epsilon - \epsilon_b)^{1/2} \quad \dots (2.30)$$

where ϵ is the total strain, ϵ_b is the strain at which the parabolic deformation begins, i.e. the zero of the parabola, B_0 is a universal constant equal to 0.0280, $\mu(0)$ is the shear modulus at the zero point and r is called deformation mode integer which may have values 1, 2, 3, ... during different stages of deformation, T is the temperature at which deformation is taking place and T_M is the melting point of the alloy, ϵ_b is generally nearly zero for most cases. Thus, putting $\epsilon_b = 0$ and substituting equation 2.30 for σ_α in equation 2.29,

$$\sigma_C = \left(\frac{2}{3}\right)^{r/2} \mu(0) B_0 \left(1 - \frac{T}{T_M}\right) \epsilon^{1/2} [v_\alpha + K v_e] \quad \dots (2.31)$$

Equation 2.31 gives the tensile stress-strain behaviour of the composite having ductile α -phase continuous, The tensile strength of the composite σ_{uc} may then be written in terms of the fracture strain ϵ_f as,

$$\sigma_{uc} = \left(\frac{2}{3}\right)^{\frac{r}{2}} \mu(0) B_0 \left(1 - \frac{T}{T_M}\right) \epsilon_f^{1/2} [v_\alpha + K' v_e] \quad \dots (2.32)$$

The application of equation 2.32 to rheocast Al-Cu alloys has been discussed in Chapter 5.

2.4 EFFECT OF POROSITY ON TENSILE STRENGTH

The quantitative influence of porosity on the mechanical properties is governed by its shape, size, distribution and the volume fraction. The shape, size and distribution are usually not fully controllable during processing and

therefore it is a common practice to correlate the mechanical properties directly to the volume fraction or the total porosity (61,72,73).

Stress inhomogeneity and reduction in effective cross sectional area are the two effects by which a material is weakened by the presence of pores. In rheocast alloys, the shrinkage porosity in castings is low because the metal is already partially solid before it enters into the mould. Large porosity in such castings may result from trapped air either because of turbulence during mould filling or because of vortex formation during stirring. These pores are normally spherical in shape. In this section therefore, a theoretical analysis of the role of uniformly distributed spherical pores in material weakening has been presented so that the deterioration of tensile strength due to porosity may be quantitatively estimated.

Consider a specimen of cross-sectional area A_0 subjected to a tensile force F . If the specimen contains randomly distributed spherical pores of average radius R_V , the number of pores per unit area, N_A , on a planar section equals $\frac{3V_P}{2\pi R_V^2}$, where V_P is the volume fraction of pores.

The total number of pores on the cross-section of the specimen is therefore equal to $\frac{3V_P A_0}{2\pi R_V^2}$.

Now, let the cross-section of the specimen be divided into the same number of cells as the number of pores with

an average cell radius R such that each cell shares a pore of average radius r_p . Fig. 2.2 depicts the structure of such a cell. It has been assumed that beyond a distance of R_p the damage by the pore has no influence and the material is bearing as much load as it would have done without the pore. It is generally not possible to define R_p precisely but in order to construct a workable model it is assumed that $R_p = n r_p$. The parameter n is greater than one and depends largely upon the inherent characteristics of the material.

The load bearing capacity of the material decreases as one approaches closer to the hole. It is therefore assumed that the force $f(r)$ carried by unit area of the material within the weakened zone varies exponentially according to the relation,

$$f(r) = \sigma_m K e^{-\ln K \cdot \frac{r-r_p}{R_p-r_p}} \dots (2.33)$$

where σ_m is the uniform stress outside the weakened zone and K is a weakening factor. The magnitude of K is limited to $0 < K < 1$. The form of equation 2.33 has been so selected that it satisfies the condition $f(r) = K \sigma_m$ at $r = r_p$ and $f(r) = \sigma_m$ at $r = R_p$ (Fig. 2.2(b)).

From equation 2.33, the force df carried by an element dr within zone A may be calculated as,

$$df = 2\pi r dr \sigma_m K e^{-\ln K \cdot \frac{r-r_p}{R_p-r_p}} \dots (2.34)$$

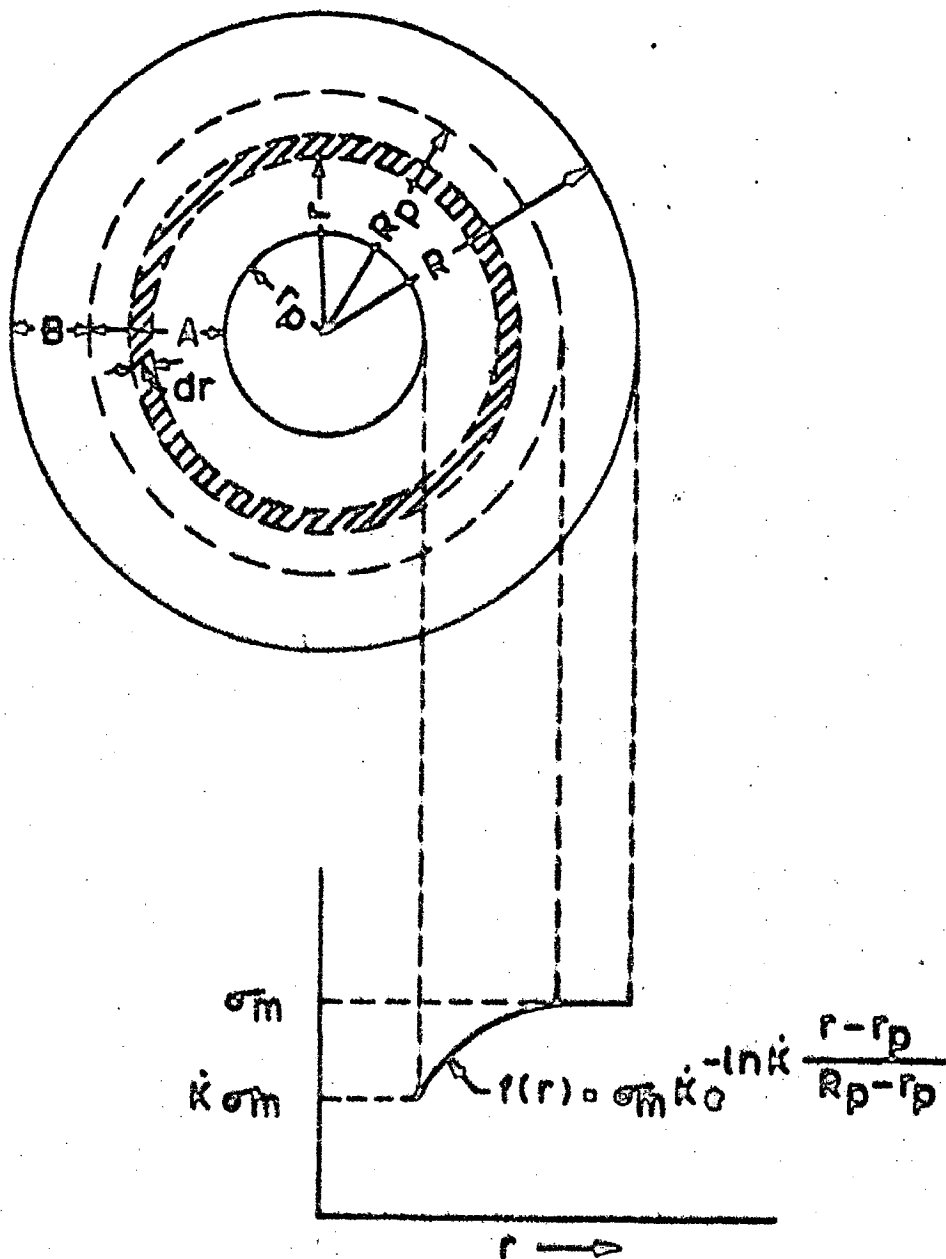


FIG. 2.2 VARIATION OF LOAD CARRYING CAPACITY OF MATERIAL NEAR A PORE ON A PLANAR SECTION PERPENDICULAR TO THE DIRECTION OF APPLIED FORCE.

Integration of equation 2.34 within the limits $r = r_p$ to $r = R_p$ gives the total force f_A carried by Zone A. Thus,

$$f_A = 2\pi \sigma_m r_p^2 \left[(n-1) \left(\frac{k-1}{\ln k} \right) + (n-1)^2 \left(\frac{k-1}{(\ln k)^2} - \frac{1}{\ln k} \right) \right] \dots (2.35)$$

The force f_B carried by zone B of the cell is given by,

$$\begin{aligned} f_B &= \sigma_m \pi (R^2 - R_p^2) \\ &= \sigma_m \pi (R^2 - n^2 r_p^2) \dots (2.36) \end{aligned}$$

The total force F applied to the specimen is obtained by adding equations 2.35 and 2.36, and multiplying by the total number of cells on the cross section. Thus,

$$\begin{aligned} F &= 3V_{PA} \sigma_m \frac{r_p^2}{R_V^2} \left[(n-1) \left(\frac{k-1}{\ln k} \right) + (n-1)^2 \left(\frac{k-1}{(\ln k)^2} - \frac{1}{\ln k} \right) \right] \\ &\quad + \frac{3V_{PA}}{2} \sigma_m \left(\frac{R^2}{R_V^2} - n^2 \frac{r_p^2}{R_V^2} \right) \dots (2.37) \end{aligned}$$

$\frac{r_p^2}{R_V^2}$ and $\frac{R^2}{R_V^2}$ can be determined experimentally. For a random distribution however it can be shown that $\frac{r_p^2}{R_V^2} = \frac{2}{3}$ and $\frac{R^2}{R_V^2} = \frac{2}{3V_P}$. Putting these values in equation 2.37 and rearranging we get,

$$\begin{aligned} \frac{F}{A_0} &= \sigma_m - \sigma_m \left[n^2 - 2(n-1) \left(\frac{k-1}{\ln k} \right) \right. \\ &\quad \left. - 2(n-1)^2 \left(\frac{k-1}{(\ln k)^2} - \frac{1}{\ln k} \right) \right] V_P \dots (2.38) \end{aligned}$$

It is now assumed that the material fails when σ_m equals σ_0 ,

the tensile strength of the pore free material, The tensile strength of the material containing pores is given by $\sigma_P^* = \frac{F}{A_0}$ and therefore equation 2.38 may be rewritten as,

$$\frac{\sigma_P^*}{\sigma_0} = 1 - \left[n^2 - 2(n-1) \left(\frac{k-1}{\ln k} \right) - 2(n-1)^2 \left(\frac{k-1}{(\ln k)^2} - \frac{1}{\ln k} \right) \right] \frac{\%P}{100} \quad \dots (2.39)$$

where P is the total porosity. ..

If the coefficient of porosity term is represented by α , equation 2.39 may be written as,

$$\frac{\sigma_P^*}{\sigma_0} = 1 - \alpha (\% P) \quad \dots (2.40)$$

α represents the magnitude of weakening for each percent of porosity and depends upon n and k . Fig.2.3 shows the isoweakening diagram which reveals that for the same weakening, i.e. same α value, a number of combinations of n and k values exist and therefore, it is not possible to obtain the values of n and k straightforward even if the value of α is experimentally known. Nevertheless, Fig.2.3 is significant in that it illustrates that for a given value of n , the maximum weakening, i.e. α_{max} is fixed and is independent of k .

The above analysis provides us with a two parameter formal equation for fitting the experimental data. This highly simplistic model equation predicts that the variation of tensile strength with porosity is linear. The limiting

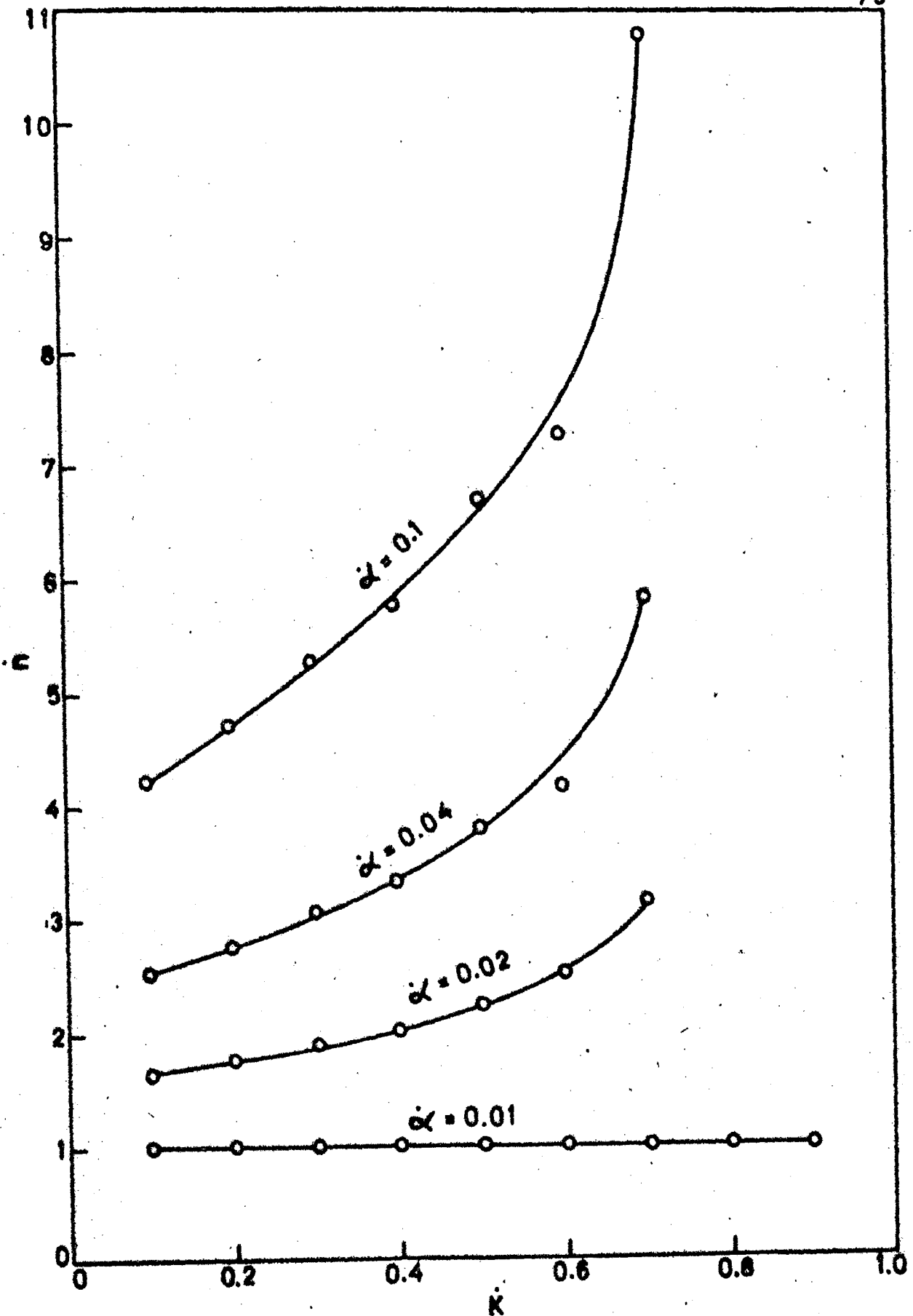


FIG.2.3 ISO-WEAKENING DIAGRAM.

porosity level upto which this model is valid can be readily found out by imposing the condition $R_p = R$.

Since $\frac{r_p^2}{R_V^2} = \frac{2}{3}$ and $\frac{R^2}{R_V^2} = \frac{2}{3V_p}$, the limiting porosity level P_c for the validity of the equation (2.39) may be given by,

$$P_c = \frac{100}{n^2} \quad \dots (2.41)$$

For the case $R_p > R$, the pore-pore interaction takes place and therefore for porosity greater than P_c , the model will not apply. The application of this model in case of rheocast alloys has been discussed in Chapter 5.

CHAPTER III

EXPERIMENTAL WORK

3.1 ALLOY SELECTION

Aluminium-copper alloys in the composition range of 4.5 to 10 weight percent copper form the base for a large number of industrially important alloys. The variation of copper content leads to the variation of α -phase and eutectic amounts in the cast alloys. Depending upon the relative amounts of these constituent phases, the strength is either α -phase controlled or eutectic controlled. As illustrated in section 2.1, for the Al-4.5% Cu alloy the strength is α -phase controlled and for the Al-10% Cu alloy it is eutectic controlled. For a systematic investigation on the basis of concepts of composite material, the need for investigating different alloy compositions in the range of 4.5 to 10% Cu cannot be overemphasized. Furthermore, from the binary equilibrium phase diagram of Al-Cu alloy system shown in Fig. 3.1, it is apparent that in this composition range, the gap between the liquidus and the solidus temperatures is sufficiently wide, the maximum being at ~6% Cu, which makes these alloys most suitable for processing by rheocasting method. On the basis of above considerations, three alloys, Al-10% Cu, Al-6% Cu and Al-4.5% Cu

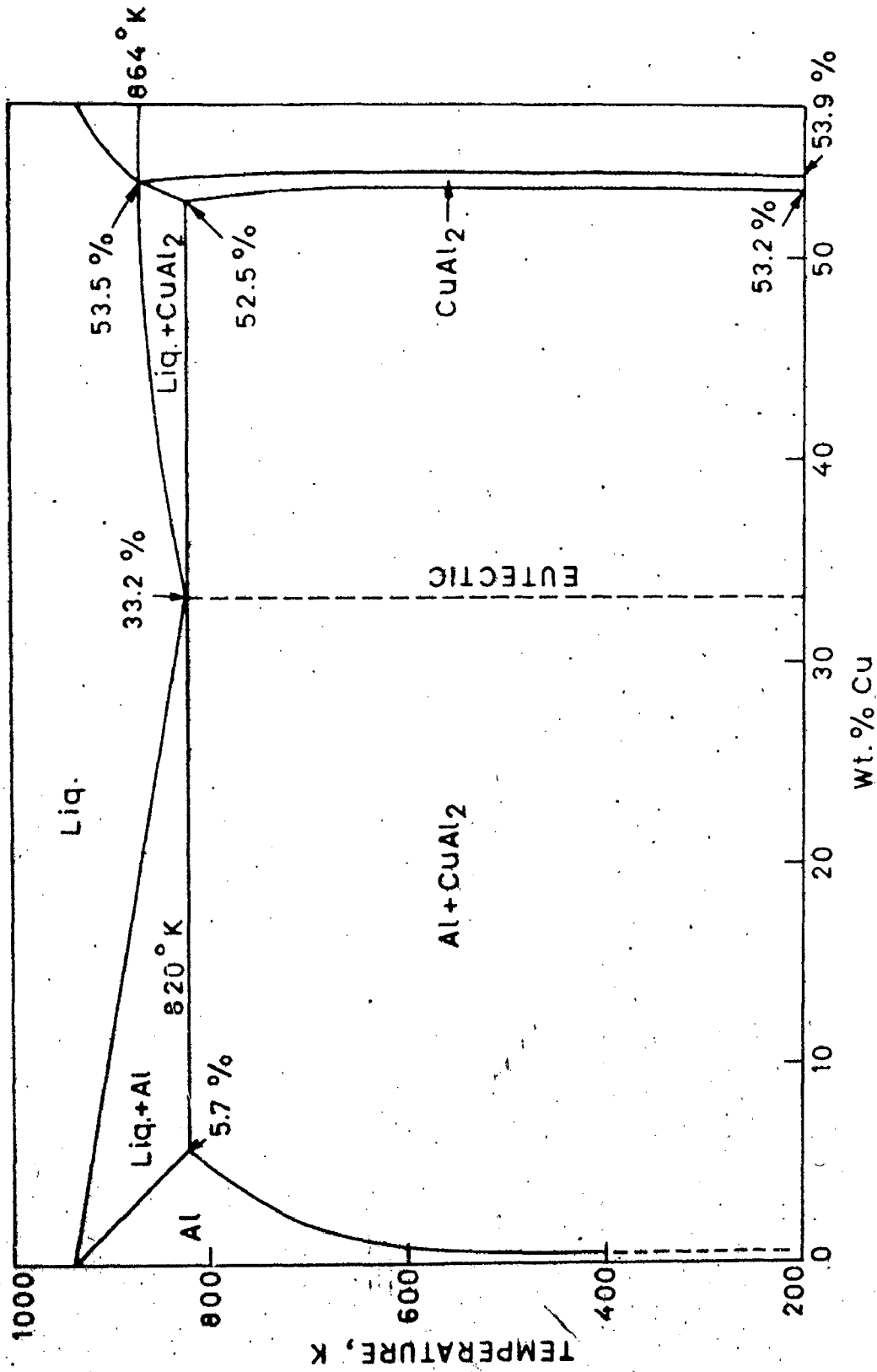


FIG. 3.1 EQUILIBRIUM PHASE DIAGRAM OF Al-Cu SYSTEM.

have been selected for the present investigation.

3.2 ALLOY PREPARATION

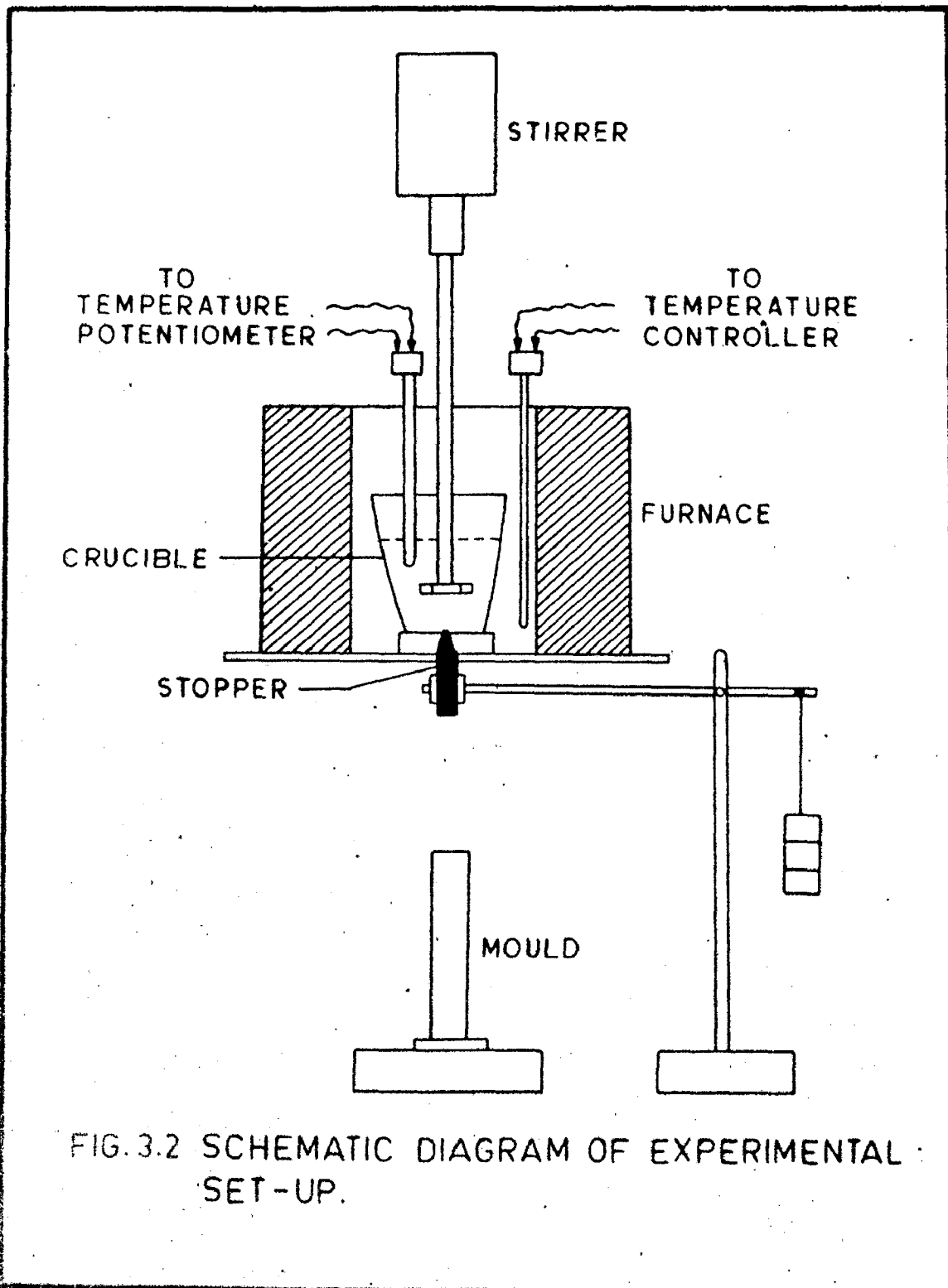
The alloys used in the present work were made by melting required amounts of aluminium and copper in a coke fired pit-furnace. Each heat consisted of about 10 Kg of the melt which was thoroughly stirred with a rod to ensure uniformity in composition. The melt was finally degassed with a Foseco degasser and sand cast into bars of approximately 40x50x600 mm size. Small pieces of about 0.5 Kg were cut out from these bars for making the test castings. The average compositions of the alloys made have been shown in table 3.1.

3.3 RHEOCASTING SET-UP

A batch type rheocasting set-up fabricated for this work has been schematically shown in figure 3.2. It mainly comprises of a melting unit, stirring and pouring devices. The melting unit consists of a furnace which was constructed by winding a 18 SWG Kanthal wire over a muffle of 125x125x260 mm size, the total resistance of the wire being 30 ohms. The muffle has its one end open and the other end closed with a hole in its centre. The open end of the muffle formed the top of the furnace which was mounted on a steel frame with sufficient clearance from the floor so that the mould could be conveniently placed right below the furnace. A

Table 3.1 Chemical analyses of alloys in weight percent

Elements \ Alloys	Al-4.5%Cu	Al-6% Cu	Al-10% Cu
Copper	4.38	6.20	10.20
Iron	0.29	0.42	0.72
Silicon	0.26	0.14	0.15
Manganese	0.01	0.01	0.02
Magnesium	-	-	-
Titanium	0.01	0.01	0.02
Zinc	0.07	0.03	0.09
Aluminium	Balance	Balance	Balance



Pt/Pt-13% Rh thermocouple placed close to the muffle wall was connected to a temperature controller, with a temperature range of 0-1600°C, to maintain the temperature of the furnace at desired level during melting. The current input to the furnace was regulated with an auto-transformer.

For melting, a graphite crucible with a 10 mm hole in its bottom was placed inside the furnace. The hole of the crucible was plugged with a graphite stopper inserted through the hole in the muffle bottom. The stopper was held in place with the help of a lever as shown in Fig.3.2. The open end of the muffle was kept covered with a thick asbestos sheet during melting.

The stirring of the melt was carried out with a stirrer having 1 HP motor with a maximum rated speed of 4000 rpm. The motor of the stirrer was held with a rigid grip right over the furnace. A flat four blade impeller of 50 mm diameter, machined out from a 3 mm thick mild-steel plate, was fastened at one end of a steel rod, the other end of which was connected to the shaft of the motor. The speed of the stirrer was varied by regulating the power input through an auto-transformer. A Strobometer capable of measuring speeds upto 18000 rpm was used for measuring the speed of the stirrer.

For measuring the temperature of the melt, a chromel/alumel thermocouple was used. The protective sheath for the thermocouple was made by drilling hole in a cast

iron rod. The thermocouple encased in the protective sheath was introduced inside the melt and the tip of the thermocouple was held just above the impeller for measuring the melt temperature during stirring. The temperature was read directly on a Leeds-Northrup, No. 8694 potentiometer, with a Fahrenheit scale. The graduation on the temperature scale was of 10°F , but the galvanometer of the potentiometer permitted readings accurate to 2.5°F . The original temperature readings in Fahrenheit scale have been converted and reported in the Kelvin scale.

The pouring was carried out by removing the graphite stopper from the bottom of the crucible. The metal pouring out of the crucible was cast in an open-top laboratory scale split-mould made of steel. The size of the mould was $30 \times 30 \times 250$ mm. The mould was kept as close to the bottom of the furnace as possible leaving only necessary clearance between the top of the mould and the bottom of the furnace for easy and unobstructed removal of the stopper. The ingot was finally cooled by spraying water over the mould.

3.4 SELECTION OF PROCESS VARIABLES

Two parameters, speed of stirring and pouring temperature, were varied for making various rheocastings. A close examination of some of the published works on Al-alloys (13,14) revealed that stirring rate below 300 rpm might not be advantageous in producing uniformly distributed non-dendritic particulate

structure characteristic of rheocasting. At the same time, if very high stirring rates are used, a vortex is formed within the melt which causes excessive entrapment of air resulting in very high porosity in the castings. It was therefore decided to make castings at moderate stirring speeds. For the Al-10% Cu and Al-6% Cu alloys, stirring speeds of 700 and 1000 rpm were employed. For the Al-4.5% Cu alloy, it was intended to investigate in greater detail because it is the most widely used Al-Cu alloy of industrial importance. For this alloy therefore, stirring speeds of 500, 700, 1000 and 1200 rpm. were employed. No restriction on the pouring temperature was imposed except that the temperature was lowered only to the extent upto which it was possible to make rheocastings without choking the hole of the crucible. No attempt was made to optimise the process parameters as the objective of the experimental work was to produce castings with varied microstructure and porosity, so that sufficient data could be generated for determining their quantitative effects on the mechanical properties.

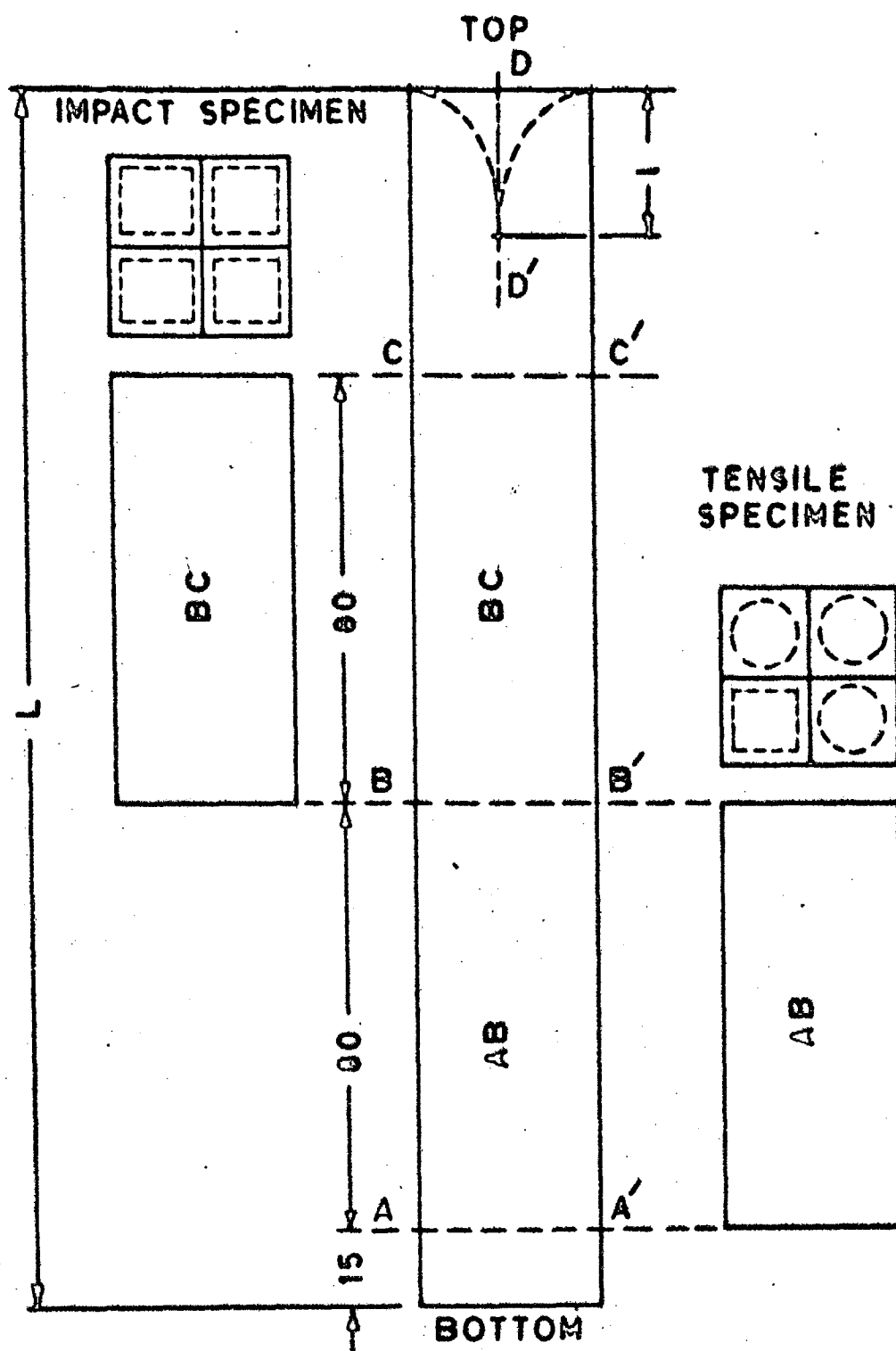
3.5 CASTING PROCEDURE

For making rheocastings, about 0.5 Kg of the alloy was melted in the graphite crucible inside the furnace maintained at 1030 K. After melting, the furnace was switched off and the melt was allowed to cool. While the melt cooled, the impeller of the stirrer was kept just above the melt for preheating. The

temperature of the melt was continuously measured with the chromel/alumel thermocouple. When the temperature came down to the liquidus temperature of the alloy, the impeller was introduced into the melt and the motor of the stirrer was secured tightly in the fixed grip just above the furnace. The liquidus temperatures of Al-10% Cu, Al-6% Cu and Al-4.5% Cu alloys were taken as 905K, 918K and 924K respectively from Figure 3.1. The stirring was then started and continued through the solidification range of the alloy. At the desired temperature, the stirring was stopped and the stopper was removed. The metal was cast by collecting the melt directly into the ingot mould kept below the furnace. In order to examine the structure of the slurry, some samples of the slurry were sucked out with a Corning glass tube fitted with a horn-bulb, and quenched in water.

Some castings were also made without stirring which were poured from ~50K above the liquidus temperature. These castings were termed as conventional castings and were used for comparison of properties with those of rheocastings.

Fig.3.3 represents a schematic diagram of a typical ingot cast by the above procedure and the scheme of sectioning of the ingot for making different measurements. During some of the preliminary trial experiments, the microstructures at all the sections, AA', BB' and CC' were examined. However, no apparent difference in the microstructures at these three



ALL DIMENSIONS IN mm

FIG.3.3 LOCATION OF VARIOUS SPECIMENS MACHINED OUT FROM THE CAST INGOT.

sections were discernible and therefore, for all subsequent castings only the microstructures at section AA' were examined. The specimens for mechanical properties evaluation were machined out from AB and BC portions of the ingot. The top portion above the section CC' was resectioned longitudinally at DD' for measuring the length of the shrinkage-pipe formed.

3.6 METALLOGRAPHY

The lowest portion of the ingot at Section AA' (Fig.3.3) was prepared for metallographic examination using standard metallographic procedure. The cloth polishing was carried out on a blazer-cloth using polishing grade alumina-suspension. The final polishing was done by electrolytic method on 'ELYPOVIST' electropolishing machine using standard electrolyte consisting of a mixture of 30% nitric acid and 70% methanol. During electropolishing the surface of the sample was continuously observed through the microscope attached to the electropolishing machine till the polishing progressed to the desired extent. The electropolishing time varied between 10 to 20 s for different samples. After polishing, all the samples were etched with Keller's reagent for about 10S, washed, dried and finally examined under 'METAVERT' optical microscope. Typical microstructural features of all the samples were photographed. The micrographs have been presented and discussed in Chapter 4.

The stereological measurements of the microstructural features were carried out to determine the volume fraction,

size and distribution of proeutectic α -particles in the rheocast samples. The volume fraction of α -particles was measured by 'point-counting' method. A grid containing 36 points was inserted into the eye-piece of the microscope. The magnification of the microscope was so adjusted that maximum resolution could be obtained and at the same time the condition of not more than one grid-point in one particle was satisfied. The number of grid-points falling on α -particles were counted at random locations. For each sample 25 such observations were taken. The volume fraction was then calculated from the relation,

$$V_p = \frac{\sum_{i=1}^{25} N_i}{25 \times 36} \quad \dots (3.1)$$

where V_p is the volume fraction and N_i is the number of grid-points falling on α -particles in any particular observation.

The size of α -particles was measured with a microscale inserted into the eye-piece of the microscope. The microscale was first calibrated with a given standard at the magnification at which the measurements were made. One division of the microscale measured 5.4 μm of the object at a magnification of 200. One hundred α -particles were randomly measured on each sample and the average size (\bar{D}) and standard deviation (σ) were calculated using standard statistical procedures (74). The results of the stereological

measurements are presented and discussed in Chapter 4.

3.7 POROSITY AND SHRINKAGE-PIPE MEASUREMENTS

Since the estimation of porosity was aimed at determining its influence on the mechanical properties, all the samples used for mechanical testing were evaluated for porosity level. The porosity value of each casting was determined by taking the average of porosity level of all the samples taken from that casting. For determining the porosity, first the density of each sample was measured by usual weight-loss method. From the observed density (ρ_o), porosity values (%P) were calculated according to the relation,

$$\% P = \frac{\rho_{th} - \rho_o}{\rho_{th}} \times 100 \quad \dots (3.2)$$

where ρ_{th} is the theoretical density of the alloy. Theoretical density was calculated from the known densities of equilibrium constituent phases of each alloy. The calculated theoretical densities of Al-4.5% Cu, Al-6% Cu and Al-10% Cu alloys are respectively 2839 kgm^{-3} , 2885 Kgm^{-3} and 3008 Kgm^{-3} .

The formation of shrinkage-pipe in ingots is inevitable due to shrinkage of liquid metal during solidification. The portion of the ingot which contains the shrinkage-pipe is normally chopped off before deformation processing operations and therefore, the actual yield of the metal is lowered.

In rheocasting since the metal entering into the ingot mould is already partially solid, a smaller shrinkage-pipe and therefore higher yield of the ingot metal is anticipated. From the published literature, it appears that no investigation relating to this aspect of rheocasting has so far been carried out. Though this did not fall within the scope of the present investigation, it was felt desirable to make some preliminary observations in this regard. The ingot casting yield was calculated according to the relation,

$$\text{casting yield (\%)} = \frac{L - l}{L} \times 100 \quad \dots (3.3)$$

where l is the length of shrinkage-pipe and L is the total length of the cast ingot. Some observations for Al-4.5% Cu alloy have been given in table 3.2. Though no systematic variation of the casting yield with process parameters has been observed, as compared to conventional casting, higher yield in case of rheocastings is evident. The absence of any direct correlation of casting yield with process parameters is probably due to random porosity behaviour which is known to compensate for the volumetric shrinkage. Nevertheless, these preliminary observations do indicate that another potential application of the rheocasting process may be in the production of ingots required for wrought end-products due to higher yield of the ingot metal.

Table 3.2 Effect of Processing Condition on Casting Yield of Al-4.5% Cu Alloy

Sl.No	Stirring Speed (r.p.m)	Pouring Temperature (K)	Casting Yield (%)
1.	700	922	94.7
2.	700	919	93.1
3.	700	914	98.6
4.	700	911	93.1
5.	1000	919	98.6
6.	1000	916	95.0
7.	1000	914	93.3
8.	1000	911	96.4
9.	1000	908	94.8
10.	1000	905	92.5
11.	Conventional Casting	960	86.8
12.	Conventional Casting	960	88.0

3.8 MECHANICAL PROPERTIES MEASUREMENTS

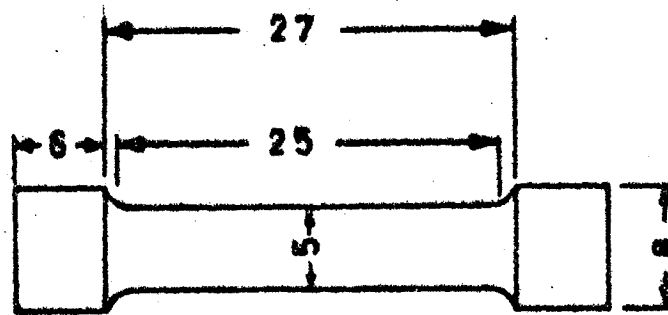
Hardness, impact and tensile tests were carried out for the evaluation of mechanical properties. Hardness indentations were made on same samples which were used for stereological measurements. Before testing, the surface was first finished with 4/0 grade emery paper and then lightly polished on blazer-cloth using polishing grade alumina-suspension. Hardness measurements were carried out on a Vicker-Brinell hardness testing machine using Vicker's scale with 5 kg of load. On each sample, five observations were taken the average of which constituted one reading.

The impact tests were carried out on an impact testing machine using a standard Izod impact notched specimen. One sample from the section AB and two from Section BC were machined out and the average Izod value of the three specimens were determined which constituted one reading. During the initial trials for Al-10% Cu alloy, it was observed that both hardness and Izod impact values were insensitive to processing conditions as shown in table 3.3. In view of these observations, hardness and impact tests were subsequently abandoned for Al-6% Cu and Al-4.5% Cu alloy.

Tensile tests were performed on a motorized Hounsfield tensometer. The dimensions of the test piece have been shown in Fig.3.4. All the specimens used for tensile tests were machined out from section AB of the ingot (figure 3.3).

Table 3.3 Effect of Processing Condition on
Hardness and Impact Strength of
Al-10% Cu Alloy

Sl.No.	Stirring Speed (r.p.m.)	Pouring Temperature (K)	Izod Impact Value (Nm)	Hardness (VHN)
1.	700	900	2	77
2.	700	896	2	85
3.	700	894	2	83
4.	700	892	2	88
5.	700	886	2	80
6.	700	880	2	83
7.	1000	900	2	87
8.	1000	898	2	83
9.	1000	894	2	82
10.	1000	892	2	85
11.	1000	886	2	83
12.	Conventional Casting	950	2	81



ALL DIMENSIONS IN mm

FIG.3.4 DIMENSIONS OF THE SPECIMEN USED FOR TENSILE TEST.

Generally three specimens were tested and the average of the three constituted one reading. All tests were carried out on a load-scale of 0-500 kg with matching beam. Both ultimate tensile strength (UTS) and percent elongation were determined. All the strength values were obtained in Kg mm^{-2} and have been reported after conversion to MNm^{-2} unit. During the tensile test, load extension curves were also recorded on an automatic recording unit attached to the tensometer. The results of the tensile tests have been presented and discussed in Chapter 5.

3.9 SEM FRACTOGRAPHIC STUDIES

- In order to gain an insight into the fracture behaviour, specimens fractured in the tensile tests were examined under Philips 501 Scanning Electron Microscope (SEM) with a maximum rated resolution of 70 \AA . A small sample from the fractured specimen was carefully cut to avoid any damage to the fractured surface. The surface opposite to the fractured surface to be examined was wheel-ground to make it plane. The sample was then glued carefully in the specimen holder of the SEM by silver paste. The fractured surface was scanned thoroughly and the features of interest were photographed. The results of the fractographic studies have been presented in Chapter 5.

CHAPTER - IV

RESULTS AND DISCUSSION: MICROSTRUCTURE

4.1 INTRODUCTION

The rheocasting process adopted for the present investigation allows the solidification to complete in two stages. The first stage is the primary solidification stage in the crucible when the melt is vigorously stirred and, the second stage is of secondary solidification which takes place after the primary solidification product is poured into the mould. The overall rheocast microstructure is therefore governed by the effects of both the stages of solidification. In case of rheocastings, the proeutectic α -phase consists of two types of particles - one, those which nucleate during primary solidification (during stirring) in the crucible and grow during the primary as well as the secondary solidification in the mould (primary particles), and the other, those which nucleate and grow independently during secondary solidification in the mould (secondary particles). In this chapter, the results of the optical microscopic study of overall cast microstructure of rheocast Al-Cu alloys have been presented and discussed with a particular emphasis on the shape and size distribution of the proeutectic α -phase. The results have been analysed on the basis of

possible conditions prevailing during the two stages of solidification and an attempt has been made to characterise the rheocast microstructures vis-a-vis process parameters. The basis of selection of process parameters for different alloys has been indicated in section 3.4. Results pertaining to Al-10% Cu, Al-6% Cu and Al-4.5% Cu alloys have been presented in sections 4.2, 4.3 and 4.4 respectively. In section 4.5, the three sets of results have been compared and discussed to elicit relevant information on the role of copper content in influencing the rheocast microstructures.

4.2 RESULTS: MICROSTRUCTURE OF Al-10% Cu ALLOY

The optical micrographs of various castings of Al-10% Cu alloy have been shown in Figs.4.1 to 4.6. Figure 4.1 shows the microstructure of conventional casting whereas Fig.4.2 to 4.6 depict the microstructures of rheocastings. A comparison of conventionally cast and rheocast microstructures clearly reveals that the morphology of proeutectic α -phase is significantly modified by the rheocasting process and its variables, namely the pouring temperature and the stirring speed. The microstructure of conventional casting in Fig.4.1 shows the dendrites of proeutectic α -phase whereas the microstructure of rheocastings in Figs.4.2 to 4.6 are characterised mostly by the non-dendritic morphology of α -phase, though the formation of dendrites to a limited extent is also evident in several samples. Further comparison

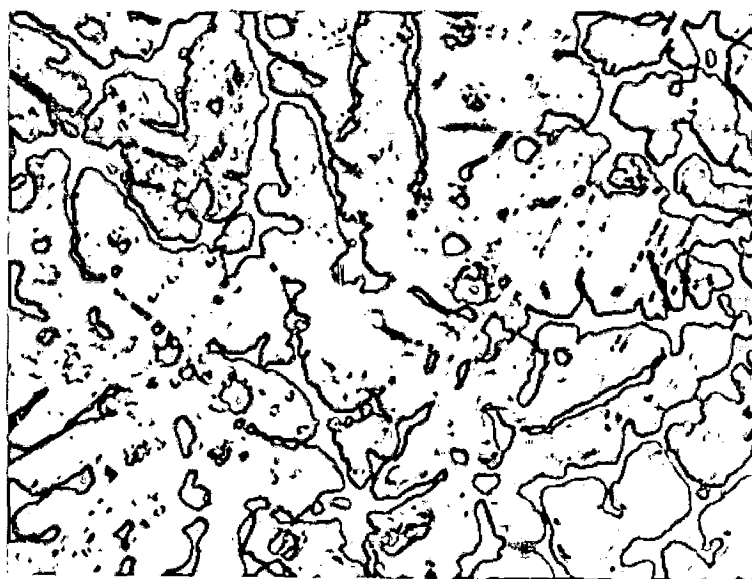
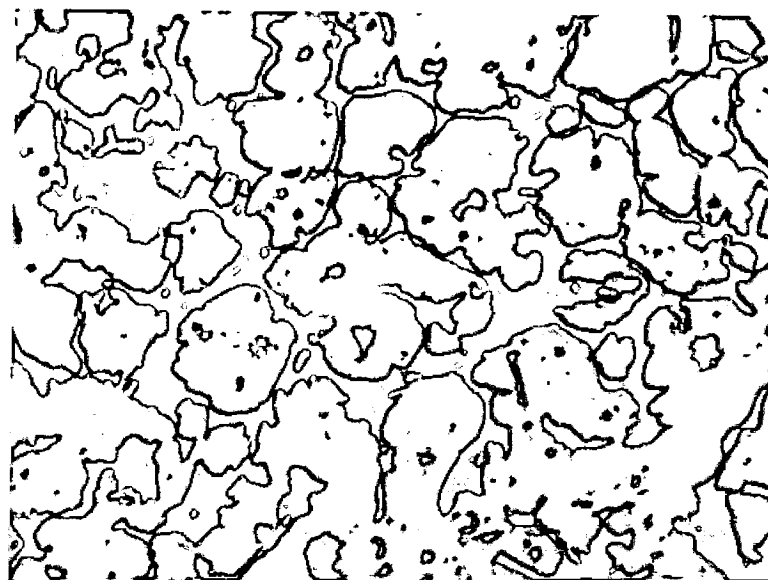
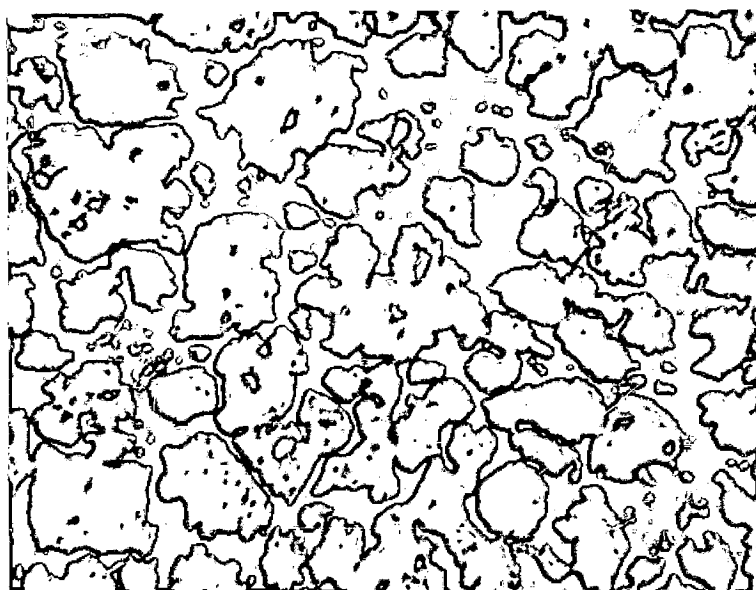


FIG.4.1 MICROSTRUCTURE OF CONVENTIONALLY
CAST Al-10% Cu ALLOY Poured FROM
950 K. Mag. X200

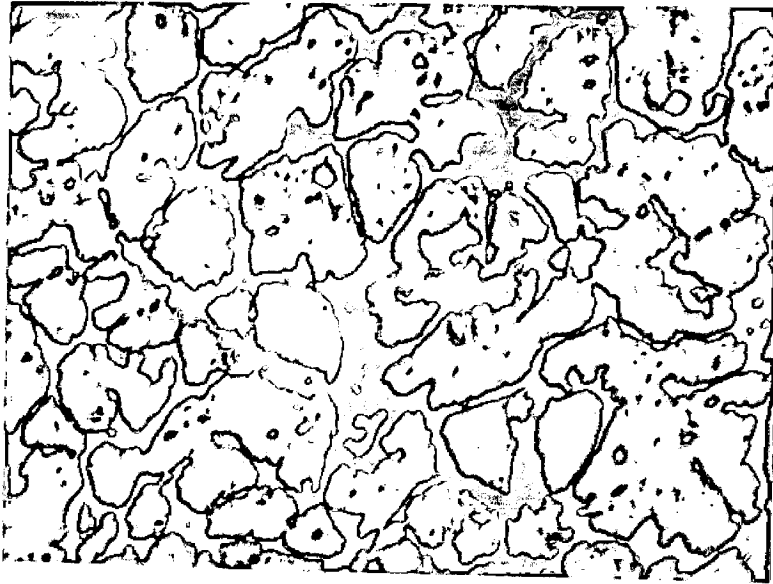


(a)

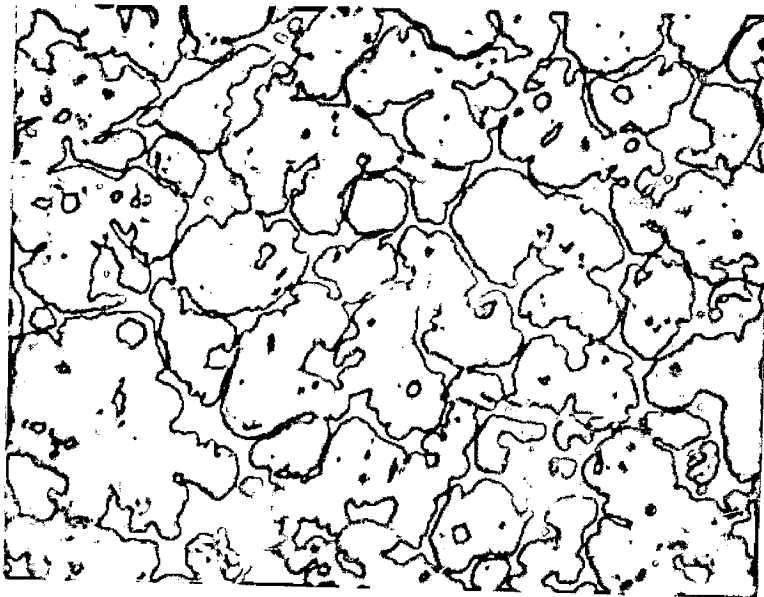


(b)

FIG. 4.2 MICROSTRUCTURE OF RHEOCAST Al-10 %
Cu ALLOY STIRRED AT 700 R.P.M. AND
POURED FROM (a.) 900 K (b) 896 K
Mag. X 200

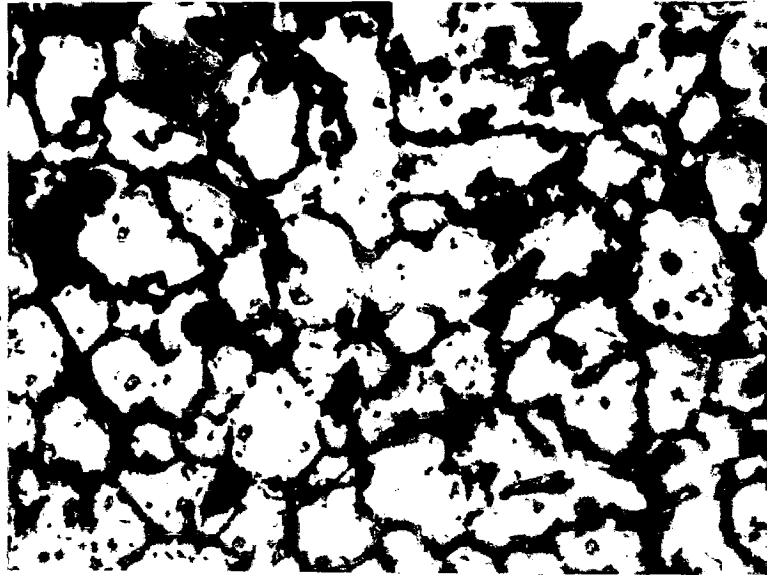


(a)

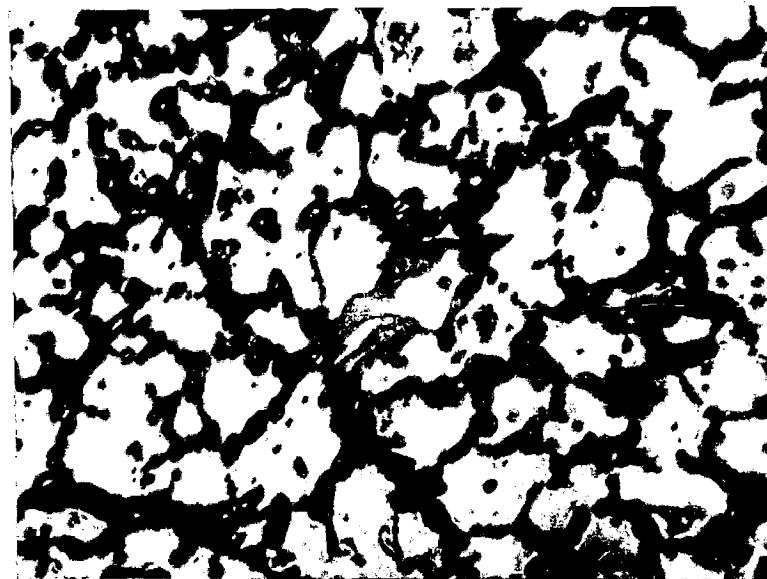


(b)

FIG. 4.3 MICROSTRUCTURE OF RHEOCAST Al-10 %
Cu ALLOY STIRRED AT 700 R.P.M. AND
POURED FROM (a) 894 K (b) 892 K.
Mag. X200



(a)

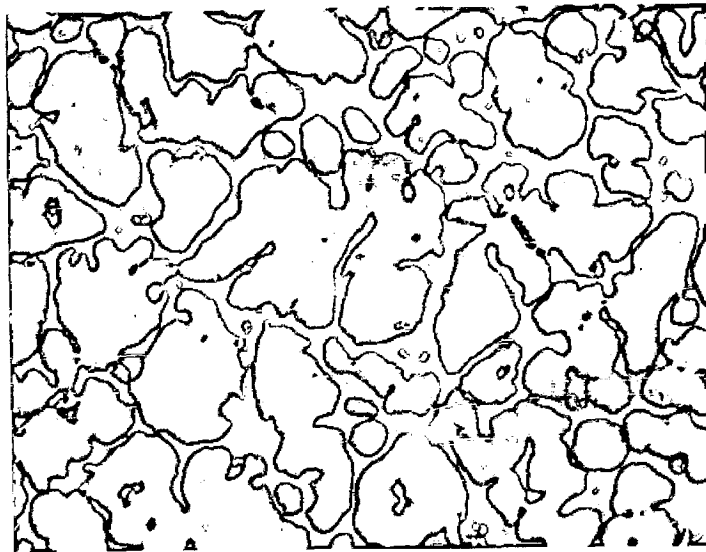


(b)

FIG.4.4 MICROSTRUCTURE OF RHEOCAST Al-10%
Cu ALLOY STIRRED AT 700 R P M AND
POURED FROM (a) 886 K (b) 880 K
Mag. X 200

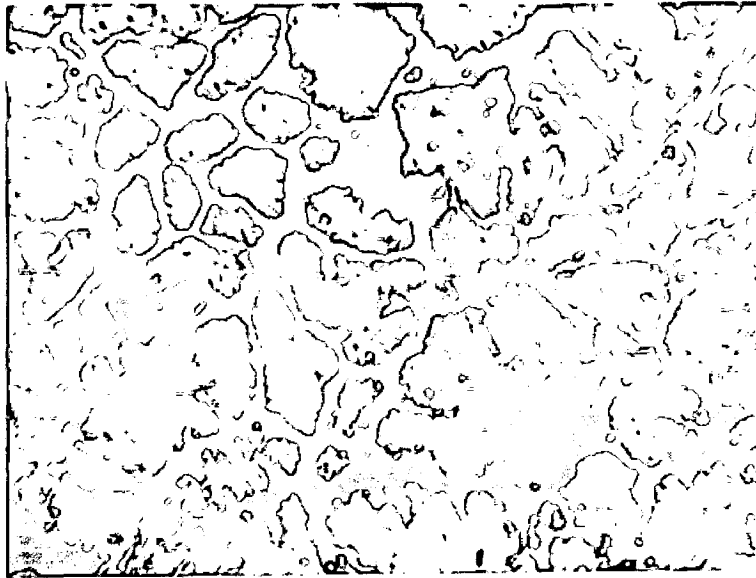


(a)



(b)

FIG.4.5 MICROSTRUCTURE OF RHEOCAST Al-10 %
Cu ALLOY STIRRED AT 1000 R.P.M. AND
POURED FROM (a) 900 K (b) 898 K.
Mag. X 200



(a)

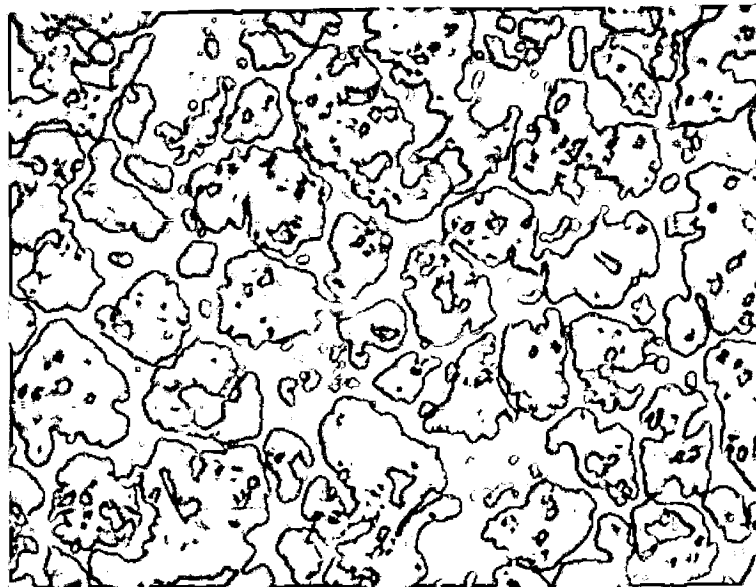
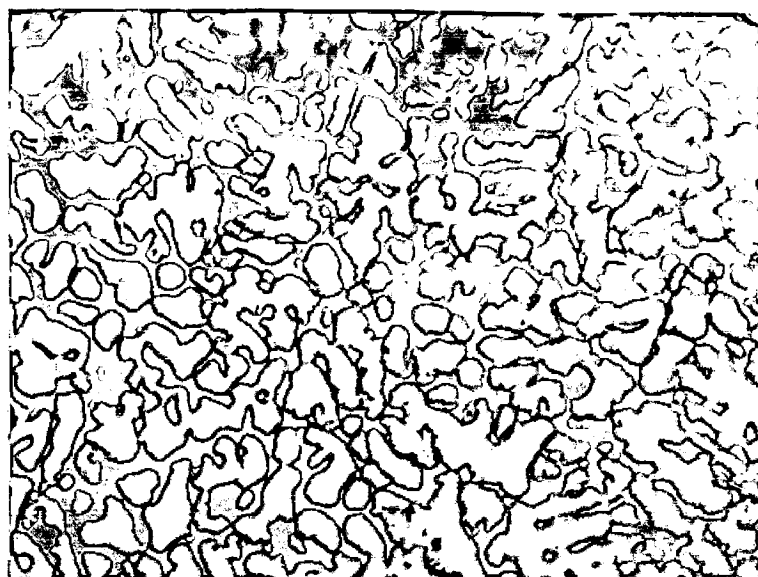
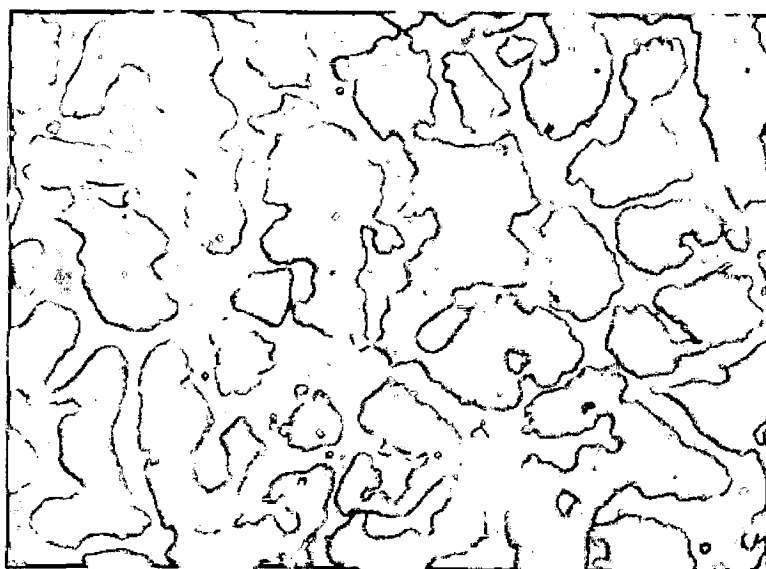


FIG.4.6 MICROSTRUCTURE OF RHEOCAST Al-10 %
Cu ALLOY STIRRED AT 1000 R.P.M. AND
POURED FROM (a) 894 K (b) 892 K.
Mag. X 200



(a)



(b)

FIG. 4.7 MICROSTRUCTURE OF RHEOCAST Al-10%
Cu ALLOY SLURRY STIRRED AT 1000 R.P.
M. AND WATER-QUENCHED, 898 K,
(a) Mag. X 200 (b) Mag. X 500

of microstructures of rheocastings made at 700 r.p.m. (Figs.4.2 to 4.4) and at 1000 r.p.m. (Figs.4.2 to 4.6) reveals that the tendency of dendrite formation is higher at 1000 r.p.m. especially at higher pouring temperatures.

The variation of average α -particle size (\bar{D}) with pouring temperature at two stirring rates 700 r.p.m. and 1000 r.p.m. has been shown in Figs.4.8 and 4.9 respectively. It is observed that \bar{D} increases with the increase in pouring temperature at both stirring speeds. However, a comparison of Figs. 4.8 and 4.9 reveals that the speed of stirring does not have any significant effect on \bar{D} .

Figures 4.10 and 4.11 represent the typical frequency distribution curves of measured α -particle size for rheocastings made at 700 r.p.m. whereas Figs.4.12 and 4.13 are for rheocastings made at 1000 r.p.m. These curves clearly show that though stirring rate has no significant effect, the size distribution is broader at higher pouring temperature than that at lower pouring temperature. The variation of size distribution with pouring temperature as indicated by standard deviation (σ) and the coefficient of variation (σ/\bar{D}) has been shown in Figs.4.14 and 4.15. It is observed that both σ and σ/\bar{D} increase with increase in pouring temperature.

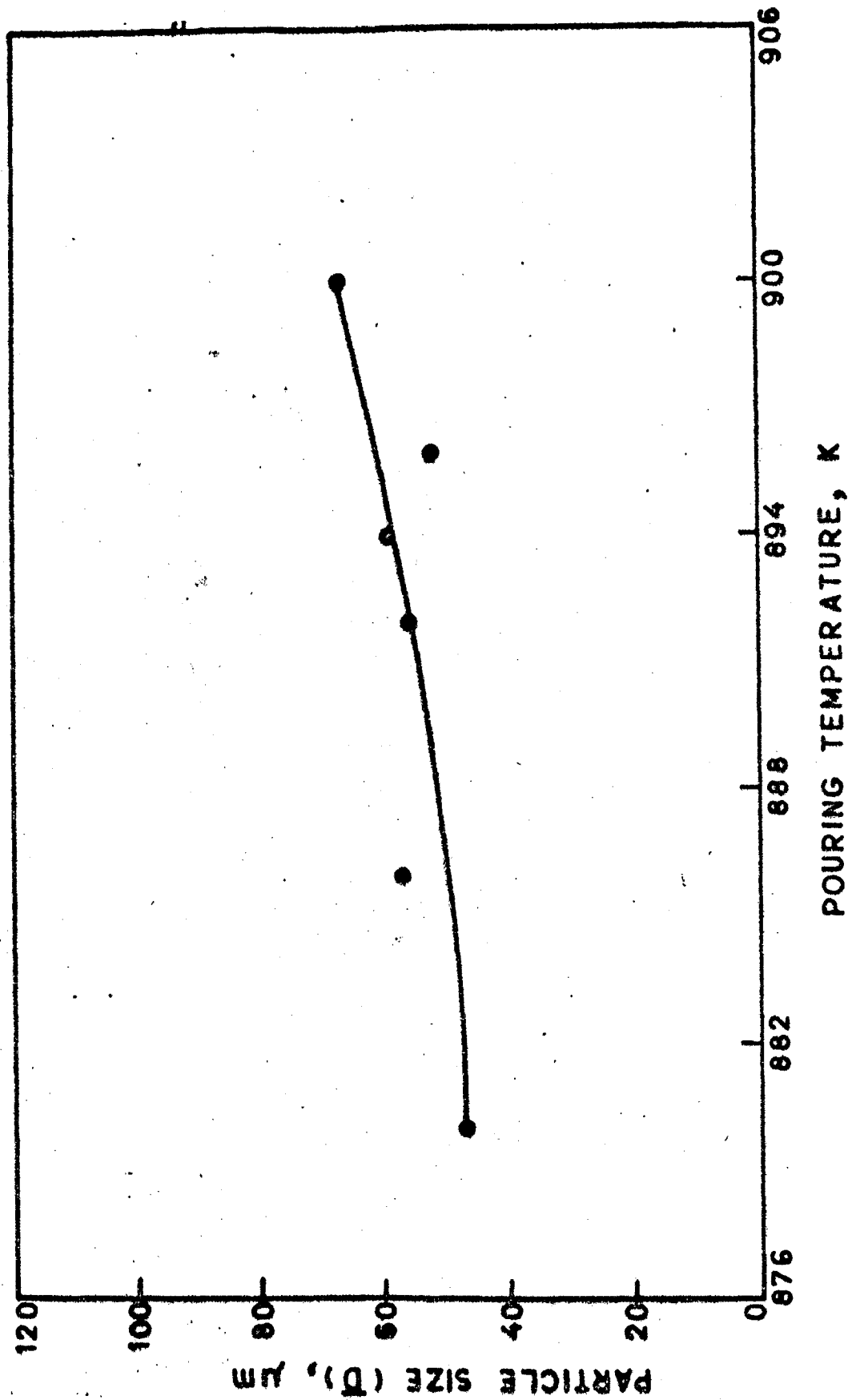


FIG.4.8 EFFECT OF POURING TEMPERATURE ON α - PARTICLE SIZE \bar{D} IN RHEOCAST Al-10% Cu ALLOY STIRRED AT 700 R.P.M.

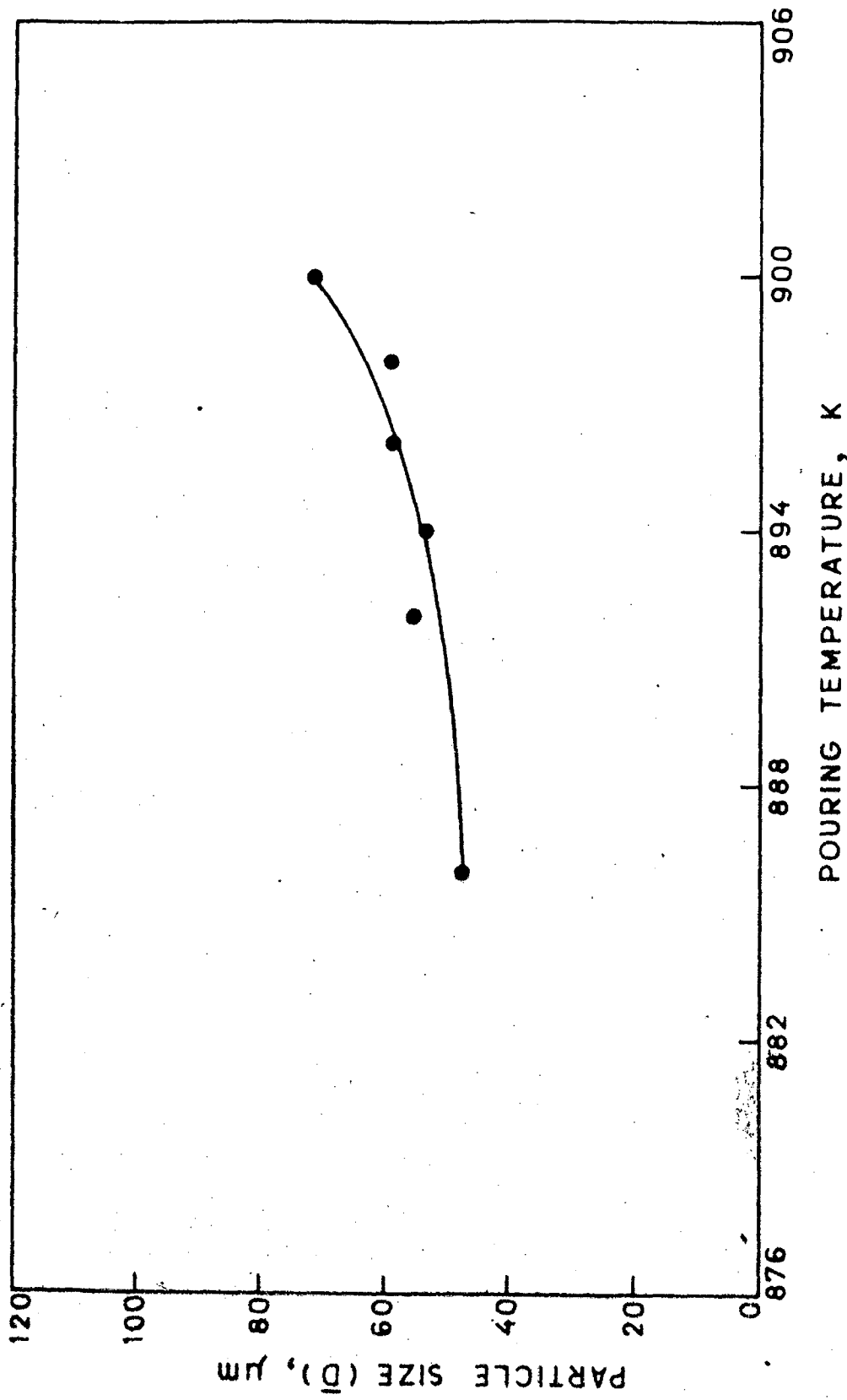


FIG. 4.9 EFFECT OF POURING TEMPERATURE ON α -PARTICLE SIZE
IN RHEOCAST Al-10% Cu ALLOY STIRRED AT 1000 R.P.M. 107

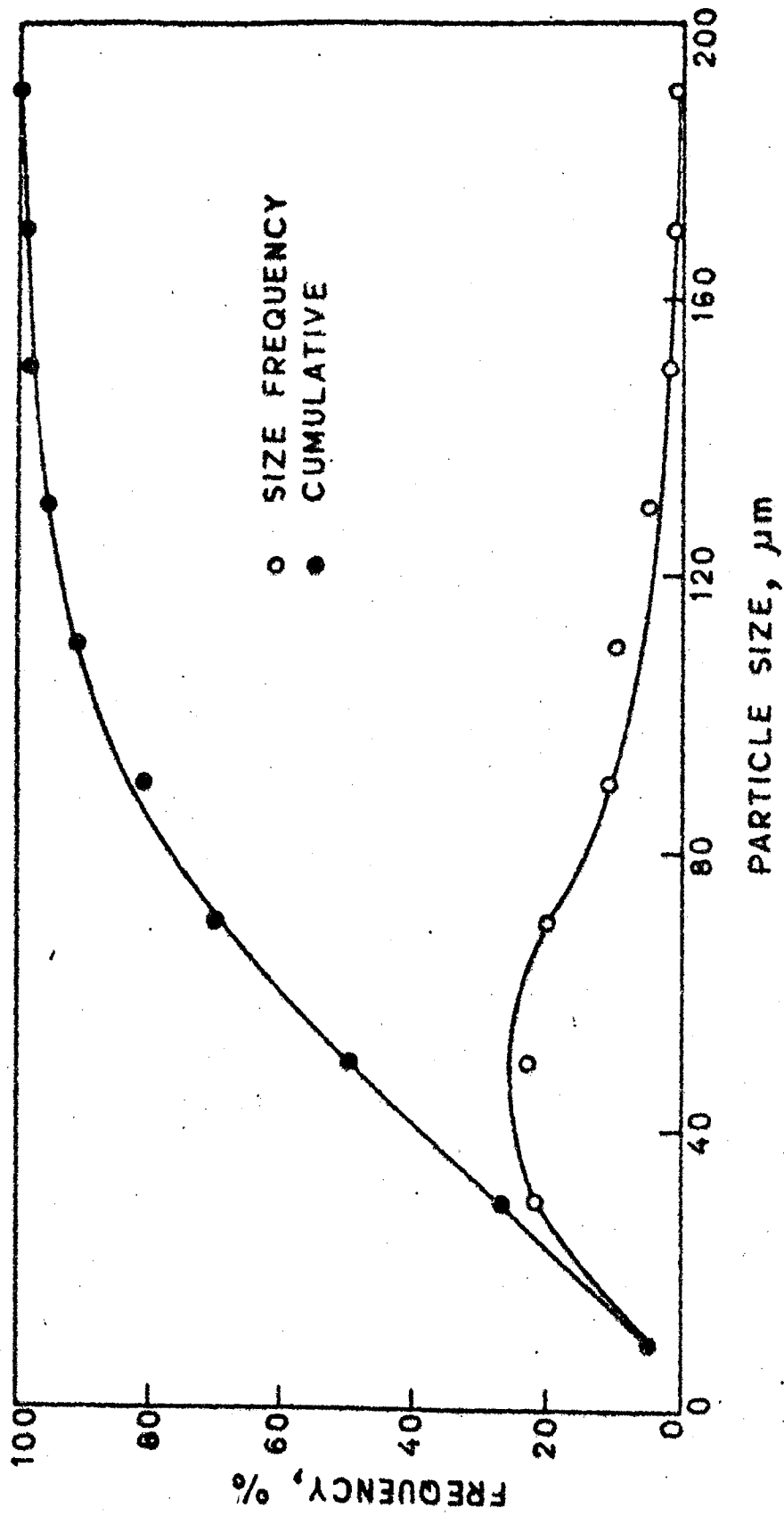


FIG. 4.10 FREQUENCY DISTRIBUTION CURVES OF α -PARTICLE SIZE IN RHEOCAST Al-10%Cu ALLOY STIRRED AT 700 R.P.M. AND Poured FROM 900 K.

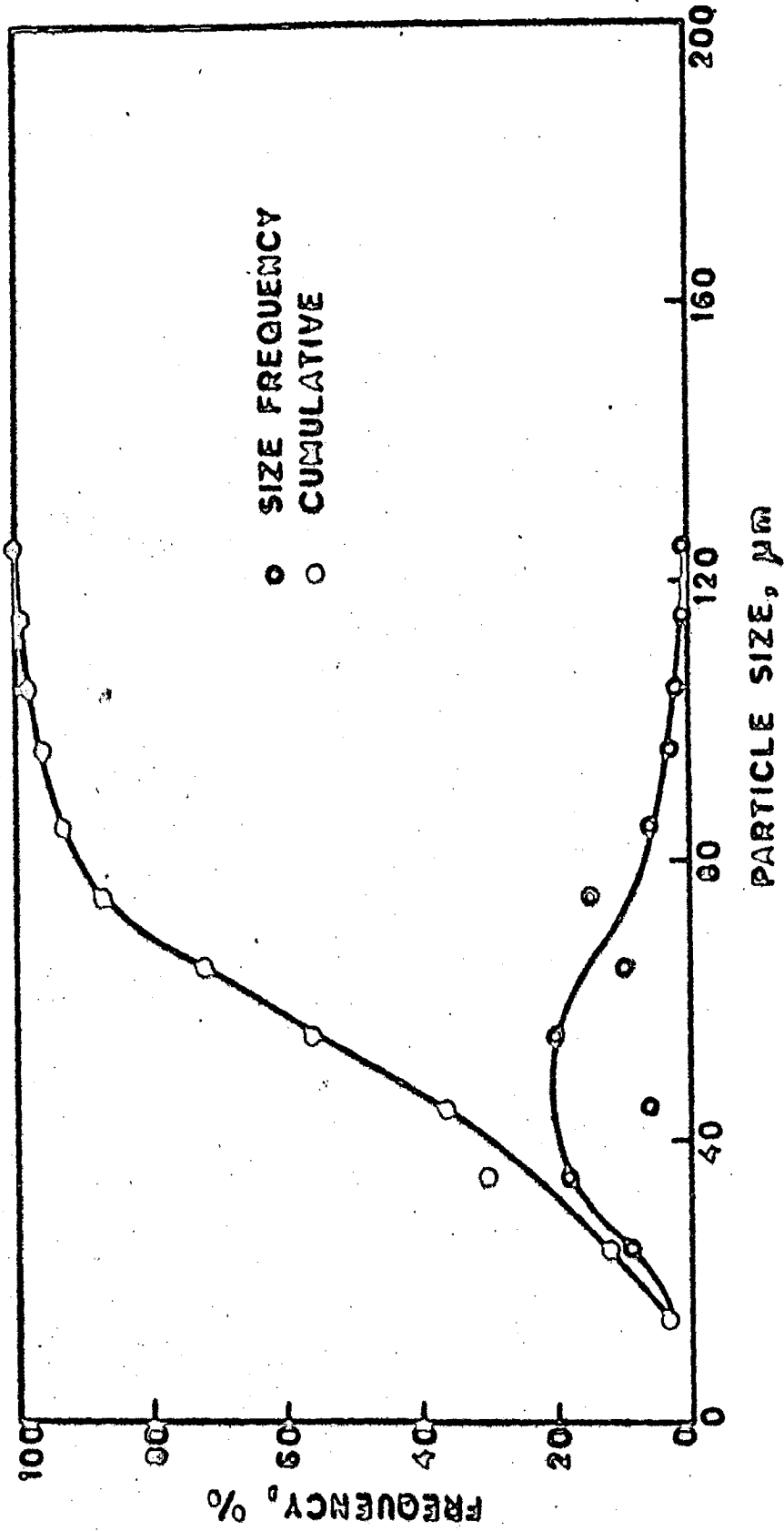


FIG. 4.11 FREQUENCY DISTRIBUTION CURVES OF α -PARTICLE SIZE IN RHEOCAST Al-10% Cu ALLOY STIRRED AT 700 R.P.M. AND Poured FROM 886 K. 88

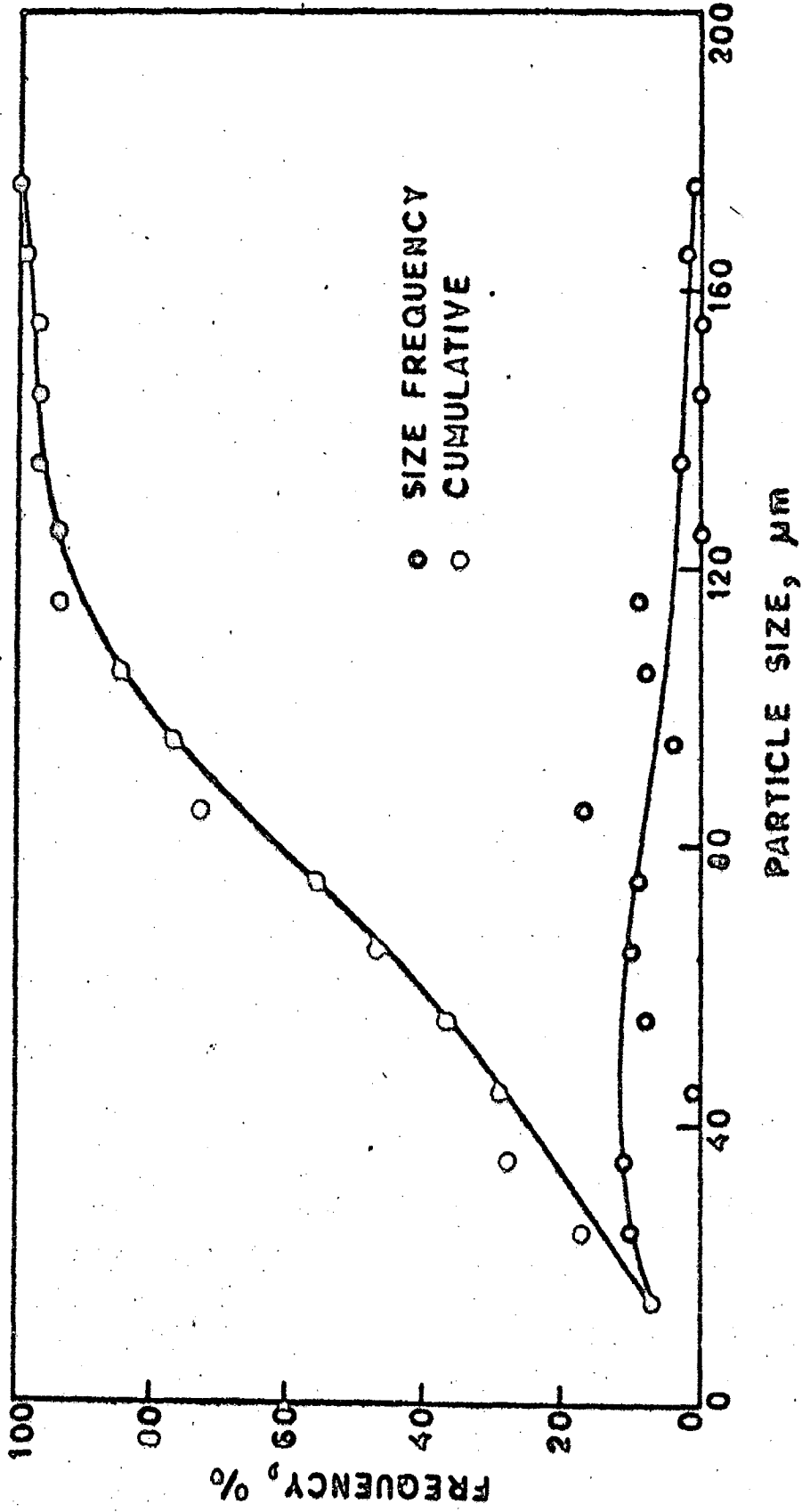


FIG. 4.12 FREQUENCY DISTRIBUTION CURVES OF α -PARTICLE SIZE IN RHEOCAST Al-10% Cu ALLOY STIRRED AT 1000 R.P.M. AND Poured FROM 900 K. 30

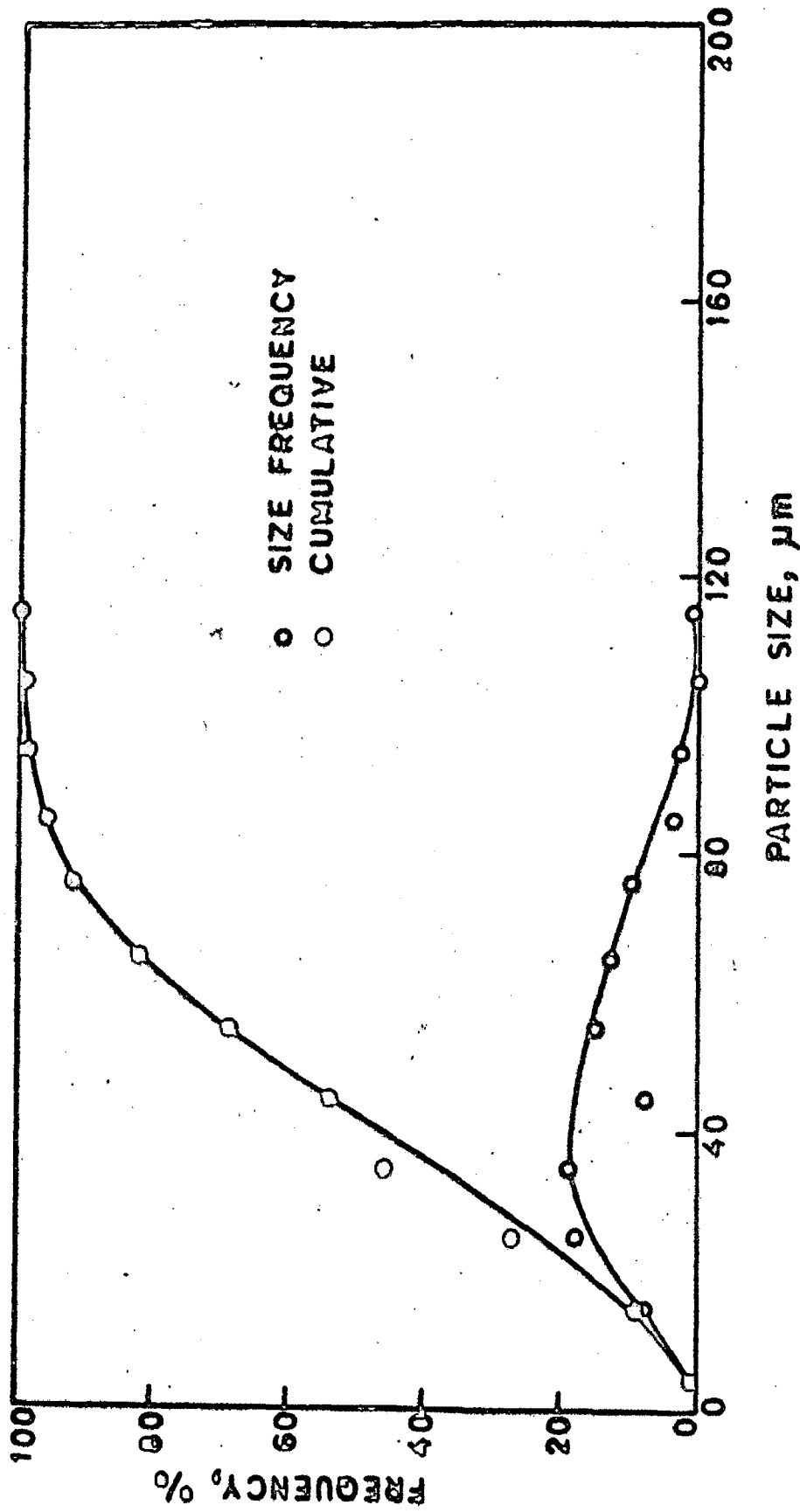


FIG. 4.13 FREQUENCY DISTRIBUTION CURVES OF α -PARTICLE SIZE
 IN RHEOCAST Al-10% Cu ALLOY STIRRED AT 1000 R.P.M.
 AND Poured FROM 886 K.

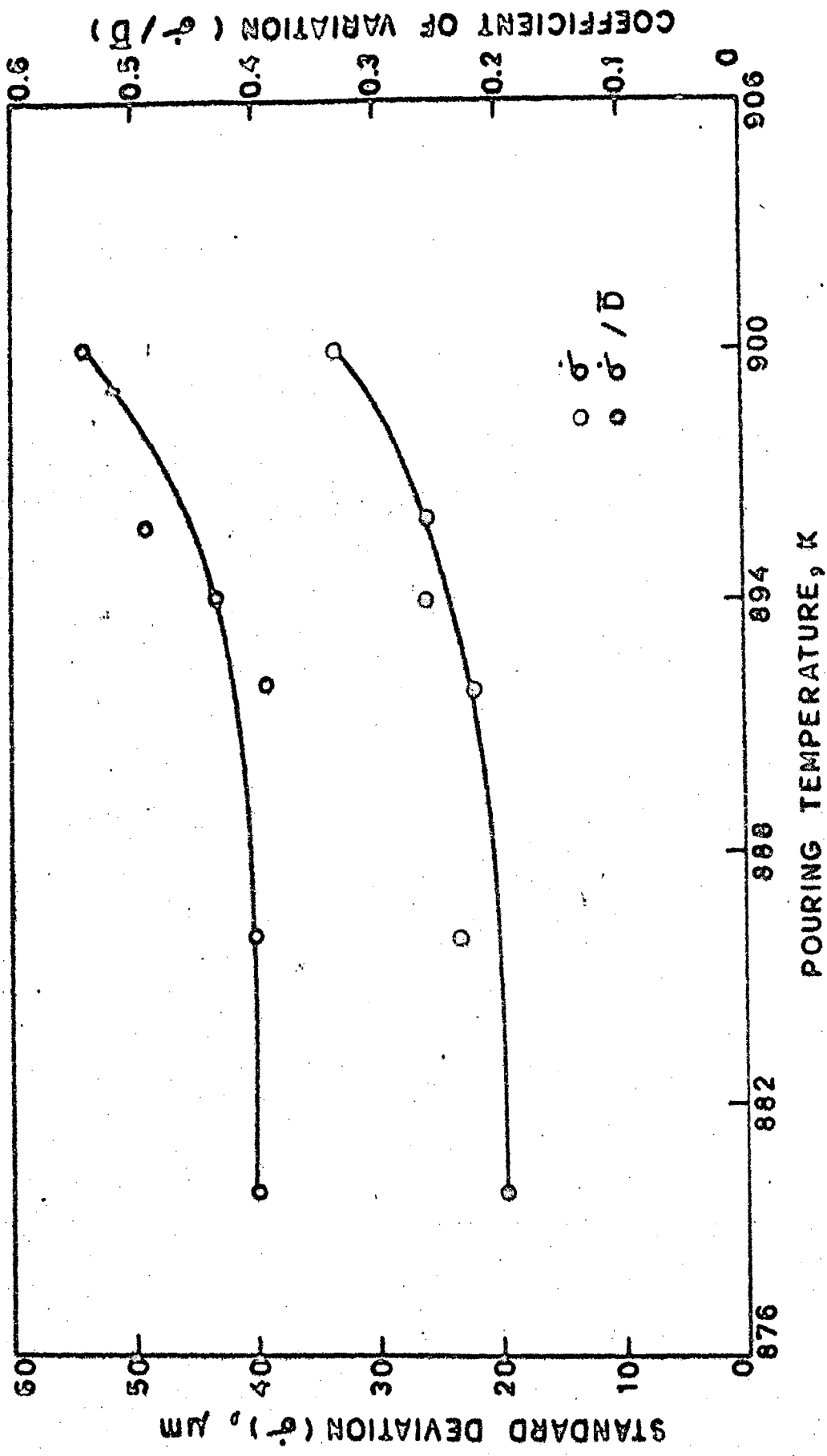


FIG. 4.14 EFFECT OF POURING TEMPERATURE ON STANDARD DEVIATION AND COEFFICIENT OF VARIATION OF α -PARTICLE SIZE IN RHEOCAST Al-10% Cu ALLOY STIRRED AT 700 R.P.M.

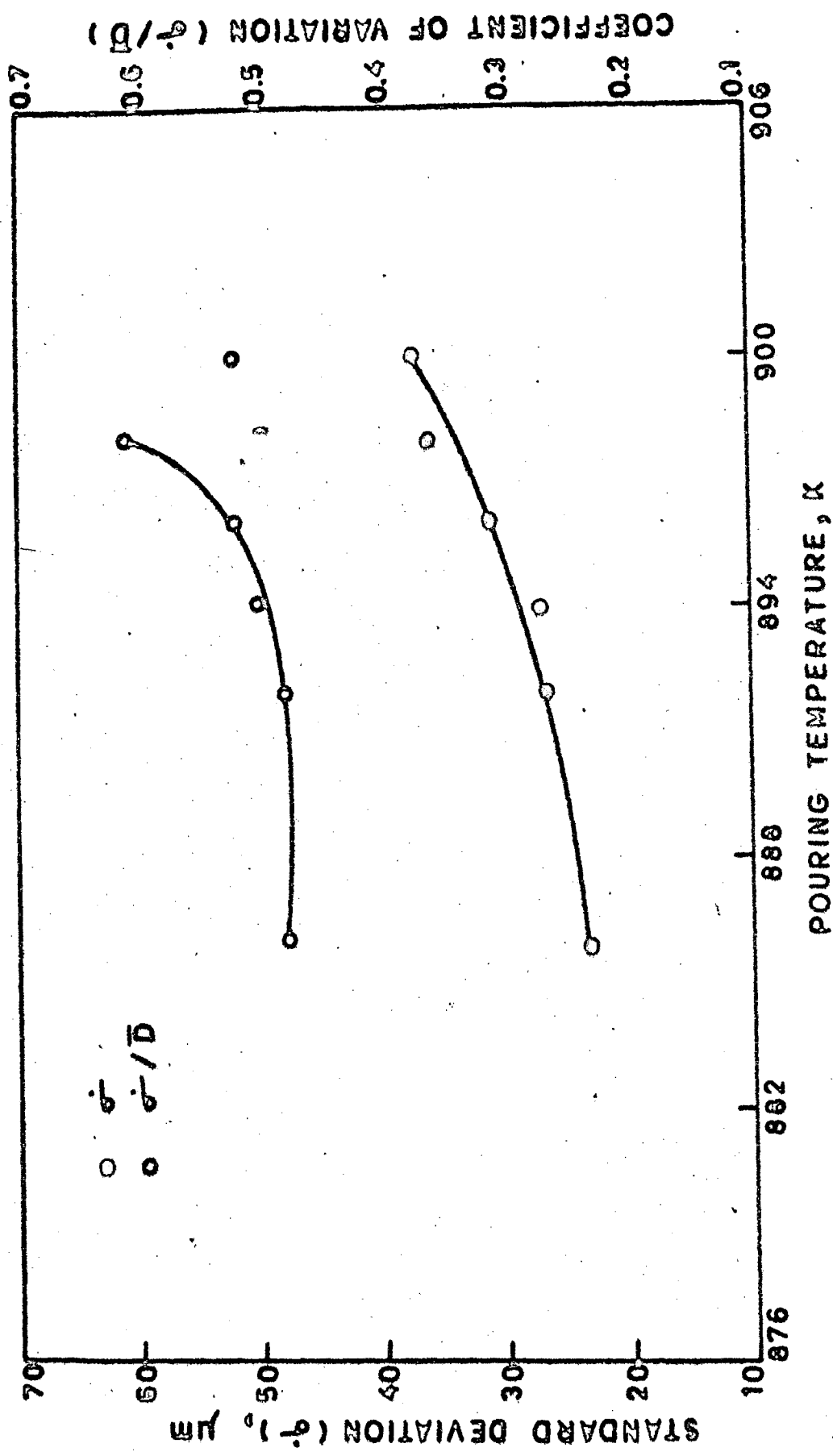


FIG.4.15 EFFECT OF POURING TEMPERATURE ON STANDARD DEVIATION AND COEFFICIENT OF VARIATION OF α -PARTICLE SIZE IN RHEOCAST Al-10%Cu ALLOY STIRRED AT 1000 R.P.M.

4.3 RESULTS: MICROSTRUCTURE OF Al-6% Cu ALLOY

The optical micrographs of various castings of Al-6% Cu alloy have been shown in Figs. 4.16 to 4.21. Figure 4.16 shows the microstructure of conventional casting whereas Figs. 4.17 to 4.21 depict the microstructure of rheocastings. From the comparison of the conventionally cast and rheocast microstructures it is evident that the morphology of proeutectic α -phase is significantly modified by the rheocasting process. The microstructure of conventional casting in Fig. 4.16 shows the dendrites of α -phase whereas the microstructures of rheocastings in Figs. 4.17 to 4.21 are characterised mostly by the non-dendritic morphology of α -phase, though the formation of dendrites to a limited extent is also evident in several samples. These observations are similar to those observed for Al-10% Cu alloy.

Generally, it is not possible to distinguish between the two types of particles - primary and secondary ones, by conventional metallography when their sizes are of the same order of magnitude. However, at lower pouring temperatures where some of the primary particles are of abnormally large size, such as the type of particles marked 'P' in Fig. 4.18(b) and 4.21, these primary particles are clearly identified from the rest of the particles. The microstructure of water-quenched slurry shown in Fig. 4.21(b) confirms that abnormally large particles 'P' observed in the rheocast samples are primary particles.



(a)

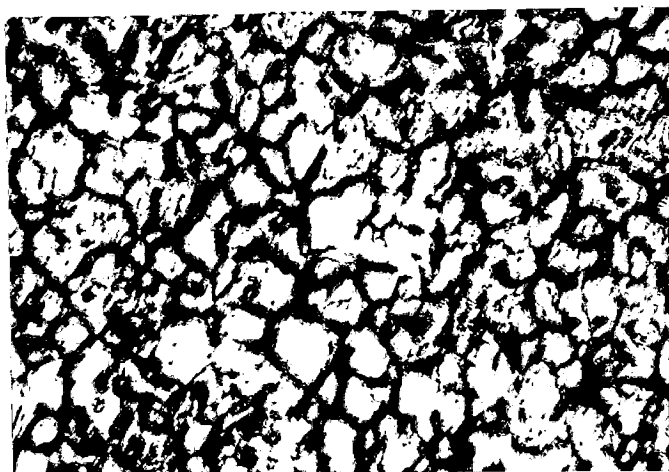


(b)

FIG. 4.16 MICROSTRUCTURE OF CONVENTIONALLY
CAST Al-6 % Cu ALLOY POURED FROM
950 K. Mag. (a) X 50 (b) X 100



(a)



(b)

FIG.4.17 MICROSTRUCTURE OF RHEOCAST Al-6 %
Cu ALLOY STIRRED AT 1000 R.P.M. AND
POURED FROM (a) 903 K (b) 898 K.
Mag. X100

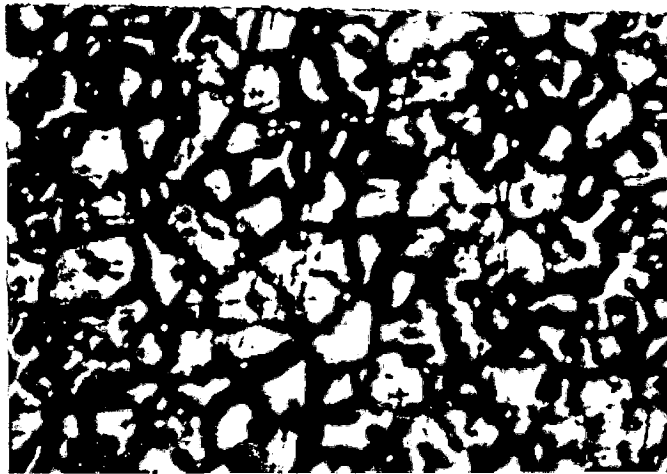


(a)



(b)

FIG. 4.18 MICROSTRUCTURE OF RHEOCAST Al-6% Cu ALLOY STIRRED AT 1000 R.P.M. AND Poured FROM (a) 895 K (b) 886 K. Mag. X100

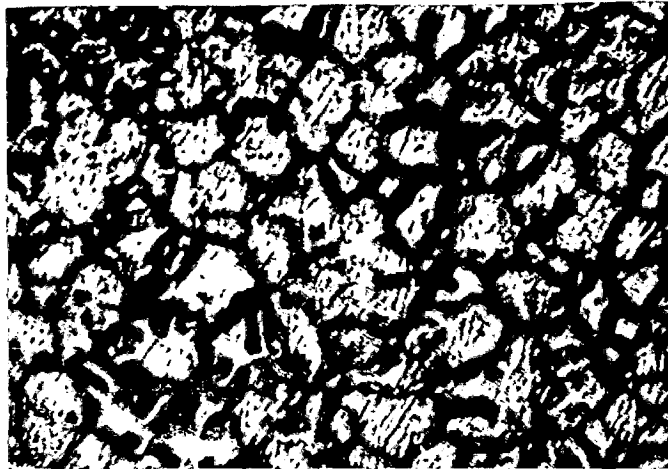


(a)

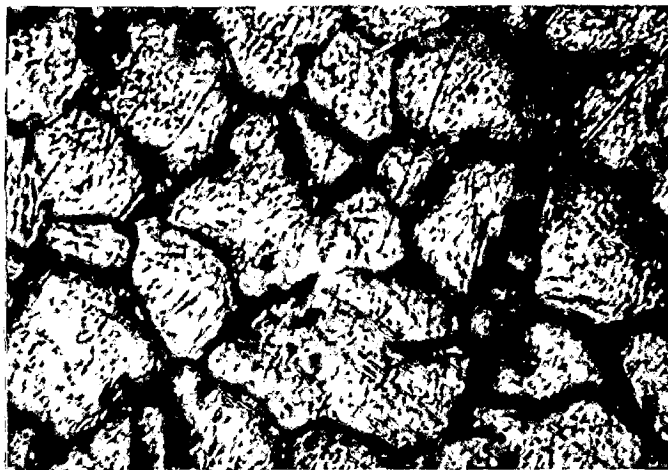


(b)

FIG. 4.19 MICROSTRUCTURE OF RHEOCAST Al-6% Cu ALLOY STIRRED AT 700 R.P.M. AND Poured FROM (a) 905 K (b) 898 K. Mag. X100

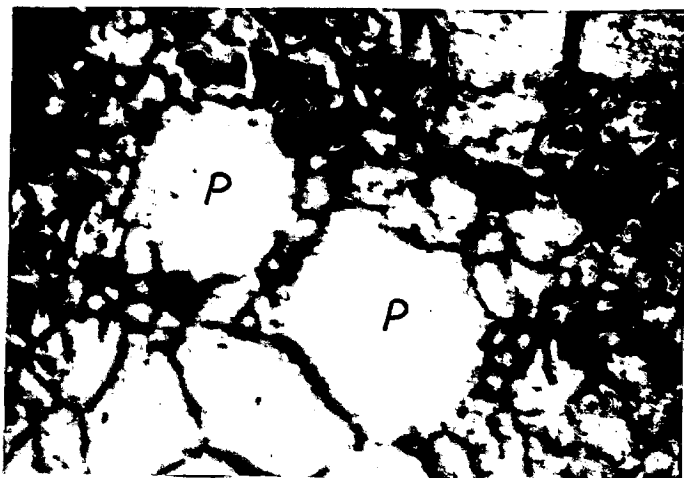


(a)



(b)

FIG.4.20 MICROSTRUCTURE OF RHEOCAST Al-6 %
Cu ALLOY STIRRED AT 700 R.P.M. AND
POURED FROM 890 K. Mag.(a) X 100
(b) X 200



(a)



(b)

FIG.4.21 MICROSTRUCTURE OF RHEOCAST Al-6 % Cu ALLOY STIRRED AT 700 R.P.M. AND Poured FROM 886 K. (a) STRUCTURE OF CAST INGOT (b) STRUCTURE OF WATER-QUENCHED SLURRY. Mag X100

The variation of α -particle size (\bar{D}) with pouring temperature at the two stirring speeds of 700 r.p.m. and 1000 r.p.m. has been shown in Figs.4.22 and 4.23 respectively. It is observed that at both stirring speeds \bar{D} remains nearly unaltered at higher pouring temperatures. Below ~ 890 K the size of some of the particles increases abruptly to a large value. Such a situation corresponds to the duplex microstructure depicted in Fig.4.18(b) and 4.21(a) where the abnormally large particles have been marked as 'P'. Though the average size of such particles is much higher, the average size of rest of the particles (small particles) is nearly of the same order of magnitude as that at higher pouring temperatures. A comparison of Figs.4.22 and 4.23 further reveals that the particle size is smaller for higher stirring rate at all pouring temperatures. This effect of stirring rate is more pronounced at lower pouring temperatures than at higher pouring temperatures.

Figures 4.24 and 4.25 represent the typical frequency distribution curves of measured α -particle size for rheocasting made at 1000 r.p.m. whereas Figs.4.26 and 4.27 are for rheocastings made at 700 r.p.m. These curves reveal that at stirring rate of 1000 r.p.m., the size distribution is similar at lower as well as higher pouring temperatures, but in case of 700 r.p.m. the size distribution is broader at lower pouring temperature. Figures 4.28 and 4.29 are intended to show the effect of pouring temperature

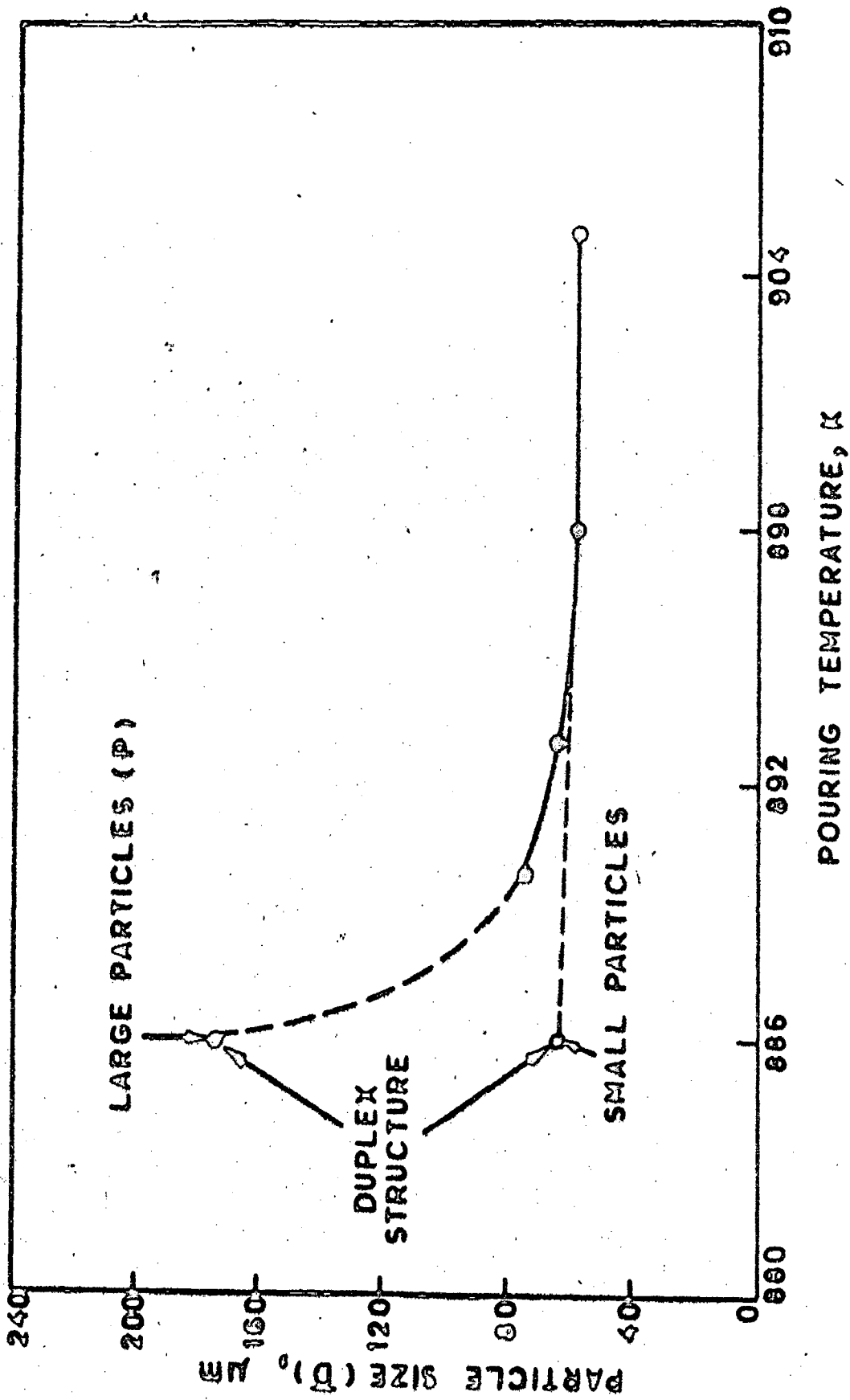


FIG.4.22 EFFECT OF POURING TEMPERATURE ON α -PARTICLE SIZE IN RHEOCAST Al-6%Cu ALLOY STIRRED AT 700 R.P.M.

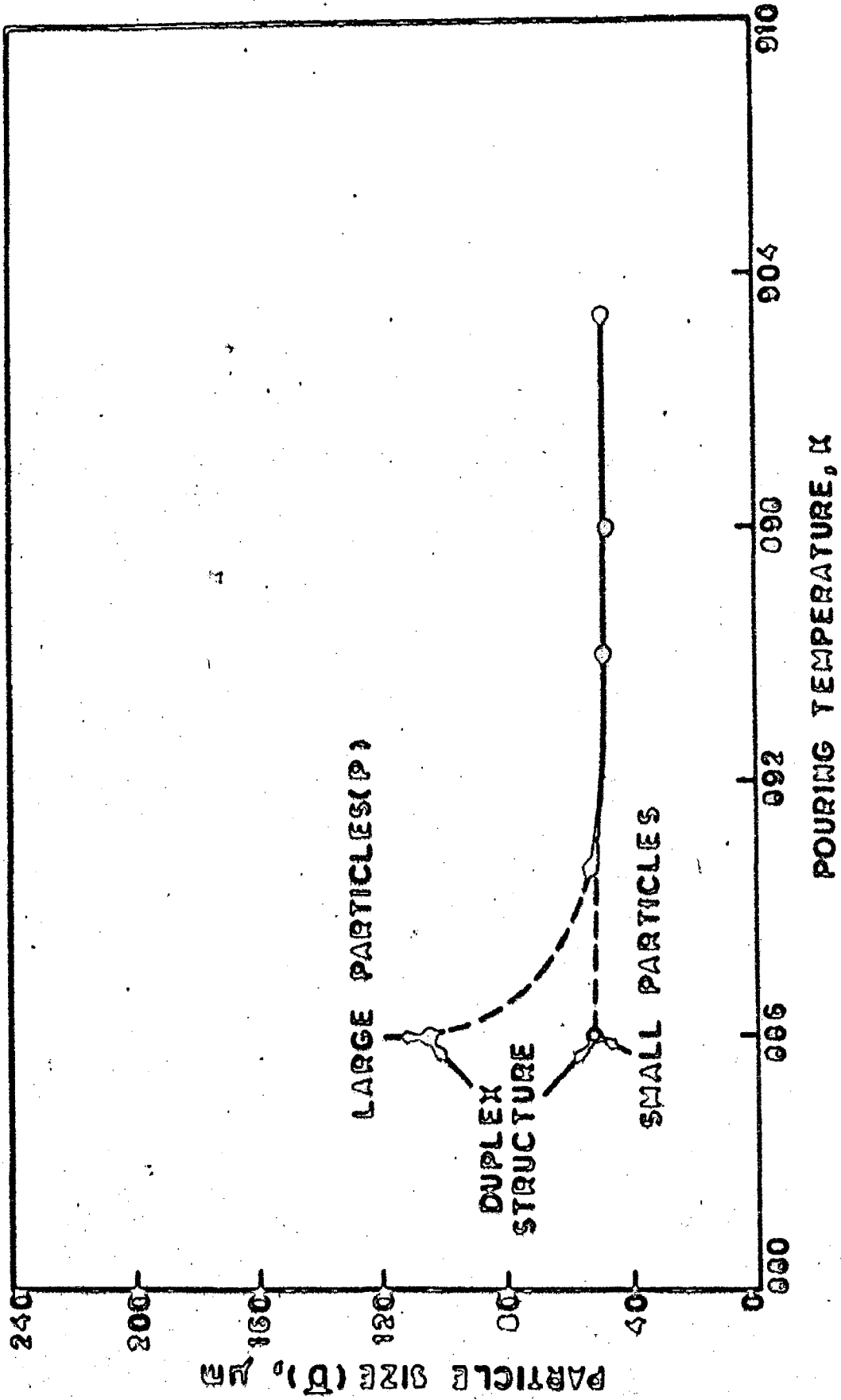


FIG. 4.23 EFFECT OF POURING TEMPERATURE ON α -PARTICLE SIZE IN RHEOCAST Al-6% Cu ALLOY STIRRED AT 1000 R.P.M. 29

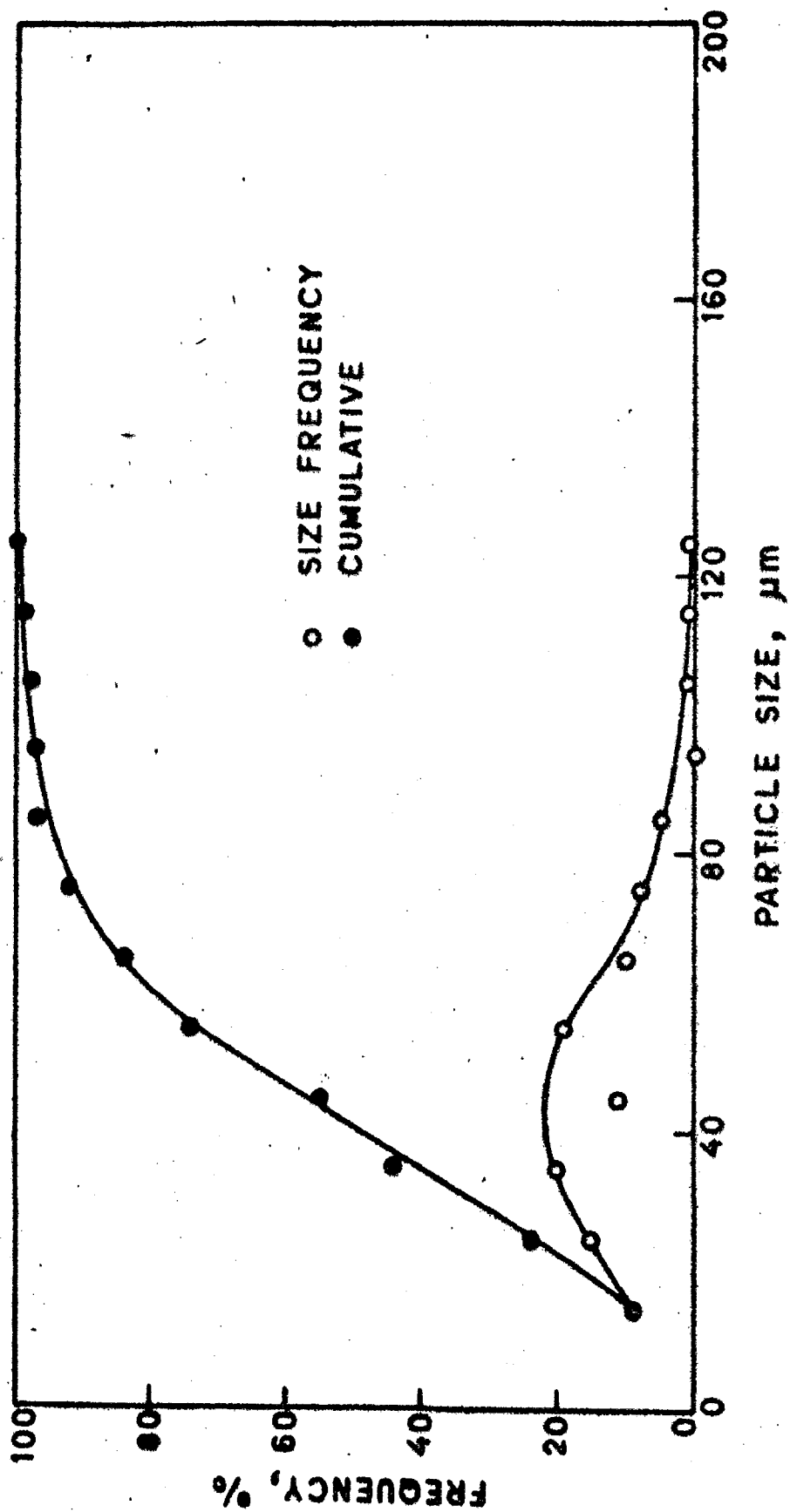


FIG.4.24 FREQUENCY DISTRIBUTION CURVES OF α -PARTICLE SIZE
 IN RHEOCAST Al-6% Cu ALLOY STIRRED AT 1000 R.P.M.
 AND Poured FROM 903 K.

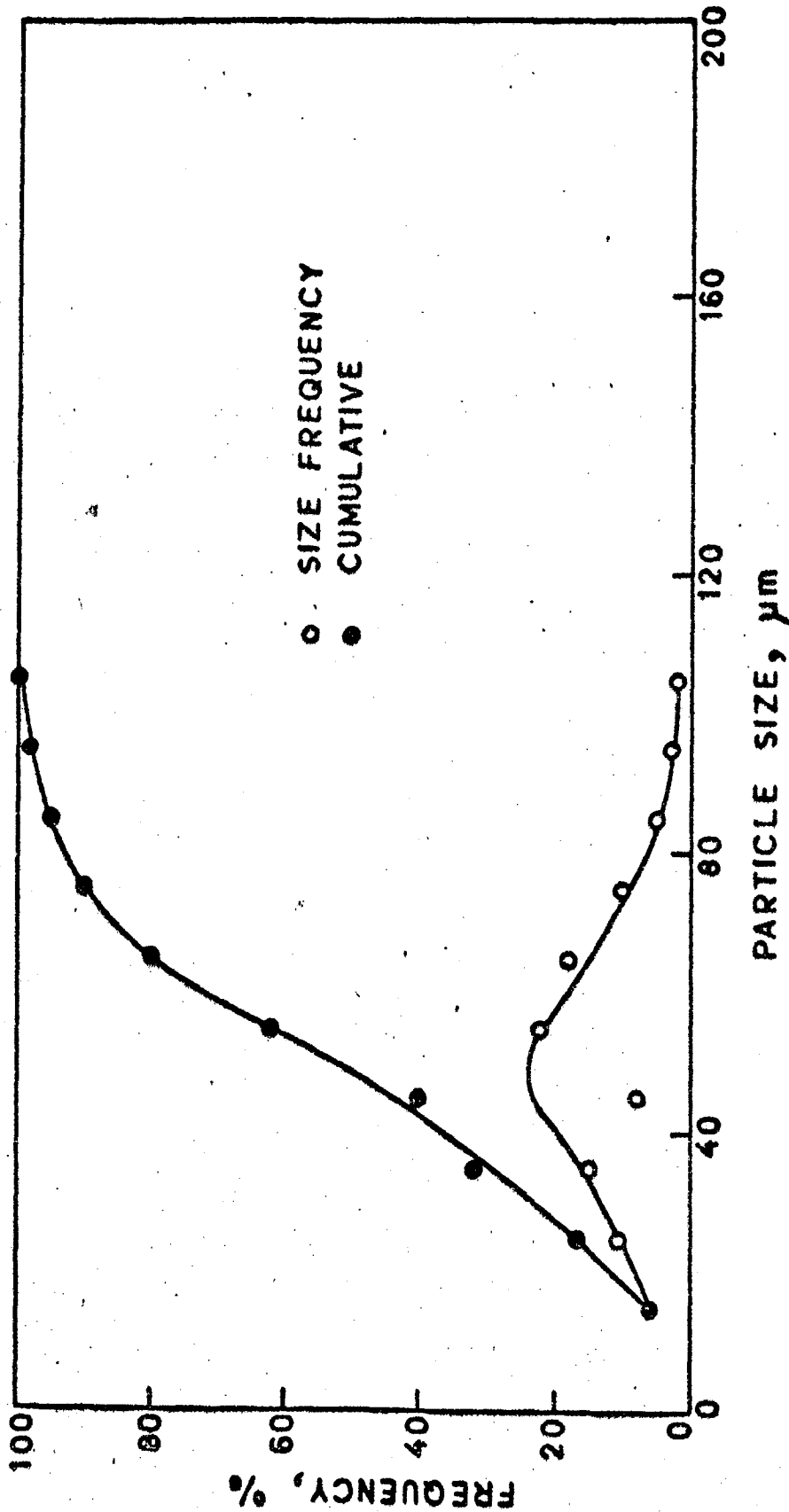


FIG. 4.25 FREQUENCY DISTRIBUTION CURVES OF α -PARTICLE SIZE IN RHEOCAST Al-6% Cu ALLOY STIRRED AT 1000 R.P.M. AND POURED FROM 890 K.

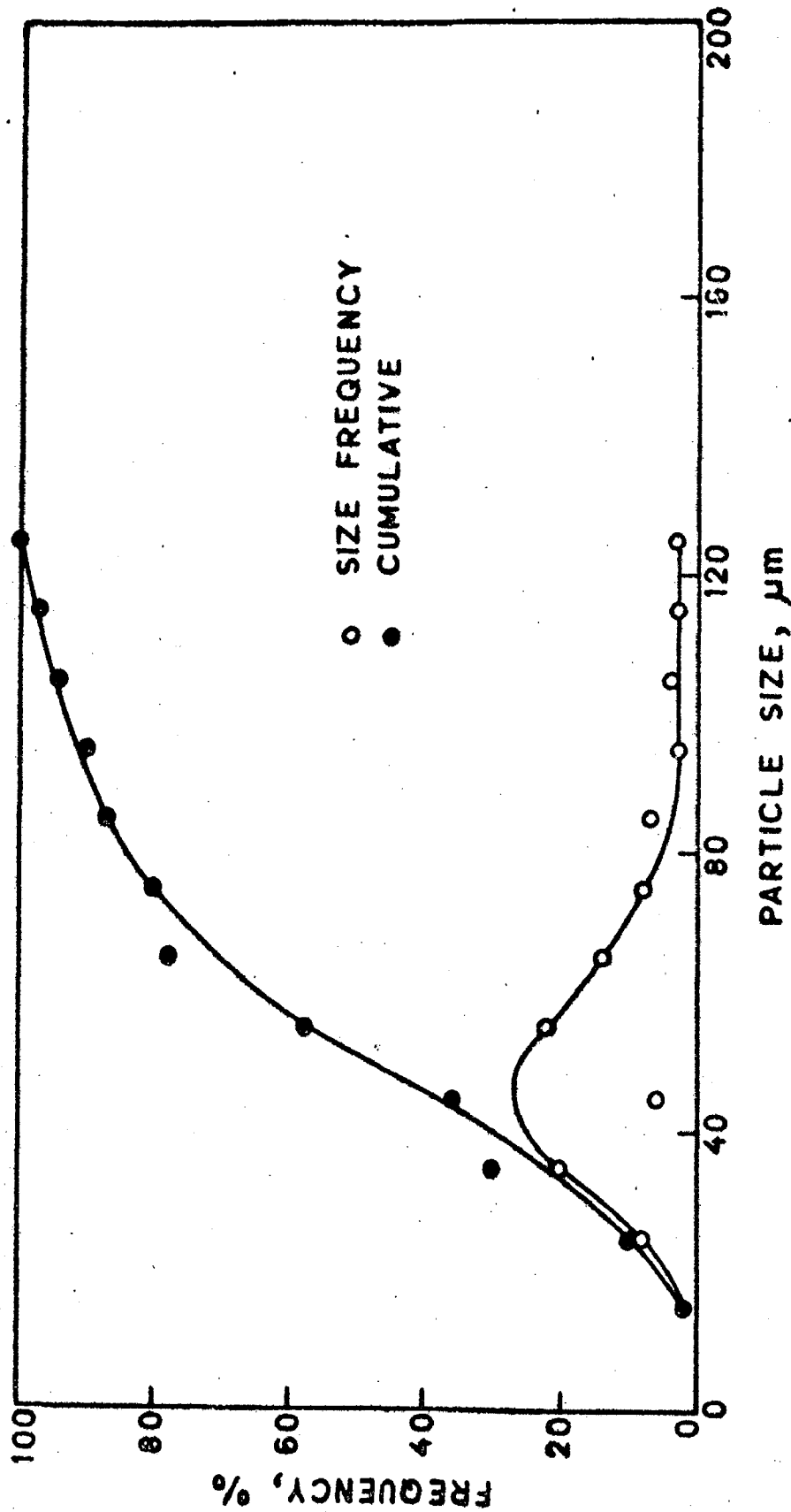


FIG. 4.26 FREQUENCY DISTRIBUTION CURVES OF α -PARTICLE SIZE IN RHEOCAST Al-6% Cu ALLOY STIRRED AT 700 R.P.M. AND POURED FROM 905 K.

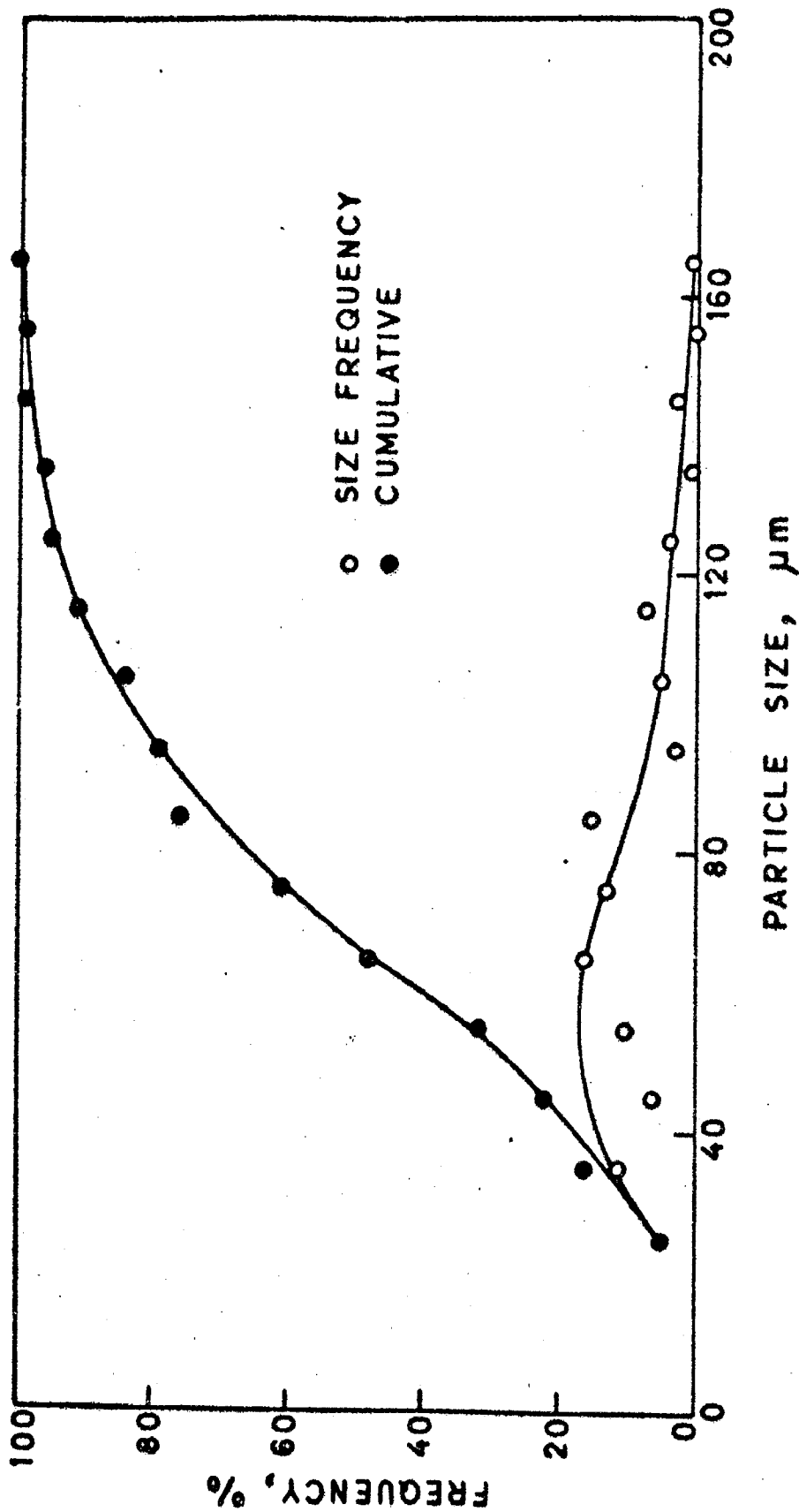


FIG. 4.27 FREQUENCY DISTRIBUTION CURVES OF α -PARTICLE SIZE IN RHEOCAST Al-6% Cu ALLOY STIRRED AT 700 R.P.M. AND Poured FROM 890 K.

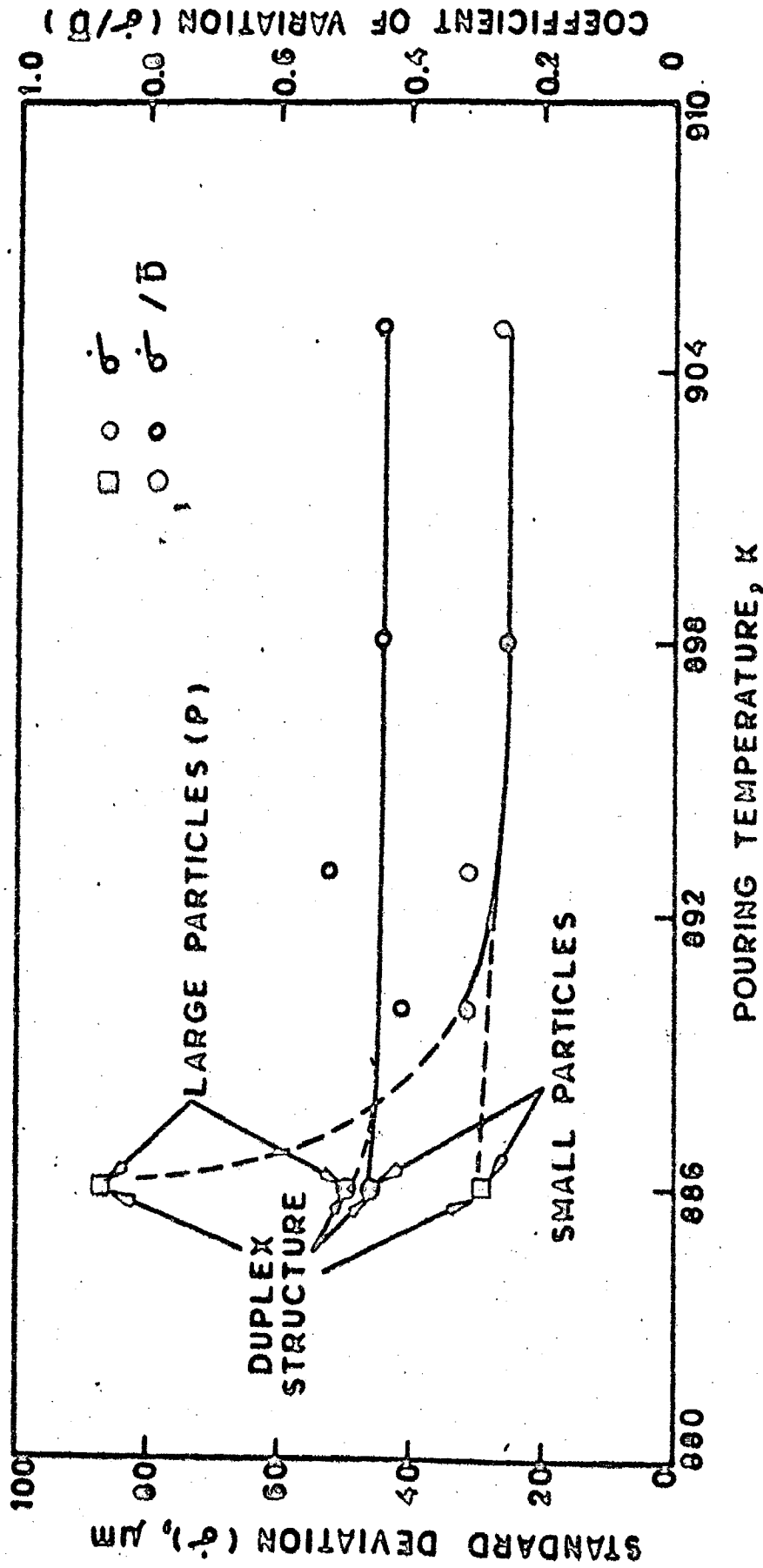


FIG. 4.20 EFFECT OF POURING TEMPERATURE ON STANDARD DEVIATION AND COEFFICIENT OF VARIATION OF α -PARTICLE SIZE IN RHEOCAST Al-6% Cu ALLOY STIRRED AT 700 R.P.M.

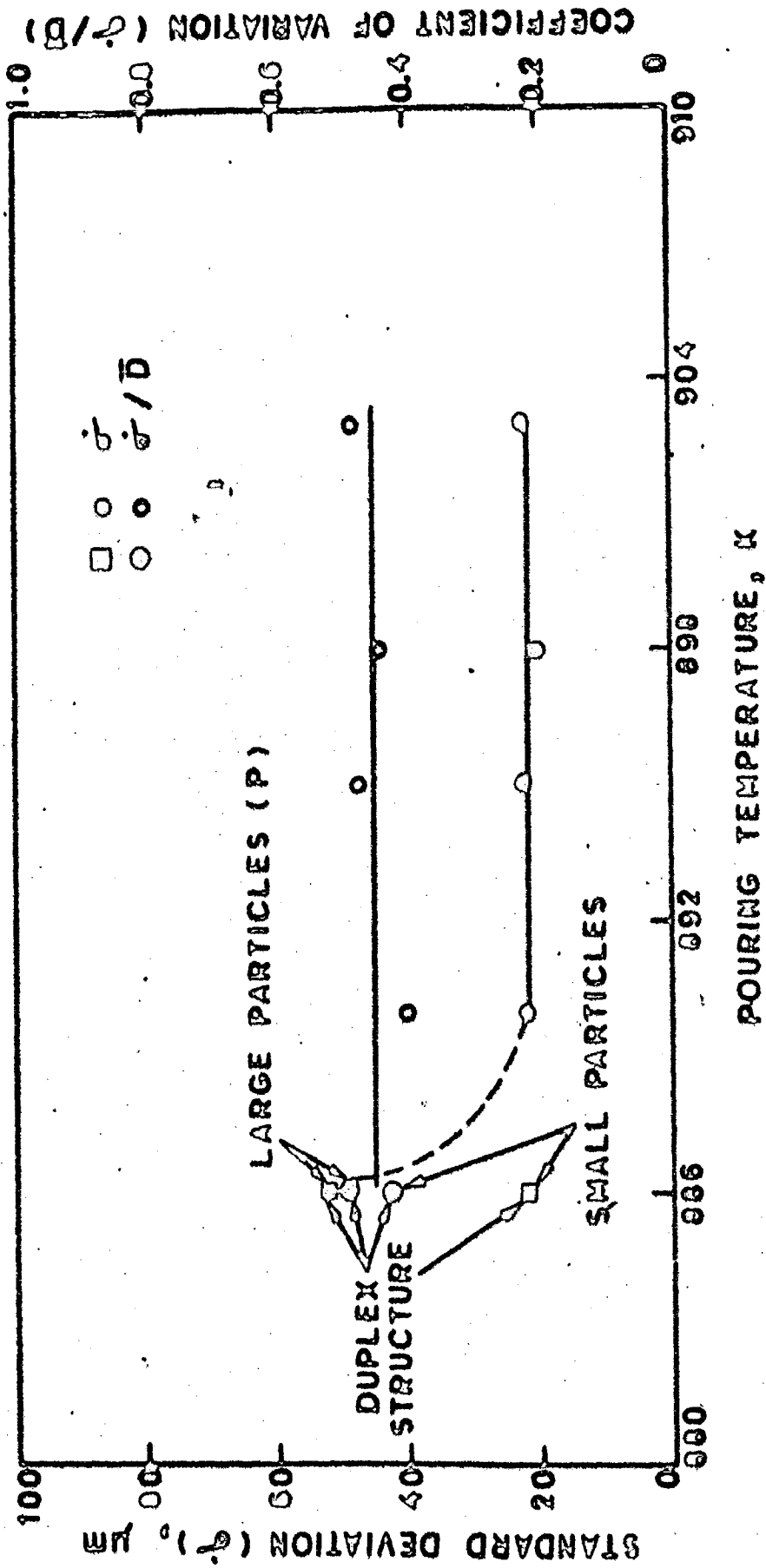
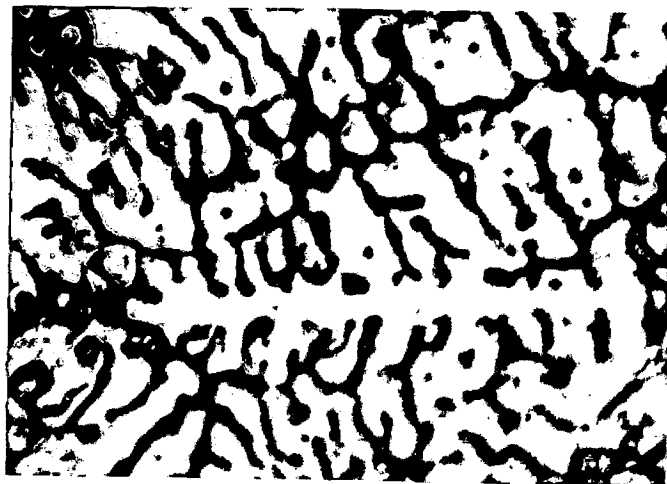


FIG. 4.29 EFFECT OF POURING TEMPERATURE ON STANDARD DEVIATION AND COEFFICIENT OF VARIATION ON α -PARTICLE SIZE IN RHEOCAST Al-6% Cu ALLOY STIRRED AT 1000 R.P.M. 20

on size distribution as indicated by the standard deviation ($\bar{\sigma}$) and the coefficient of variation ($\bar{\sigma} / \bar{D}$). It is observed that $\bar{\sigma}$ and $\bar{\sigma} / \bar{D}$ are not significantly influenced by pouring temperature except that at lower temperatures and lower stirring speed, the standard deviation $\bar{\sigma}$ is higher.

4.4 RESULTS: MICROSTRUCTURE OF Al-4.5% Cu ALLOY

The optical micrographs of various castings of Al-4.5% Cu alloy have been shown in Fig.4.30 to 4.37. Figure 4.30 shows the microstructure of conventional casting whereas Figs.4.31 to 4.37 depict the typical microstructures of rheocastings. A comparison of conventionally cast and rheocast microstructures clearly reveals that significant modification in the cast microstructure may be obtained by the rheocasting process. The microstructure of conventional casting in Fig.4.30 shows the dendrites of α -phase while the microstructures of rheocast samples are characterised by mostly the non-dendritic morphology of α -phase, though the dendritic morphology is also evident to a limited extent in several samples. At lower temperatures some of the primary particles such as the type marked 'P' in Fig.4.34 are clearly identified from rest of the particles. These observations are similar to the observations made in case of Al-6% Cu alloy rheocastings. Figure 4.35 shows selected regions within some of the large 'P' particles and it may be observed that some boundaries are present within these particles. These boundaries

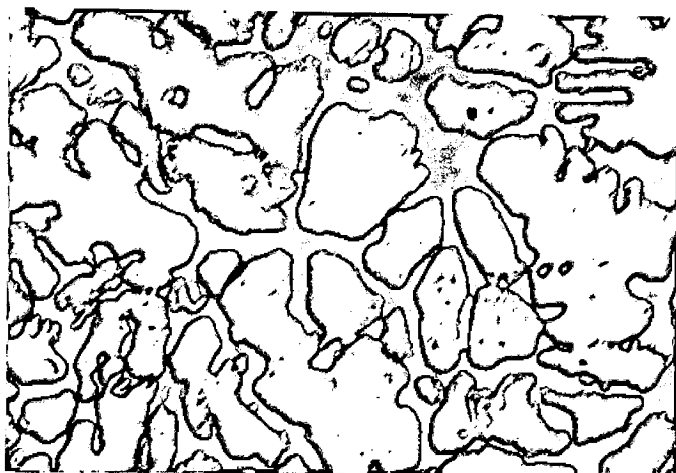


(b)

FIG.4.30 MICROSTRUCTURE OF CONVENTIONALLY
CAST Al-4.5 % Cu ALLOY Poured FROM
960 K. Mag. (a) X100 (b) X 200

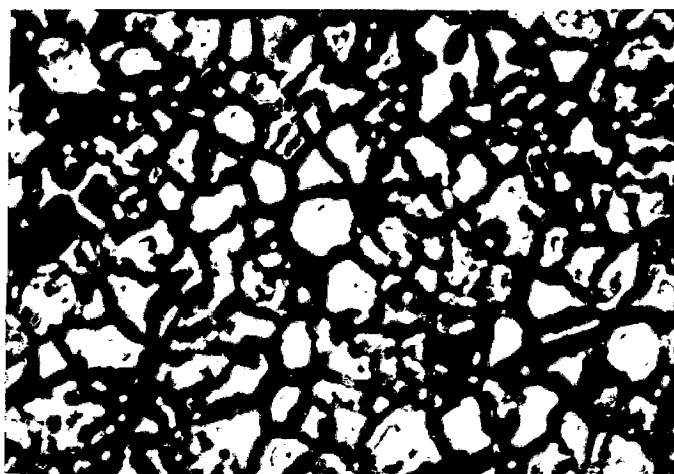


(a)

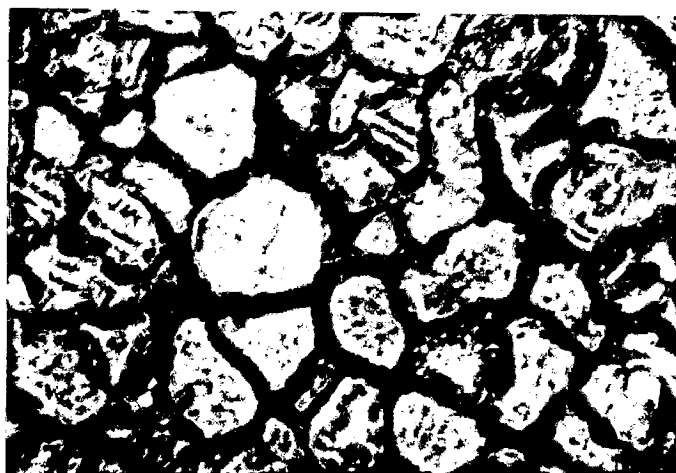


(b)

FIG.4.31 MICROSTRUCTURE OF RHEOCAST Al-4.5%
Cu ALLOY STIRRED AT 1000 R.P.M. AND
POURED FROM 919 K. Mag. (a) X 100
(b) X 200

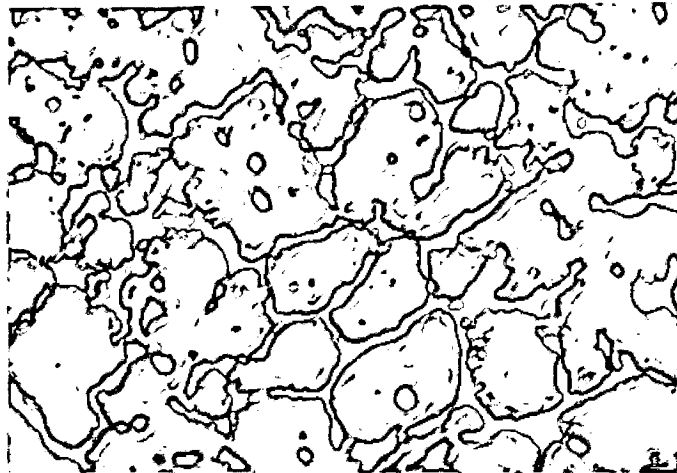


(a)

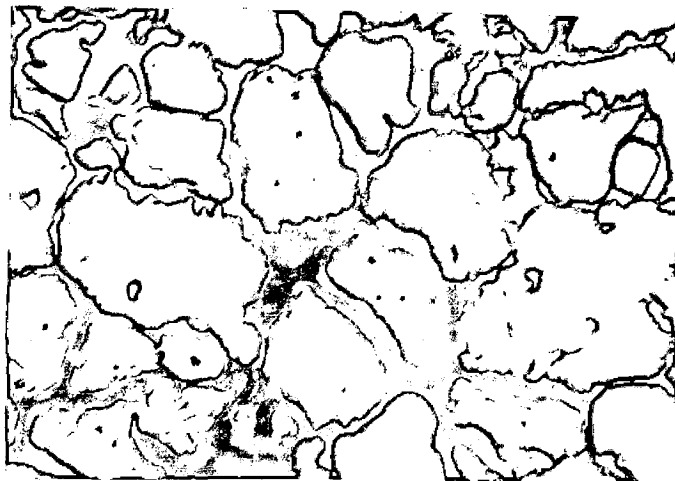


(b)

FIG.4.32 MICROSTRUCTURE OF RHEOCAST Al-4.5%
Cu ALLOY STIRRED AT 1000 R.P.M. AND
POURED FROM 916. K. Mag.(a) X 100
(b) X 200

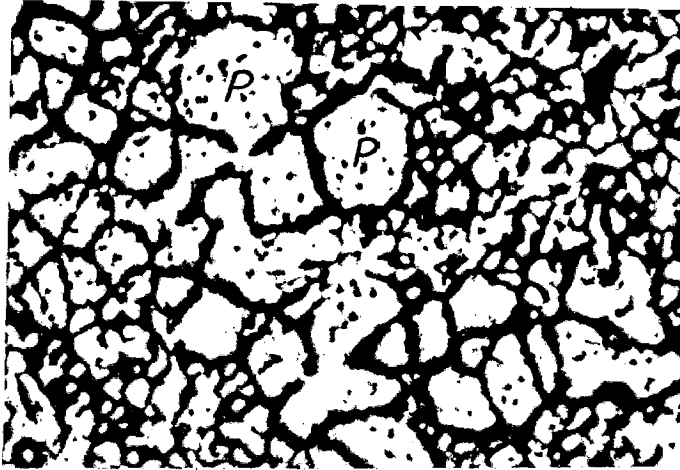


(a)



(b)

FIG. 4.33 MICROSTRUCTURE OF RHEOCAST Al-4.5 %
Cu ALLOY STIRRED AT 1000 R.P.M. AND
POURED FROM (a) 914 K (b) 911 K .
Mag. X 200



(a)



(b)

FIG.4.34 MICROSTRUCTURE OF RHEOCAST Al-4.5% Cu ALLOY STIRRED AT 1000 R.P.M. AND Poured FROM (a) 908 K, Mag. X 50 (b) 905 K, Mag. X 100

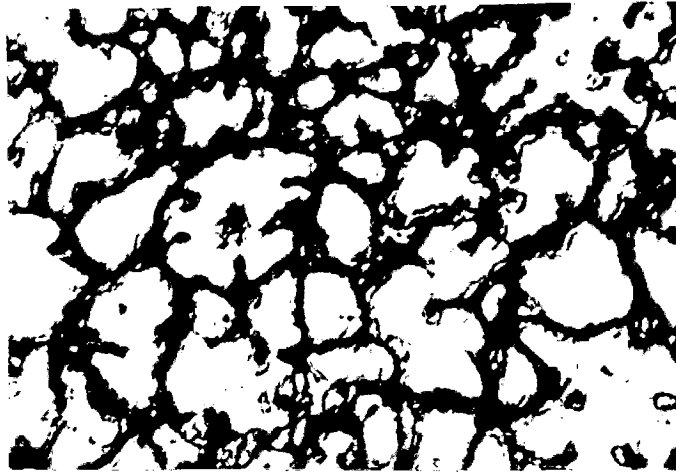


(a)

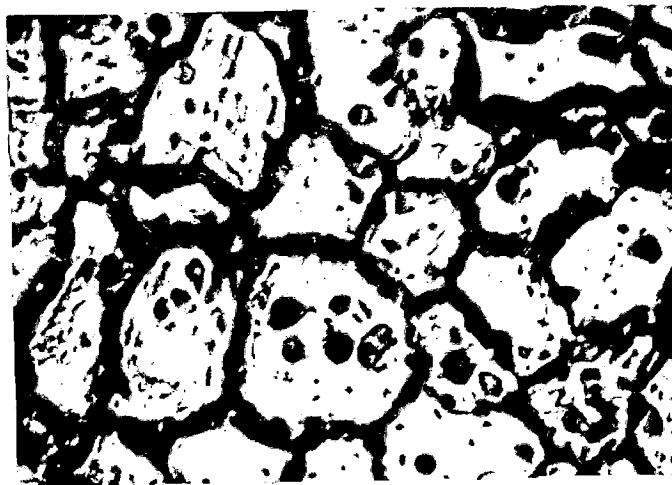


(b)

FIG. 4.35 MICROSTRUCTURE SHOWING THE EVIDENCE OF BOUNDARIES (SHOWN BY ARROW) WITHIN LARGE PRIMARY PARTICLES (P) SHOWN IN FIG 4.34 (b).
Mag. (a) X 200 (b) X 500



(a)

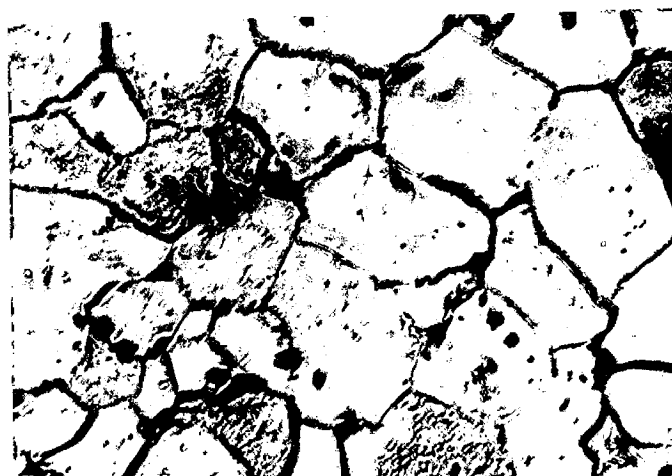


(b)

FIG.4.36 MICROSTRUCTURE OF RHEOCAST Al-4.5%
Cu ALLOY STIRRED AT 700 R.P.M. AND
POURED FROM (a) 922 K (b) 919 K.
Mag. X200



(a)



(b)

FIG.4.37 MICROSTRUCTURE OF RHEOCAST Al-4.5%
Cu ALLOY STIRRED AT 700 R.P.M. AND
POURED FROM (a) 914 K (b) 911 K.
Mag. X 200

provide an evidence that these particles have formed by particle coalescence.

Figures 4.31 to 4.34 and Figs. 4.36 to 4.37 represent the microstructures of rheocastings stirred at 1000 r.p.m. and 700 r.p.m. respectively. From a close examination of these micrographs two important effects of the process parameters are worth noting. Firstly, the dendritic morphology and the extent of segregation are more marked at higher pouring temperatures (compare Fig.4.31(a) with Fig.4.34(b) and Fig.4.36(a) with Fig.4.37(b)). The extent of segregation has been identified from the abundance of black region in the microstructures. The segregation is markedly low at lower stirring speed especially at lower pouring temperature (compare Fig.4.33(b) with Fig.4.37(b)).

The variation of average α -particle size (\bar{D}) with pouring temperature at various stirring speeds has been shown in Figs.4.38 to 4.41. At all stirring speeds, it is observed that \bar{D} is smaller at higher pouring temperatures and larger at lower pouring temperatures. However, at lower stirring speeds, the rate of increase of \bar{D} with decrease in pouring temperature is much greater than that observed at higher stirring speeds. In the duplex structure, the variation of the size of large particles 'P' and the rest of the particles as shown in Fig.4.40 is qualitatively similar to the trends observed in case Al-6% Cu alloy. However, in the

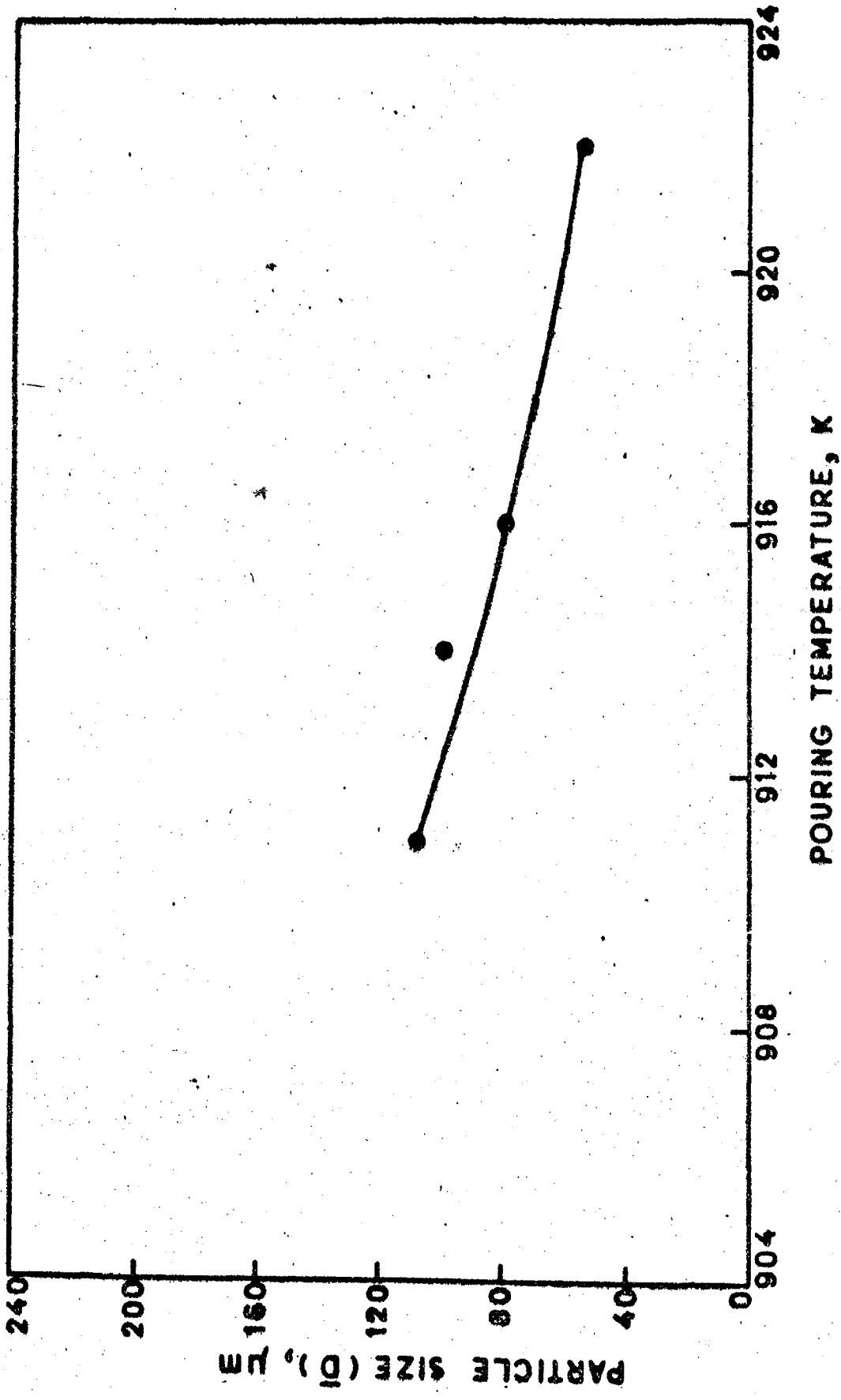


FIG.4.38 EFFECT OF POURING TEMPERATURE ON α -PARTICLE SIZE IN RHEOCAST Al-4.5 % Cu ALLOY STIRRED AT 500 R.P.M.

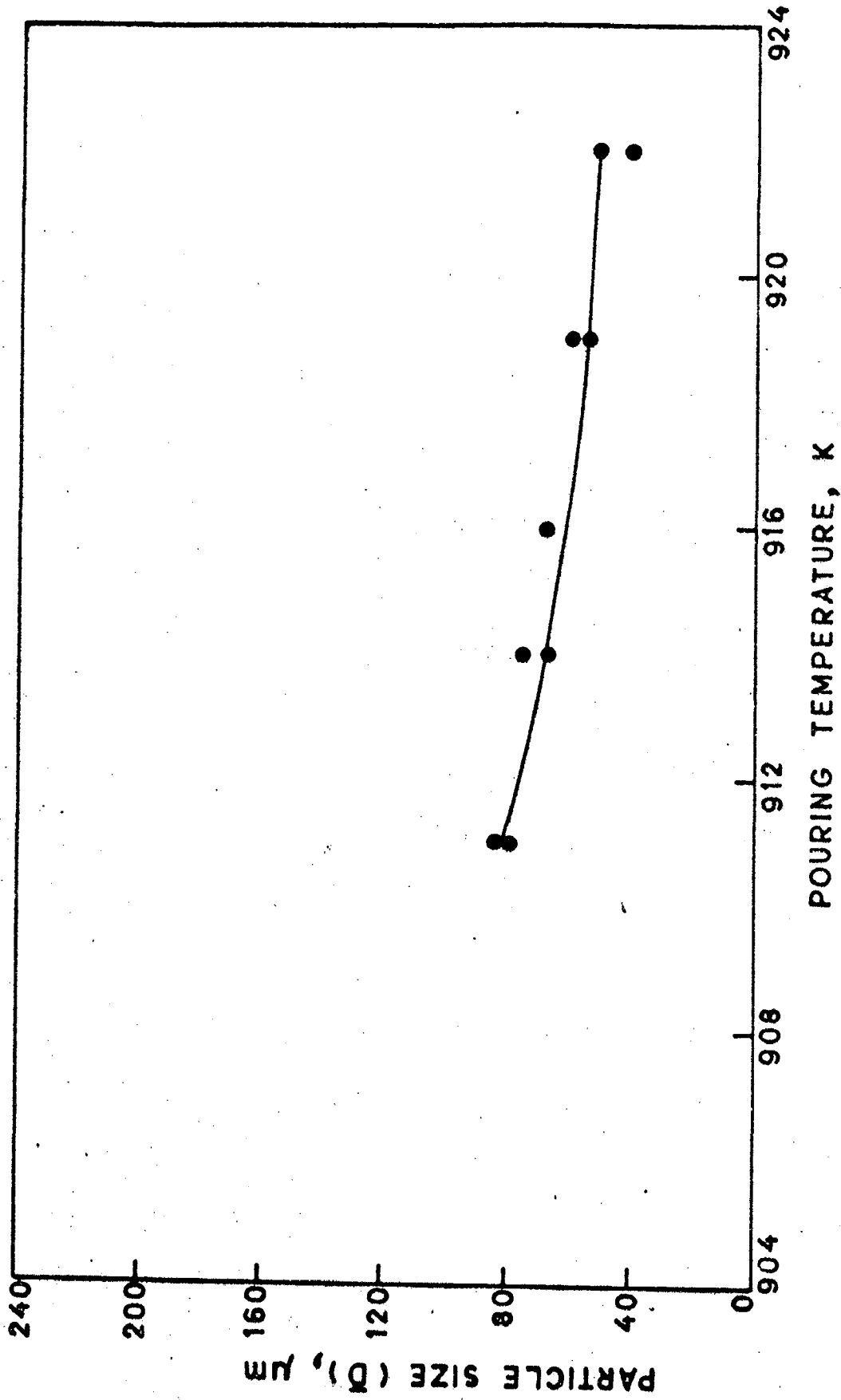


FIG. 4.39 EFFECT OF POURING TEMPERATURE ON α -PARTICLE SIZE
IN RHEOCAST Al-4.5% Cu ALLOY STIRRED AT 700 R.P.M.

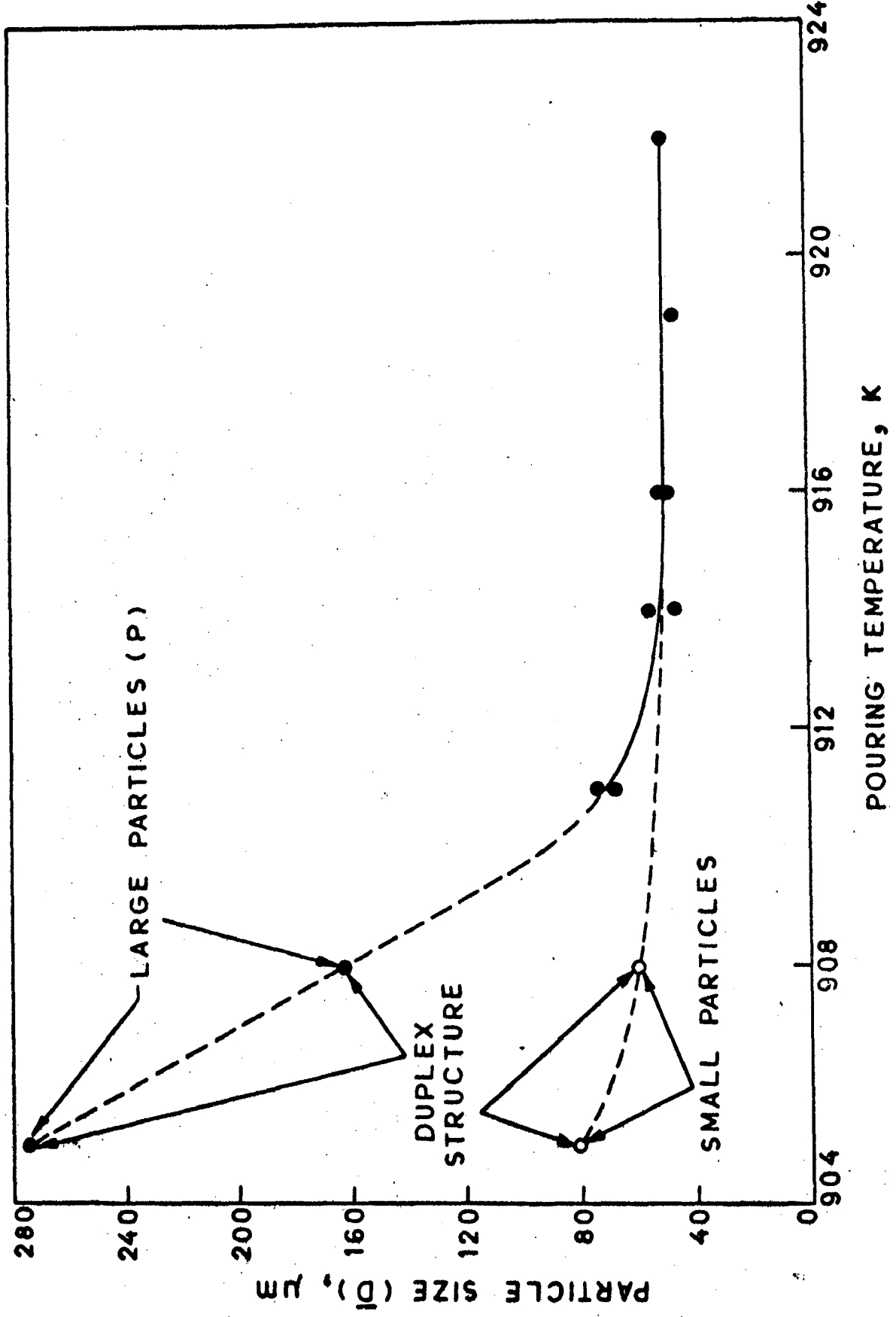


FIG. 4.40 EFFECT OF POURING TEMPERATURE ON α -PARTICLE SIZE IN RHEOCAST Al-4.5%Cu ALLOY STIRRED AT 1000 R.P.M.

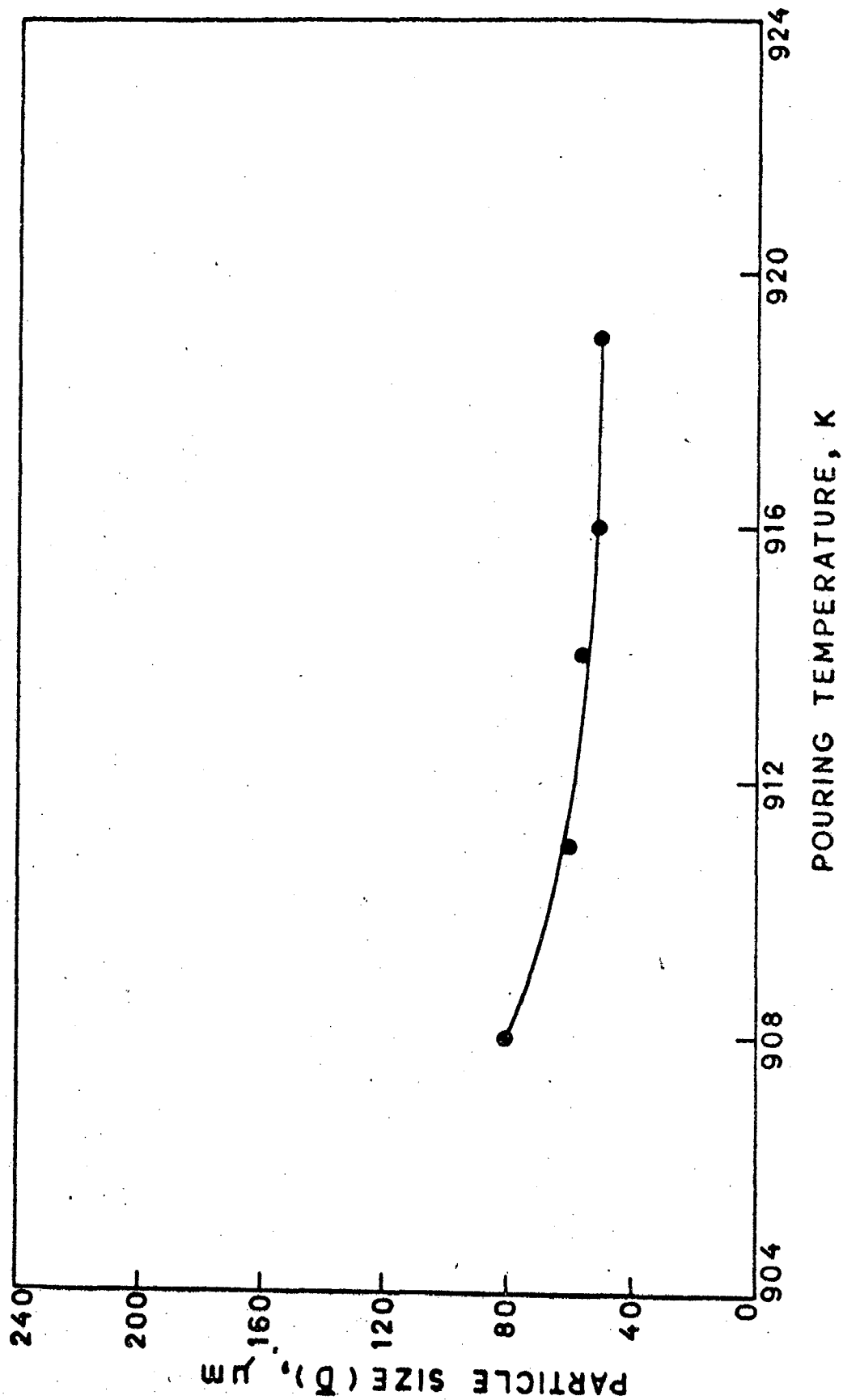
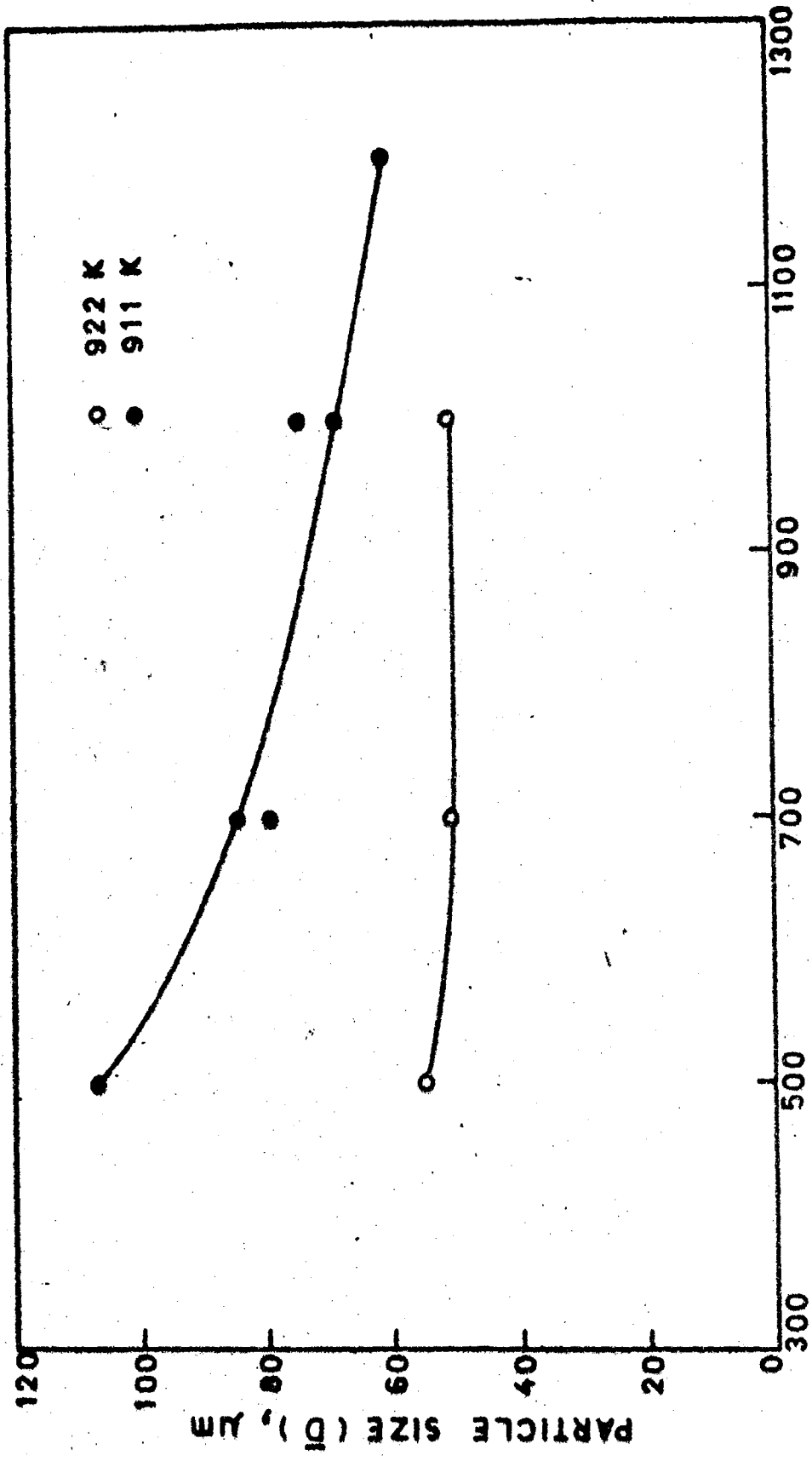


FIG. 4.41 EFFECT OF POURING TEMPERATURE ON α -PARTICLE SIZE
IN RHEOCAST Al-4.5% Cu ALLOY STIRRED AT 1200 R.P.M.

present case such a trend has been observed only for stirring at 1000 r.p.m.

Figure 4.42 is intended to show the effect of stirring rate on \bar{D} . Two temperatures 922K and 911K have been arbitrarily chosen to examine the effect of stirring rate at a higher pouring temperature and at a lower pouring temperature. It is observed that at higher pouring temperature, the stirring rate has no significant effect on \bar{D} . However, at lower pouring temperature, \bar{D} decreases with increase in stirring rate.

Figure 4.43 to 4.46 show typical frequency distribution curves of measured α -particle size for rheocastings made at 700 r.p.m. and 1000 r.p.m. Figures 4.47 to 4.50 are intended to show the effect of pouring temperature at various stirring speeds on the size distribution of α -particles as indicated by the standard deviation (σ) and the coefficient of variation (σ/\bar{D}). In general, it is observed that the variation of σ is similar to the variation of \bar{D} with pouring temperature. At stirring rates of 500 r.p.m. and 700 r.p.m., σ increases with the decrease in pouring temperature. At stirring rates of 1000 and 1200 r.p.m., σ remains unaltered at higher pouring temperatures but increases with decrease in pouring temperature at lower pouring temperatures. It is further observed that at low stirring speeds of 500 r.p.m. and 700 r.p.m., σ/\bar{D} increases with the decrease in pouring temperature, but at higher stirring speeds of 1000 r.p.m. and 1200 r.p.m.,



STIRRING RATE, r.p.m.

FIG.4.42 EFFECT OF STIRRING RATE ON α -PARTICLE SIZE IN RHEO-CAST Al-4.5%Cu ALLOY Poured FROM 922 K AND 911 K.

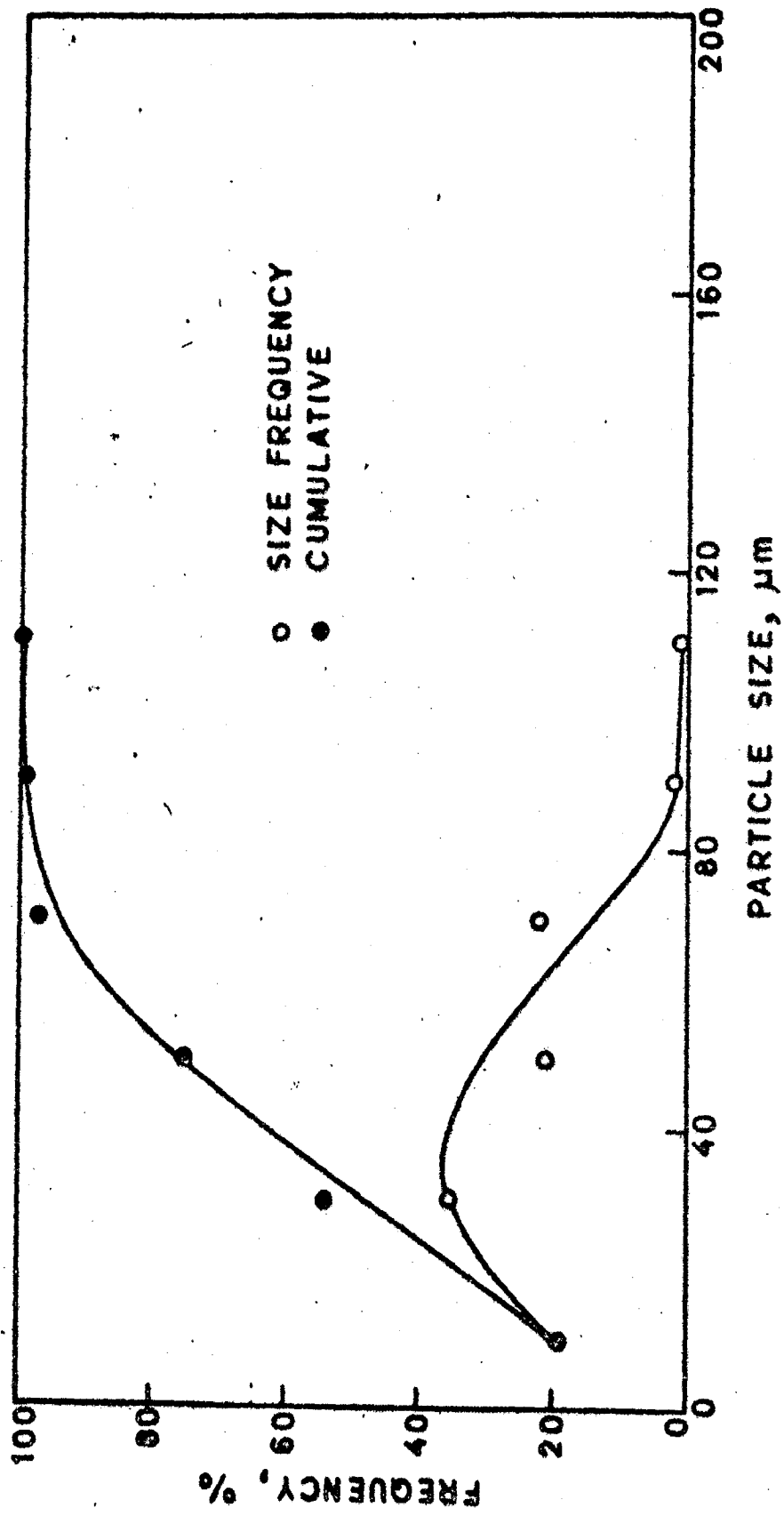


FIG. 4.43 FREQUENCY DISTRIBUTION CURVES OF α -PARTICLE SIZE IN RHEOCAST Al-4.5% Cu ALLOY STIRRED AT 700 R.P.M. AND POURED FROM 922 K.

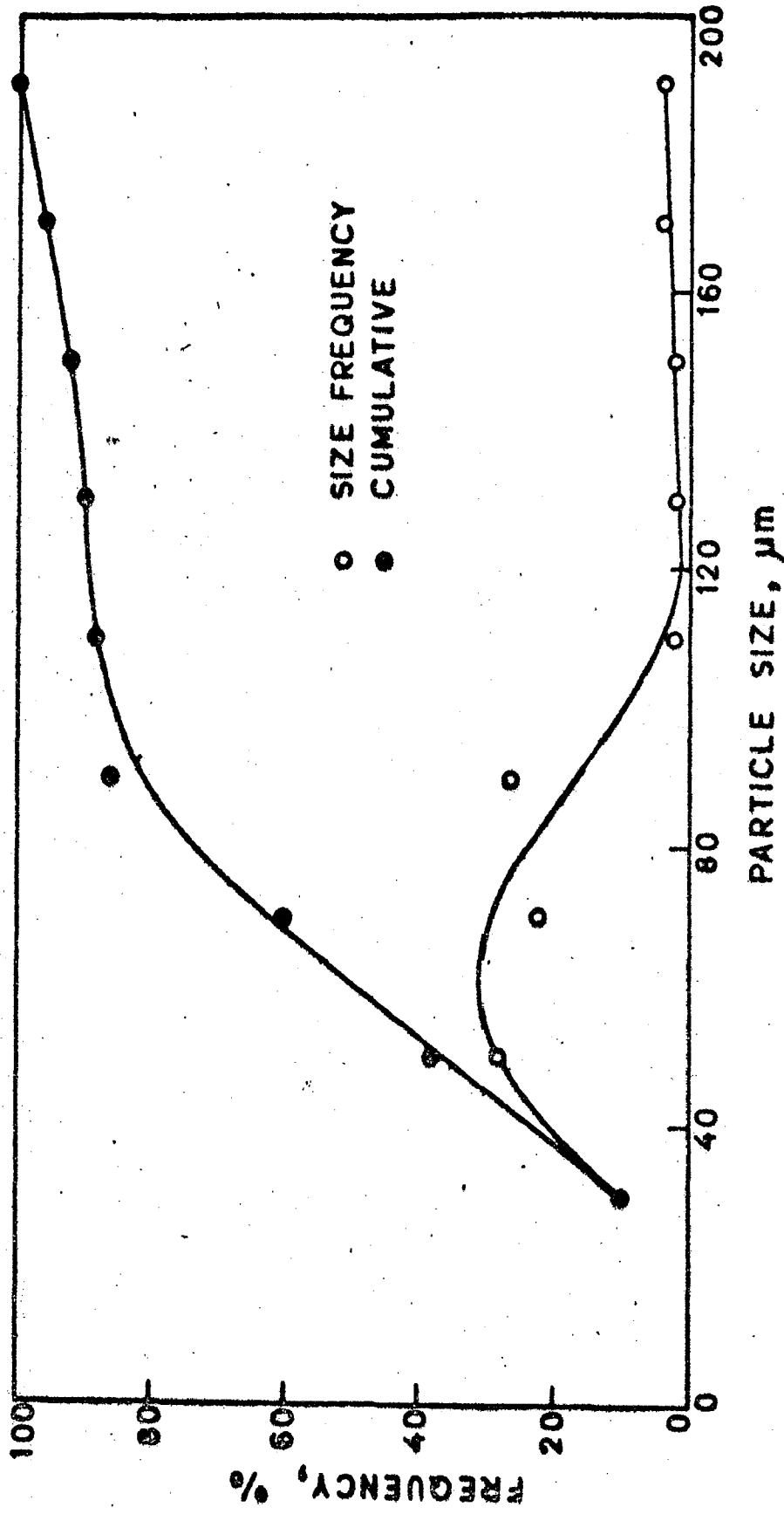


FIG.4.44 FREQUENCY DISTRIBUTION CURVES OF α -PARTICLE SIZE IN RHEOCAST Al-4.5% Cu ALLOY STIRRED AT 700 R.P.M. AND POURED FROM 911 K.

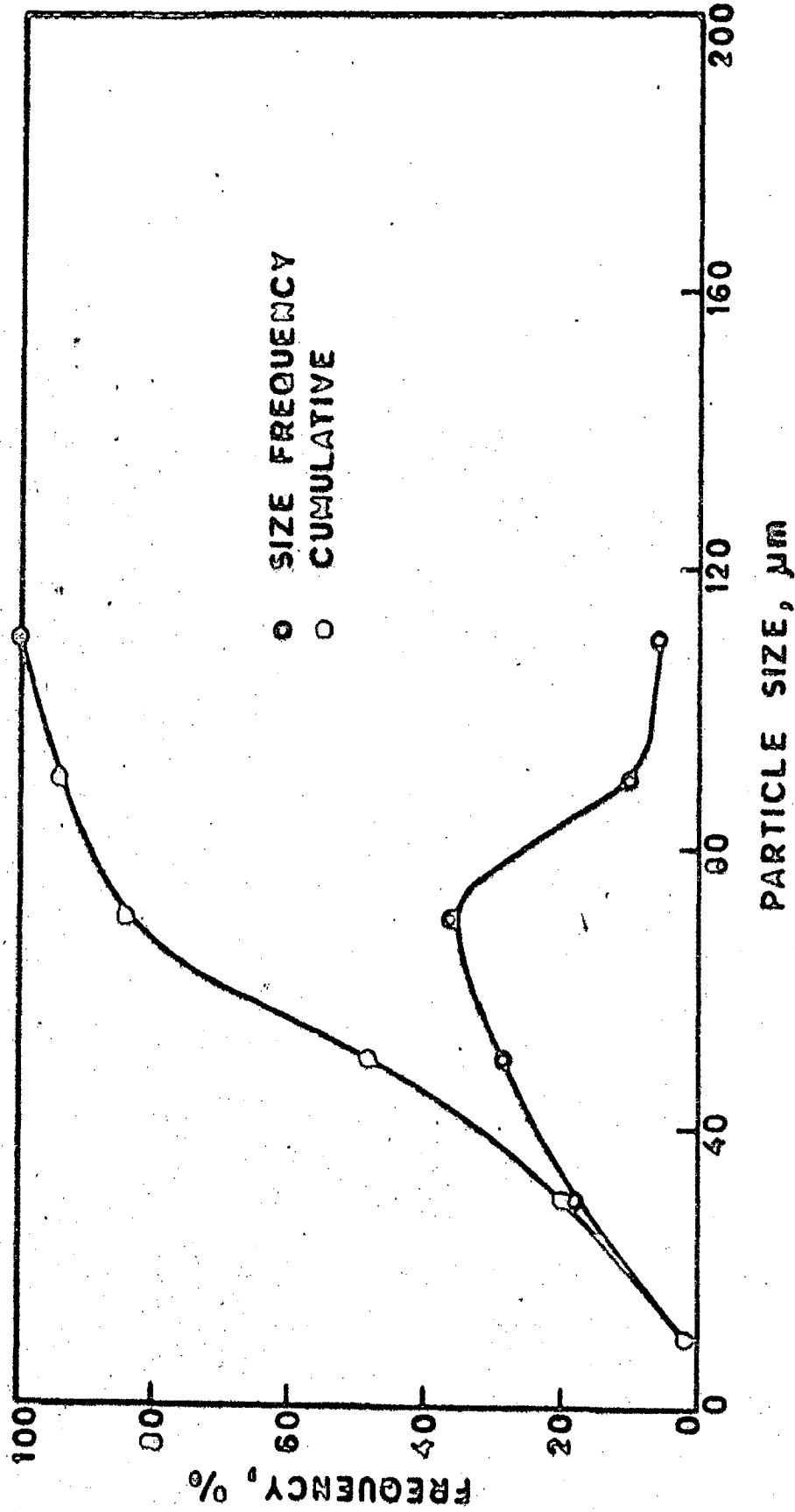


FIG. 4.45 FREQUENCY DISTRIBUTION CURVES OF α -PARTICLE SIZE
 IN RHEOCAST Al-4.5% Cu ALLOY STIRRED AT 1000
 R.P.M. AND Poured FROM 922 K.

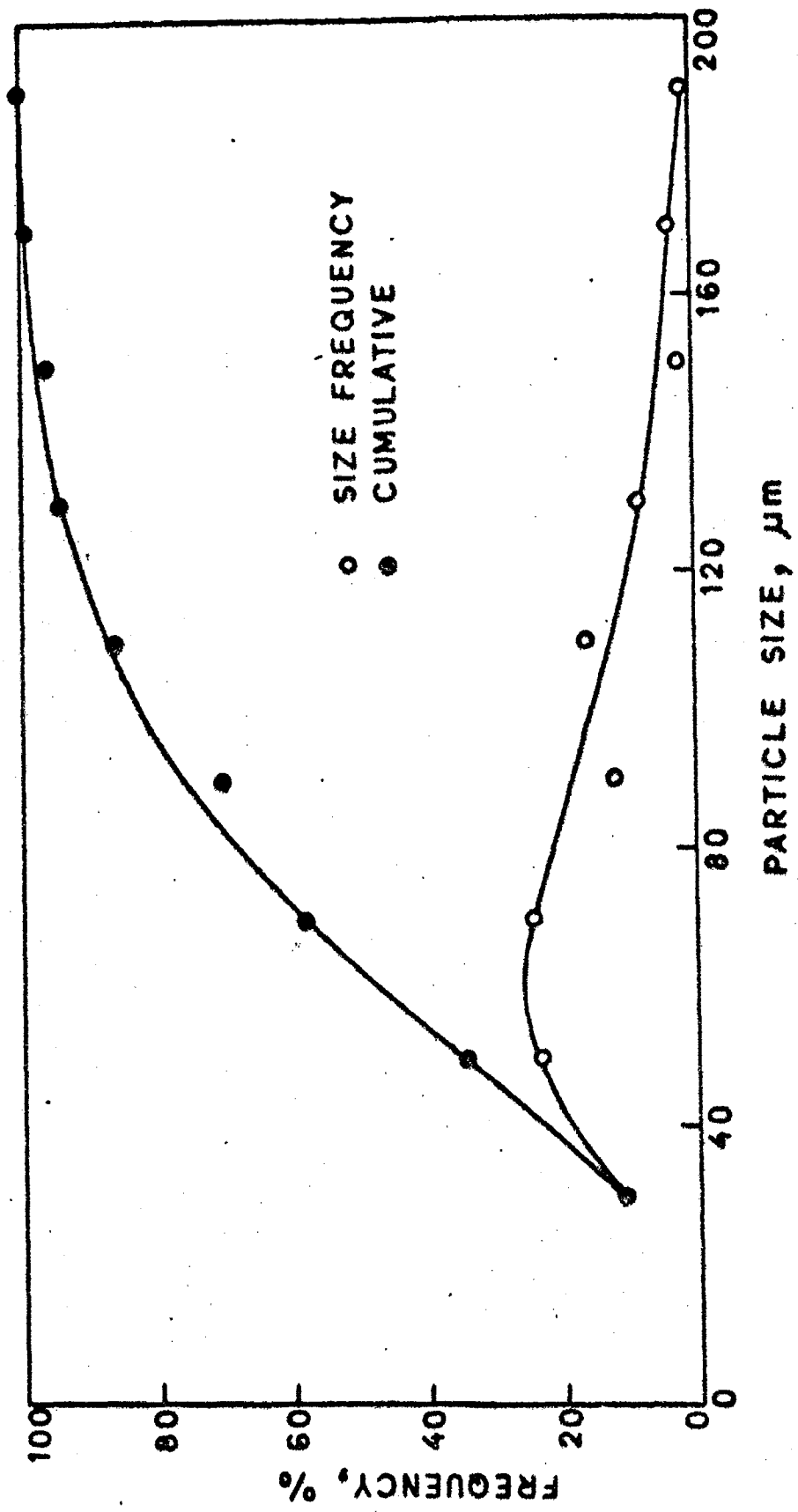


FIG.4.46 FREQUENCY DISTRIBUTION CURVES OF α -PARTICLE SIZE IN RHEOCAST Al-4.5% Cu ALLOY STIRRED AT 1000 R.P.M. AND POURED FROM 911 K.

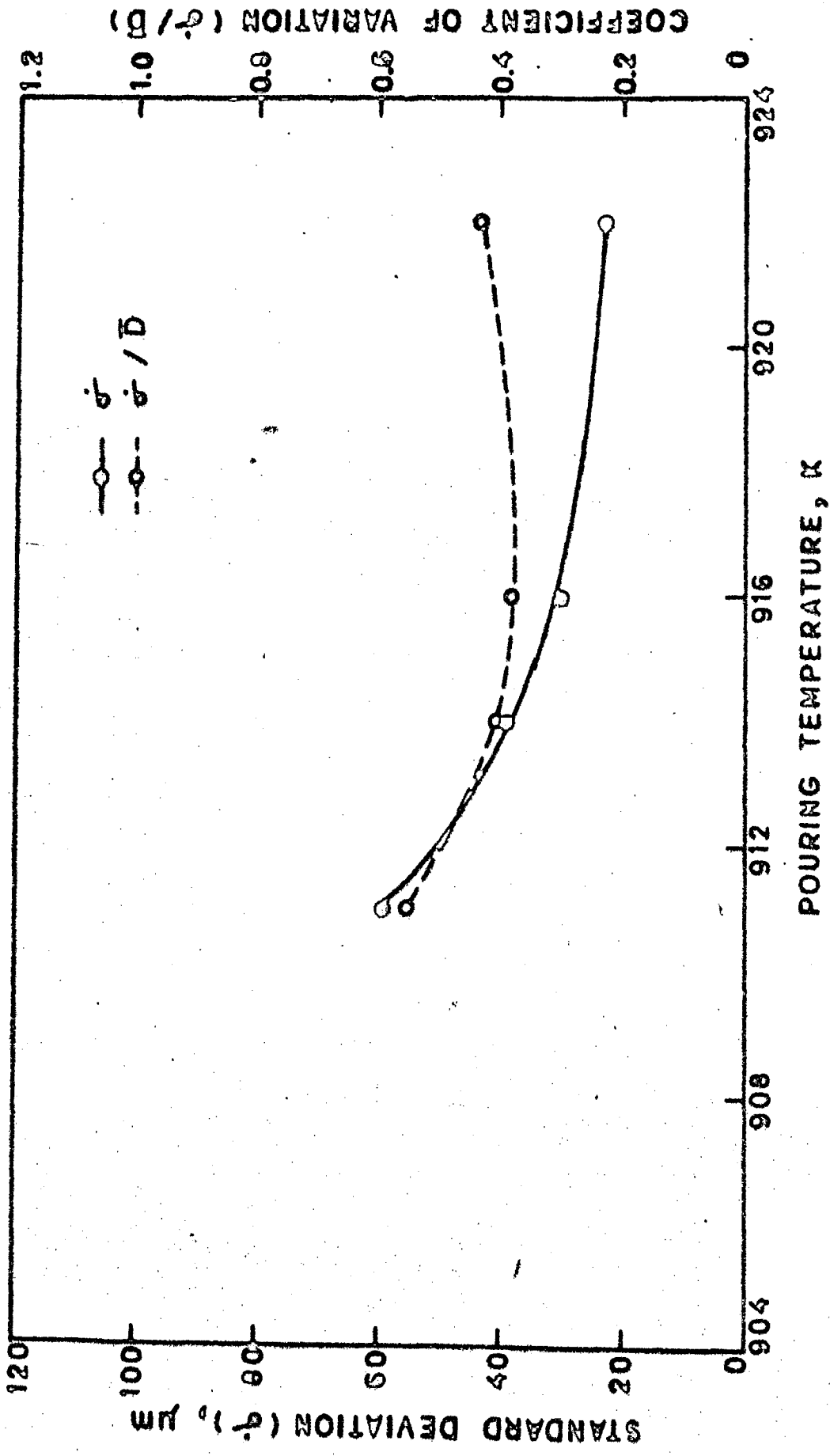


FIG. 4.47 EFFECT OF POURING TEMPERATURE ON STANDARD DEVIATION AND COEFFICIENT OF VARIATION OF α -PARTICLE SIZE IN RHEOCAST Al-4.5% Cu ALLOY STIRRED AT 500 R.P.M. 51

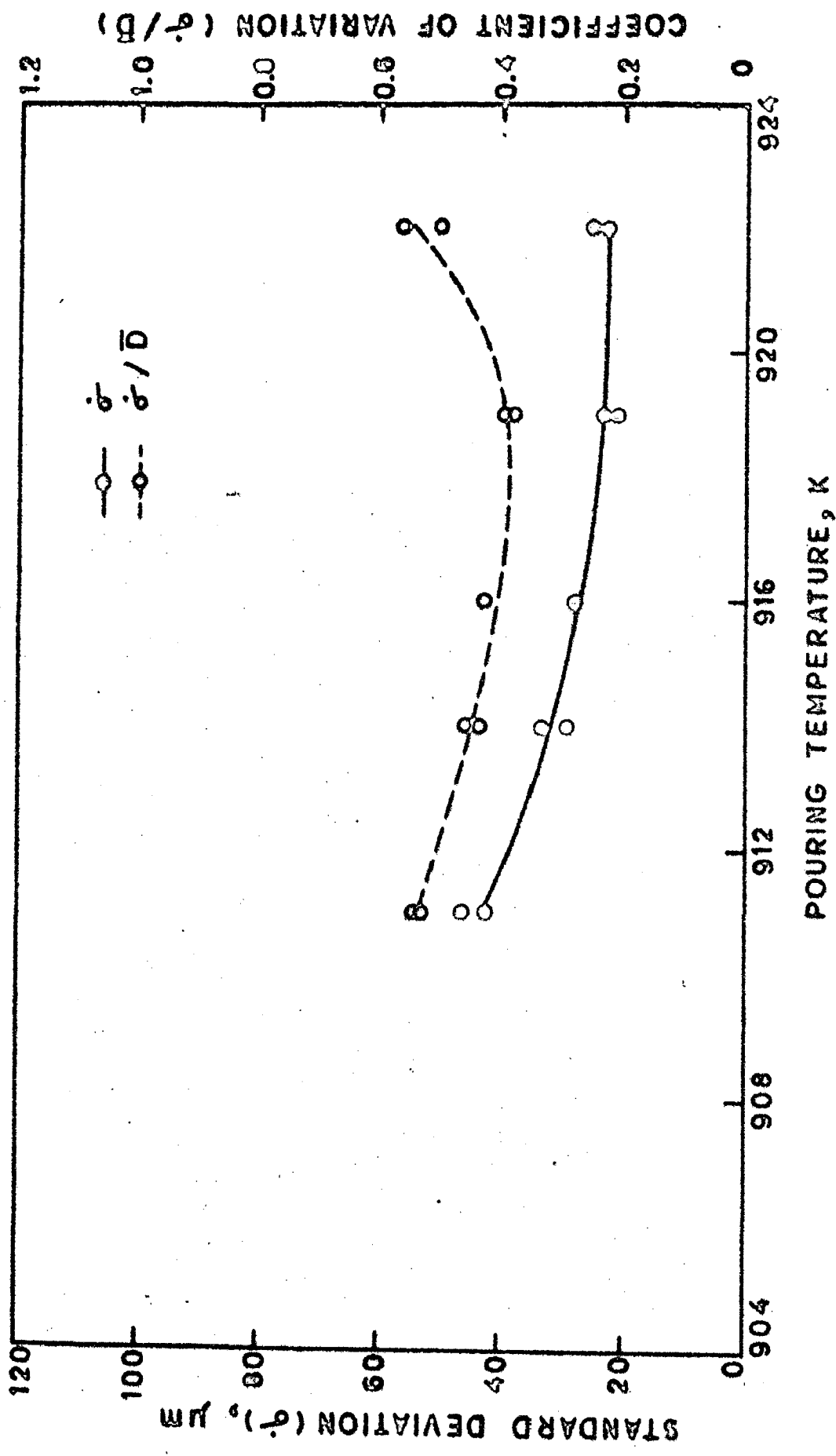


FIG. 4.48 EFFECT OF POURING TEMPERATURE ON STANDARD DEVIATION AND COEFFICIENT OF VARIATION OF α -PARTICLE SIZE IN RHEOCAST Al-4.5% Cu ALLOY STIRRED AT 700 R.P.M. 58

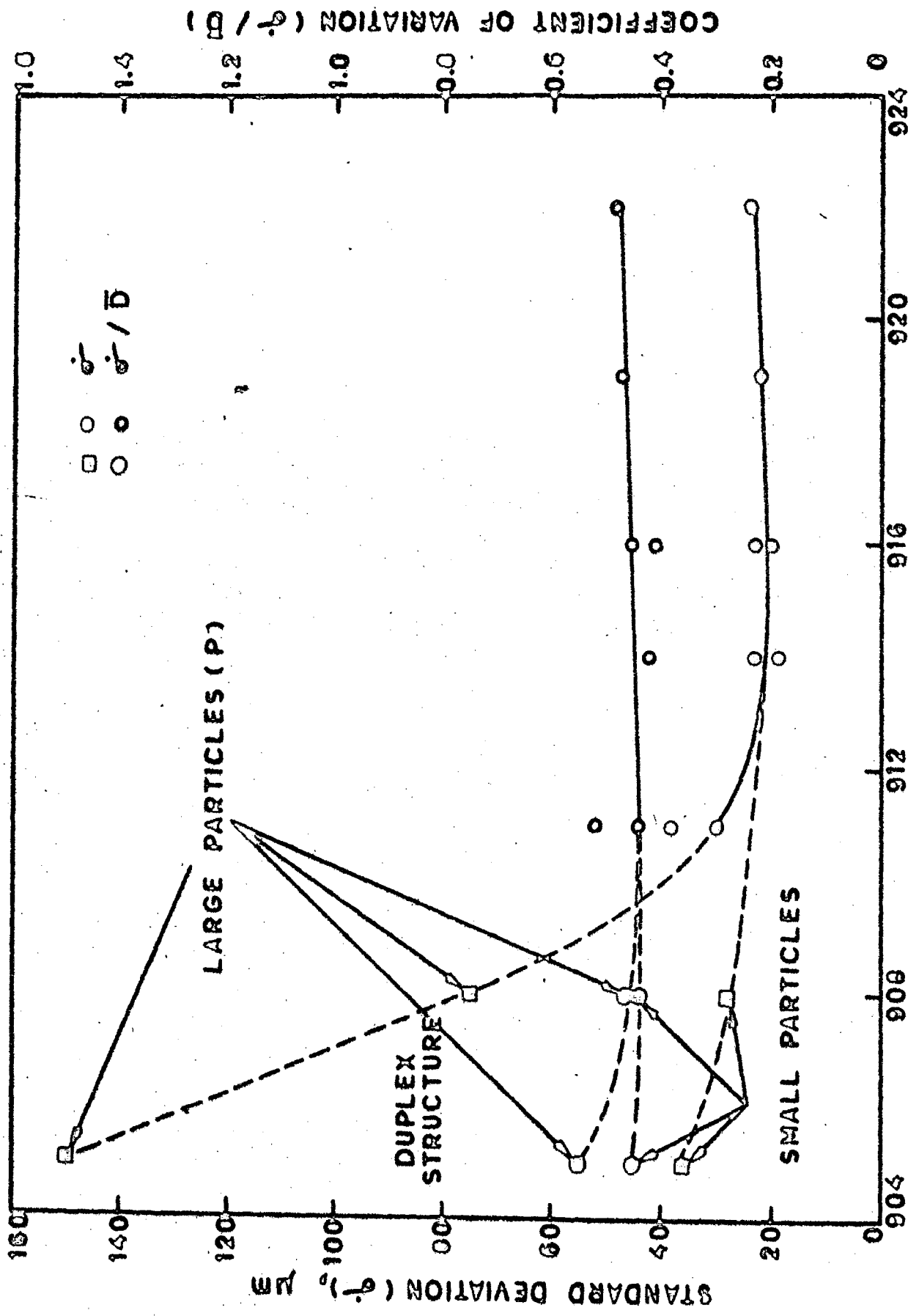


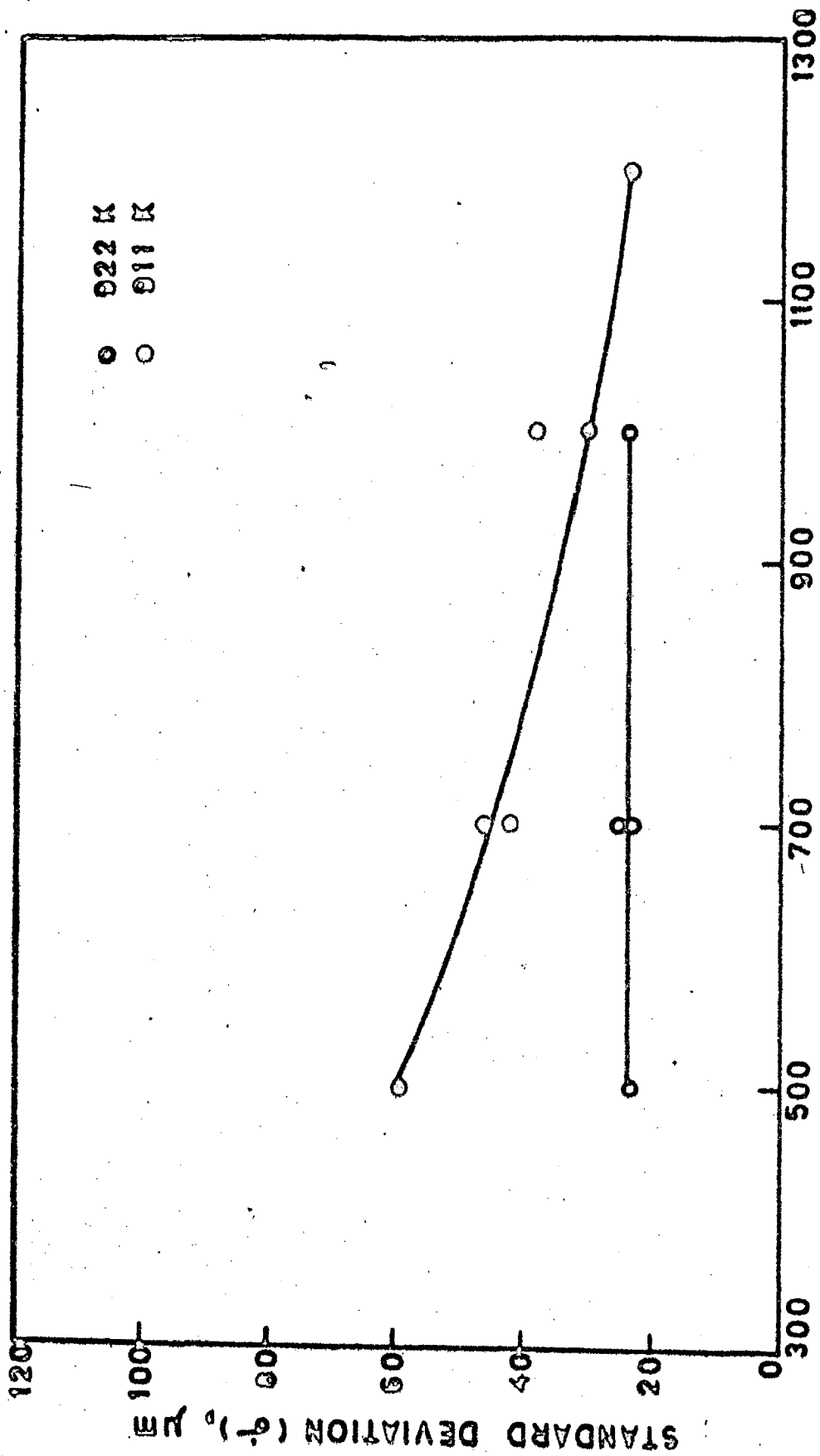
FIG.4.49 EFFECT OF POURING TEMPERATURE ON STANDARD DEVIATION AND COEFFICIENT OF VARIATION OF α -PARTICLE SIZE IN RHEOCAST Al-4.5% Cu ALLOY STIRRED AT 1000 R.P.M.

σ/\bar{D} does not vary significantly with pouring temperature.

Figure 4.51 is intended to show the effect of stirring rate on σ at a higher pouring temperature 922K and at a lower pouring temperature 911 K. It is observed that at 922K the stirring rate has no significant effect on σ , but at 911K it decreases with increasing stirring rate. Figure 4.52 shows the variation of σ/\bar{D} with stirring rate at 922K and 911K. The effect of stirring rate at 922K is insignificant but at 911K, σ/\bar{D} appears to decrease slightly with increase in stirring rate.

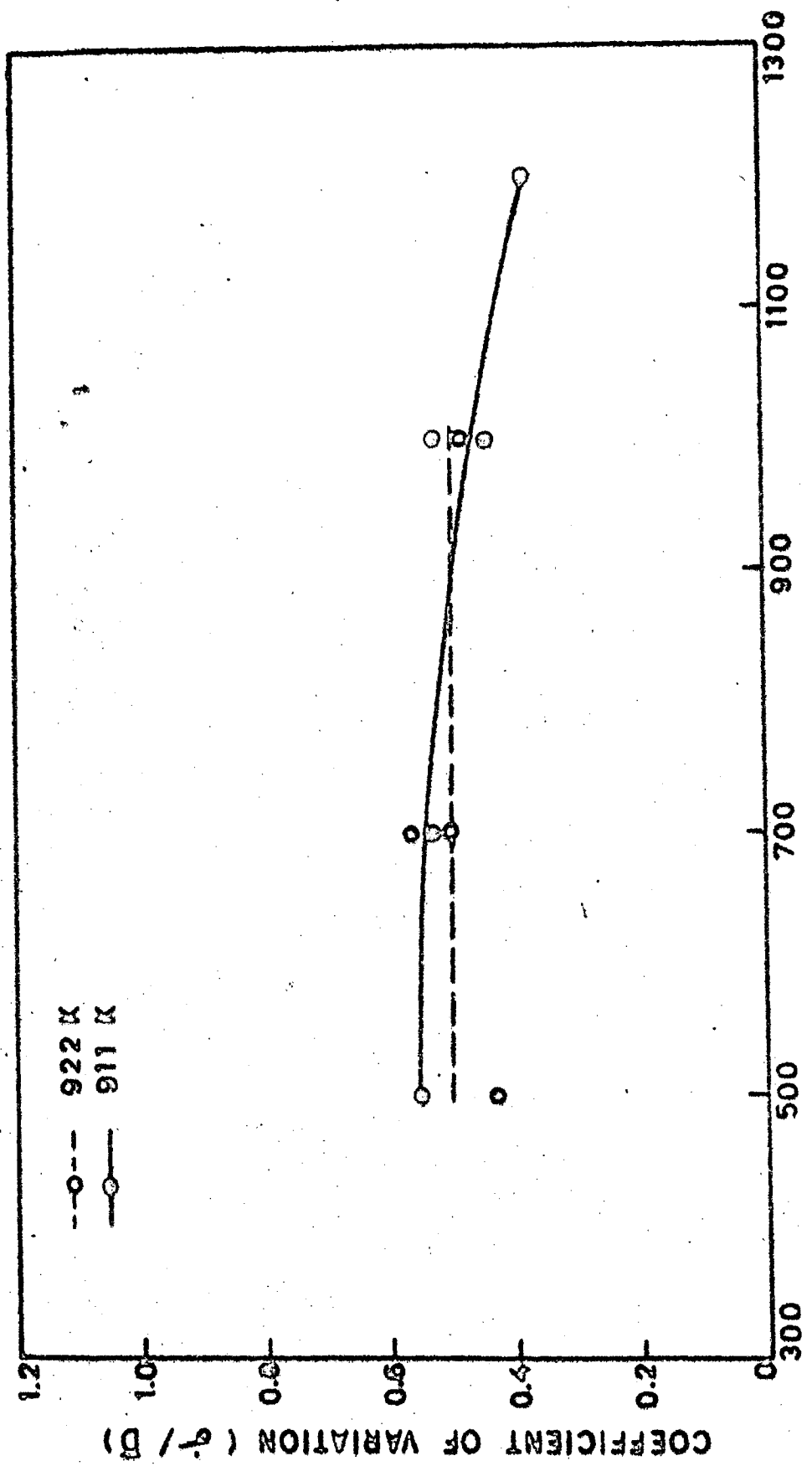
4.5 DISCUSSION: MICROSTRUCTURE OF RHEOCAST Al-Cu ALLOYS

The three sets of results on the microstructural features of rheocast Al-10% Cu, Al-6% Cu and Al-4.5% Cu alloys presented in sections 4.2, 4.3 and 4.4 respectively clearly show that the characteristic dendritic morphology of proeutectic α -phase obtainable in conventional casting is transformed into non-dendritic spheroidal morphology by rheocasting process. However, some dendrites have been observed in the rheocast samples especially at higher pouring temperatures and higher stirring rates. The formation of these dendrites in rheocast samples may be attributed either to the conditions prevailing during the primary solidification or during the secondary solidification in the mould. A typical water quenched slurry structure has been shown in Fig.4.7. Though the tendency of dendrite



STIRRING RATE, r.p.m.

FIG. 4.51 EFFECT OF STIRRING RATE ON STANDARD DEVIATION OF α -PARTICLE SIZE IN RHEOCAST Al-4.5% Cu ALLOY Poured FROM 922 K AND 911 K.



STIRRING RATE, r.p.m.

FIG. 4.52 EFFECT OF STIRRING RATE ON COEFFICIENT OF VARIATION OF α -PARTICLE SIZE IN RHEOCAST Al-4.5% Cu ALLOY Poured from 922 K and 911 K.

formation is quite evident, it is difficult to bring out as to whether this tendency is due to primary solidification or secondary solidification as the particles formed during primary solidification and during secondary solidification are not distinguishable from each other. Since the formation of dendrite is more marked at higher pouring temperature where the extent of solidification in the mould is more, it is reasonable to assume that the subsequent solidification in the mould is primarily responsible for this effect.

In a stirred melt when solid particles are continuously forming the particles always pass through such zones where the shear forces are weak and the colliding particles may remain in contact with each other for a longer time without disruption by the fluid forces. This contact time may be sufficient to result in the formation of bonds between the particles by sintering which eventually leads to the formation of a few particles much larger in size than the particles from which they form. The contact time between the particles is increased at lower temperatures because of higher solid content in the melt. This phenomenon of particle coalescence and sintering results in the formation of abnormally large primary particles marked 'P' in Figs. 4.18(b), 4.21(a) and 4.34. A further evidence of particle coalescence is obtained from Fig. 4.35 which shows the boundaries within the large primary particles. Apaydin et al(14) have also observed such boundaries in case of Al-Mg alloys. Though their findings

remain inconclusive, they consider that such boundaries are formed by particle coalescence. Ichikawa and Miwa(27) have also expressed the possibility of particle coalescence during stirring. Even in unstirred melts, Oblak and Rand(28) have shown that the primary particles grow by particle-coalescence mechanism in the liquid-solid region. From the foregoing, it appears that large primary particles are formed by particle coalescence mechanism.

It is well known that stirring increases the cooling rate of the melt where the cooling rate is not precisely controlled and the melt is allowed to cool naturally as in the present investigation. In Fig.1.10 it has been shown that a thermal gradient within the bulk of the liquid might exist when the cooling rate is high which is expected to favour dendritic growth even when the melt is vigorously agitated. It has also been observed by Flemings(56) that at higher cooling rates, at least above a certain minimum, dendritic or semi-dendritic particles instead of characteristic spheroidal ones are formed in case of rheocastings of aluminium, bronze and steels. It appears, therefore that the larger extent of dendrite formation at higher stirring rate is the manifestation of increase in cooling rate.

From the comparison of the results of Al-10% Cu, Al-6% Cu and Al-4.5% Cu alloy it is evident that the large primary particles 'P' have formed only in case of low copper alloys, i.e. Al-6% Cu and Al-4.5% Cu alloys. The

absence of such particles in case of Al-10% Cu alloy may be attributed to the effect of copper content on the growth kinetics of α -phase. Chien and Kattamis (75) have shown that the growth rate of α -phase in Al-Cu alloys decreases with the increase in copper content. It is, therefore, not unreasonable to assume that when the copper content is high, the neck formation between the colliding particles will be at a slower rate leading to the formation of weaker inter-particle bond. Such a bond can be easily broken by the fluid forces preventing the particles from coalescence. In contrast to this, the faster neck growth in low copper alloys will result in stronger bonds not easily disrupted by fluid forces and thus, the particles coalesce. The absence of any large particles formed by coalescence in Al-20% Cu alloy (13) and Al-10% Cu alloy and the occurrence of such particles in Al-6% Cu alloy and Al-4.5% Cu alloys provide adequate evidence in support of the role of copper content in particle coalescence phenomenon. At this stage, it is also pertinent to examine the effect of stirring rate on the particle coalescence phenomenon. When a lower stirring rate is employed, the fluid forces are weaker, neutral zones within the liquid extend over to a larger region and the particles remain in contact with each other for a longer time. It follows then that at lower stirring rate, particle coalescence will be favoured even when the solid fraction in the slurry is not high. However, this can happen only

when the growth rate is high, i.e. in case of lower copper alloys such as Al-4.5% Cu alloy. A possible consequence of these facts is that at low stirring rates large scale particle coalescence will take place and it will not be possible to identify the particles formed by coalescence. In contrast to this, when higher stirring rates are employed, the fluid forces are strong, neutral zones extend over to a limited region and colliding particles remain in contact only for a short time. Thus, with increasing stirring rate, the minimum solid fraction required for successful coalescence is increased and only a few coalesced particles are formed which are easily identified in the microstructure. This explains the results of Al-4.5% Cu alloy that large primary particles 'P' are formed only at 1000 r.p.m. For 1200 r.p.m. even for pouring temperature of 908K, the duplex structure has not been observed. This is because the particle coalescence is postponed to much higher solid fraction at this stirring rate. Therefore, it is likely that the duplex structure in case 1200 r.p.m. will form only when the temperature is brought below 908K.

In the normal solidification of a single phase binary alloy, the segregation of the solute results as a consequence to the non-equilibrium nature of the solidification. In a stirred melt, the segregation equation in terms of liquid composition is given by (4.5),

$$C_L = C_0(1-f_s)^{[k'-1]} \quad \dots (4.1)$$

where C_L is the bulk liquid composition, C_0 is the initial composition of the alloy, f_s is the fraction of solid particles formed and k' is effective partition coefficient. The effect of stirring rate on segregation is related through its effect on k' . If k' for a low stirring speed be designated as $(k')_{LS}$ and for a high stirring speed $(k')_{HS}$, the segregation equation during the primary solidification 4.1 may be rewritten as,

$$(C_L)_{LS} = C_0(1-f_s) [(k')_{LS}^{-1}] \quad \dots (4.2)$$

$$(C_L)_{HS} = C_0(1-f_s) [(k')_{HS}^{-1}] \quad \dots (4.3)$$

where $(C_L)_{LS}$ and $(C_L)_{HS}$ are bulk liquid composition after f_s amount of solid has formed at a low stirring speed and at a high stirring speed respectively. Combining equations 4.2 and 4.3,

$$\frac{(C_L)_{LS}}{(C_L)_{HS}} = (1-f_s) [(k')_{LS}^{-1} - (k')_{HS}^{-1}] \quad \dots (4.4)$$

It is known (45) that under constant growth rate condition, k' is minimum when the stirring is maximum, and therefore, it may be assumed that $(k')_{LS}$ is greater than $(k')_{HS}$. It follows then that $[(k')_{LS}^{-1} - (k')_{HS}^{-1}]$ is a positive quantity and since $(1-f_s)$ is less than unity, $(C_L)_{LS}/(C_L)_{HS}$ is also less than unity, i.e. $(C_L)_{LS} < (C_L)_{HS}$. The final solidification of the liquid having composition $(C_L)_{LS}$ or $(C_L)_{HS}$

obtained after primary solidification, occurs in the mould (secondary solidification). Since the composition of the liquid obtained at low stirring speed, $(C_L)_{LS}$, is lower than that at higher stirring speed, $(C_L)_{HS}$, lesser amount of segregation product is expected to form after final solidification in the mould. This is what exactly has been observed in the present case.

For the Al-10% Cu and Al-6% Cu alloys marked influence of processing condition on segregation has not been observed. In fact, Fig.3.1 shows that Al-4.5% Cu lies in the single phase region of the phase diagram and any segregation forming the second phase is easily identified. In contrast to this, Al-10% Cu and Al-6% Cu alloys lie in the two phase region where any variation in the segregation effect due to processing condition is difficult to detect visually unless a quantitative estimate is made with an accuracy within the range of variation of segregation with processing condition.

The effect of processing condition on particle size and its distribution has been found to be different for different alloy composition. Decreasing the pouring temperature has been found to decrease \bar{D} , σ and σ/\bar{D} in case of Al-10% Cu alloy, whereas in the case of Al-6% Cu alloy, \bar{D} , σ and σ/\bar{D} have not been found to vary significantly with pouring temperature except at very low pouring temperatures where the particle coalescence leads to sudden increase in the size of some of primary particles. In case of the Al-4.5% Cu alloy, \bar{D} , σ and σ/\bar{D}

have been found to increase with decrease in pouring temperature at low stirring speeds. At higher stirring speeds, the dependence of \bar{D} , $\bar{\sigma}$ and $\bar{\sigma}/\bar{D}$ on pouring temperature is similar to the observations for Al-6% Cu alloy.

Stirring rate has not been found to have any effect on particle size and its distribution in case of high copper alloy, i.e. Al-10% Cu alloy. For the lower copper alloys, i.e. Al-6% Cu and Al-4.5% Cu, increasing the stirring rate has been found to decrease the \bar{r} -particle size and its distribution.

The dependence of particle size and its distribution on process parameters may be examined with reference to equation 1.6, 1.15 and 1.13. These equations may be rewritten as,

$$\frac{\bar{R}}{\bar{I}} = A \Delta T \exp(B/\Delta T^2) \quad \dots (4.5)$$

$$V_p \bar{R} = A_2 \left[1 - \left(\frac{T_L}{\Delta T_L + \Delta T} \right)^{\frac{1}{1-k}} \right] \Delta T \quad \dots (4.6)$$

$$\bar{r} = \left(\frac{3}{\pi a^2} \right)^{1/3} (V_p \bar{R} \times \frac{\bar{R}}{\bar{I}})^{1/3} \quad \dots (4.7)$$

where R is growth rate, I is nucleation rate, ΔT gives the temperature by which the temperature of the melt is brought below the liquidus temperature, ΔT_L is the difference between the liquidus temperature of the alloy and the melting temperature of pure component, k is equilibrium partition coefficient, \bar{r} is average particle size, V_p is the volume fraction of

solid formed, and A , A_2 and a are constants. A close examination of equation 4.5 reveals that the variation of \dot{R}/I with ΔT passes through a minima which occurs at $\Delta T = \sqrt{B}$. This value of ΔT may be designated as ΔT_{\min} . When ΔT is lowered below ΔT_{\min} , $\frac{\dot{R}}{I}$ increases but the parameter $V_p \dot{R}$ decreases as can be seen from equation 4.6. The change in particle size with decreasing ΔT will depend upon the relative effects of $\frac{\dot{R}}{I}$ and $V_p \dot{R}$ according to equation 4.7.

The observed experimental result for high copper alloy (Al-10% Cu alloy) that the particle size increases with the increase in pouring temperature (decrease in ΔT) suggests that for this alloy ΔT_{\min} is high and the pouring temperatures varied lie in the range having ΔT less than ΔT_{\min} where $\frac{\dot{R}}{I}$ increases when ΔT decreases. If ΔT is sufficiently away from ΔT_{\min} , $\frac{\dot{R}}{I}$ will become overbearing because of the exponential term and more than compensate the decrease in $V_p \dot{R}$. Thus, particle size as given by equation 4.7 will increase with the increase in pouring temperature. However, in the lower copper alloy (Al-4.5% Cu), the observation that particle size decreases with increase in pouring temperature (decrease in ΔT) suggests that ΔT_{\min} is lower for this alloy and therefore the range in which the pouring temperatures have been varied lies for ΔT greater than ΔT_{\min} where both $\frac{\dot{R}}{I}$ and $V_p \dot{R}$ decrease with decrease in ΔT . Thus, the particle size will decrease with increase in pouring

temperature. For the intermediate copper content (Al-6% Cu), the observation that the particle size does not change with pouring temperature, suggests that pouring temperatures employed lie in the range of ΔT less than ΔT_{\min} , but sufficiently near it so that increase in $\frac{R}{I}$ is almost compensated by decrease in $V_p R$ and therefore the particle size is independent of pouring temperature. From the foregoing it is apparent that the copper content has a distinct influence on ΔT_{\min} which increases with increase in copper content. Since for high copper content (Al-10% Cu) the particle size has been found to decrease and for low copper content (Al-4.5% Cu) the particle size has been found to increase with decrease in pouring temperature, the change in the value of ΔT_{\min} with copper content further implies that at higher copper content the transformation is nucleation dominant and at lower copper content the transformation is growth dominant. This is in accordance with the observations of Chien and Kattamis (75) that the growth rate of α -phase increases as the copper content is lowered. It appears therefore that for intermediate copper content (Al-6% Cu) the growth and nucleation effects are equivalent so that the pouring temperature has no effect on particle size.

The effect of stirring rate on particle size is related to the increase in the maximum number of nuclei, N_{\max} , either because of the increase in cooling rate or removal of solid particles from the surfaces of the crucible wall and stirrer

by the fluid forces. This implies that the effect of increasing the stirring rate is to make the transformation more nucleation dominant. In case the alloy composition favours nucleation dominant transformation, the effect of stirring on nucleation events may not be pronounced because of already prevailing high nucleation activity. Consequently, no effect of stirring rate on particle size is anticipated as observed in case of Al-10% Cu alloy. For the low copper alloys, therefore, where growth conditions, both diffusion controlled and particle coalescence are significant, the increase in stirring rate, increases the dominance of nucleation events and consequently the particle size is decreased. However, such an effect is likely to be observed in case of low pouring temperatures where the effect of secondary solidification is insignificant. At higher pouring temperatures, the primary solidification proceeds only to a limited extent and any effect of stirring rate is unlikely to be observed. This explains the results of the low copper alloys on the dependence of α -particle size on processing conditions.

When a transformation proceeds with the growth process dominating, the growth of particles forming during the early stages of solidification will result in the formation of particles much bigger in size than the particles forming during the later stages of solidification. Such a situation is expected to give rise to a broad size

distribution. On the other hand, if the transformation proceeds with the nucleation events dominating, the difference between the sizes of particles forming during different stages of solidification will not be large and therefore, the size distribution will become narrow. For the case when both the growth and nucleation effects are equivalent, the size distribution is not expected to change with the pouring temperature. From the foregoing, it is apparent that in case of Al-10% Cu alloy, where the nucleation effect is dominant, $\bar{\sigma}$ and $\bar{\sigma}/\bar{D}$ will decrease with pouring temperature; in case of Al-6% Cu alloy, where the growth and nucleation effects are equivalent, $\bar{\sigma}$ and $\bar{\sigma}/\bar{D}$ will not change with pouring temperature and; in case of Al-4.5% Cu alloy, where the growth effect is dominant, $\bar{\sigma}$ and $\bar{\sigma}/\bar{D}$ will increase with decrease in pouring temperature. However, in case of Al-4.5% Cu alloy, $\bar{\sigma}$ and $\bar{\sigma}/\bar{D}$ have not been found to vary with the pouring temperature at higher stirring speeds. This clearly shows that the nucleation effect has been enhanced at higher stirring rate so that the growth and nucleation effects become equivalent. Since increasing the stirring rate has the effect of enhancing the nucleation dominance during the solidification, the present observation that stirring rate has no significant influence on size distribution in case of Al-10% Cu alloy and it lowers the values of $\bar{\sigma}$ and $\bar{\sigma}/\bar{D}$ in case of lower copper alloys, is therefore in accordance with the general expectations.

CHAPTER V

RESULTS AND DISCUSSION: MECHANICAL PROPERTIES

5.1 INTRODUCTION

In this chapter, results pertaining to tensile properties of rheocast Al-10% Cu, Al-6% Cu and Al-4.5% Cu alloys have been presented and discussed in the light of theoretical models developed in Chapter 2. The results for the Al-10% Cu alloy have been presented in Section 5.2 whereas those for the Al-6% Cu and Al-4.5% Cu alloys have been presented in Section 5.3. After eliminating the contribution of porosity, the strength levels of rheocastings have been compared with those of conventional castings, and the role of rheocast microstructure in modifying the mechanical properties has been assessed. In order to gain an insight into the mechanism by which the mechanical properties are governed, SEM fractographic observations of tensile fractured surfaces have also been made and results have been presented and discussed in Section 5.5.

5.2 MECHANICAL PROPERTIES OF RHEOCAST AL-10% Cu ALLOY

Tensile strengths of various castings of Al-10% Cu alloy have been presented in table 5.1. All the castings tested

Table 5.1- Effect of processing condition on mechanical properties of Al-10% Cu alloy

S.No	Stirring speed r.p.m.	Pouring Temperature K	Porosity %	Tensile Strength MNm^{-2}	% Elongation
1.	700	900	11.0	172	0
2.	700	896	3.8	170	0
3.	700	894	3.8	164	0
4.	700	892	7.9	170	0
5.	700	886	10.3	166	0
6.	700	880	4.1	184	0
7.	1000	900	3.2	211	0
8.	1000	898	1.5	201	0
9.	1000	896	20.7	113	0
10.	1000	894	0.6	194	0
11.	1000	892	1.7	196	0
12.	1000	886	4.5	172	0
13.	Conventional casting		6.3	216	0

are extremely brittle and do not show any permanent elongation within the accuracy of measurement. A typical tensile load extension curve showing the brittle nature of the material has been depicted in Fig. 5.1. Table 5.1 shows that no direct correlation exists between the tensile strength and the processing condition.

The measured volume fraction of α -particles in the Al-10% Cu alloy is 70%. It has been shown in Section 2.1 that the critical amount of α -phase above which the particles touch each other is 78.5%. Since for the Al-10% Cu alloy the volume fraction of α -particles is less than this critical value, α -particles are assumed to be present as discrete particles and the $\alpha + \text{CuAl}_2$ eutectic phase is continuous. The theoretical analysis presented in Section 2.2 for such a composite shows that the tensile strength, σ_{uc} , may be described in terms of contributions of the matrix (i.e. eutectic) and α -particles from the rule of mixtures. The governing equation 2.26 may then be rewritten as,

$$\sigma_{uc} = \sigma_{um} V_m + \frac{4 V_p \sigma_{um}}{\pi^2} (\bar{D}_i \bar{Z})^2 \quad \dots (5.1)$$

where σ_{um} is the tensile strength of the eutectic, V_m and V_p are volume fractions of matrix and α -particles respectively, \bar{D}_i is the average size of α -particles on a planar section, and \bar{Z} is the average of reciprocal of measured D_i values. The first term in the right hand side of equation 5.1 gives the contribution of the matrix and the second term gives

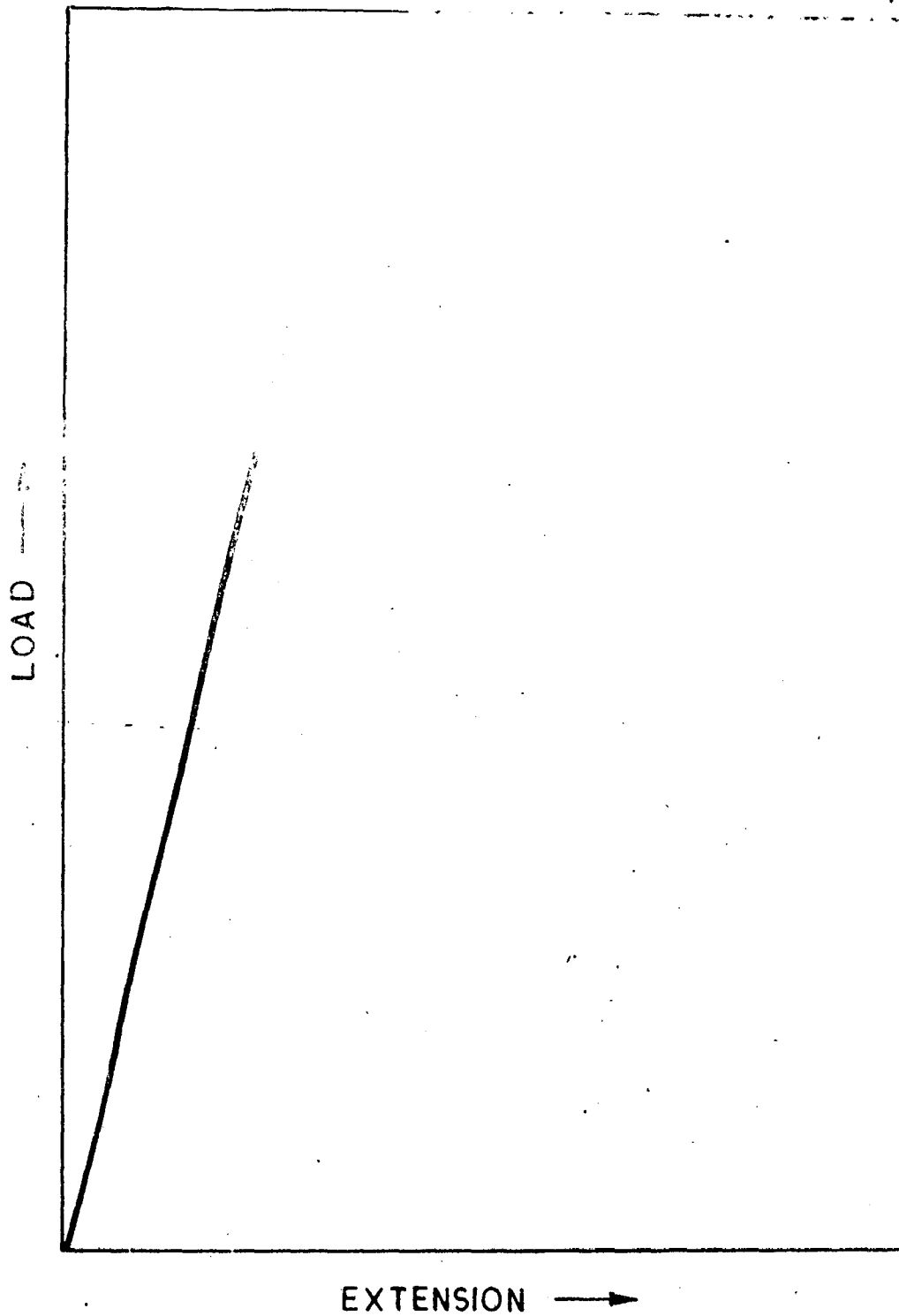


FIG. 5.1 SCHEMATIC REPRESENTATION OF TENSILE LOAD-EXTENSION CURVE FOR Al-10% Cu ALLOY.

the contribution of particles. If a typical value of 250 MNm^{-2} is assumed for σ_{um} (76), equation 5.1 may be rewritten as,

$$\sigma_{uc} = 75 \cdot 70 \cdot 92 (\bar{D}_1 \bar{Z})^2 \quad \dots (5.2)$$

From the measured value of $\bar{D}_1 \bar{Z}$ for various castings the tensile strength may be calculated on the basis of equation 5.2. The calculated strength values have been compared with the experimental values in Fig. 5.2. It is observed that the experimental values are lower than the theoretical values. This discrepancy between the two sets of strength values may be attributed to the porosity in castings.

In order to evaluate the effect of porosity, equation 2.40 may be rewritten as,

$$\sigma_p^* = \sigma_0 - \sigma_0 \alpha (\%P) \quad \dots (5.3)$$

where σ_p^* is the tensile strength of the material containing P% porosity, σ_0 is the tensile strength of pore-free material and α is a factor which gives the magnitude of damage caused by the presence of pores. As, shown in equation 2.39, α depends upon two parameters n and K , where n defines the zone of stress inhomogeneity around the pores and K is a weakening factor. The parameters n and K are constants for a particular material and pore

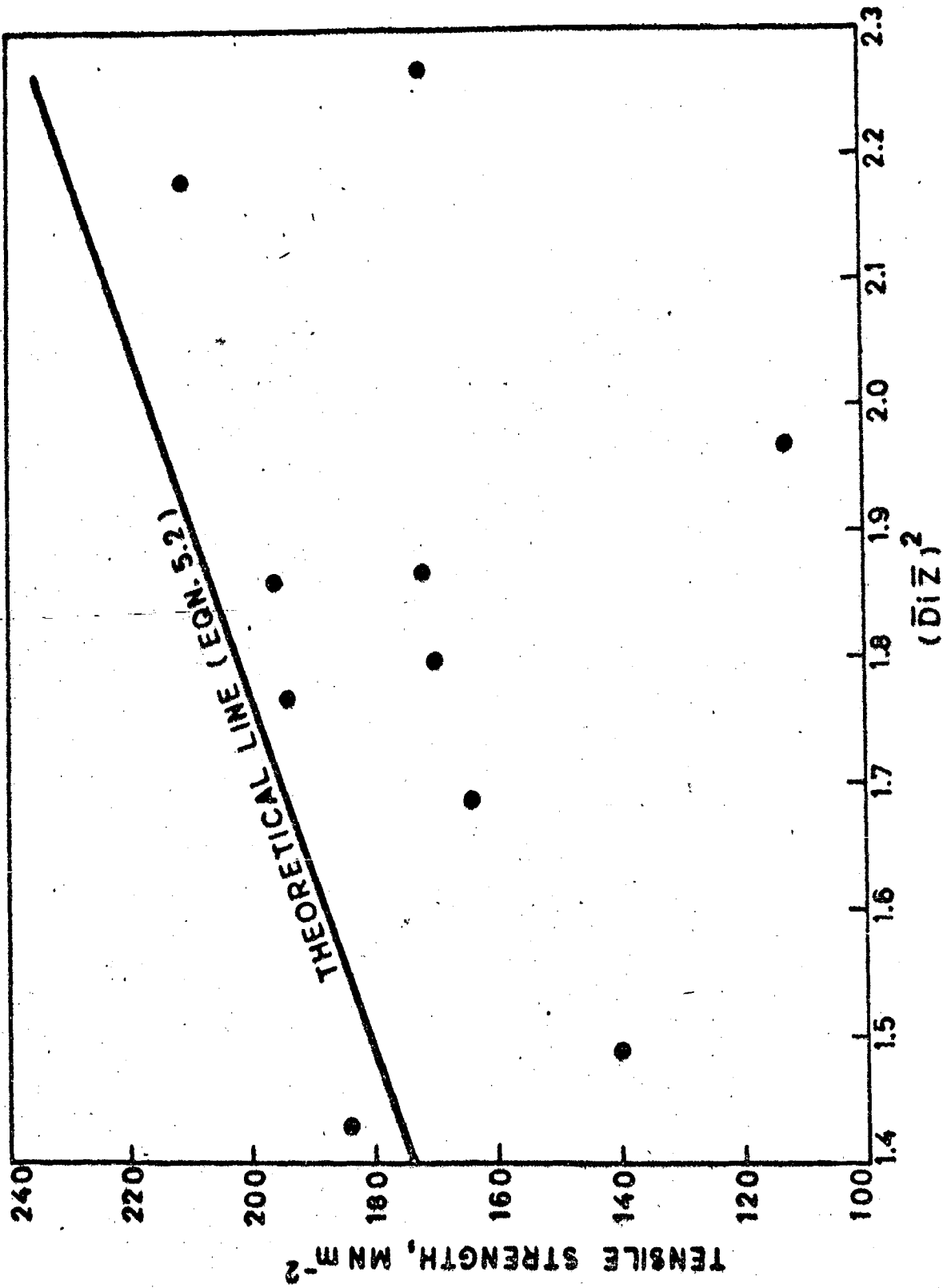


FIG. 5.2 COMPARISON BETWEEN EXPERIMENTAL AND CALCULATED (ACCORDING TO EQUATION 5.2) TENSILE STRENGTH VALUES OF RHEOCAST Al-10% Cu ALLOY.

geometry. For a theoretical estimate of α , the values of n and K must be known a priori. Since in the present case values of n and K are not known, the magnitude of α cannot be evaluated directly.

In order to circumvent the difficulty in quantifying the effect of porosity, an empirical correlation has been proposed which relates the tensile strength with microstructural parameters and the porosity. The form of correlation equation has been assumed as,

$$\sigma_{uc} = A+B(\bar{D}_i \bar{Z})^2 - C(\% P) \quad \dots (5.4)$$

where A, B and C are constants. The first two terms in the right hand side of equation 5.4 has been selected to take into account the effect of microstructure according to equation 5.1. Since a linear dependence of strength on porosity has been predicted theoretically (equation 5.3), the last term in equation 5.4 has been included to impart a linear and negative contribution of porosity to the strength.

Since in the rheocasting process only α -particles vary with the processing condition, the contribution of eutectic may be assumed to be constant equal to $\sigma_{um} V_m$, i.e. 75 MNm^{-2} . The correlation equation 5.4 may then be rewritten as,

$$\sigma_{uc} = 75+B(\bar{D}_i \bar{Z})^2 - C(\% P) \quad \dots (5.5)$$

From the least square fit of the experimental data in equation 5.5, the coefficients B and C have been evaluated as 67.97 and 4.71 respectively. Thus, the proposed correlation equation may be finally written as,

$$\sigma_{uc} = 75 + 67.97(\bar{D}_1 \bar{Z})^2 - 4.71(\%P) \quad \dots (5.6)$$

A comparison of equations 5.2 and 5.6 reveals that the microstructural contribution to the strength as predicted theoretically by equation 5.2 is closely in agreement with the contribution obtained from the analysis of experimental data (equation 5.6). Equation 5.6 may then be used to evaluate the tensile strengths of rheocastings with varying microstructure and porosity. For various rheocastings the strength values calculated according to equation 5.6 have been compared with experimental values in Fig. 5.3. It is observed that the agreement between the calculated and experimental values is generally good within $\pm 10\%$ deviation.

In table 5.1 the tensile strength of conventional casting has also been given for a comparison with rheocasting. The porosity level in the conventional casting is 6.3%. For making an assessment as to how the strength of conventional casting compares with those of rheocastings due to microstructural modifications brought about by rheocasting process, the strength values of rheocastings have been calculated using equation 5.6 for a porosity level of 6.3% and have been plotted in Fig. 5.4 against the particle parameter $(\bar{D}_1 \bar{Z})^2$. The

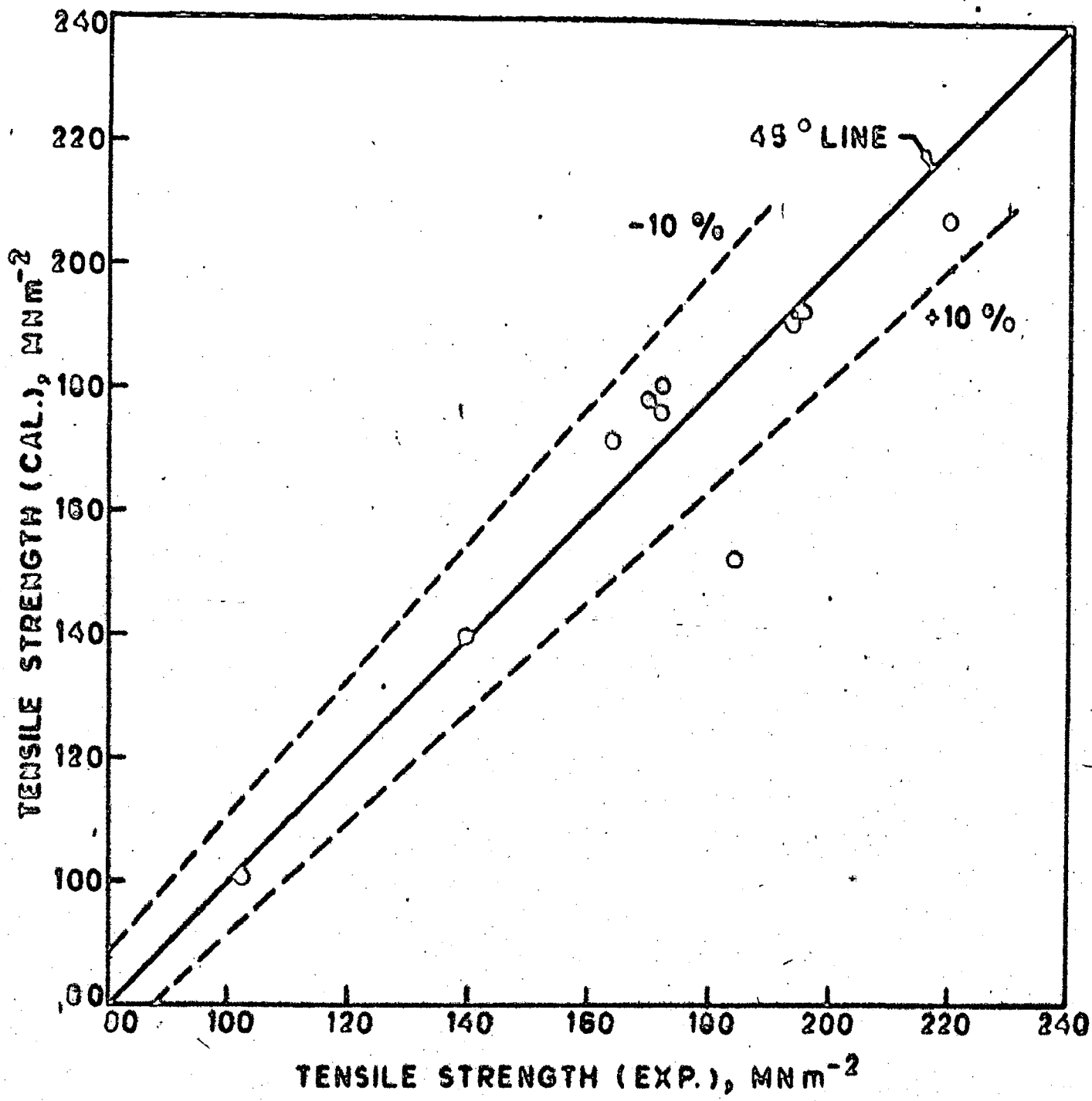


FIG. 5.3 COMPARISON BETWEEN EXPERIMENTAL AND CALCULATED (ACCORDING TO EQUATION 5.6) TENSILE STRENGTH VALUES OF RHEOCAST Al-10% Cu ALLOY.

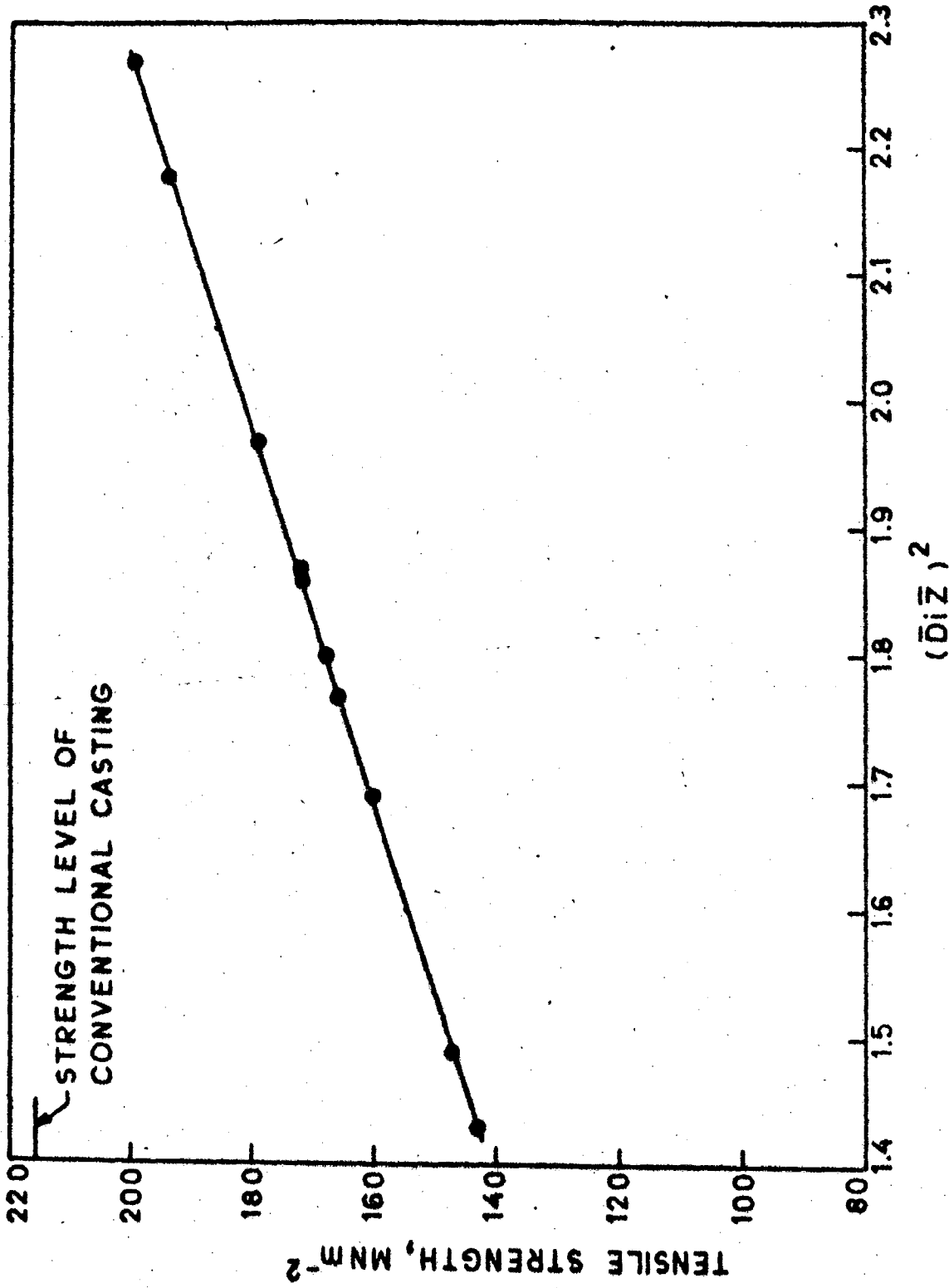


FIG. 5.4 VARIATION OF TENSILE STRENGTH WITH $(\bar{D}z)^2$ IN RHEOCAST Al-10% Cu ALLOY AT 6.3% POROSITY LEVEL.

strength level of conventional casting has also been indicated in this figure. It is observed that for the $\bar{D}_1 \bar{Z}$ values obtained in the present investigation, all the rheocastings have lower strength than the conventional casting at equivalent porosity level. Figure 5.4 also shows that at higher $\bar{D}_1 \bar{Z}$ values, the rheocastings approach the strength level of conventional casting. It follows therefore that in order to maximise the strength of rheocastings, the process variables should be so selected that the $\bar{D}_1 \bar{Z}$ is maximum.

In section 4.2, results pertaining to the variation of \bar{D}_1 (or \bar{D}) with process parameters have been presented. However, the relationship between $\bar{D}_1 \bar{Z}$ and process parameters is not precisely known. Intuitively, it is felt that $\bar{D}_1 \bar{Z}$ might be dependent upon the size distribution and therefore, a plot between $\bar{D}_1 \bar{Z}$ and $\dot{\sigma} / \bar{D}$ has been made in Fig. 5.5. It is observed that $\bar{D}_1 \bar{Z}$ increases with increase in $\dot{\sigma} / \bar{D}$. It follows then that in order to maximise $\bar{D}_1 \bar{Z}$, $\dot{\sigma} / \bar{D}$ should be maximised. In Section 4.2, it has been shown that $\dot{\sigma} / \bar{D}$ is not significantly affected by the stirring speed, but it increases with increase in pouring temperature. Thus, higher the pouring temperature, higher is the $\bar{D}_1 \bar{Z}$ value and consequently higher is the tensile strength. This observation is significant in that it suggests that for the processing condition where the effect of primary solidification is minimum and maximum opportunity is available

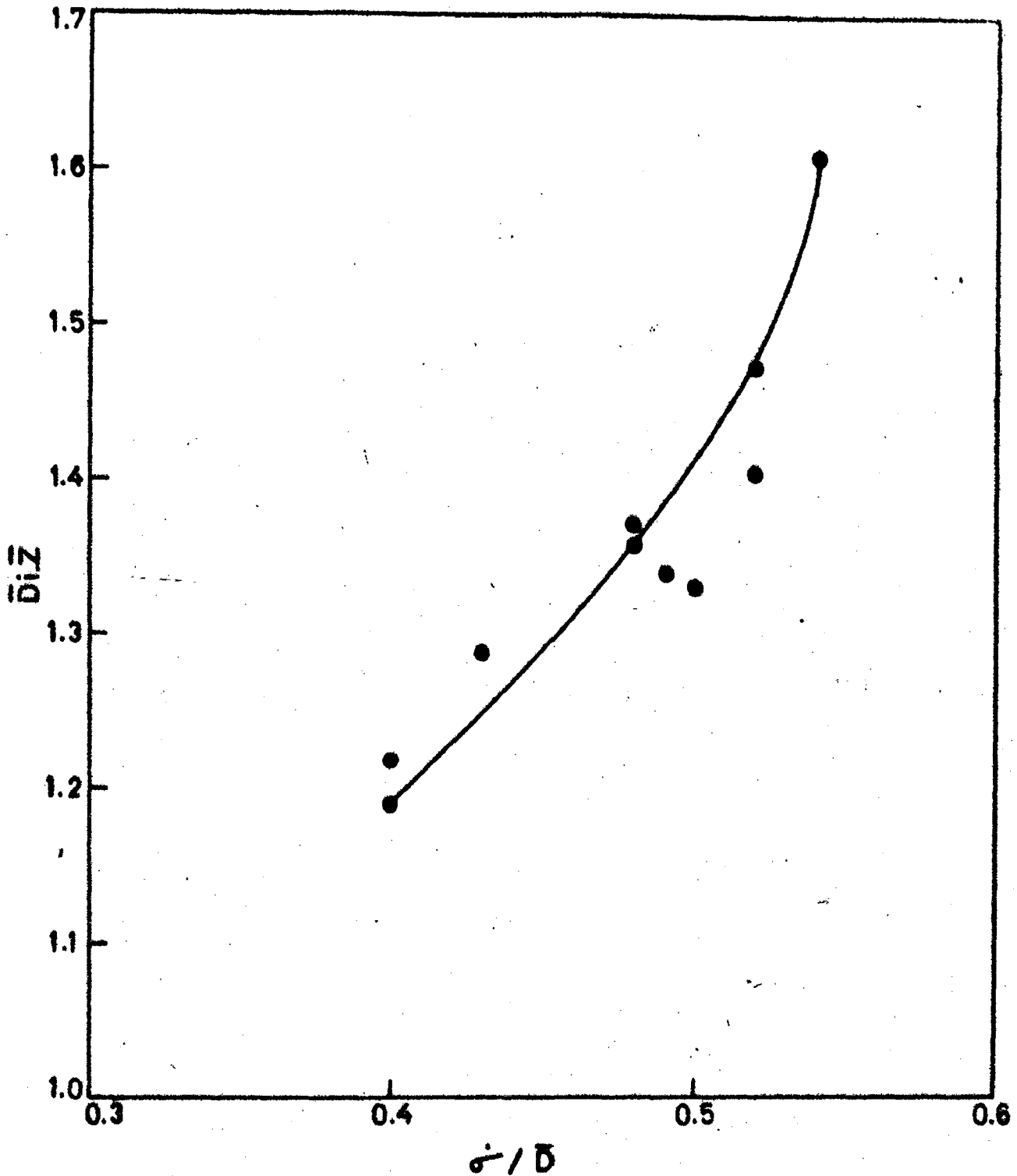


FIG. 5.5 DEPENDENCE OF \bar{D} ON COEFFICIENT OF VARIATION OF α -PARTICLE SIZE (σ/\bar{D}).

for dendritic solidification in the mould, the strength is maximum. Such a processing condition approaches the condition of conventional casting. It may, therefore, be inferred that tensile strength higher than that of conventional casting cannot be obtained through the microstructural modifications brought about the rheocasting process when applied to cast Al-10% Cu alloy.

The published literature does not provide any information on the subject to enable comparison with the present findings. However, it is pertinent to examine the model of Evans et al(78) for the fracture toughness of brittle matrix-ductile particle composites. It has been proposed that the role of ductile particles is to restrain the crack propagation through the brittle matrix. The mechanism by which such a restraint is affected is believed to be compressive stresses which ligaments of unbroken particles joining the crack faces exert to restrain the displacement of crack faces. It has been suggested that for the above mechanism to be operative, particles of cylindrical morphology should be used instead of spheroidal particles. When spheroidal particles are employed, the crack in the matrix simply bypasses the particles and no crack-particle interaction results. It appears therefore that the low strengths of rheocastings containing spheroidal particles is related to the inability of α -particles to restrain crack propagation through the eutectic matrix.

5.3 MECHANICAL PROPERTIES OF Al-6% Cu Al-4.5% Cu ALLOYS

Tensile strength and percent elongation of various castings of Al-6% Cu and Al-4.5% Cu alloy have been presented in tables 5.2 and 5.3 respectively. In contrast to the Al-10% Cu alloy, significant permanent elongation has been observed in the present case. Figures 5.6 and 5.7 show the typical tensile load extension curves for Al-6% Cu and Al-4.5% Cu alloys. These curves show significant plastic deformation associated with serrations in the flow curves. From tables 5.2 and 5.3 it is apparent that no direct correlation exists between the tensile strength and the processing condition.

The measured volume fractions of α -particles in Al-6% Cu and Al-4.5% Cu alloys are 82% and 86% respectively. These volume fractions are greater than the critical volume fraction at which the particles touch each other. Thus, in these alloys α -particles are expected to be continuous. The strength, σ_{uc} , of such a type of composite material has been given theoretically by equation 2.29, which may be rewritten as,

$$\sigma_{uc} = \sigma_{u\alpha} [V_{\alpha} + K' V_c] \quad \dots (5.6)$$

where $\sigma_{u\alpha}$ is the tensile strength of α -phase, V_{α} and V_c are volume fractions of α -phase and eutectic respectively and K' is a factor which determines the extent to which the

Table 5.2- Effect of processing condition on mechanical properties of Al-6% Cu alloy

S.No.	Stirring speed r.p.m.	Pouring Temperature K	Porosity %	Tensile Strength MNm ⁻²	% Elonga- tion
1.	700	905	3.6	151	3.1
2.	700	898	3.3	175	3.8
3.	700	890	4.3	163	3.9
4.	700	886	9.4	136	3.8
5.	1000	903	4.1	156	3.5
6.	1000	898	4.1	154	3.9
7.	1000	895	3.0	180	4.6
8.	1000	890	4.5	152	3.4
9.	1000	886	2.7	186	5.4
10.	Conventional casting		3.5	173	5.0

Table 5.3- Effect of processing condition on mechanical properties of Al-4.5% Cu alloy

S.No.	Stirring Speed r.p.m.	Pouring Temperature K	Porosity %	Tensile Strength MNm ⁻²	% Elongation
1.	500	922	2.3	156	5.9
2.	500	916	4.9	161	4.9
3.	500	914	6.0	123	9.3
4.	500	911	6.8	126	9.5
5.	700	922	1.2	170	5.7
6.	700	919	4.8	132	7.2
7.	700	916	5.9	116	10.6
8.	700	914	4.5	147	8.1
9.	700	911	7.1	138	5.0
10.	1000	922	5.5	130	4.3
11.	1000	919	7.8	126	4.6
12.	1000	916	1.3	162	5.9
13.	1000	914	1.4	165	5.7
14.	1000	911	4.1	140	7.1
15.	1000	908	6.3	136	9.2
16.	1000	905	4.1	149	10.4
17.	1200	919	12.0	92	3.4
18.	1200	916	7.0	131	7.7
19.	1200	914	8.8	99	5.2
20.	1200	911	3.1	148	5.5
21.	1200	908	11.5	92	4.7
22.	Conventional casting		1.5	152	1.5

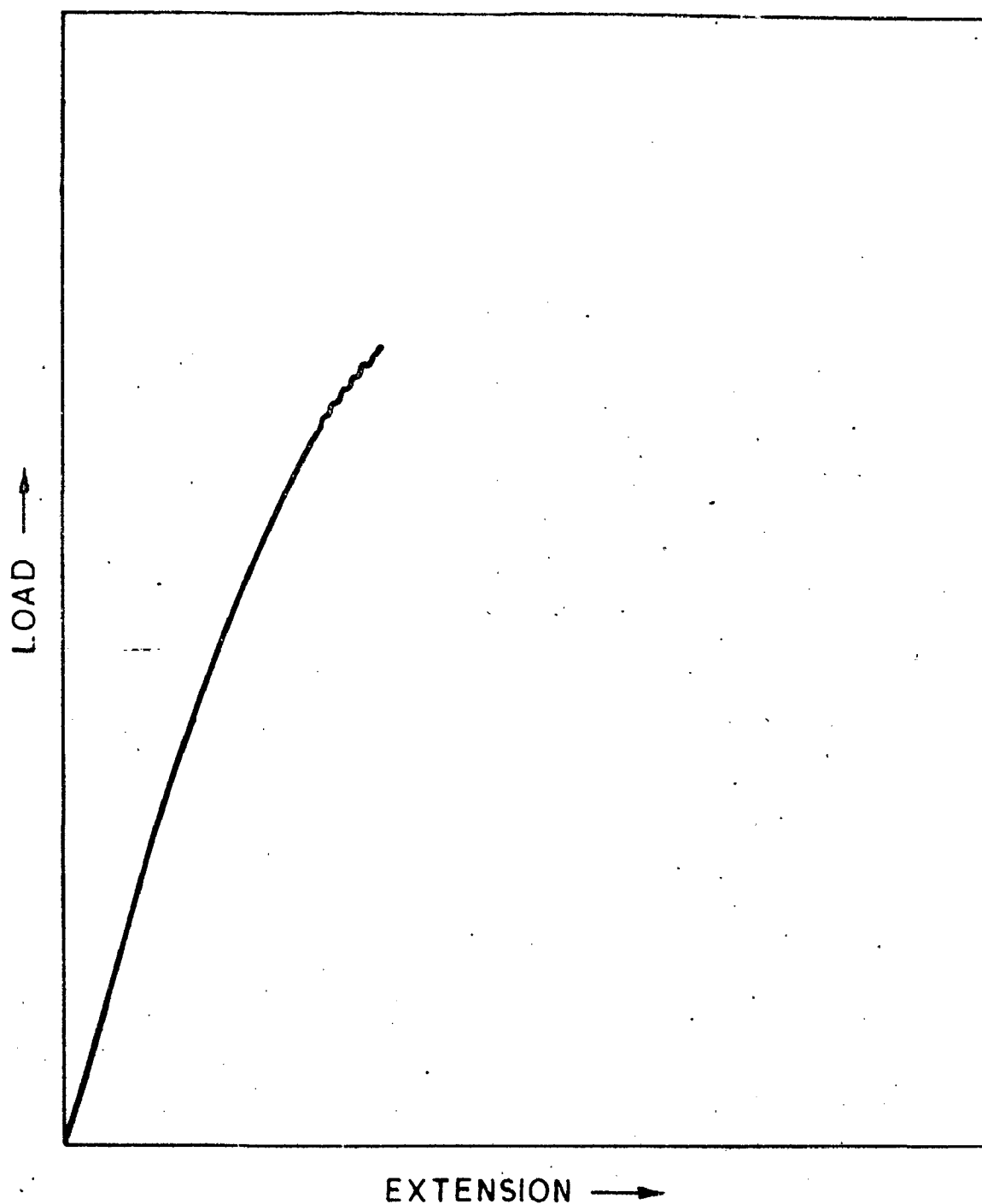


FIG. 5.6 SCHEMATIC REPRESENTATION OF TENSILE LOAD-EXTENSION CURVE FOR Al-6% Cu ALLOY.

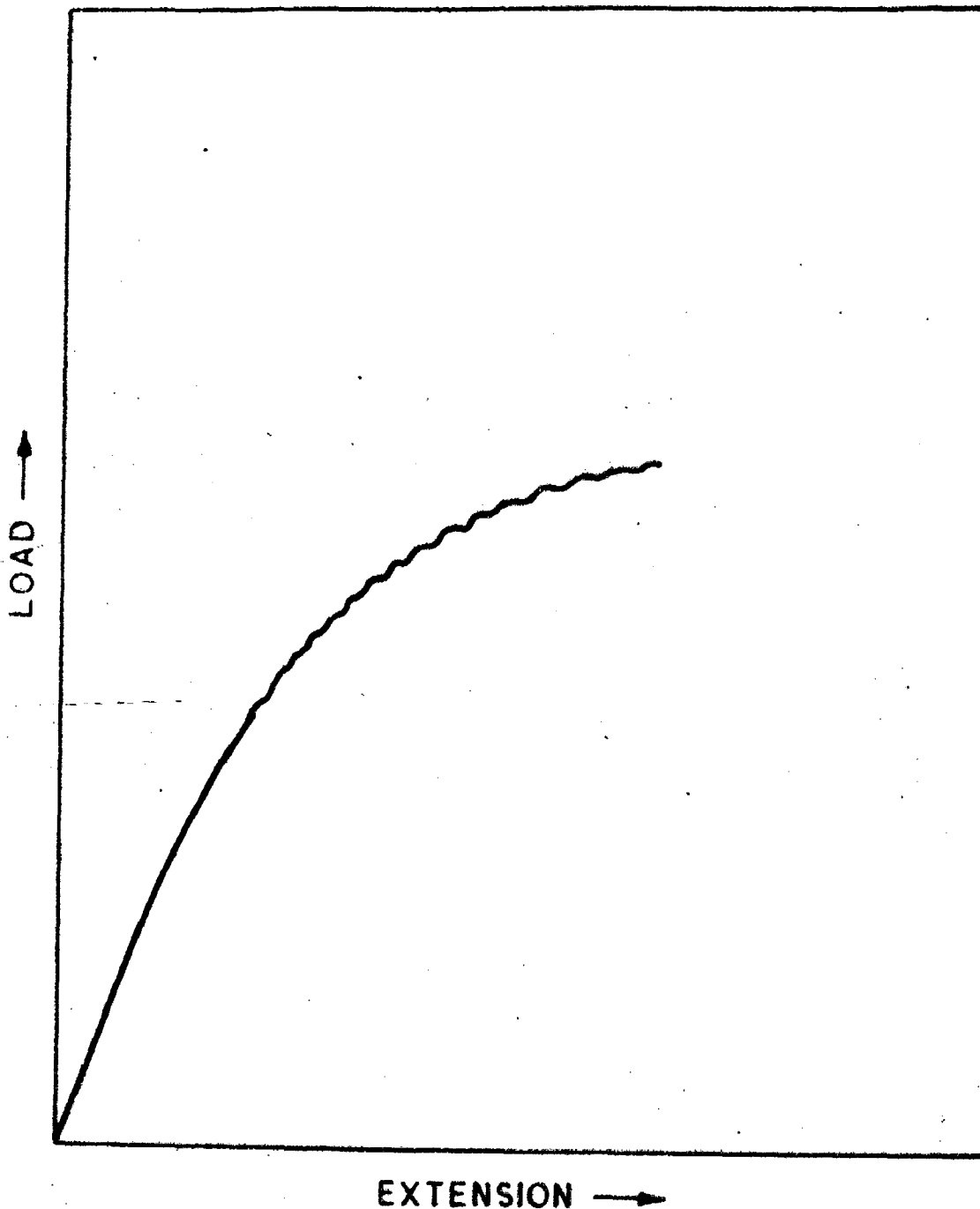


FIG. 5.7 SCHEMATIC REPRESENTATION OF TENSILE LOAD-EXTENSION CURVE FOR Al-4.5% Cu ALLOY.

stress is transferred from the α -phase to the discontinuous eutectic, and depends upon the morphology and distribution of eutectic. Generally, the morphology and distribution of eutectic formed in such alloys are not regular and therefore, it is not possible to characterise them on the basis of metallographic observations. It follows then that K' is not an experimentally determinable parameter and therefore, direct application of equation 5.6 in predicting the tensile strength is not feasible.

In order to assess as to whether the type of equation 5.6 may be used to analyse the observed experimental results the general expression for the composite stress as a function of strain (ϵ) may be written from equation 2.31 as,

$$\sigma_c(\epsilon) = A' \epsilon^{1/2} [v_\alpha + K' v_c] \quad \dots (5.7)$$

If the stress corresponding to the start of serrated flow is given by $\sigma_c(\epsilon_s)$, it may be written that,

$$\sigma_c(\epsilon_s) = A' \epsilon_s^{1/2} [v_\alpha + K' v_c] \quad \dots (5.8)$$

where ϵ_s is the strain at which the serrated flow begins, as observed in the load-extension curves. Similarly, the composite stress at fracture $\sigma_c(\epsilon_f) = \sigma_{uc}$ as a function of fracture strain (ϵ_f) is given by,

$$\sigma_c(\epsilon_f) = A' \epsilon_f^{1/2} [v_\alpha + K' v_c] \quad \dots (5.9)$$

Combining equations 5.8 and 5.9,

$$\frac{\sigma_c(\epsilon_f)}{\sigma_c(\epsilon_s)} = \left[\frac{\epsilon_f}{\epsilon_s} \right]^{1/2} \quad \dots (5.10)$$

On the basis of the experimentally observed values of ϵ_f , ϵ_s , $\sigma_c(\epsilon_f)$ and $\sigma_c(\epsilon_s)$, a plot may be made between $\frac{\sigma_c(\epsilon_f)}{\sigma_c(\epsilon_s)}$ and $\left[\frac{\epsilon_f}{\epsilon_s} \right]^{1/2}$. Such a plot for Al-6% Cu and Al-4.5% Cu alloy has been shown in Figs. 5.8 and 5.9 respectively and the experimental points are well distributed around the line with the slope of one and therefore the validity of equation 5.10 is confirmed.

In order to examine the effect of α -particle size on the tensile strength, an empirical correlation has been proposed which relates the tensile strength with mean diameter of α -particles and porosity. The form of the correlation has been assumed as,

$$\sigma_{uc} = A + B[\bar{D}]^{-1/2} - C(\% P) \quad \dots (5.11)$$

where A, B and C are constants and \bar{D} is the average particle size. The first two terms in the right hand side of equation 5.11 take into account the effect of microstructure. This form of contribution of microstructure showing dependence of strength on the inverse square root of particle size is similar to the well known Hall-Petch relation which is commonly used to relate

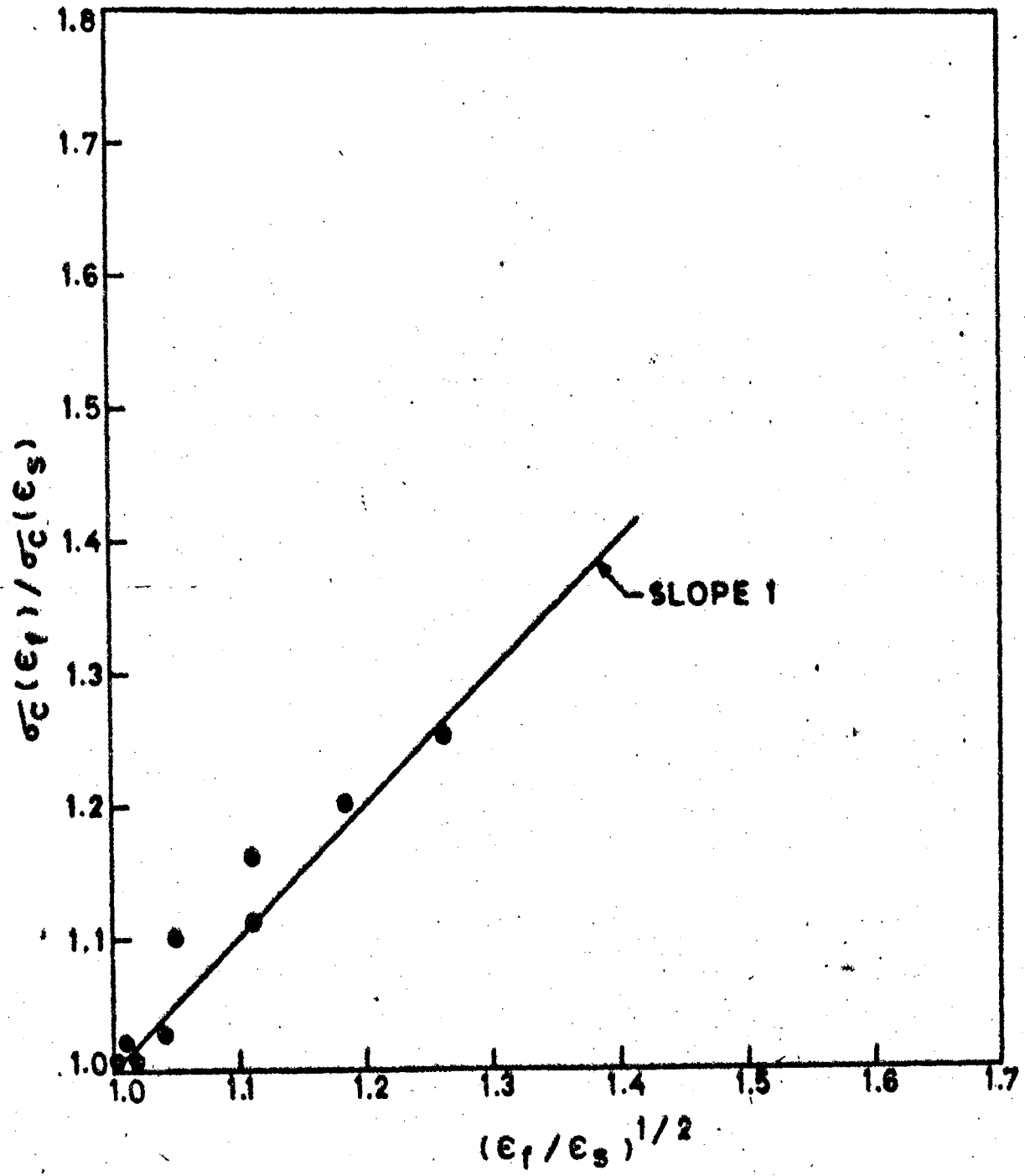


FIG. 5.8 RELATIONSHIP BETWEEN $\sigma_c(\epsilon_f) / \sigma_c(\epsilon_s)$ AND $(\epsilon_f / \epsilon_s)^{1/2}$ ACCORDING TO EQUATION 5.10 FOR RHEOCAST Al-6% Cu ALLOY.

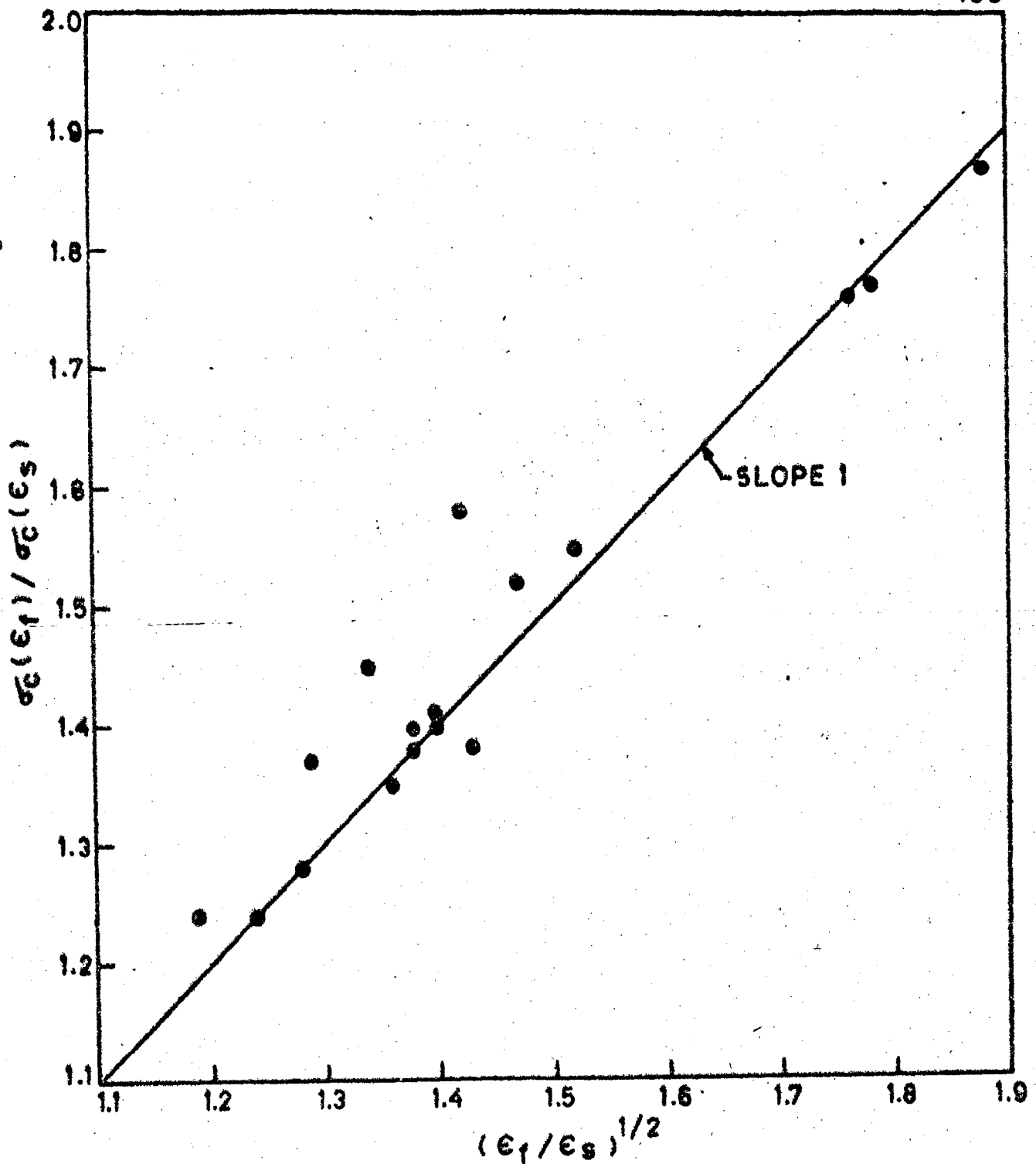


FIG. 5.9 RELATIONSHIP BETWEEN $\sigma_c(\epsilon_f) / \sigma_c(\epsilon_s)$ AND $(\epsilon_f / \epsilon_s)^{1/2}$ ACCORDING TO EQUATION 5.10 FOR RHEOCAST Al-4.5% Cu ALLOY.

the tensile flow stress with the grain size. In most metals and alloys this type of relationship has extensively been used to describe empirically the dependence of fracture strength or tensile strength on particle size (64,77). The third term in the right hand side of equation 5.11 takes into account the effect of porosity and has the similar form as used in equation 5.4 for the Al-10% Cu alloy.

From the least square fit of the experimental data in equation 5.11, the coefficients A,B and C have been evaluated for the Al-6% Cu and Al-4.5% Cu alloys from which the final correlation equations have been found out respectively as,

$$\sigma_{uc}(\text{Al-6\% Cu}) = 194.8 + 42[\bar{D}]^{-1/2} - 7.08(\%P) \dots (5.12)$$

$$\sigma_{uc}(\text{Al-4.5\% Cu}) = 159.3 + 81[\bar{D}]^{-1/2} - 6.15(\%P) \dots (5.13)$$

For various rheocastings the strength values calculated according to equations 5.12 and 5.13 have been compared with the experimental values in Figs.5.10 and 5.11 for Al-6% Cu and Al-4.5% Cu alloys respectively. It is observed that the agreement between the calculated and experimental strength values is generally good within $\pm 10\%$ deviation. In Figs.5.10 and 5.11, the strength values of rheocastings containing duplex structure has also been shown which have been calculated on the basis of both large

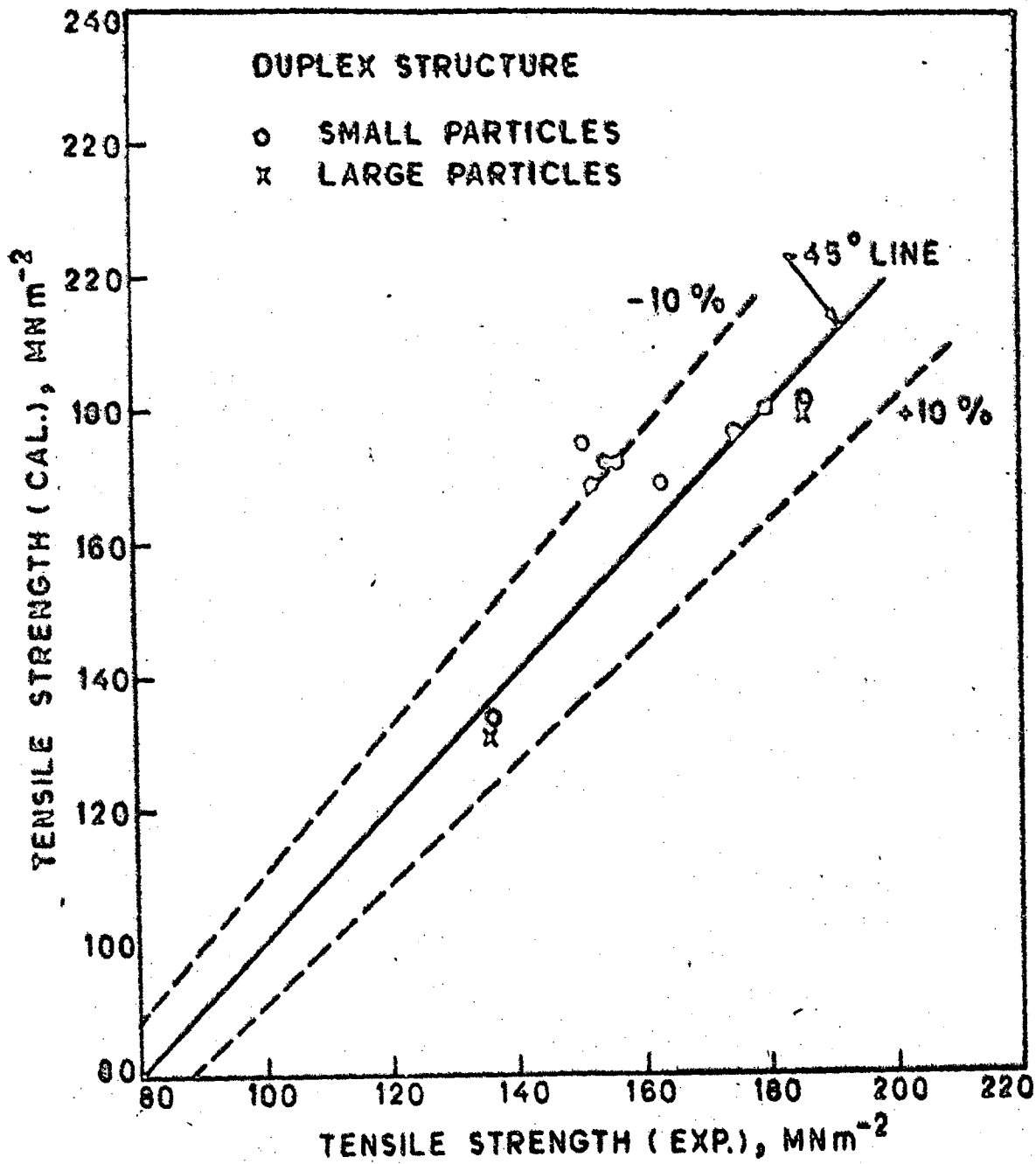


FIG. 5.10 COMPARISON BETWEEN EXPERIMENTAL AND CALCULATED (ACCORDING TO EQUATION 5.12) TENSILE STRENGTH VALUES OF RHEOCAST Al-6% Cu ALLOY.

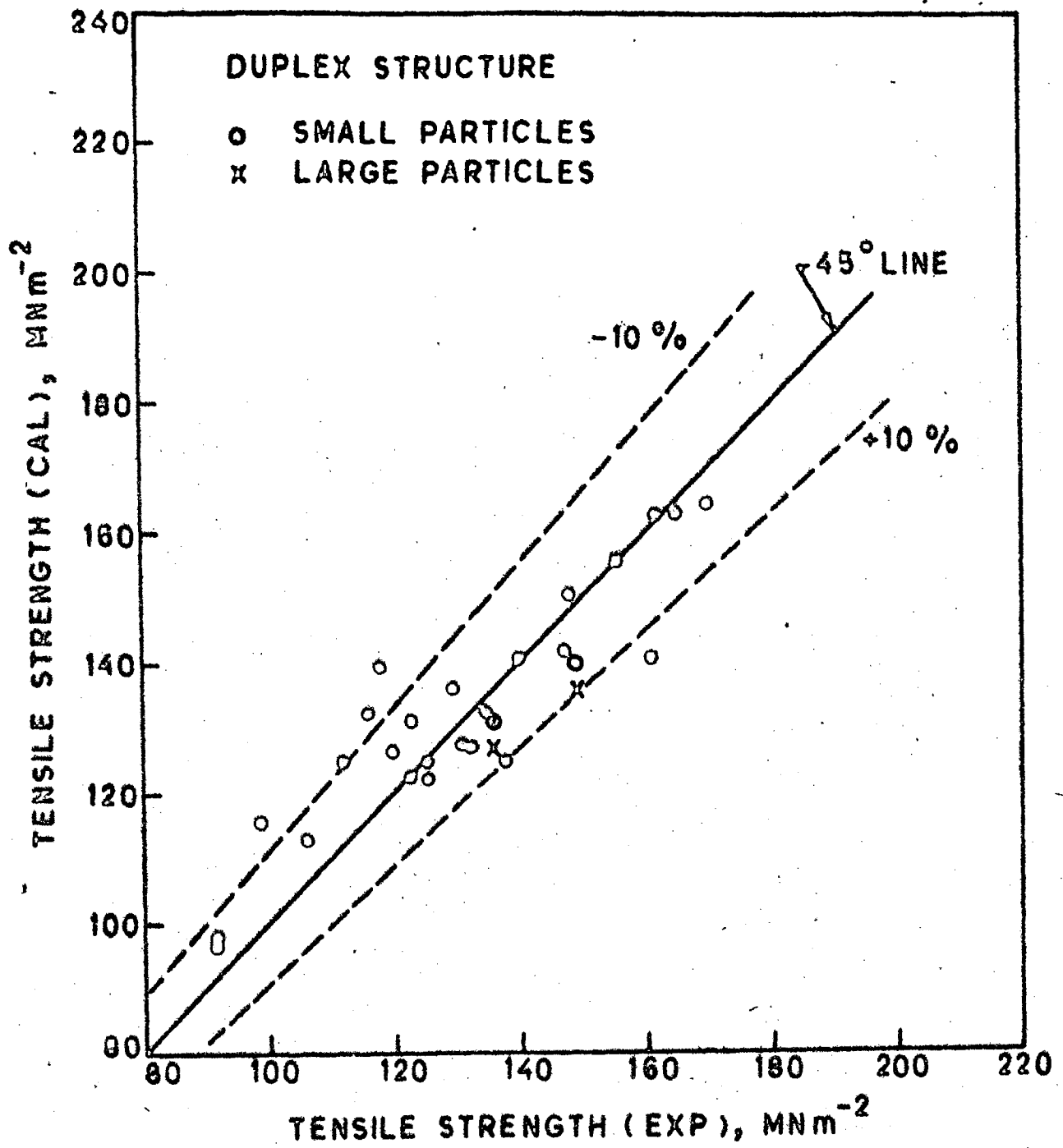


FIG.5.11 COMPARISON BETWEEN EXPERIMENTAL AND CALCULATED (ACCORDING TO EQUATION 5.13) TENSILE STRENGTH VALUES OF RHEOCAST Al-4.5% Cu ALLOY.

primary particles and small particles. It is observed that such a microstructure has no pronounced effect on the strength.

In tables 5.2 and 5.3 the tensile strength of conventional casting has also been given for comparison with rheocastings. The porosity level in the conventional casting of Al-6% Cu alloy is 3.5% and for the Al-4.5% Cu alloy it is 1.5%. For making an assessment as to how the strength of conventional casting compares with those of rheocastings due to microstructural modifications brought about by rheocasting process the strength values of rheocastings due to microstructural modifications brought about by rheocasting process the strength values of rheocastings have been calculated using equations 5.12 and 5.13 for porosity levels of 3.5% and 1.5% for the Al-6% Cu and Al-4.5% Cu alloys respectively, and have been plotted against $[\bar{D}]^{-1/2}$ in Figs. 5.12 and 5.13. The strength levels of conventional casting have also been indicated in these figures. It is apparent from these figures that the α -particle size does not have any pronounced effect on the strength. Though the strength of rheocastings is slightly higher than that of conventional casting the difference is negligibly small. However, these curves do suggest that if the process parameters are so selected that very fine α -particle size is obtained, some improvement in strength may be possible. In order to achieve this objective, from the results presented

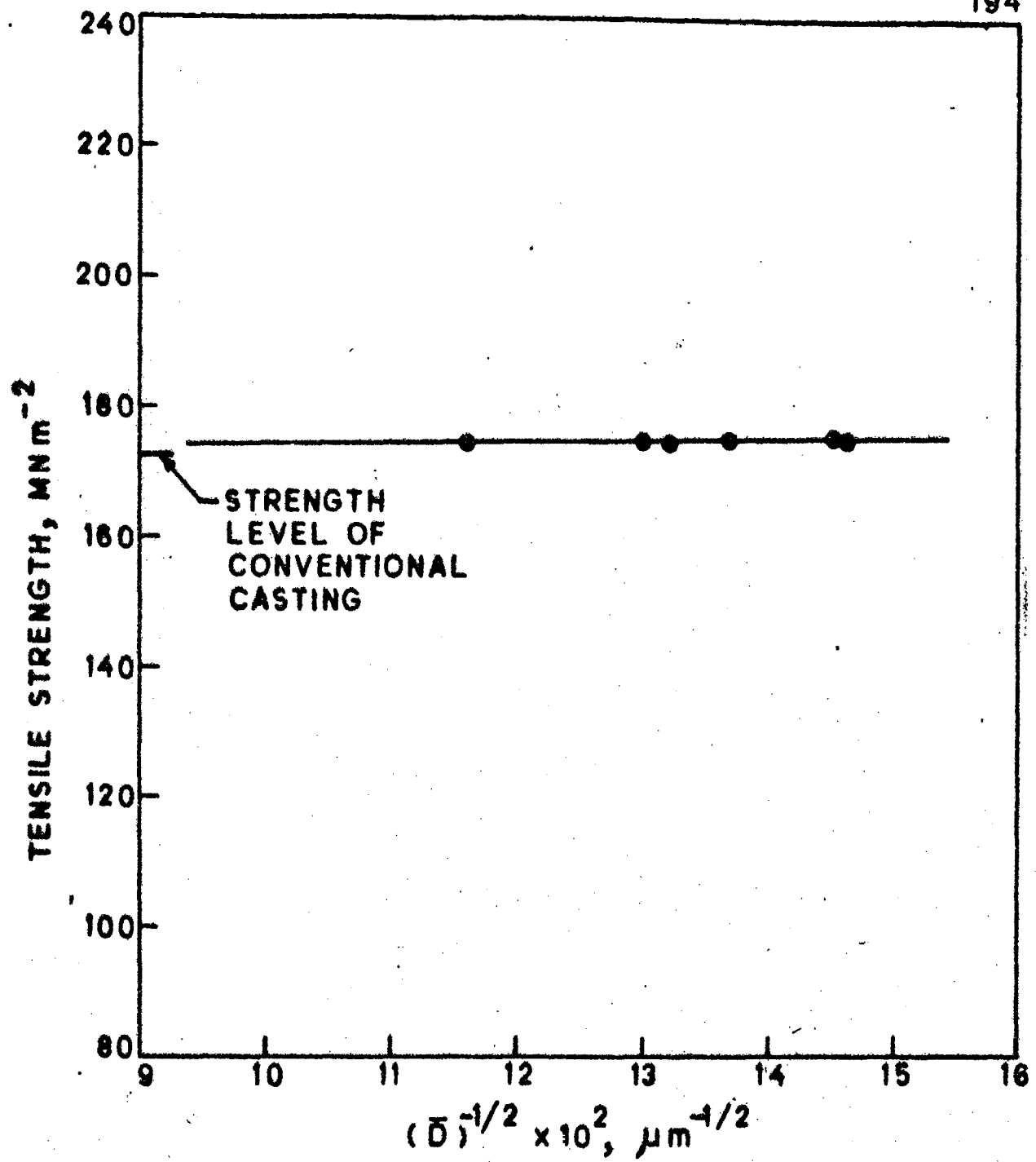


FIG. 5.12 VARIATION OF TENSILE STRENGTH WITH α -PARTICLE SIZE IN RHEOCAST Al-6%Cu ALLOY AT 3.5% POROSITY LEVEL.

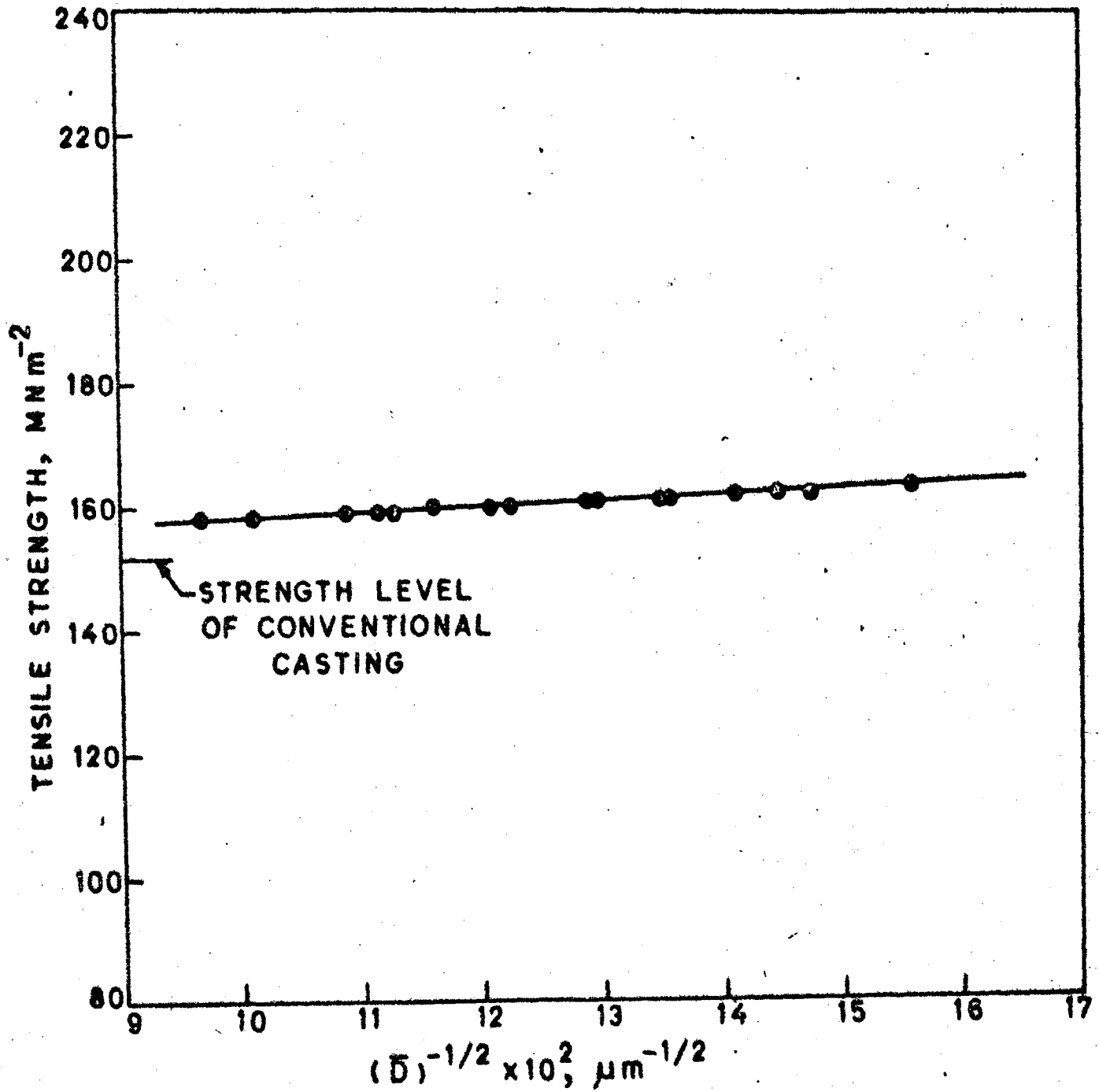


FIG. 5.13 VARIATION OF TENSILE STRENGTH WITH α -PARTICLE SIZE IN RHEOCAST Al-4.5%Cu ALLOY AT 1.5% POROSITY LEVEL.

in Sections 4.3 and 4.4, high stirring speed and high pouring temperature might be considered as appropriate processing condition. However, Fig. 4.42 shows that the rate of decrease of α -particle size decreases as the stirring speed is increased and if the pouring temperature is high, the effect of stirring speed is insignificant. Thus, it appears that considerable refinement of α -particle size is unlikely to be achieved by rheocasting process and therefore, a significant improvement in the strength through the microstructural modification, brought about by the rheocasting process is a remote possibility.

5.4 FRACTURE BEHAVIOUR

The fracture behaviour of various castings has been studied by Scanning Electron Microscopy (SEM). Figures 5.14 to 5.17 show the morphology of proeutectic α -phase as revealed by SEM examination of tensile fractured surfaces at the shrinkage porosity in the specimen. From the comparison of these fractographs it is apparent that α -particles in case of Al-10% Cu alloy do not form a continuous phase (Fig. 5.14), whereas in case of Al-6% Cu and Al-4.5% Cu alloys, α -particles join each other to form a continuous phase (Figs. 5.15 and 5.16). The joined α -particles in Figs. 5.15 and 5.16 form a chain and exhibit a morphology having a close resemblance with that of a dendrite. In

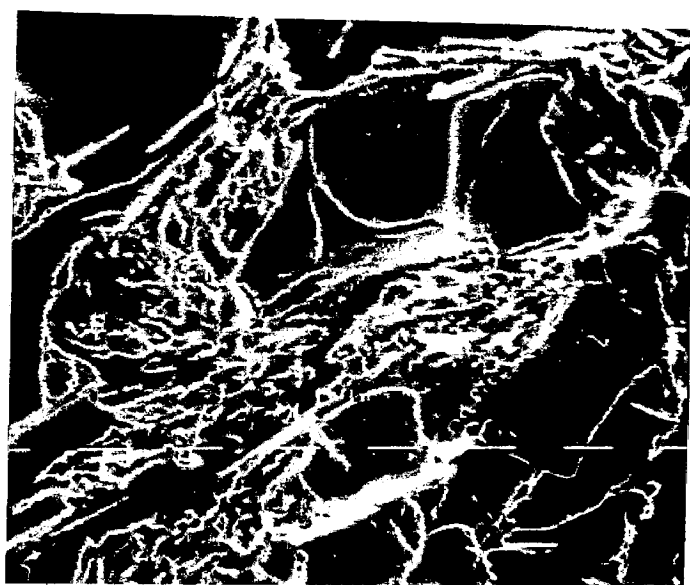


FIG. 5.14 SEM FRACTOGRAPH OF RHEOCAST Al-10%
Cu ALLOY SHOWING DISCONTINUOUS α -
PHASE. Mag. X 832



FIG. 5.15 SEM FRACTOGRAPH OF RHEOCAST Al-6% Cu ALLOY SHOWING JOINED AND CONTINUOUS α -PHASE PARTICLES. Mag. X448

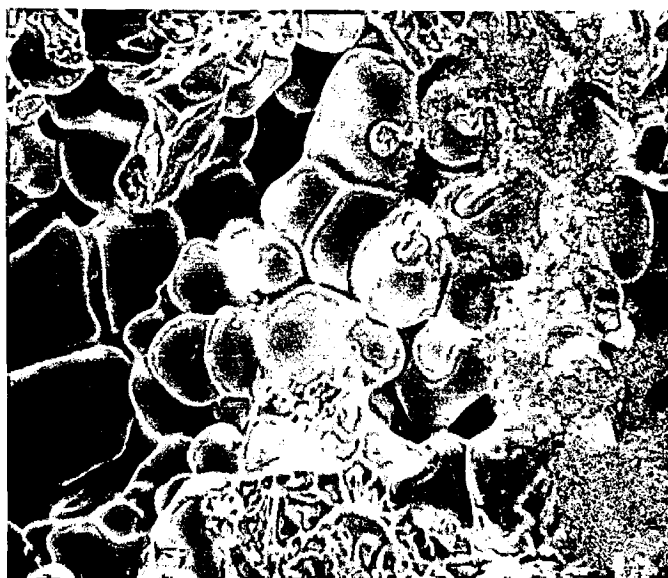


FIG. 5.16 SEM FRACTOGRAPH OF RHEOCAST Al-4.5 %
Cu ALLOY SHOWING JOINED AND CONTI-
NUOUS α -PHASE PARTICLES. Mag. X 352



FIG. 5.17 SEM FRACTOGRAPH OF CONVENTIONALLY
CAST Al-4.5% Cu ALLOY SHOWING DEN-
DRITIC MORPHOLOGY OF α -PHASE.
Mag. X 640

Fig.5.17, a typical dendrite of α -phase as observed in conventionally cast specimen has been shown. A comparison of Figs.5.15 and 5.16 with Fig.5.17 suggests that the characteristic directionality of dendritic morphology and the distinct primary and secondary branches are not present in Figs.5.15 and 5.16, and therefore, the α -phase in Figs.5.15 and 5.16 is not dendritic but has formed by joining of α -particles forming a continuous phase. These observations lend support to the theoretical predictions presented in Section 2.1 that the α -phase is a discontinuous phase in Al-10% Cu alloy and is a continuous phase in Al-6% Cu and Al-4.5% Cu alloys.

Fig.5.18 depicts the features in a selected region of the fractured surface of the rheocast Al-10% Cu alloy. It is observed that the fracture has occurred mostly along α -CuAl₂ interface in the eutectic matrix by cleavage mode (marked C in the fractograph). In certain places the fracture has propagated from below the CuAl₂ plate to above it and thus retaining a part of CuAl₂ marked D. Wherever the fracture path has moved through the α -phase, the fracture has taken place by nucleation of microvoids and their coalescence (marked R in the fractograph). The fracture of α -phase by microvoid nucleation and coalescence has not been observed in abundance and Fig.5.18 is representative of a selected region of the fractured surface where the α -phase has been found to fracture.

A close examination of areas where CuAl₂ plates are

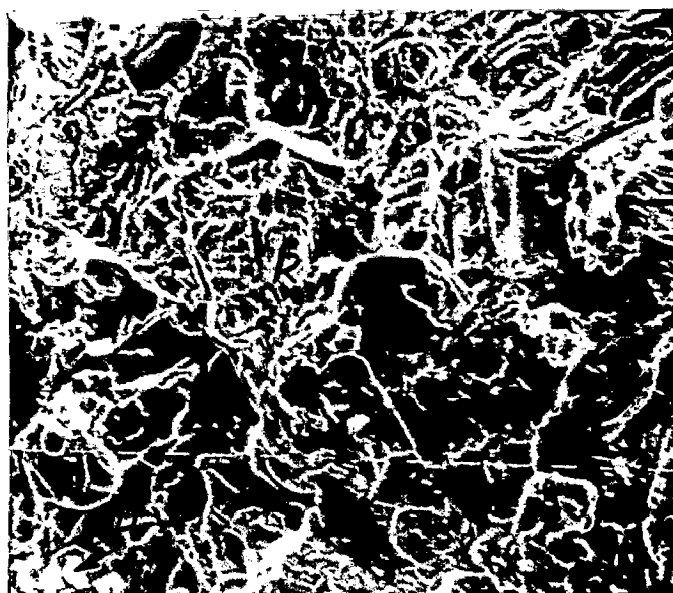


FIG. 5.18 SEM FRACTOGRAPH OF RHEOCAST Al-10 %
Cu ALLOY SHOWING CLEAVAGE OF EUTEC-
TIC AND RUPTURE OF α -PHASE.

Mag. X 416

perpendicular to the fractured surface shows extensive secondary cracking of the α -CuAl₂ interface in the eutectic, Fig. 5.19. Similar mode of cracking of the eutectic along α -Cu Al₂ interface has also been reported earlier (79). Figure 5.20 represents the general appearance of the fractured surface in which large number of dimples are observed. These dimples do not appear to have formed as a result of extensive plastic deformation since the Al-10%Cu alloy has been found to fail in a brittle manner (Section 5.2). The most probable origin of such dimples appears to be decohesion and pull-out of α -particles as observed in case of short fibres in fibre-reinforced composites. Further examination of an area inside a dimple reveals that α -phase of the eutectic has also been scooped out alongwith primary α -particles leaving behind only the CuAl₂ (Fig. 5.21). Since the eutectic α is mechanically trapped between CuAl₂ phase, small cracks in CuAl₂ have appeared during the pull-out. Such a situation has been found to be at places where the α -phase of the eutectic has grown over the primary α -particles during secondary solidification. The extent of growth of α -phase of the eutectic on primary α -particles has probably prevented the pull-out of all the α -particles and in such cases the crack has propagated through the α -particles, as indicated by R in Fig. 5.18. Figures 5.20 and 5.21 therefore provide an evidence that the α -particles have generally been pulled out and consequently dimples have formed.



FIG. 5.19 SEM FRACTOGRAPH OF RHEOCAST Al-10 %
Cu ALLOY SHOWING SECONDARY CRACKING
IN EUTECTIC ALONG α -CuAl₂ INTERFACE.
Mag. X1875

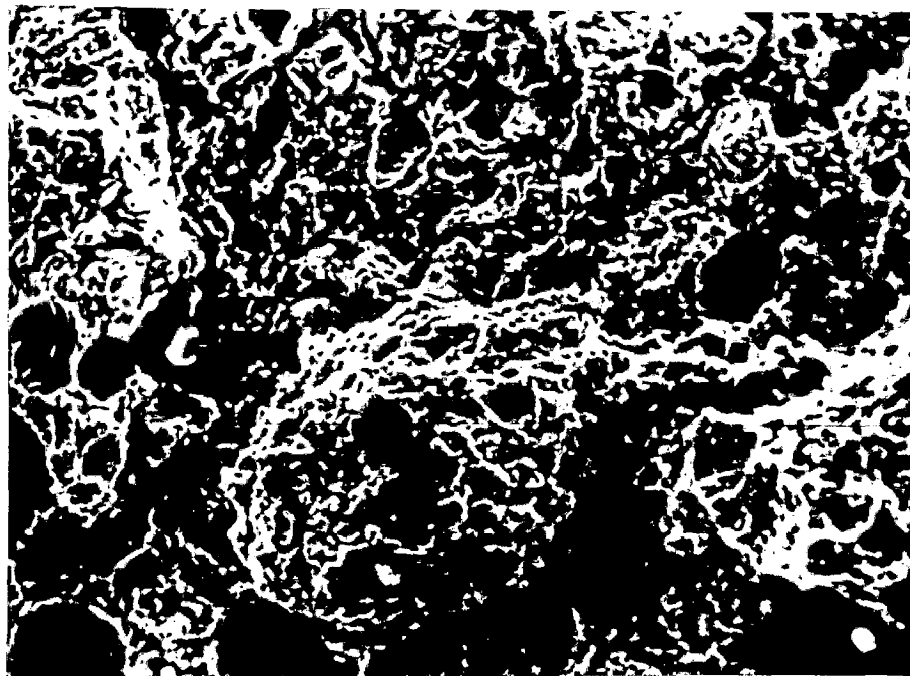


FIG. 5.20 SEM FRACTOGRAPH OF RHEOCAST Al-10 %
Cu ALLOY SHOWING DIMPLES FORMED BY
PULL-OUT OF α -PARTICLES. Mag. X104

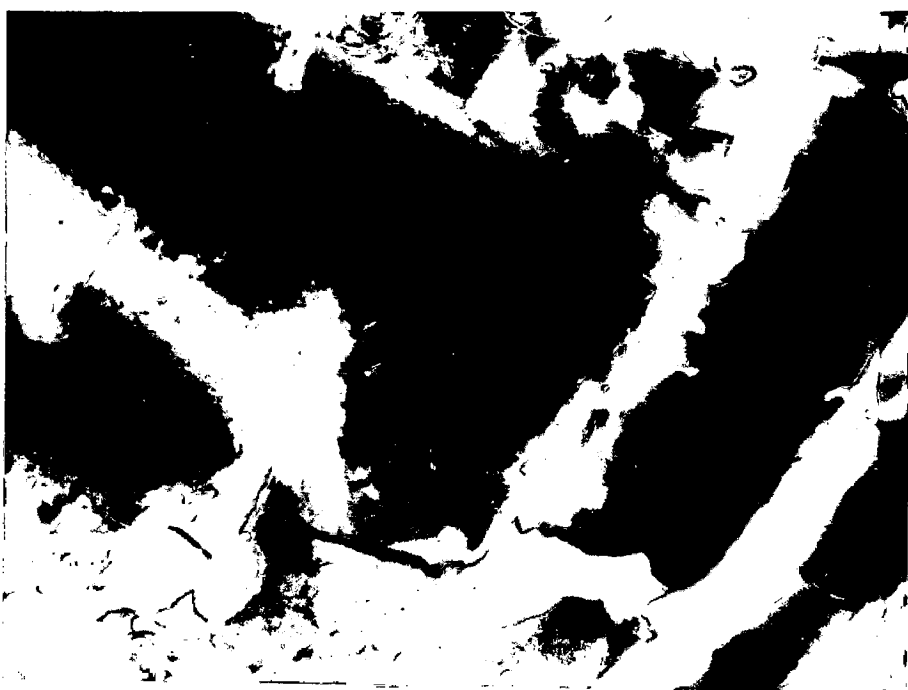


FIG. 5.21 SEM FRACTOGRAPH OF RHEOCAST Al-10 %
Cu ALLOY SHOWING CRACKS IN CuAl_2 DUE
TO PULL-OUT OF α -PHASE OF EUTECTIC.
Mag. X1875

The above observations lead to the conclusion that the fracture in case of Al-10% Cu alloy has occurred primarily by cleavage along α -CuAl₂ interface of the eutectic and pull-out of α -phase. It is known (80) that the pull-out of particles is favoured if the particles are spherical in shape. It follows therefore, that the pro-eutectic α -phase has not been effective in restraining the fracture process. It is obvious from the foregoing that the morphological modifications of α -phase brought about by the rheocasting process will favour pull-out of the α -phase and therefore, strength higher than that of conventional casting exhibiting dendritic morphology is unlikely to be achieved. This conclusion based on the fractographic observations is in agreement with the experimental results presented in Section 5.2.

The fracture mode in case of lower copper alloys, Al-6% Cu and Al-4.5% Cu, has been found to be different from the one observed in case of Al-10% Cu alloy. The general appearance of the fractured surface presented in Figs. 5.22 and 5.23 consists of rupture of α -phase by microvoid nucleation and coalescence (marked R), and cleavage of the eutectic (marked C). Figure 5.23 for the Al-4.5% Cu alloy depicts additional feature of ledge like cleavage facets (marked L) which has been observed only in the selected regions of the fractured surface.



FIG. 5.22 SEM FRACTOGRAPH OF RHEOCAST Al-6 %
Cu ALLOY SHOWING CLEAVAGE OF EUTEC-
TIC AND RUPTURE OF α -PHASE.
Mag. X352

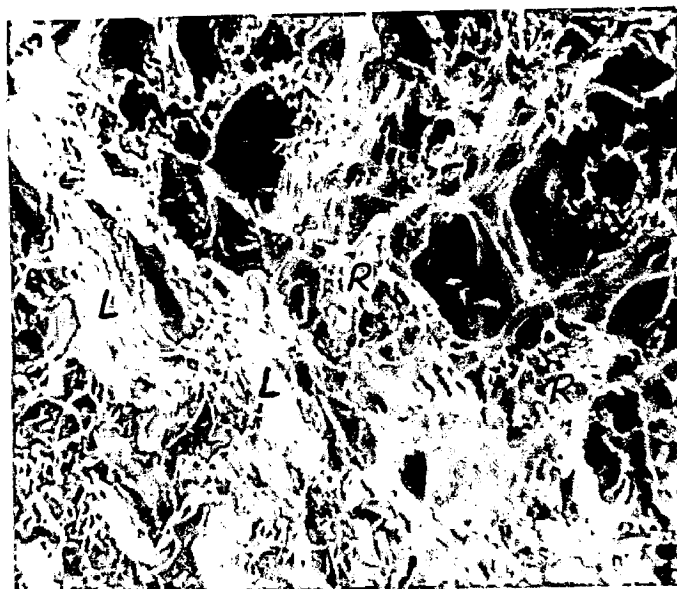


FIG. 5.23 SEM FRACTOGRAPH OF RHEOCAST Al-4.5%
Cu ALLOY SHOWING CLEAVAGE OF EUTEC-
TIC AND RUPTURE OF α -PHASE.
Mag. X352

A close examination of areas where the CuAl_2 is perpendicular to the fractured surface, Fig. 5.24 and 5.25, reveals that the secondary cracks in the eutectic have not followed the preferential path of $\alpha\text{-CuAl}_2$ interface as in the case of Al-10% Cu alloy because of extensive plastic strain at lower stress levels in these alloys which has caused crack propagation mostly through the α -phase by microvoid nucleation and coalescence. The existing stress level in such cases is not sufficient to cause secondary cracking along $\alpha\text{-CuAl}_2$ interface. The fracture of the α -phase has been observed to occur at the neck formed by joining of particles (shown by arrows in Fig. 5.26).

The above observations suggest that in case of lower copper alloys, Al-6% Cu and Al-4.5% Cu, the fracture has taken place both by cleavage of eutectic area and fracture of the proeutectic α -phase. The experimental results presented in Section 5.3 show significant plastic deformation in these alloys and appear to be associated with the deformation and fracture of α -phase as evident from fractographic observations.

On the basis of results of the fractographic study presented in the preceding paragraphs, it may be concluded that as the copper content in the alloys is lowered from 10% to 4.5%, the fracture process becomes dominated by the rupture of α -phase by microvoid nucleation and coalescence. While mostly cleavage of eutectic and a limited



FIG. 5.24 SEM FRACTOGRAPH OF RHEOCAST Al-6%
Cu ALLOY SHOWING NO PREFERENTIAL
SECONDARY CRACKING OF EUTECTIC
ALONG α -CuAl₂ INTERFACE. Mag. X2375



FIG. 5.25 SEM FRACTOGRAPH OF RHEOCAST Al-4.5% Cu ALLOY SHOWING NO PREFERENTIAL SECONDARY CRACKING OF EUTECTIC ALONG α -CuAl₂ INTERFACE. Mag. X2500



FIG. 5.26 SEM FRACTOGRAPH OF RHEOCAST Al-4.5 %
Cu ALLOY SHOWING FRACTURE OF α -
PARTICLES AT THE NECK FORMED BY
JOINING OF PARTICLES. Mag. X700

extent of rupture of α -phase have been observed in case of Al-10% Cu alloy, only a limited extent of eutectic cleavage and a large extent of rupture of α -phase have been observed in case of the lower copper alloys. It is apparent therefore that in case of the 10% Cu alloy the strength is governed primarily by the fracture of the eutectic whereas the fracture of α -phase governs the strength in lower copper alloys. This conclusion shows that the assumptions made in the development of theoretical models on the basis of composite theories (Section 2.1) that the strength is eutectic controlled in case of Al-10% Cu alloy and α -phase controlled in case of Al-6% Cu and Al-4.5% Cu alloys, are confirmed by the fractographic observations.

CHAPTER VI

CONCLUSIONS

1. The characteristic dendritic morphology of proeutectic α -phase obtainable in conventional casting is significantly modified and transformed into non-dendritic spheroidal particles by rheocasting process.
2. Lower copper content, lower pouring temperature and lower stirring speed provide favourable condition for coalescence of α -particles and sintering, leading to the formation of some abnormally large primary particles in the rheocast microstructure.
3. The variation of α -particle size with processing condition depends upon alloy composition. The average α -particle size increases, remains unaltered and decreases with increasing pouring temperature for Al-10% Cu, Al-6% Cu and Al-4.5% Cu alloys respectively. Stirring speed has not been found to have any significant effect in case Al-10% Cu alloy. In case of Al-6% Cu and Al-4.5% Cu alloys, particle size decreases with increasing speed. The distribution of α -particle size varies similarly with process parameters as the average α -particle size.

4. The amount of α -phase is a critical factor which determines the mechanism by which the strength of rheocast Al-Cu alloys is governed. For α -phase less than 78.5% (in Al-10% Cu alloy), the strength is primarily determined by the eutectic and for α -phase greater than 78.5% (in Al-6% Cu and Al-4.5% Cu alloys), the contribution α -phase to the strength is dominating.

5. Rheocast Al-10% Cu alloy has lower strength than the conventionally cast alloy at equivalent porosity level. The strength of rheocastings depends upon a particle parameter $\bar{D}_i \bar{Z}$ which varies with processing condition. To maximise $\bar{D}_i \bar{Z}$ and so the strength, the appropriate processing condition approaches to that of conventional casting and therefore, rheocastings with higher strength than conventional casting cannot be produced through microstructural modification by rheocasting process.

6. Strength of rheocast Al-6% Cu and Al-4.5% Cu alloys is of the same order of magnitude as the strength of conventional casting at equivalent porosity level. α -particles join each other to form a continuous chain and the strength is primarily contributed by the α -phase and therefore, these castings show appreciable elongation. No significant effect of α -particle size or morphology on strength has been observed.

7. Fracture behaviour is strongly influenced by copper content in the alloys. As the copper content is lowered, the

extent of rupture of α -phase by microvoid nucleation and coalescence is increased.

8. In Al-10% Cu alloy, where the strength is primarily determined by the eutectic, brittle fracture has been observed. The fracture is mostly due to cleavage of eutectic and pull-out of α -particles.

9. In Al-6% Cu and Al-4.5% Cu alloys, where the strength is primarily α -phase controlled, ductile fracture has been observed. The fracture is mostly due to fracture of α -phase by microvoid nucleation and coalescence, and cleavage of eutectic. The fracture of α -phase occurs preferentially at the neck formed by joining of α -particles.

10. Fractographic observations confirm that any significant improvement in the strength of cast Al-Cu alloys in the composition range of 4.5 to 10% Cu is not likely through microstructural modifications by rheocasting process.

REFERENCES

1. D.B.Spencer, R.Mehrabian and M.C.Flemings, Rheological Behaviour of Sn-15% Pb in the Crystalline Range, Met. Trans., Vol.3, p.1925,(1972).
2. P.A.Joly and R.Mehrabian, 'The rheology of a partially solid alloy', Jl. of Materials Science, Vol.11,p.1393(1972).
3. R.Mehrabian and M.C.Flemings, New Trends in Materials Processing, ASM, Metals Park USA p.98(1976).
4. K.P. Young, Extending Die Life, Proc.Workshop on Rheocasting, Army Materials and Mechanics Research Centre, U.S.A., p.79,(1978).
5. F.J.Kievits and K.V.Prabhakar, Rheocasting (Stir-Casting) of Aluminium Alloys, Proc. Symposium on Quality Control of Engineering Alloys and the Role of Metal Science, Delft. p.203,(1978).
6. U.Feurer, U.Schraner and H.Zoller, Stranggiessen teilerst-arter Aluminiumlegierungen, Aluminium, Vol.52,p.659,(1976).
7. R.Mehrabian and M.C.Flemings, Die Casting of Partially Solidified Alloys, Trans. AFS, Vol.80, p.173,(1972).
8. E.F.Fascetta, R.G.Riek, R.Mehrabian and M. C.Flemings, Die-Casting Partially Solidified High Copper Content Alloys, AFS Cast Metals Research Journal, p.167, (1973).
9. A.Celso and R.Gomez, Diverse Rheocasting Techniques for Grain Refinement of Al and Al-alloys, Proc. Conf. Primer Congreso Nacional de Metalurgia, Universidad Tecnica del Estado, Santiago, Chile, p.228-238,(1980).
10. A.C.F. de Arruda and R.G.dos Santos, Pouring through a Multiple-Flow device: A new Rheocasting Technique, Proc. Conf.Materials Processing and Performance, ASME, New York, p.167-170,(1980).
11. S.S.Zatulovskii and Yu. Ya. Skok, Suspension Casting: a way of Increasing Casting Quality, Liteinoe Proizvod, Vol.5, p.20-21, (1979)

12. J.M.Oblak and W.H.Rand, Structure and Properties of the Rheocast Ferrous Alloy 440C, Met.Trans., Vol.7B, p.705-709, (1976).
13. A Vogel, Turbulent Flow and Solidification: Stir-Cast Microstructure, Metal Science, Vol.12, p.576-578, (1978).
14. N.Apaydin, K.V.Prabhakar and R.D.Doherty, Special Grain Boundaries in Rheocast Al-Mg., Materials Science and Engg. Vol.46, p.145-150, (1980).
15. R.Mehrabian and M.C.Flemings, Casting Semi-Solid Aluminium Alloys, Aluminium, Vol.51, p.710-715, (1975).
16. A.Vogel, R.D.Doherty and B.Cantor, Stir-cast Microstructure and Slow Crack Growth, Proc. Conf. Solidification and Casting of Metals, Sheffield, p.518-525, (1979).
17. R.Ichikawa and K.Miwa, Apparent Viscosity and Structure in Partially Solidified Hyper-Eutectic Al-Mn Alloy under Stirring, Jl. of Japan Institute of Metals, Vol.45, No.2, p.189, (1981).
18. K.Miwa and R.Ichikawa, Apparent Viscosity and Structure in Al-Si Alloys Partially Solidified under Stirring, Jl. of Japan Institute of Metals, Vol.45, No.8, p.853, (1981).
19. A.Sawy, N.E.Mahallawy and M.Taha, Effect of some Processing Variables on the Structure and Properties of Al-4.5% Cu Alloy formed by Stir Casting, Proc. 7th International Light Metals Congress, Vienna, p.58, (1981).
20. G.W.Swartzbeck and T.Z.Kattamis, Fatigue Behaviour of Aluminium-Copper Alloy Exhibiting a Duplex Dendritic Structure, Met.Trans., Vol.4, p.2667-2669, (1973).
21. P.A.Parkhutik and V.S.Ocheretyanyi, Die Casting of Solid-Liquid Aluminium Alloys, Liteinoe Proizvod, Vol.5, p.24-25 (1976).
22. N.Apaydin, Effect of Stirring on the Bulk Solidification of Hypoeutectic and Eutectic Al-Si Alloys, Jl. of Materials Science Letters, Vol.1, p.39-43, (1982).
23. G.H.West and B.Seymour, Casting with Metal Slurries, Production Engg. (London), Vol.58, p.31-33, (1979).
24. Die Casting Semi-Solid Metals, Machinery (London), Vol.125, p.146-150, (1974).

25. I.I.Prokhorov, L.I.Romanov and S.N.Krasotskaya, The Structure and Properties of Aluminium Alloys Cast in the Molten Solid State, *Liteinoe Proizvod*, Vol.8, p.10-11, (1979).
26. R.Ichikawa and J.Suzuki, Castability of a Pasty Semi-solid Al-alloy into a shell mould, *Jl. of Japan Foundrymen's Society*, Vol.52, p.475, (1980).
27. R.Ichikawa and K.Miwa, Apparent Viscosity and Structure in Partially Solidified Al-Cu Alloys, *Jl. of Japan Inst. Metals*, Vol.42, p.1023, (1978).
28. J.M.Oblak and W.H. Rand, Solid-Liquid Phase Characterization of Several Rheocast High Performance Alloys, *Met. Trans.*, Vol.7B, p.699-703, (1976).
29. M.C.Flemings, J.F.Boylan and R.L.Bye, Thixocasting Steel Parts, *Metals Abstract*, 51-0406, (April 1980).
30. David Van Cleave, Semi Solid Metal Slurries Make Sounder Castings, *Iron Age Metalwork. Int.*, Vol. 18, p.34-35, (1977).
31. M.C.Flemings, K.P. Young and R.G.Riek, Thixocasting of Steel, *Engineering Index*, 083133, (1978).
32. R.Mehrabian, D.G.Backman, T.V.Murty, S.Hong and C.Levi, Casting of Partially Solid Metals and Metal Non-metal Composites, *Engineering Index*, 018511, (1978).
33. T.Z.Kattamis, Casting of Semi-Solid Metals, *Proc.Symposium on Quality Control of Engg. Alloys and the Role of Metals Science*, Delft, p.189-201, (1978).
34. K.P.Young, R.G.Riek and M.C.Flemings, Structure and Properties of Thixocast Steels, *Metals Technology*, Vol.6, p.130-137, (1979).
35. Y.V.Murty, D.G.Backman and R.Mehrabian, Structure, Heat Treatment and Properties of Rheocast Alloys, *Proc.Workshop on Rheocasting*, Army Materials and Mechanics Research Centre, USA, p.95-107, (1978).
36. K.P.Young, Mechanical Properties of Thixocast Alloys, *Proc. Workshop on Rheocasting*, Army Materials and Mechanics Research Centre, USA, p.109-111, (1978).
37. Researchers Solving Problems in Ferrous Die Casting, *Iron Age Metalwork Int.*, Vol.15, p.31-32, (1976).

38. M.A. Taha and N.A.E. Mahallawy, Structure and Mechanical Properties of Steel produced by Rheocasting, Proc. 3rd. International Conf. on Mechanical Behaviour of Materials (ed. K.J.Miller and R.F.Smith), Pergamon Press, England, p.537, (1980).
39. E.Fascetta, R.G.Riek, R.Mehrabian and M.C.Flemings, Die Casting Partially Solidified High Copper Content Alloys, Giessereipraxis, Vol.10, p.173-179, (1975).
40. K.P.Young, J.F.Boyland, B.E. Bond, R.G.Riek, R.Z.Bye and M.C.Flemings, Thixocasting Copper-base Alloys, Die Casting Engineer, Vol.21, p.46-52,(1977).
41. R.G.Riek, A.Vrachnos, K.P.Young, N.Matsumoto and R.Mehrabian, Machine Casting of a Partially Solidified High Copper Content Alloy, A.F.S. Transactions, Vol.83, p.25-30,(1975).
42. M.C.Flemings et al, AFS Int.Cast Metals Research Journal, Vol. 1, p.11-22, (1976).
43. C.C.Law, J.D.Hostetler and L.F.Schulmeister, Microstructure-Property Relations in a Machine Thixocast Co-base Super-alloy, Materials Science and Engg., Vol.38, p.123-137,(1979).
44. A.Vogel and B.Cantor, Stability of a Spherical Particle Growing From a Stirred Melt, Jl. of Crystal Growth, Vol.37, p.309-316, (1977).
45. M.C.Flemings, Solidification Processing, McGraw-Hill Inc., (1974).
46. G.J.Davies, Solidification and Casting, Applied Science Publishers Ltd., London, (1973).
47. B.Chalmers, in Liquids: Structure, Properties, Solid Interactions, ed.T.J.Hughel, Elsevier, Amsterdam, p.308,(1965).
48. B.Vonnegut, Thermodynamics in Physical Metallurgy, ASM, Cleaveland, p.282, (1950).
49. W.A.Tiller and S.O'Hara, On the Mechanisms of Crystal Multiplication during Solidification in the presence of Fluid Motion, The Solidification of Metals, ISIP 110, p.27-36.

50. F.A.Crossley, R.D.Fisher and A.G.Metcalf, Viscous Shear as an Agent for Grain Refinement in Cast Metal, Trans.Met.Soc.AIME, Vol.221, p.419-420,(1961).
51. V.Kondic, Microstructure of Cast Metal, Acta Met.Vol.6, p.660, (1958).
52. K.A.Jackson, J.D.Hunt, D.R.Uhlmann and T.P.Seward, Trans. Met.Soc.AIME, Vol.236, p.149, (1966).
53. W.W.Mullins and R.F.Sekerka, Journal of Applied Physics, Vol.34, p.323, (1963).
54. B.Chalmers, Principles of Solidification, John Wiley and Sons, (1964).
55. B.Chalmers, Shapes and Sizes of Grains in Castings, Solidification, ASM Publication, p.295, (1971).
56. M.C.Flemings, The Principles of Rheocasting and Application to High Temperature Alloys, Proc. Workshop on Rheocasting, Army Materials and Mechanics Research Centre, U.S.A., p.33-39, (1978).
57. B.Cantor and A.Vogel, Dendritic Solidification and Fluid Flow, Jl. of Crystal Growth, Vol.41, p.109-123,(1977).
58. J.C.Vandam and F.H.Mischgofsky, Stircasting of Transparent Organic Alloys: Thixotropy and Rosette Formation, Jl. of Materials Science, Vol.17, No.4, p.989, (1982).
59. S.D.E. Ramati, G.J.Abbaschian and R.Mehrabian, The Structure of a Partially Solid Alloy, Met.Trans., Vol.9B, p.241-245, (1978).
60. A.Kelly and G.J.Davies, The Principles of the Fibre Reinforcement of Metals, Metallurgical Reviews, Vol.10, p.1-77 (1965).
61. L.J.Broutman and R.H.Krock, Modern Composite Materials, Addison-Wesley Publishing Co., (1967).
62. D.C.Drucker, Engineering and Continuum Aspects of High Strength Materials, Division of Engineering, Brown University, Tech.Report No.7, (1964).

63. A.Kelly and R.B.Nicholson, Strengthening Methods in Crystals, Elsevier, London, (1971).
64. A.Kelly, Strong Solids, Clarendon Press-Oxford, (1973).
65. J.O.Outwater and M.C.Murphy, 26th Annual Conference, Society of Plastics Industry, Paper No.11C, (1969).
66. A.S.Argon, J.Im and R.Safoglu, Cavity Formation from Inclusions in Ductile Fracture, Met.Trans., Vol. 6A p.825, (1975).
67. J.H.Schmitt and J.M.Jalinier, Damage in Sheet Metal Forming-I. Physical Behaviour, Acta Met., Vol.30, No.9, p.1789, (1982).
68. P.S.Theocaris and S.A.Paipetis, Stresses in Three Dimensional Composites with Limiting Shear Properties, in Developments in Composite Materials-1(ed. G.S.Holister), Applied Science Publishers, London, p.197(1977).
69. K.Sezawa and B.Miyazaki, Proc.Japan Soc. Mech.Engrs., Vol.31, p.625, (1928).
70. R.T.DeHoff and F.N. Rhines, Quantitative Microscopy, McGraw-Hill Book Company, p.140, (1968).
71. J.F.Bell, The Experimental Foundations of Solid Mechanics, in Handuch Der Physik, Vol.VIa/1 (Mechanics of Solids 1), Springer-Verlag, Germany, p.551, (1973).
72. D.C.Phillips, R.A.J.Sambell and D.H.Bowen, The Mechanical Properties of Carbon Fibre Reinforced Pyrex Glass, Jl. of Material Science, Vol.7, p.1454, (1972).
73. K.Radhakrishna, S.Seshan and M.R.Seshadri, Effect of Porosity on Mechanical Properties of Aluminium Alloy Castings, Trans.Ind.Inst. of Metals, Vol.34, No.2, p.169, (1981).
74. J.Topping, Errors of Observation and their Treatment, Chapman and Hall, London, (1972).
75. K.H.Chien and T.Z.Kattamis, Z.Metallkunde, Vol.61, p.475, (1970).

76. M.M.Faraq, N.E.Mahallawy and M.Taha, The Relation between the Structure and Strength of Al-Cu Eutectic Alloys, in the Microstructure and Design of Alloys, Institute of Metals and Iron and Steel Institute, London, Vol.1, p.266, (1973).
77. G.E.Dieter, Mechanical Metallurgy, McGraw-Hill, p.39, (1961).
78. A.G.Evans, A.H.Heuer and D.L.Porter, The Fracture Toughness of Ceramics, Advances in Research on Strength and Fracture of Materials (ed. D.M.R.Taplin), Vol.1, Pergamon Press, p.529, (1978).
79. A.Pattnaik and A.Lawley, A Study of Deformation and Fracture in Al-Cu Al₂ Composites by Acoustic Emission, in the Microstructure and Design of Alloys, Institute of Metals and, Iron and Steel Institute, London, Vol.1, p.250, (1973).
80. G.A. Cooper and M.R.Piggott, Cracking and Fracture in Composites, Advances in Research on Strength and Fracture of Materials (ed. D.M.R.Taplin), Vol.1, Pergamon Press, p.557 (1978).

APPENDIXCopy of papers published

1. 'Microstructure and Mechanical Properties of Rheocast Al-10 Wt.% Cu Alloy'- Z-Metallkunde, Vol.73, pp.420-425, (1982).
2. 'Microstructure of Rheocast Hypoeutectic Al-Cu Alloys'- Z-Metallkunde, Vol.73, pp.714-716, (1982).

Microstructure and Mechanical Properties of Rheocast Al-10 wt.% Cu Alloy *)

Priya R. Prasad*, Subrata Ray*, Jawahar L. Gaindhar** and Madan L. Kapoor*

(* Department of Metallurgical Engineering and ** Department of Mechanical and Industrial Engineering, University of Roorkee, Roorkee-247672, India)

The effect of the pouring temperature and the speed of the stirrer on the microstructure and mechanical properties of rheocast Al-10 wt.% Cu alloy ingots has been investigated. The morphology, size and distribution of proeutectic α -phase are significantly modified by the pouring temperature and the stirring rate. The average size of the α -particles and the non-sphericity in shape characterised by length to diameter ratio has been found to increase with higher pouring temperature. All rheocastings have been found to possess lower tensile strength than that of conventional casting. It has been explained on the basis of the observed higher porosity in certain rheocast samples and the breakdown of dendritic network of α -phase in general. SEM fractographic observations have led to the conclusion that the dendritic network of ductile α -phase obtained by conventional casting is more effective in restraining the crack propagation through the brittle eutectic matrix than the dispersed spheroidal particles obtained by rheocasting.

Gefüge und mechanische Eigenschaften von rheocastet Al-10 Masse-% Cu-Legierungen

Der Einfluß der Abgießtemperatur und der Rührgeschwindigkeit auf das Gefüge und die mechanischen Eigenschaften von durch Rheocasting (Gießen mit teilerstarter Schmelze) hergestellten Barren einer Al-10 Masse-% Cu-Legierung wurden untersucht. Morphologie, Größe und Verteilung der proeutektischen α -Phase werden durch die Abgießtemperatur und die Rührgeschwindigkeit deutlich modifiziert. Die mittlere Größe und Abweichung von der Kugelgestalt (charakteristisch durch das Verhältnis Länge/Durchmesser) steigen mit zunehmender Abgießtemperatur. Die Rheocastings besitzen eine niedrigere Zugfestigkeit als konventionelle Abgüsse, was durch die beobachtete höhere Porosität und das Zusammenbrechen des Dendritennetzwerks der α -Phase erklärt wird. REM-Fraktographie führt zu dem Schluß, daß das Dendritennetzwerk der duktilen α -Phase in konventionellen Abgüssen der Rißausbreitung in der spröden eutektischen Matrix besser widersteht als die sphärischen Teilchen, die beim Rheocasting erhalten werden.

A new metal casting process – "Rheocasting" – has been developed^{1) to 4)} in which a liquid alloy is vigorously agitated during its partial solidification to yield a slurry comprising of non-dendritic solid particles uniformly suspended in the remaining liquid. When the slurry has sufficient fluidity depending on the extent of solid formed and the speed of agitation, it can be subsequently cast into desired shapes by conventional methods, such as die casting. Because of lower pouring temperature, semi-solid state and higher viscosity of the slurry as compared to fully liquid alloy, it has been claimed that there is an improvement in casting quality and the die-life enhances through this process^{5) to 9)}.

Most of the publications relating to rheocasting deal with the characterisation of structure and properties of alloy slurries and their dependence on process variables^{10) to 14)}. However, success of rheocasting process in industry largely depends upon its ability to produce castings of improved mechanical properties. This is especially true for low melting point alloys where longer die life is not the primary requirement. Various rheocast and thixocast copper alloys, aluminium alloys, cobalt-base alloys and steels have been reported^{9) 15) 17) 18)} to possess mechanical properties comparable with or superior to those of conventional castings. However, results to the contrary for some of the above mentioned alloys have also been published^{16) 19) 20) 21)}. From these accounts it appears that the mechanical behaviour of rheocastings has neither been

clearly understood nor its dependence on the processing condition has been systematically investigated so far.

Rheocasting of hypoeutectic Al-Cu alloys permits dispersion of ductile aluminium-rich primary α -solid solution in a brittle matrix of $\alpha + \text{Cu Al}_2$ eutectic. Such duplex structures can significantly modify the mechanical properties depending upon the extent to which the ductile dispersed phase is able to arrest the propagation of crack through the brittle matrix. In the present investigation, therefore, an Al-10 wt.% Cu casting alloy has been selected in an attempt to examine the influence of rheocasting process variables on the microstructure and mechanical properties of the resulting products.

Experimental Methods

Apparatus and Procedure

The details of experimental set-up used in the present investigation is schematically shown in fig. 1. For each casting about 500 gm of Al-10 wt.% Cu alloy prepared from commercial purity aluminium was melted in the graphite crucible having a 12 mm dia hole at the bottom plugged with a graphite stopper. The furnace was then switched off and the melt was allowed to cool naturally. The melt temperature was continuously measured with a sheathed chromel-alumel thermocouple using a temperature potentiometer. When temperature came down to the liquidus, the stirrer having a four blade impeller was introduced and the melt was agitated vigorously during its primary solidification. The speed of the stirrer was measured with a stro-

*) This work forms a part of Ph. D. thesis work of P. R. Prasad.

bometer. The average cooling rate during primary solidification was 0.05 Ks^{-1} . At the desired pouring temperature, stirring was stopped, the graphite stopper removed and the slurry was cast into a $30 \times 30 \times 250 \text{ mm}$ ingot mould made of steel. The flow rate of the slurry was determined by measuring the total time taken by the slurry to pour out through the bottom hole of the crucible. In order to study the slurry structure just before casting, some samples

were sucked out from the top of the crucible with a Corning glass tube fitted with a horn-bulb, and quenched in water.

Metallography

Suitable metallographic samples were cut from each casting and then electropolished for optical microscopic studies. α -particle size and its distribution in each sample were determined by standard techniques of quantitative metallography.

Porosity and Mechanical Properties

The density for each casting was determined by usual weight loss method from which the porosity was calculated. Tensile test, hardness and impact tests were carried out to determine the mechanical properties. Tensile tests were carried out on a Hounsfield Tensometer and impact test on an Izod impact testing machine. Hardness values were measured on a Vicker-Brinell hardness testing machine using Vicker's scale with 5 kg of load. Fractured tensile and impact specimens were examined under SEM to study the mode of fracture.

Results and Discussion

Microstructure

From the optical micrographs of conventional casting and rheocastings depicted in fig. 2, it is apparent that the morphology, size and distribution of proeutectic α -phase (hereinafter called α -particles) are significantly modified

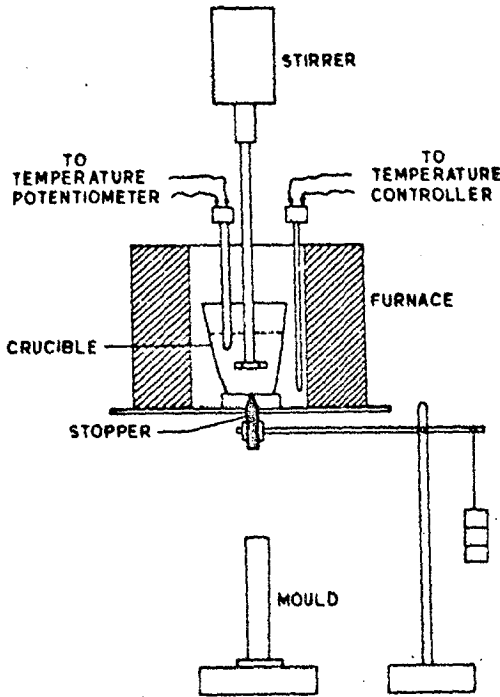


Fig. 1. Schematic of rheocasting set-up.

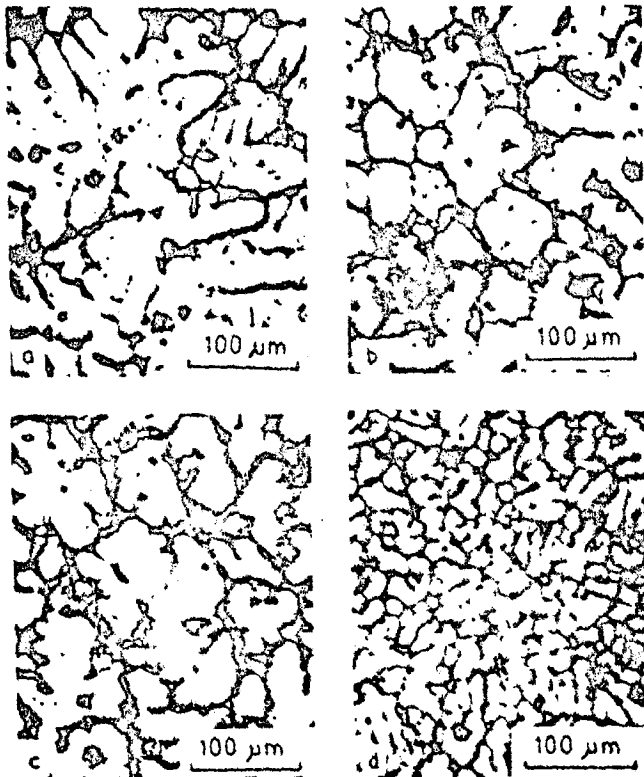


Fig. 2 a to d. Optical micrographs depicting microstructure of (a) conventional casting, (b) rheocasting at 700 rpm and 900 K, (c) rheocasting at 1000 rpm and 900 K and (d) slurry stirred at 1000 rpm and quenched in water from 900 K.

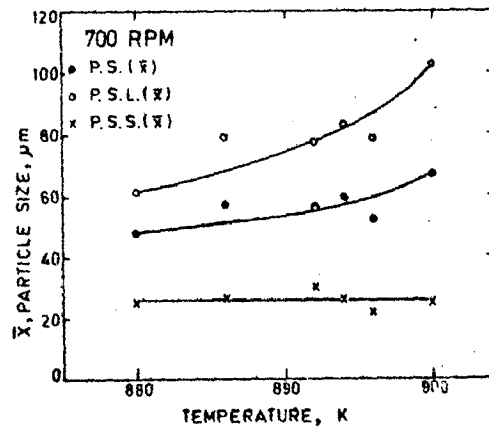


Fig. 3a. 700 rpm.

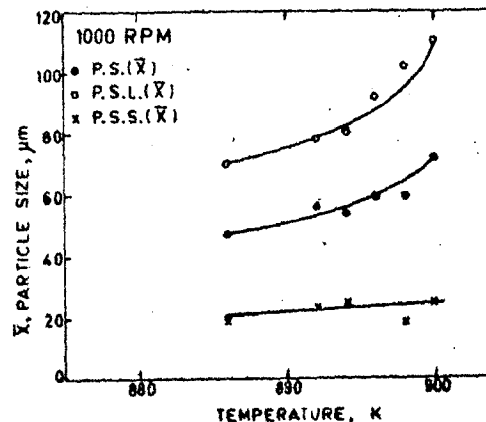


Fig. 3b. 1000 rpm.

Fig. 3a and b. Variation of α -particle size with pouring temperature for two stirring speeds.

by rheocasting process and its variables namely, the pouring temperature and the speed of agitation. The conventionally cast sample (fig. 2a) shows dendrites of α -phase whereas the rheocast samples are marked by a very small extent of dendritic solidification observed only in certain samples. In the rheocasting process followed here, the slurry has been cast in the permanent mould and so it is possible that the extent of dendritic solidification observed could have been taken place either during the formation of slurry or during the solidification in the mould or both. It has been generally observed that a higher speed of agitation enhances the extent of dendritic solidification as revealed by fig. 2b and c. A higher pouring temperature also acts in a similar fashion. In an effort to preserve the structure, the slurry has been quenched and the resulting microstructure for a sample with an agitation speed of

1000 r.p.m. is shown in fig. 2d. The tendency of dendrite formation in the slurry can be clearly identified in this microstructure. The smaller particle size of this quenched structure indicates that the slurry structure has been preserved to a large extent. This tendency of dendrite formation at a higher agitation speed can be explained in terms of higher cooling rate of the slurry in the furnace. Flemings¹³⁾ has concluded on the basis of his experimental observation that when the cooling rate exceeds a particular value

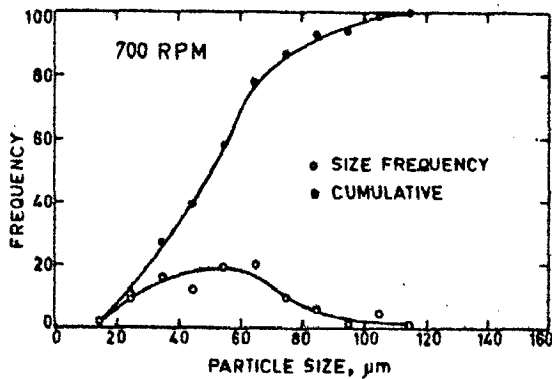


Fig. 4a. 700 rpm.

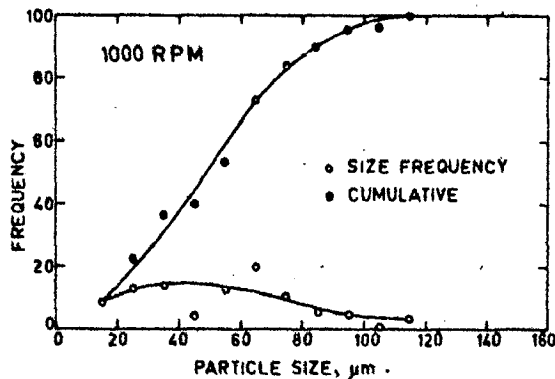


Fig. 4b. 1000 rpm.

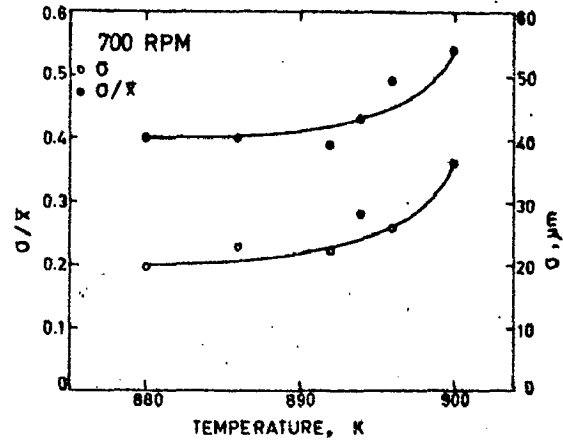


Fig. 5a. 700 rpm.

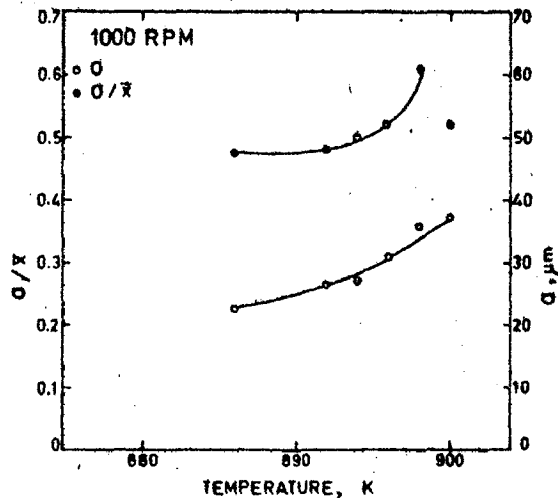


Fig. 5b. 1000 rpm.

Fig. 4a and b. Typical frequency distribution curves for α -particle size for alloy rheocast for two stirring speeds.

Fig. 5a and b. Effect of pouring temperature on standard deviation (σ) and coefficient of variation (σ/\bar{X}) of α -particle size for rheocastings for two stirring speeds.

Table 1. Effect of process variables on the shape and size of α -particles, and mechanical properties.

Sl. No.	Stirrer speed, r.p.m.	Pouring Temp. K	l/d	\bar{X} μm	UTS MNm^{-2}	Elongation %	Izod Impact value, Nm	Hardness VHN
1	700	900	1.6	66.6	172	0	2	77
2	700	896	1.6	51.6	170	0	2	85
3	700	894	1.6	59.3	164	0	2	83
4	700	892	1.6	56.2	170	0	2	88
5	700	886	1.4	56.8	168	0	2	80
6	700	880	1.4	49.5	184	0	2	83
7	1000	900	1.9	71.6	211	0	2	87
8	1000	898	1.6	59.6	201	0	2	83
9	1000	894	1.6	59.2	194	0	2	82
10	1000	892	1.4	55.2	196	0	2	85
11	1000	886	1.7	47.6	172	0	2	83
12	-	950	-	-	216	0	2	81

under a given condition, the dendritic mode of solidification appears in the slurry and enhances with further increase in cooling rate. The higher pouring temperature may promote a tendency of dendritic coarsening of proeutectic α -phase in the mould.

The variation of average particle size (\bar{X}) with pouring temperature at two stirring rates at 700 and 1000 r.p.m. has been revealed by figs. 3a and b. The largest particles measured in top twenty five percent and the smallest particles measured in last twenty five percent of cumulative curve has been designated as PSL (\bar{X}) and P.S.S. (\bar{X}) respectively in figs. 3a and b following the size distribution analysis reported in literature¹²). Both \bar{X} and PSL (\bar{X}) have been found to decrease with decreasing temperature. However, stirring rate does not seem to have any marked effect on \bar{X} and PSL (\bar{X}). These observations suggest that the effect of stirring rate on the particle size during primary solidification is completely marred by the large extent of growth of particles during secondary solidification. Higher pouring temperature offers greater opportunity for subsequent growth and hence leads to an increase in average particle size. Growth during secondary solidification promotes non-sphericity characterised by length to diameter ratio (l/d) as shown in table 1. An increase in the pouring temperature promotes greater non-sphericity but does not show any significant influence on PSS (\bar{X}).

Typical curves showing measured size distribution of α -particles are given in figs. 4a and b. The effect of pouring temperature on standard deviation (σ) and coefficient of variation (σ/\bar{X}), calculated from the size distribution data, has been shown in figs. 5a and b. It is observed that both σ and σ/\bar{X} decrease with decrease in pouring temperature. For all pouring temperature values of σ and σ/\bar{X} are slightly higher for higher stirring rate. This observation is contrary to the general observations¹¹⁾¹²⁾ in case of water-quenched slurries. This is again attributed to the effect of secondary solidification discussed in preceding paragraphs. The influence of stirring rate is reflected in slightly lower value of PSS (\bar{X}) for higher stirring rate (compare figs. 3a and b). This results in broader size distribution curve for higher stirring rate yielding higher values of σ and σ/\bar{X} .

Mechanical Properties

Results of mechanical tests are summarized in table 1. No change in hardness, Izod value and elongation has been observed within the limits of experimental accuracy. All castings, whether rheo- or conventional, were found to be extremely brittle as reflected in tensile and impact tests. Significant variation in tensile strength with casting condition was observed, but surprisingly all rheocastings showed lower tensile strength compared to the conventional casting.

Casting quality was evaluated on the basis of porosity in order to assess its role in the variation in tensile strength with casting condition. High porosity ranging from 3.8 to 11 % was observed for rheocastings at 700 r.p.m. The porosity values for castings at 1000 r.p.m. ranged from 0.6 to 4.5 % as against 6 % for conventional casting indicating that the casting quality can be improved by rheocasting employing high stirring rate. This observation is quite in line with the results of radiographic examination on steels and copper base alloys reported in literature²⁰⁾ and it has been attributed to semi-solid state and rheological properties of slurries. At low stirring rates and consequent high viscosity of the slurry sound castings may not be produced as the

last portions to solidify may not properly flow to compensate for solidification shrinkage. This probably accounts for higher porosity for castings at 700 r.p.m. Slurry flow-rate measured through the 12 mm diameter hole at the bottom of crucible also indicates somewhat lower values ranging from 125 to 173 gs^{-1} for 700 r.p.m. as compared to 142 to 186 gs^{-1} for 1000 r.p.m. implying higher viscosity at lower stirring rate. In many cases hole of the crucible got choked and, therefore, only a few data on flow rate could be obtained.

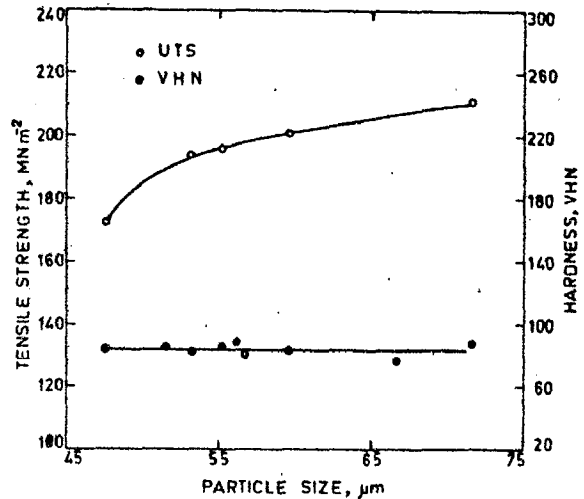


Fig. 6. Effect of α -particle size on tensile strength and hardness of rheocastings at 1000 rpm.

The absence of any regular trend in the mechanical properties of rheocast alloys stirred at 700 r.p.m. may be attributed to random porosity behaviour. For casting at 1000 r.p.m. showing low porosity, a plot of tensile strength versus α -particle size was made as shown in fig. 6. The general trend shows an increase in tensile strength with the increase in particle size. Incidentally, larger particle sizes have been observed in samples with higher length to diameter ratio resulting from the slurries cast at higher pouring temperature. For large particles with more of dendrites, the tensile strength is comparable to that of conventional casting which is 216 MNm^{-2} . It is generally expected that finer size of ductile particles dispersed in brittle matrix will increase the strength by limiting the size of most severe flaw in the matrix when the inter-particle distance is of the order of critical crack size. This phenomenon has been demonstrated by Nason²³⁾ for spherical tungsten particles dispersed in glass. However, in the present investigation, for castings showing smaller particle size and with greater sphericity of α -particles, lower strength values have been observed suggesting that the above mechanism of strengthening is not applicable in the present case probably because the interparticle spacing is greater than the critical crack size for the eutectic matrix. For castings having larger particle size and elongated shape, the strength values are higher. These castings have been obtained by pouring from relatively higher temperature resulting in larger extent of dendritic growth in the mould resulting in elongated α -particles as evident in fig. 2c.

On the basis of a model, Evans et al.²²⁾ have anticipated that a composite of cylindrical ductile particles dispersed in brittle matrix will have higher strength compared to that of a composite containing spherical particles. The cylindrical ductile particles restrain the extension of crack and its further propagation is possible by pull-outs or failure of

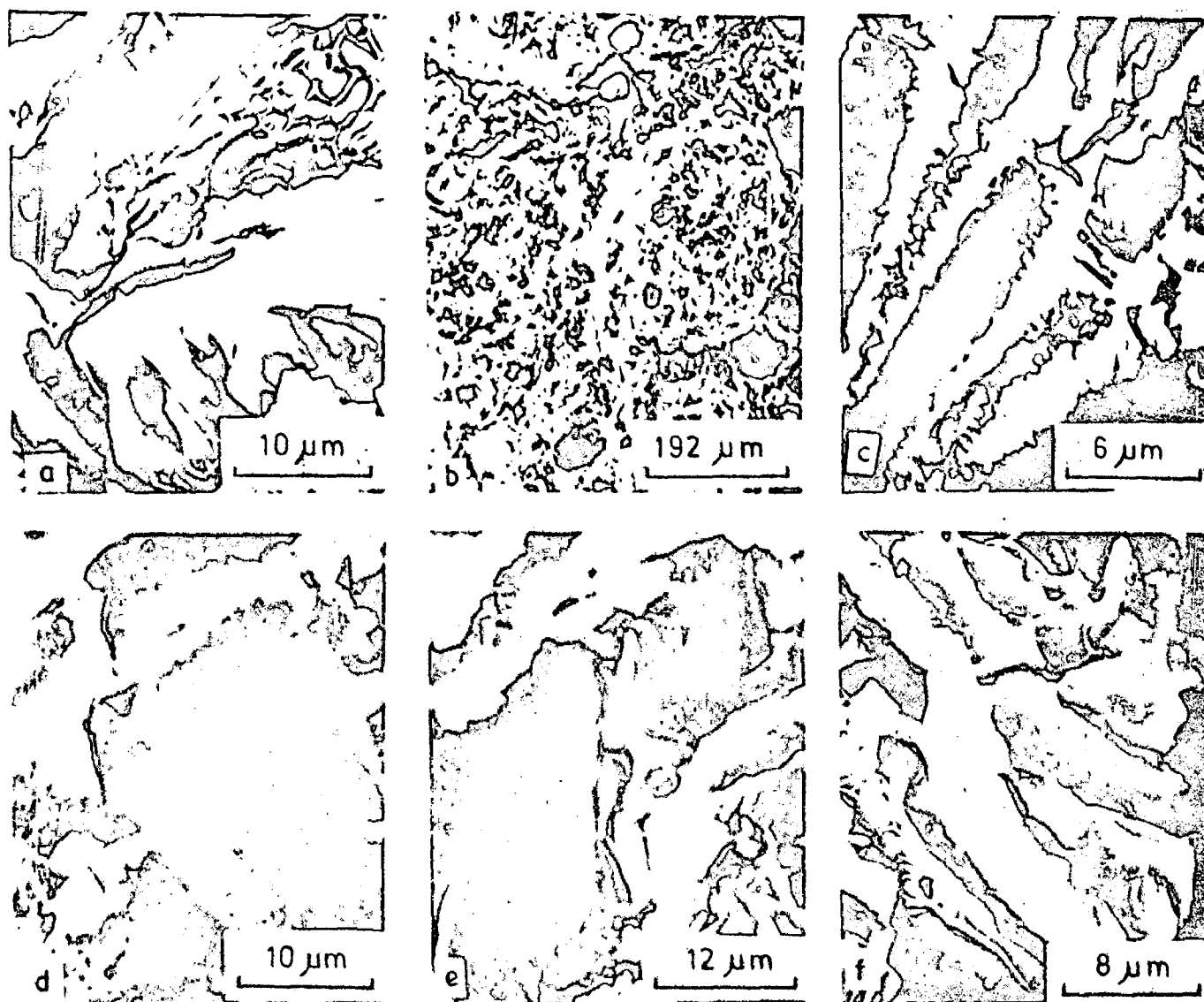


Fig. 7a to f. SEM fractographs showing (a) extensive cracking of α -CuAl₂ interface, (b) pull-out of α -particles, (c) ductile failure of eutectic α -lamellae grown over proeutectic α -particles, (d) failure of α -lamellae not originating from proeutectic α -particles, (e) fracture of α -particles and exposed dendrite arms, (f) α -particle restraining a crack.

ductile particles. The present observations of higher strength for elongated α -particle composites are in agreement with their expectations.

Examination of the fractured surface under SEM reveals that the crack has generally been initiated either at the inclusion or at the α -CuAl₂ interface in the eutectic matrix as shown in fig. 7a. Invariably in all the samples it has been observed that α -CuAl₂ interface has cracked extensively. In the samples with nearly spheroidal particles the cracks have propagated by easily pulling out the ductile particles from its path as shown in fig. 7b. The restraining effect of these particles has been insignificant as reflected by lower strength and absence of any appreciable elongation. A further examination into some of the voids left after the pull-out of ductile particles shows that the eutectic α -lamellae adjacent to the void have failed in a ductile manner indicating that these α -lamellae have grown over proeutectic ductile particles, as shown in fig. 7c, while in some other voids the lamellae did not show any ductile failure as shown in fig. 7d probably because these lamellae did not originate from the proeutectic particles but terminated there due to impingement effect. However, in both these types of voids we notice that some small cracks have initiated and are arrested in these lamellae.

The composites containing the elongated particles did not show many voids caused by the pull-out. The role of the elongated ductile particles in restraining the cracks can be clearly seen in fig. 7f. As a result these samples have shown higher strength although no appreciable elongation has been observed.

The samples cast conventionally to solidify the α -phase in a dendritic network have shown the highest strength and the examination of the fractured surface shows that the crack could not propagate through and through without breaking the ductile α -phase as shown in fig. 7e. The network could obviously restrain the cracks much more effectively compared to the spherical and even the elongated particles.

Conclusions

(1) The morphology, size and distribution of proeutectic α -phase are significantly modified by rheocasting process and its variables namely, the pouring temperature and the stirring speed. Both \bar{X} and σ/\bar{X} have been found to increase with increase in pouring temperature. Higher values of σ/\bar{X} and l/d ratio have been observed for stirring at 1000 r.p.m. as compared to those at 700 r.p.m. Stirring

rate has, however, no marked influence on the observed average particle size (\bar{X}).

(2) High porosity ranging from 3.8 to 11% was observed for rheocasting at 700 r.p.m. but rheocastings at 1000 r.p.m. showed low porosity from .6 to 4.5% as against 6% for conventional casting. This confirms that the soundness of casting may be improved by rheocasting process employing higher stirring rate.

(3) Rheocast Al-10 wt.% Cu alloy has generally lower tensile strength than the conventionally cast alloy either due to higher porosity obtained in certain rheocast alloy or due to breakdown of dendritic network of proeutectic α -phase. SEM fractographic studies have revealed that the dendritic network is more effective in restraining crack propagation through the brittle eutectic resulting in higher tensile strength in conventionally cast alloy.

Literature

- 1) R. MEHRABIAN and M. C. FLEMINGS, *Trans. AFS* **80** (1972) 173.
- 2) M. C. FLEMINGS and R. MEHRABIAN, *Trans. AFS* **81** (1973) 81.
- 3) E. F. FASCETTA, R. G. RIEK, R. MEHRABIAN and M. C. FLEMINGS, *AFS Cast Met. Res. JI.* **9** (4) (1973) 167.
- 4) M. C. FLEMINGS, *Proc. Workshop on Rheocasting, Army Materials and Mechanics Research Centre, U.S.A.*, R. D. French and S. H. Frank, eds., (Feb. 1977) 3.
- 5) R. MEHRABIAN and M. C. FLEMINGS, *New Trends in Materials Processing*, ASM (1976) 98.
- 6) M. C. FLEMINGS, R. G. RIEK and K. P. YOUNG, *AFS Int. Cast Met. Res. JI.* **1** (3) (1976) 11.
- 7) D. Van CLEAVE, *Iron Age Metalwork. Int.* **18** (12) (1977) 34.
- 8) T. Z. KATTAMIS, *Proc. Symp. on Quality Control of Engg. Alloys and the Role of Metals Science*, H. Nieswaag and J. W. Sch-wut, eds., Delft (1977) 189.
- 9) P. A. PARKHUTIK and V. S. OCHERETANYI, *Liteinoe Proizvod* **5** (1976) 24.
- 10) D. B. SPENCER, R. MEHRABIAN and M. C. FLEMINGS, *Met. Trans.* **3** (1972) 1925.
- 11) P. A. JOLY and R. MEHRABIAN, *J. Mat. Sc.* **11** (1976) 1393.
- 12) S. D. E. RAMATI, G. J. ABBASCHIAN and R. MEHRABIAN, *Met. Trans.* **9B** (1978) 241.
- 13) M. C. FLEMINGS, *Proc. Workshop on Rheocasting, Army Materials and Mechanics Research Centre, U.S.A.*, R. D. French and S. H. Frank, eds., (Feb. 1977) 33.
- 14) S. D. E. RAMATI, D. G. BACKMAN, Y. V. MURTY, G. J. ABBASCHIAN and R. MEHRABIAN, *ibid.*, p. 13.
- 15) Y. V. MURTY, D. G. BACKMAN and R. MEHRABIAN, *ibid.*, p. 95.
- 16) J. M. OBLAK and W. H. RAND, *Met. Trans.* **7B** (1976) 705.
- 17) *Iron Age Metalwork. Int.* **15** (2) (1976) 31.
- 18) I. I. PROKHOROV, L. I. ROMANOV and S. N. KRASOTSKAYA, *Liteinoe Proizvod* **8** (1979) 10.
- 19) K. P. YOUNG, *Proc. Workshop on Rheocasting, Army Materials and Mechanics Research Centre, U.S.A.*, R. D. French and S. H. Frank, eds., (Feb. 1977) 109.
- 20) K. P. YOUNG, R. G. RIEK and M. C. FLEMINGS, *Metals Technology* **6** (4) (1979) 130.
- 21) C. C. LAW, J. D. HOSTETLER and L. F. SCHULMEISTER, *Mat. Sc. Engg.* **38** (2) (1979) 123.
- 22) A. G. EVANS, A. H. HEUER and D. L. PORTER, in *Advances in Research on the Strength and Fracture of Materials*, Vol. 1., D. M. R. Taplin, ed., Pergamon Press, Oxford (1978) 529.
- 23) D. O. NASON, in *Modern Composite Materials*, L. J. Broutman and R. H. Krock, eds., Addison-Wesley, Reading, MA (1967) 72.

(Eingegangen am 30. September 1981)

Zeiss - Partner der Industrie bei Auflichtuntersuchungen zur Material-, Produkt- und Qualitätskontrolle



Beispiel: Mikroskop Standard WL.

Ideal für das Werkstofflabor, für Untersuchungen im Hellfeld, Dunkelfeld und Differential-Interferenzkontrast bei metallografischen Normvergrößerungen.

Rasch ergänzbar für weitere Untersuchungsverfahren.

Aufflichtkondensator mit Lichtleiterbeleuchtung, mit Objektivrevolver oder Schnellwechsel für Einzelobjektive Epiplan HD.

(Druckschrift: 41-117)

Beispiel: Mikroskop Universal M.

Speziell konzipiert für Metallografen, Werkstoffprüfer und Techniker, die alle bekannten und künftigen Kontrastierungsverfahren nutzen und die schnell zwischen verschiedenen Untersuchungsmethoden wechseln wollen.

(Druckschrift: 41-140)

Beispiel: Inverses Mikroskop ICM 405.

Umgekehrte Bauweise, die viele Vorteile bringt. Hohe Stabilität begünstigt die Untersuchung schwerer, großformatiger Objekte.

Automatische Mikrofotografie auf Großbild- und Kleinbildformat.

(Druckschrift: 41-635)



Nutzen Sie unser Informationsangebot.
Schreiben Sie an
Carl Zeiss
D-7082 Oberkochen

Microstructure of Rheocast Hypoeutectic Al-Cu Alloys*

Priya Ranjan Prasad*, Subrata Ray*, Jawahar Lal Gaiindhar**, and Madan Lal Kapoor*

(* Department of Metallurgical Engineering and ** Department of Mech. and Industrial Engineering, University of Roorkee, Roorkee-247672, India)

Microstructural features of rheocast hypoeutectic Al-Cu alloy containing 6% and 10% Cu, have been compared. The average size of the proeutectic α -phase particles in the 6% Cu alloy has been found to increase with decrease in pouring temperature and some abnormally large α -particles, believed to be formed by 'particle coalescence', have been observed at 886 K. However, no such particles have been observed in case of the 10% Cu alloy even at 880 K. The difference in the microstructural features of these rheocast alloys has been explained on the basis of the influence of copper content on the growth rate of α -phase particles.

Gefüge von rheocasted untereutektischen Al-Cu-Legierungen

Die Gefügemorphologie von rheocasted (Gießen mit teilerstarrter Schmelze) untereutektischer Al-Cu-Legierungen mit 6 und 10% Cu wurden verglichen. Die Durchschnittsgröße der proeutektischen α -Teilchen in der 6% Cu-Legierung steigt mit abnehmender Gießtemperatur, und einige abnormal große α -Teilchen, die sich wahrscheinlich durch „Teilchen-Koaleszenz“ bilden, wurden bis 886 K beobachtet. In der 10% Cu-Legierung wurden jedoch keine solchen Teilchen gefunden, auch nicht bei 880 K. Der Unterschied in der Gefügeausbildung dieser rheocasted Legierungen wird mit dem Einfluß des Cu-Gehaltes auf die Wachstumsgeschwindigkeit der α -Teilchen erklärt.

Rheocasting is an emerging solidification processing technique based on vigorous agitation of a solidifying melt by mechanical stirring which yields a partially solidified alloy slurry suitable for subsequent casting by conventional methods. The structure of the slurry is unique in that it contains non-dendritic spheroidal solid particles suspended in the remaining liquid¹⁾²⁾. The size and distribution of these particles have been related to process variables primarily the cooling rate and the degree of agitation³⁾⁴⁾⁵⁾.

The isothermal coarsening of these particles in solid-liquid temperature range has been shown⁶⁾ to occur by both diffusion controlled growth and particles-coalescence in absence of stirring. Even during stirring, the solid particles have been thought to grow by particle-coalescence or growth-twinning mechanism⁷⁾. However, the published literature does not throw any light as to the factors responsible for promoting a particular growth behaviour. The significance of the mechanism of growth does not lie only in determining the progress of solidification during slurry production or subsequent casting in the mould, but the size, distribution, and morphology of the particles in cast structure is also governed by the prevailing growth mechanism. In this paper, the microstructural features of rheocast hypoeutectic Al-Cu alloys have been presented with a view to identify the possible growth mechanisms responsible for observed rheocast microstructures.

Experimental Work

The experimental set-up has been shown in an earlier publication⁸⁾. Two hypoeutectic Al-Cu alloys with 6 wt.% and 10 wt.% Cu were used in the present investigation. For each casting about 500 g of the alloy was melted in the graphite crucible having a 12 mm hole at the bottom plugged with a graphite stopper. The furnace was then switched off and the melt was allowed to cool in the furnace. The melt tem-

perature was continuously measured with a sheathed chromel-alumel thermocouple using a temperature potentiometer. When temperature came down to the liquidus, the stirrer having a four blade impeller was introduced and the melt was agitated vigorously during its primary solidification. The speed of the stirrer was measured with a strobometer. The average cooling rate during primary solidification was 0.5 Ks⁻¹. At the desired pouring temperature, stirring was stopped, the graphite stopper removed, and the slurry was cast into a 30 × 30 × 250 mm ingot mould made of steel. In order to study the slurry structure just before casting, some samples were sucked out from the top of the crucible with a Corning glass tube fitted with a horn-bulb, and quenched in water. Suitable samples were cut from each casting for optical microscopic studies and the size and distribution of proeutectic α -particles in each sample were determined by standard techniques of quantitative metallography.

Figures 1 and 2 reveal typical microstructures of rheocast Al-6%Cu and Al-10%Cu alloy ingots respectively. The proeutectic α -phase particles observed in these micrographs consist of two types of particles—one, those which nucleate during primary solidification, but grow both during primary as well as subsequent solidification in the mould (primary particles); and the other, those which nucleate and grow independently in the mould during final solidification (secondary particles). It is generally not possible to identify the two types of particles by conventional metallography when their sizes are of the same order of magnitude. However, in case of Al-6%Cu alloy, some of the primary particles, marked P in fig. 1c, are easily identified at 886 K because of their characteristic size and morphology.

The variation of average size of α -particles with pouring temperature has been shown in figs. 3 and 4 for Al-6%Cu and Al-10%Cu alloys, respectively. In case of Al-6%Cu alloy, the average particle size remains unaltered until the pour-

* This work forms a part of Ph. D. Thesis work of P. R. Prasad.

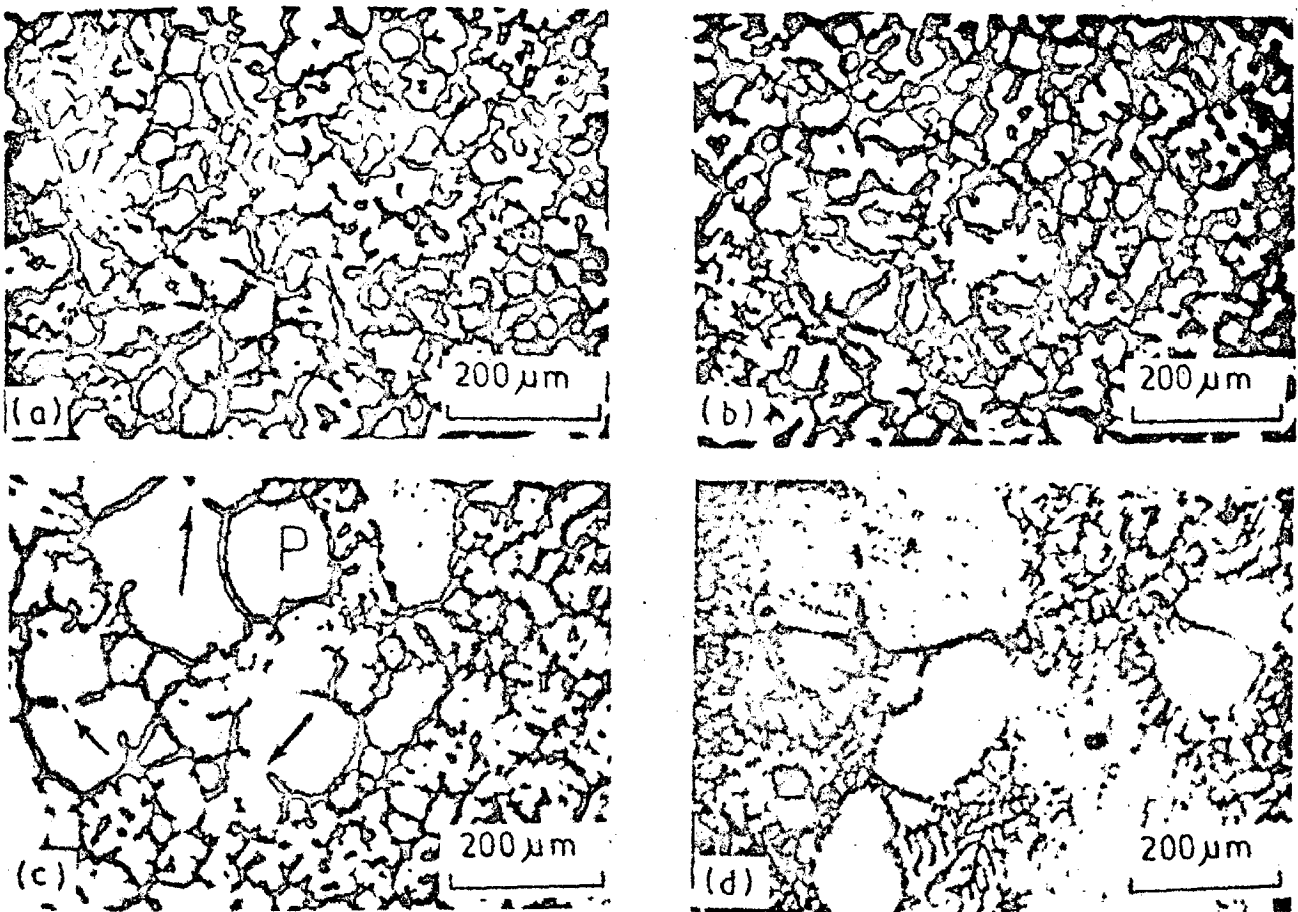


Fig. 1a to d. Optical micrographs of rheocast Al-6%Cu alloy: stirring rate 700 rpm, pouring temperature (a) 905 K, (b) 898 K, (c) stirring rate 1000 rpm, pouring temperature 886 K and (d) slurry water-quenched from 886 K.

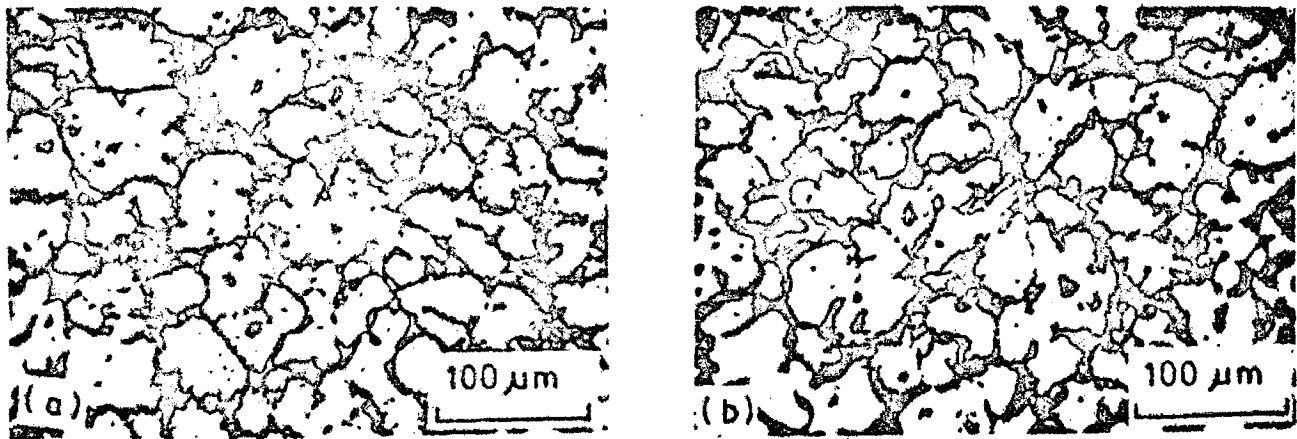


Fig. 2a and b. Optical micrographs of rheocast Al-10%Cu alloy: stirring rate 700 rpm, pouring temperature (a) 896 K and (b) 880 K.

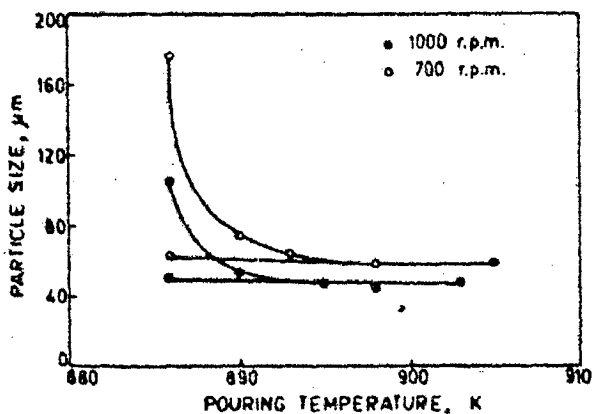


Fig. 3. Effect of pouring temperature on the average size of α -particles in rheocast Al-6%Cu alloy ingots.

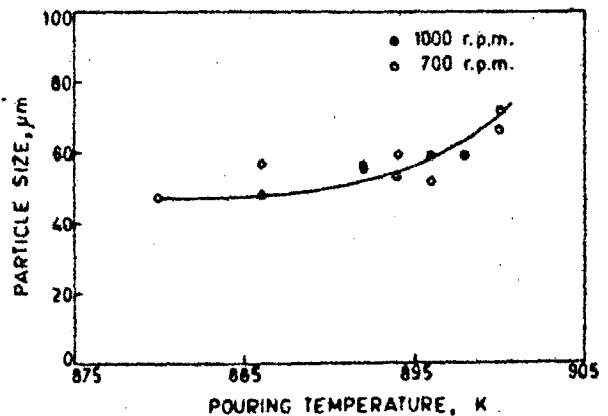


Fig. 4. Effect of pouring temperature on the average size of α -particles in rheocast Al-10%Cu alloy ingots.

ing temperature is lowered to 886 K when a sudden increase in the size of some of the primary particles is observed as indicated in fig. 3. However, the size of secondary particles remains nearly the same as the average particle size observed at higher pouring temperatures. Such a situation corresponds to the microstructure depicted in fig. 1c. Microstructure of waterquenched sample, shown in fig. 1d, confirmed that the large particles are the primary particles and not those formed in the mould. The average particle size is lower for higher stirring rate at all pouring temperatures.

The sudden increase in the size of primary particles between 890 and 886 K cannot be explained simply on the basis of diffusion controlled growth. The most probable mechanism accountable for such an abnormal growth appears to be the coalescence and sintering of particles. Obviously, the probability of coalescence is increased at lower pouring temperature (alternatively, higher fraction of solid particles in the slurry) as observed in the present case. During stirring, solid particles moving within the slurry always pass through such zones where the hydrodynamic forces are weak and insufficient to disrupt the interparticle bond formed after the collision of the particles. The growth of the neck formed between the colliding particles, indicated by arrow in fig. 1c, eventually leads to the formation of particles much bigger in size than the particles from which they form. The evidence of "special boundaries" observed⁷⁾⁹⁾ within the primary particles also speaks in favour of coalescence mechanism for the formation of large primary particles.

For Al-10%Cu alloy, it is observed in fig. 4 that the average particle size increases with the increase in pouring temperature and the stirring rate has no marked influence on the average size of the particles. Even at 880 K, no large primary particles formed by coalescence are observed, fig. 3b. This discrepancy between the observed microstructural features of Al-6%Cu and Al-10%Cu alloy rheocastings is attributed to the difference in copper content of the two alloys. It is known¹⁰⁾ that the growth rate of proeutectic α -phase in Al-Cu alloys decreases with increase in copper content. Obviously then, the neck formation between the colliding particles will be at a slower rate for the 10%Cu alloy leading to a weaker interparticle bond. Such a bond could be easily broken by the hydrodynamic forces preventing the particles from coalescence. In contrast to

this, the faster neck growth in 6%Cu alloy will result in stronger bonds not easily disrupted by hydrodynamic forces and thus the particles coalesce. The absence of large primary particles formed by coalescence in Al-20%Cu alloy⁵⁾ and the occurrence of such particles in Al-4,5%Cu alloy⁹⁾ provide further evidence in support of the role of copper content on the microstructural features of rheocast Al-Cu alloys outlined above.

Conclusions

On the basis of the results of the present investigation on the microstructural features of rheocast hypoeutectic Al-Cu alloys, following conclusions may be drawn:

1. With the decrease in pouring temperature, the average size of the proeutectic α -phase particles increases in case of Al-6%Cu alloy and decreases in case of Al-10%Cu alloy.
2. Higher stirring rate decreases the average size of the α -particles in case of the 6%Cu alloy but has no marked influence in case of the 10%Cu alloy.
3. Lower copper content provides favourable condition for particle coalescence and sintering, leading to the formation of some abnormally large α -particles at lower pouring temperature.

Literature

- 1) D. B. SPENCER, R. MEHRABIAN, and M. C. FLEMINGS, *Met. Trans.* **3** (1972) 1925.
- 2) R. MEHRABIAN and M. C. FLEMINGS, *New Trends in Materials Processing* ASM, Metals Park (1976) 98.
- 3) P. A. JOLY and R. MEHRABIAN, *J. Mater. Sci.* **11** (1976) 1393.
- 4) S. D. E. RAMATI, G. J. ABBASCHIAN, and R. MEHRABIAN, *Met. Trans.* **9B** (1978) 241.
- 5) A. VOGEL, *Metal Science* **12** (1978) 576.
- 6) J. M. OBLAK and W. H. RAND, *Met. Trans.* **7B** (1976) 699.
- 7) N. APAYDIN, K. V. PRABHAKAR, and R. D. DOHERTY, *Mater. Sci. Eng.* **48** (1980) 145.
- 8) P. R. PRASAD, S. RAY, J. L. GAINDHAR, and M. L. KAPOOR, *Z. Metallkde.* **73** (1982) 420.
- 9) P. R. PRASAD, S. RAY, J. L. GAINDHAR, and M. L. KAPOOR, to be published.
- 10) K. H. CHIEN and T. Z. KATTAMIS, *Z. Metallkde.* **61** (1970) 475.

(Eingegangen am 23. März 1982)

